SYSTEM IDENTIFICATION AND TRAJECTORY OPTIMIZATION FOR GUIDED STORE SEPARATION

By

RYAN E. CARTER

A DISSERTATION PRESENTED TO THE GRADUATE SCHOOL
OF THE UNIVERSITY OF FLORIDA IN PARTIAL FULFILLMENT
OF THE REQUIREMENTS FOR THE DEGREE OF
DOCTOR OF PHILOSOPHY

UNIVERSITY OF FLORIDA

2012

Dedicated to my wife Melanie and my five children Ethan, Isaac, Levi, Micah, and Rose, for their unconditional love, encouragement, and support. To my children: May you be blessed with the opportunity to fulfill your dreams as I have mine.

ACKNOWLEDGMENTS

If I have seen further, it is by standing upon the shoulders of giants.

— Sir Isaac Newton, *Letter to Robert Hooke, February 1676*

Though individuals often receive the credit for significant accomplishments, it is usually a collaborative effort with many contributions made behind the scenes. Such is the case for this work.

I would like to thank the Air Force SEEK EAGLE Office (AFSEO) for sponsoring this research and academic endeavor. The AFSEO has provided a challenging and satisfying work environment for many years and I look forward to more to come. Additionally, I am appreciative the Science, Mathematics, and Research for Transformation (SMART) Scholarship Program which provided the majority of the financial resources to conduct this research. I would especially like to thank Dr. Richard Lind for his guidance and advice throughout my doctoral studies.

I would also like to thank my friends and family for their support and encouragement. My wife Melanie and our five children (Ethan, Isaac, Levi, Micah, and Rose) have played a significant role in my academic achievements by providing a lively and flourishing home life. My father is often my source of motivation and my deep respect for him has led to many achievements that I would have otherwise never attempted. Most significantly, I am thankful for my relationship with Jesus Christ, the author and finisher of my faith.

TABLE OF CONTENTS

LIST OF TABLES

LIST OF FIGURES

Abstract of Dissertation Presented to the Graduate School
of the University of Florida in Partial Fulfillment of the
Requirements for the Degree of Doctor of Philosophy

SYSTEM IDENTIFICATION AND TRAJECTORY OPTIMIZATION FOR GUIDED STORE SEPARATION

By

Ryan E. Carter

August 2012

Chair: Richard C. Lind
Major: Mechanical and Aerospace Engineering

Combat aircraft utilize expendable stores such as missiles, bombs, flares, and external tanks to execute their missions. Safe and acceptable separation of these stores from the parent aircraft is essential for meeting the mission objectives. In many cases, the employed missile or bomb includes an onboard guidance and control system to enable precise engagement of the selected target. Due to potential interference, the guidance and control system is usually not activated until the store is sufficiently far away from the aircraft. This delay may result in large perturbations from the desired flight attitude caused by separation transients, significantly reducing the effectiveness of the store and jeopardizing mission objectives. The purpose of this research is to investigate the use of a transitional control system to guide the store during separation. The transitional control system, or “store separation autopilot”, explicitly accounts for the nonuniform flow field through characterization of the spatially variant aerodynamics of the store during separation. This approach can be used to mitigate aircraft-store interference and leverage aerodynamic interaction to improve separation characteristics.

This investigation proceeds in three phases. First, system identification is used to determine a parametric model for the spatially variant aerodynamics. Second, the store separation problem is recast into a trajectory optimization problem, and optimal control theory is used to establish a framework for designing a suitable reference trajectory with explicit dependence on the spatially variant aerodynamics. Third, neighboring optimal

control is used to construct a linear-optimal feedback controller for correcting deviations from the nominal reference trajectory due varying initial conditions, modeling errors, and flowfield perturbations. An extended case study based on actual wind tunnel and flight test measurements is used throughout to illustrate the effectiveness of the approach and to highlight the anticipated benefits of guided store separation.

CHAPTER 1
BACKGROUND AND INTRODUCTION

1.1 Motivation

Tactical fighter and bomber aircraft have been used to carry and deliver ordinance since shortly after the dawn of aviation. In the earliest stages of air combat, separation of stores from the parent aircraft was of little concern. However, during the Vietnam War, the employment of heavy stores from larger jet-powered aircraft, such as the McDonnell Douglas F-4 Phantom, began to present difficulties for aircraft-store compatibility. Specifically, scenarios in high-speed flight were encountered where the released store failed to separate cleanly from the aircraft and instead became a projectile threatening the aircraft and on occasion re-contacting the aircraft in flight causing catastrophic damage and loss of life.

A store released from an aircraft in flight must traverse a nonuniform and unsteady flow field that may include complex shock interactions, large velocity gradients, regions of locally separated or reversed airflow, and severe flow angularity in the form of sidewash and downwash. Stores released from an internal weapons bay may also be subjected to a wake disturbance from the spoiler, dynamic pressure and velocity gradients across the shear layer, high frequency vibrations due to acoustic noise, and large perturbations in flow properties due to cavity oscillations.

Although the region of nonuniform flow near the aircraft is exceedingly small compared to the full length of the store ballistic or fly-out trajectory, the effects are significant. The flow field characteristics may cause the store to exhibit behavior that compromises the safety of the airframe and crew or that compromises the effectiveness of the store itself. Prediction of the flight characteristics of the store in the vicinity of the aircraft is therefore vitally important for ensuring the safety and effectiveness of the release. Modeling and Simulation capabilities also play an integral role in the cost-effective assessment of separation characteristics for a range of aircraft and store

configurations throughout the aircraft flight envelope. For challenging programs, the corresponding ground and flight test activities require a significant amount of time and resources to complete. Thus, store separation engineering is an integral part of air combat system development.

1.2 Problem Description

Store separation engineering, a subset of aircraft-store compatibility, is concerned with the flight characteristics of a store in proximity of the aircraft and other stores. Ground test, flight test, simulation, and analysis procedures have been developed which largely address the safety-of-flight issues first encountered in the Vietnam era. In most cases, the store can be ejected away from the aircraft with a sufficient vertical velocity and nose-down pitch rate to ensure safe separation. However, with the advent of smart weapons, standoff capabilities, and focused lethality the challenge in successful store separation has shifted from safety to acceptability [2]. Whereas an unsafe separation may threaten the parent aircraft, an unacceptable separation may result in a failed mission or significant collateral damage due to guidance problems, loss of control, or damage to the store caused by the separation transients.

Modern sophisticated “smart” weapons are equipped with sensitive onboard electronics including inertial measurement systems, GPS units, sensors, seekers, and guidance computers. Standoff capability (the desirable ability to release a munition far away from the intended target) has resulted in complex aerodynamic shapes with neutral dynamic stability margins designed for maximum glide performance and minimal energy loss. Focused lethality (the desirable ability to destroy a designated target while minimizing collateral damage) has resulted in munitions that are smaller and lighter and therefore more dramatically affected by the exigent flow field surrounding the aircraft in flight. These tendencies have increased the sensitivity to separation-induced transients [2], potentially leading to large angular rates and attitudes, excessive energy loss, sensor saturation, structural limits, or departure from stable flight modes [3]. The

challenge in store separation is thus to ensure safety while also maintaining acceptability across the flight envelope.

Modern munitions are designed with an onboard guidance and control system to enable precise engagement of the intended targets. However, the control system is not usually activated until the store is sufficiently far away from the aircraft to avoid any potential interference. Often, the separation-induced transients result in large perturbations from the desired flight attitudes that require a dedicated “rate-capture” phase for recovery before the munition can begin the fly-out trajectory. In the relatively few cases where the autopilot is engaged earlier (to prevent build-up of irrecoverable rates and attitudes), the mutual aerodynamic interference between the store and aircraft is neglected in the autopilot design leading to increased risk through reduced confidence in simulation capabilities and potentially unsafe behavior of the autopilot reacting to flow field perturbations without consideration of the nearby aircraft.

The purpose of this research is to investigate the feasibility of using a transitional control system, designed with the separation-induced transients in mind, to guide the store along a preferred trajectory.

1.3 Research Objectives

The primary objective of this research is to develop a comprehensive approach to improve the separation characteristics of modern ejector-launched guided munitions by utilizing a transitional control system, or “store separation autopilot”, to guide the store along an optimal trajectory. This investigation is intended to show the significant increase in safety and acceptability that can be achieved through guided store separation with minimal addition in cost and complexity of the guidance and control system.

This dissertation is outlined as follows. First, a brief overview of store separation modeling & simulation methodology is presented. Emphasis is placed on established wind tunnel based prediction methods with some discussion of complementary CFD

based methods. The rigid body equations of motion are derived and the aerodynamic modeling approach used most frequently in store separation analysis is presented. An overview of flight test data reduction and trajectory matching is discussed and demonstrated with actual flight test results. This brief presentation of established store separation modeling and simulation capabilities provides the foundation for the remaining developments.

Next, System Identification (SID) techniques are used to develop a parametric model for the spatially variant aerodynamic characteristics of a store during separation. For nonlinear aerodynamic modeling of aircraft, it is common to use a multivariate polynomial model structure with constant coefficients determined from experimental data [4]. This approach is extended to the store separation problem by postulating a multivariate polynomial model with spatially variant coefficients. The spatially variant coefficients are parametrized as nonlinear functions consistent with the dominant flow field characteristics and physically meaningful boundary conditions. The result of this venture into system identification is a nonlinear parametric model capable of capturing the salient store separation aerodynamics in a compact matrix expression. This reduced order model is a valuable asset in its own right, offering insight into physical drivers of store separation and providing an analytical framework for control system analysis and design. Although the parametric model in this study is an analytical representation of tabular time-averaged wind tunnel data, the techniques could also be applied to aerodynamic data obtained from time-accurate Computational Fluid Dynamics (CFD) trajectories. Extension of these methods to time-variant flowfield data (e.g. turbulence) is left as a future development, though some pointers are given for how this may be achieved.

Third, the store separation problem, with associated safety and acceptability objectives, is restated as a trajectory optimization problem and application of classical optimal control theory is used to develop a solution methodology that yields a candidate

optimal trajectory with respect to the chosen costs and constraints. Indirect optimal control methods are emphasized due to the decreased computational burden compared to direct methods, as well as the additional physical insight offered by development of the 1st order optimality conditions. An example of trajectory optimization is presented using the planar store separation equations of motion and a simplified parametric aerodynamic model. The simplified example is instructive and provides a solid starting point for a more in-depth case study considered subsequently.

Fourth, with the open loop optimal trajectory solution as a reference, a store separation autopilot is developed using the concept of neighboring optimal control (NOC). The separation autopilot is a linear-optimal feedback controller that corrects for deviations from the nominal trajectory due to disturbances, modeling uncertainties, and varying initial conditions. The proposed infinite horizon neighboring optimal control (IHNOC) strategy accounts for the spatially variant aerodynamics near the aircraft and converges to a linear time invariant controller in far field conditions. The performance of the separation autopilot is examined subject to a range of initial conditions, random perturbations, and parameter variations.

Finally, the results above are extended to the full six degree-of-freedom (6DOF), nonlinear, wind tunnel based simulation for select aircraft configurations and flight conditions. The simulated performance of the controlled store separation approach is compared with uncontrolled trajectories for the same initial conditions. Comparisons with flight test data illustrate the significant improvement achievable with guided store separation.

The cumulative process of system identification, trajectory optimization and feedback control represents a comprehensive approach for achieving guided store separation in a realistic environment. A graphical depiction of this process is shown in Figure 6-1. A case study including a representative store with associated wind tunnel

and flight test data is presented throughout to demonstrate the anticipated benefits of guided store separation.

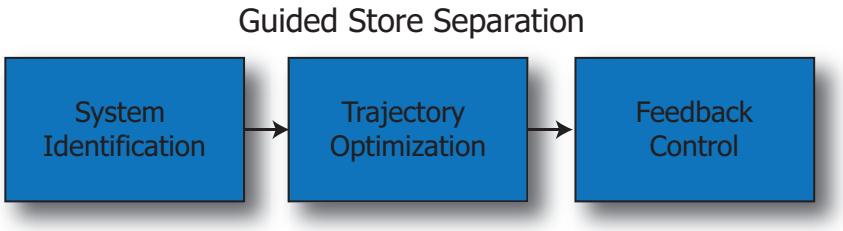

Figure 1-1. Relationship between system identification, trajectory optimization, and feedback control for guided store separation.

1.4 Representative Case Study

The techniques developed during the course of this research are applicable to a wide range of aircraft/store combinations. However, to illustrate the methods, a particular case study was selected. The case study includes the F-16 Fighting Falcon and a representative mid-size, vertically ejector-launched guided munition. Separation of a representative munition from the F-16 is shown in 1-2.

Figure 1-2. F-16 release of a representative guided munition.

The F-16 is a multi-role supersonic fighter aircraft originally developed by General Dynamics. The F-16 can be configured in an air-to-air or air-to-ground configuration and

is equipped to carry a range of external stores. The selected F-16 case study provides an ideal example for presenting established store separation analysis techniques as well as extending the existing capability to include system identification and trajectory optimization. Additional detail on the case study is discussed in later sections and representative wind tunnel and flight test data are presented throughout.

1.5 Contributions

The primary contribution of this research is the development and demonstration of a feasible strategy for implementing guided store separation. Previous studies have highlighted the use of active control to improve separation characteristics, primarily as a side benefit of demonstrating the use of a new CFD capability [5, 6]. However, this is the first work to consider guidance and control specifically for store separation. Guidance herein refers to the determination of the preferred path from release to a stable trimmed flight condition with explicit dependence on the aerodynamic interaction between the store and aircraft. Control herein refers to the manipulation of the aerodynamic forces using control surface deflections to steer the store along the preferred trajectory in the presence of disturbances. In particular, this is the first attempt to determine an optimal trajectory for store separation. This is also the first attempt to design a "store separation autopilot" with explicit dependence on the aerodynamic interaction between the store and aircraft. The dependence of the guidance and control system on the spatially variant aerodynamics relies on a parametric model developed using system identification. This model is also the first attempt to develop a parametric model for store separation aerodynamics. These contributions in terms of system identification, trajectory optimization, and feedback control are summarized below

- Application of system identification to parametric modeling of store separation aerodynamics. Freestream aerodynamics are modeled using a nonlinear multivariate polynomial with constant coefficients. Aircraft/store aerodynamic interference is modeled using a nonlinear multivariate polynomial with spatially variant coefficients. The freestream and interference aerodynamic models are unified in a compact matrix representation that captures the dominant

aerodynamic characteristics of a store during separation and satisfies certain physically meaningful boundary conditions.

- Application of optimal control theory to determine an optimal store separation trajectory for a particular flight condition and flow field of interest. Safety and acceptability performance metrics are quantified as a quadratic cost function. The 1st order necessary conditions for optimal store separation with explicit dependence on spatially variant aerodynamics are developed. Solutions to the optimal control problem are approximated using indirect numerical methods to solve the two-point boundary value problem. Using this approach, the aerodynamic interaction between the store and aircraft is leveraged to improve separation characteristics.

- Application of neighboring optimal control to develop a linear-optimal feedback controller that accounts for deviations from the optimal store separation trajectory. A novel statement of the neighboring optimal control problem with judicious selection of cost and constraints leads to a formulation referred to as Infinite Horizon Neighboring Optimal Control (IHNOC). IHNOC is used to construct a store separation autopilot that accounts for the spatially variant aerodynamics near the aircraft and converges to a linear time invariant controller in far field conditions. Performance of the store separation autopilot in the presence of varying initial conditions, random disturbances, and parameter variations is considered.

The contributions stated above are specific to the field of store separation engineering. Indeed, the focus and intent of this research has been application of identification and control theory to the particular challenges in store separation with the vision of developing technology which may find real-world application in the near future. However, this is not to exclude the academic contributions also gained by this research. Store separation may be considered one particular realization of a class of systems with rapidly varying parameters that depend nonlinearly on the state, e.g. a nonlinear parameter varying system (NLPV). General theory for control of a NLPV system does not exist. However, consideration of store separation provides valuable insight into such a system and the methods developed herein may be useful for application to similar systems.

The concept of infinite horizon neighboring optimal control (IHNOC) introduced here is also a valuable academic contribution. The IHNOC strategy can be used to improve performance for a system that must traverse a nonlinear operating or startup

condition, followed by operation near an equilibrium condition for an indeterminate length of time. An ad-hoc approach to controlling a system that exhibits this type of behavior is to switch between two disparate controllers, but this is an inefficient method that may introduce discontinuities in performance and exacerbate nonlinearities. The alternative IHNOC approach considered here utilizes a single continuous full-state feedback controller that converges to a time-invariant linear-optimal controller as the system nonlinearities are dissipated. The store separation problem can be further identified as a NLPV system that converges to a linear time-invariant (LTI) system under suitable control, and the IHNOC provides an ideal solution for this particular system. The application of IHNOC to systems other than store separation is beyond the scope of this research, but the extended example considered here provides a solid foundation for further development.

Finally, identification and control of flight characteristics in a rapidly varying nonuniform flow field is not limited to store separation. It is also important to other aerospace problems including landing of an aircraft in ground effect or variable winds, aircraft wake-vortex encounter, flight through a microburst or wind shear, flight through severe wind fields in an urban environment, employment of hypersonic research vehicles from high-altitude carrier planes, and flight of multiple aircraft in close proximity such as cooperative configuration or aerial refueling, to name a few. Extension of the methods developed herein to these and similar problems is beyond the scope of the present work. Nevertheless, the theoretical insight gained by application of identification and control to a particular example of problems with spatially variant aerodynamics is instructive.

CHAPTER 2
MATHEMATICAL MODELING OF STORE SEPARATION

2.1 Overview

Mathematical modeling and simulation (M&S) is used to reduce the risk, cost, and schedule of aircraft-stores compatibility efforts and provides a valuable toolset for the practicing store separation engineer. In a general store separation program, M&S will be used to develop a streamlined and cost-effective wind tunnel test, perform sensitivity and uncertainty analyses to determine best and worst-case predicted outcomes, down select to configurations and flight conditions of interest for flight test, assess the risk of each individual flight test event, and ultimately provide a certification recommendation to the authorizing agency for operational use.

The modeling and simulation framework for store separation typically includes aerodynamic data obtained from flight testing, computational fluid dynamics (CFD), and wind tunnel testing. CFD provides a direct and increasingly reliable method for determining store separation characteristics and is often used as an acceptable alternative to wind tunnel test data. CFD can be used to generate time-accurate dynamic store separation trajectories to match flight test [7] or static time-averaged flow field solutions for use in offline simulations [8, 9]. In some anticipated low-risk cases, CFD has been used as the sole source of aerodynamic data to determine separation characteristics prior to or even in lieu of flight test. However, in many applications CFD is not capable of replacing the wind tunnel entirely. Wind tunnel testing has long been the dominant approach for characterizing store separation aerodynamics. Although not without limitations, wind tunnel testing remains the method of choice for projects with limited prior testing, aggressive capability requirements, or a substantial number of configurations and flight conditions. In the most general case, CFD is used as a valuable complement to wind tunnel test data, leveraging the strength of each resource to complete the program with a suitable balance between costs, schedule, and risk.

Emphasis for the present analysis has been placed on modeling with wind tunnel data. The primary reason for this selection is the requirement to perform rapid simulations for identification and optimization. However, given the interchangeable roles of CFD and wind tunnel resources for store separation analysis, some effort has been made to maintain applicability of the research methodologies to both data sources.

Mathematical modeling for store separation involves statement of the rigid body equations of motion and development of mathematical models for each of the relevant components that influence the store during separation. These models may include aircraft maneuvering, ejector performance [10, 11], constraint mechanisms such as rails or pivots [12], aerodynamic effects [13], configuration changes such as deploying wings or fins [14], and control surface deflections [15]. The rigorous development of each of these models is beyond the scope of the present work; instead, emphasis will be placed primarily on rigid body dynamics, aerodynamic modeling, and flight test validation. These three areas provide a sufficient foundation in store separation to support development of system identification and trajectory optimization techniques in Chapters 3 through 5.

2.2 Store Separation Equations of Motion

Mathematical modeling of store separation is accomplished by dividing the separation event into three sequential phases based on the characteristic motion of the store relative to the aircraft. During the first phase, the store is in continuous contact with the aircraft and rigidly attached to the aircraft so the store and aircraft act as a single rigid body. During the second phase, the store and aircraft are in continuous contact but the store is moving relative to the aircraft. The contact forces between the aircraft and store due to the ejector or constraint hardware determine the relative motion. Finally, during the third phase, the store is in free flight and moving relative to the aircraft under the influence of the nonuniform flow field.

The first phase (a single aircraft-store rigid body) is valuable for analysis of flight test results, but has little bearing on the simulation of a store during separation. Indeed, the trajectory time is initiated at the instant of release, so all prior motion has only a secondary effect on the separation through specification of the initial conditions of inertial and flow field properties.

The second phase is highly situation dependent. Development of a suitable ejector or constraint model can be a significant undertaking in itself, often requiring substantial ground test data and analysis to be modeled adequately [11]. For most applications, simulation of the contact forces applied to the store during separation is straightforward when sufficient ground test data are available [16]. This research presumes that an adequate ejector and/or constraint model can be specified. The end-of-stroke conditions (measured or predicted) form the initial conditions for the free-flight phase.

The third phase, consisting of the store in free flight relative to the aircraft, is historically the most difficult to characterize due to mutual aerodynamic interference and it is also the region in which safety and acceptability are determined. Therefore, this region is of particular interest for system identification and trajectory optimization.

The equations of motion for a store in free flight are similar to the equations of motion for an aircraft in free flight since both are governed by the same physical principles. However, a careful distinction is necessary due to the relative motion of two neighboring bodies. Of particular interest is the store motion relative to the aircraft. For this reason, the conventional flight dynamics reference frames, coordinate systems, motion variables and nomenclature are modified to suit the unique application to store separation.

2.2.1 Reference Frames and Coordinate Systems

Analysis of a store separating from an aircraft requires the development of a variety of reference frames and coordinate systems to parameterize the motion variables. Inertial quantities are used to predict the trajectory of the store, relative position and

velocity are used to relate the motion of the store to a maneuvering aircraft, and the local velocity relative to the wind is necessary to estimate the aerodynamic loads on the store during release.

Reference frames and coordinate systems are dissimilar entities. Reference frames are models of physical objects consisting of mutually fixed points, whereas coordinate systems are abstract mathematical devices with no real physical counterpart [17]. A reference frame, defined as a collection of at least three points in three-dimensional Euclidean space such that the distance between any two points in the collection does not change with time [18], is representative of an idealized rigid body. In contrast, a coordinate system is a mathematical construct used to measure the parameters of motion between reference frames.

Distinguishing between reference frames and coordinate systems allows derivation of a vector form of the differential equations of motion that is coordinate-free and appropriate for implementation in any suitable coordinate system. This provides a physical basis for understanding the equations of motion before coordinate systems are introduced with the associated algebraic complexity. Once the differential equations have been expressed in a particular coordinate system, the final step prior to modeling and simulation is to develop a matrix representation of the equations of motion. The matrix representation provides a convenient form for programming the equations of motion in a digital simulation. This three-part process of coordinate-free modeling, coordinate system implementation, and matrix representation provides a systematic way to approach a complicated dynamics problem. Several noted authors including Kane and Levinson [19], Rao [18], and Zipfel [17] have helped to develop and refine this process, adding significantly to the theoretical understanding and practical application of rigid body dynamics. The author has found this process to be particularly valuable for store separation given the distinctive nature and relative complexity of the problem.

The reference frames of interest to store separation include the earth frame, inertial frame, flight frame, aircraft frame, store body frame, atmospheric wind frame, and store wind frame. While in principle it is possible to have multiple coordinate systems attached to each frame (and oriented differently), the coordinate systems are uniquely related to the corresponding frame. In particular, we make use of the earth axis, inertial axis, flight axis, aircraft axis, store body axis, atmospheric wind axis, and store wind axis. Although the names of the reference frames and coordinate axes overlap, it should be noted that reference frames and coordinate systems are different entities and used in different ways. The distinction should become clear through the context of the subsequent discussion. For completion, the reference frames and coordinate axes are defined here.

Aircraft Axis $A\{\mathbf{a}_x, \mathbf{a}_y, \mathbf{a}_z\}$. The Aircraft Axis $A\{\mathbf{a}_x, \mathbf{a}_y, \mathbf{a}_z\}$ is established in the Aircraft Reference Frame A. The aircraft axis is closely related to the conventional aircraft body axis encountered in flight dynamics literature (the directions are aligned; only the points of origin are different). The origin of the aircraft axis, O_A, is coincident with the store CG at release and fixed with respect to the aircraft. The aircraft reference frame rotates to maintain constant orientation with respect to the aircraft at all times. The $\mathbf{a}_x$ direction is parallel to the aircraft body axis and positive in the forward direction as seen by the pilot. The $\mathbf{a}_y$ direction is perpendicular to $\mathbf{a}_x$ and positive out of the right wing of the aircraft (starboard) as seen by the pilot. The $\mathbf{a}_z$ direction is defined by $\mathbf{a}_z = \mathbf{a}_x \times \mathbf{a}_y$ and by consequence is positive downward as seen by the pilot. A graphical depiction of the aircraft axis is shown in Figure 2-1.

Store Body Axis $B\{\mathbf{b}_x, \mathbf{b}_y, \mathbf{b}_z\}$. The Store Body Axis $B\{\mathbf{b}_x, \mathbf{b}_y, \mathbf{b}_z\}$ is established in the Store Body Reference Frame B . The origin of the store body axis, O_B , is determined by the store CG, which may in principle change during the trajectory (due to changing configurations or burning propellant). The $\mathbf{b}_x$ direction is aligned with the centerline of the store and positive out of the nose. The $\mathbf{b}_z$ direction is perpendicular to $\mathbf{b}_x$ and positive downward. The $\mathbf{b}_y$ direction is determined by $\mathbf{b}_y = \mathbf{b}_z \times \mathbf{b}_x$ and by

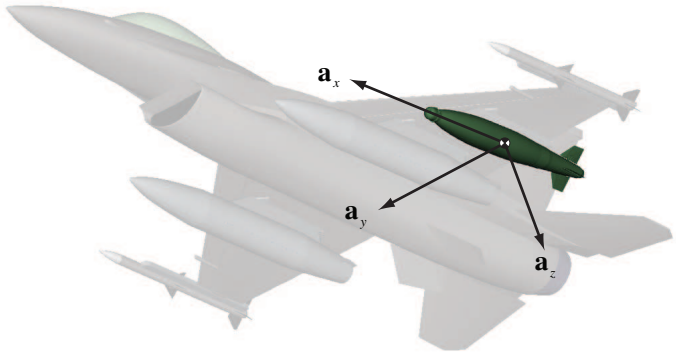

Figure 2-1. Definition of aircraft axis coordinate system.

consequence is positive out of the starboard side of the store. The body axis is oriented with respect to the aircraft axis by the installed incidence angles. The store body axis is shown graphically in Figure 2-2.

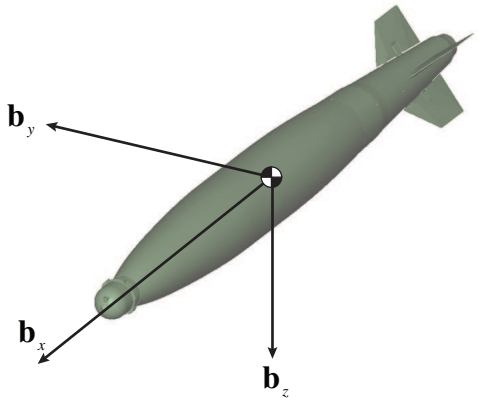

Figure 2-2. Definition of store body axis coordinate system.

Earth Axis $E\{\mathbf{e}_x, \mathbf{e}_y, \mathbf{e}_z\}$. The Earth Axis $E\{\mathbf{e}_x, \mathbf{e}_y, \mathbf{e}_z\}$ is established within the Earth Reference Frame E. For typical flight vehicle navigation equations, the north-east-down directions with reference to the latitude and longitude of the vehicle determine the earth axis directions. However, for store separation, a local approximation is sufficient. Implicit in this approximation is the assumption of a flat earth. The earth axis origin O_E is defined as the store CG at the moment of release. The origin is fixed in

space relative to the surface of the earth. The primary direction of interest for the earth axis is the local vertical $\mathbf{e}_z$, which defines the orientation of the gravity vector. The vector $\mathbf{e}_y$ is perpendicular to $\mathbf{e}_z$ and is positive out of the right wing of the aircraft (starboard) as seen by the pilot. The vector $\mathbf{e}_x$ is defined by the cross product $\mathbf{e}_x = \mathbf{e}_y \times \mathbf{e}_z$ and by consequence lies in the local horizontal plane positive in the forward direction as seen by the pilot.

Inertial Axis $I\{\mathbf{i}_x, \mathbf{i}_y, \mathbf{i}_z\}$. The Inertial Axis $I\{\mathbf{i}_x, \mathbf{i}_y, \mathbf{i}_z\}$ is established in the Inertial Reference Frame I. The choice of an inertial reference frame is of crucial importance for dynamics problems in general and flight mechanics problems in particular. An inertial reference frame is adequately described as a reference frame at rest with respect to the distant stars. In many flight vehicle applications, the earth itself can serve as a suitable reference frame. In store separation analysis, a further approximation is warranted. The inertial reference frame is selected as a hypothetical frame moving at a constant translational velocity relative to the earth, where the velocity and orientation of the frame are determined by the aircraft flight axis velocity and orientation at the instant the store is released. This provides an important advantage of referencing the inertial motion of the store and the aircraft to the same inertial reference frame and provides a convenient way to describe the relative motion between the store and aircraft. In the limiting case of straight and level flight during release, the aircraft itself becomes a suitable inertial reference frame and the store motion relative to the aircraft is directly obtained. For more general aircraft maneuvers, a transformation is straightforward using the common inertial reference frame. The origin of the inertial axis, O_I, is coincident with the store CG at the moment of release and travels in a straight line with a constant velocity equal to the velocity of the flight axis at the instant of release. The $\mathbf{i}_x$ direction is defined by the velocity vector of the aircraft flight axis at the moment of release and remains at a constant orientation with respect to the earth. The $\mathbf{i}_y$ direction is positive in the direction of the right wing of the aircraft (starboard) as seen by the pilot. The $\mathbf{i}_z$ direction is

determined by $\mathbf{i}_z = \mathbf{i}_x \times \mathbf{i}_y$ and consequently is positive in the downward direction. If the aircraft flight path angle and bank angle at $t = 0$ are both identically zero, which is the most common scenario of interest for store separation, then the inertial axis $I\{\mathbf{i}_x, \mathbf{i}_y, \mathbf{i}_z\}$ is aligned with the earth axis $E\{\mathbf{e}_x, \mathbf{e}_y, \mathbf{e}_z\}$, with the origin of the inertial axis moving at a constant velocity relative to the origin of the earth axis.

Flight Axis $F\{\mathbf{f}_x, \mathbf{f}_y, \mathbf{f}_z\}$. The Flight Axis $F\{\mathbf{f}_x, \mathbf{f}_y, \mathbf{f}_z\}$ is established in the Flight Reference Frame F . The flight axis is defined by the direction of the aircraft velocity vector throughout the trajectory. The flight axis is coincident with the inertial axis at the instant of release, but translates and rotates relative to the inertial axis as the aircraft velocity vector changes. For steady flight conditions, the flight axis and inertial axis remain coincident throughout the trajectory. The origin of the flight axis, O_F , is defined as a point coincident with the store CG at the moment of release but is fixed relative to the aircraft and thus translates along with the aircraft during the maneuver. The $\mathbf{f}_x$ direction is aligned with the aircraft velocity vector throughout the maneuver. The orientation of the $\mathbf{f}_x$ direction with respect to the $\mathbf{e}_x$ direction is determined by the aircraft flight path angle. The $\mathbf{f}_y$ direction is perpendicular to $\mathbf{f}_x$ and positive out of the right wing (starboard) as seen by the pilot. The orientation of the $\mathbf{f}_y$ direction with respect to the $\mathbf{e}_y$ direction is determined by the aircraft bank angle. If the aircraft flight path angle and bank angle are identically zero throughout the trajectory, then the flight axis is aligned with the earth axis (and consequently the inertial axis). The orientation of the aircraft axis with respect to the flight axis is determined by the aircraft incidence angles (angle of attack and angle of sideslip). In steady flight, the incidence angles are constant and the orientation of the aircraft axis with respect to the flight axis is constant. The relationship between the flight axis, inertial axis, and earth axis is shown in Figure 2-3.[1]

[1] Displacement of the inertial axis is exaggerated for clarity.

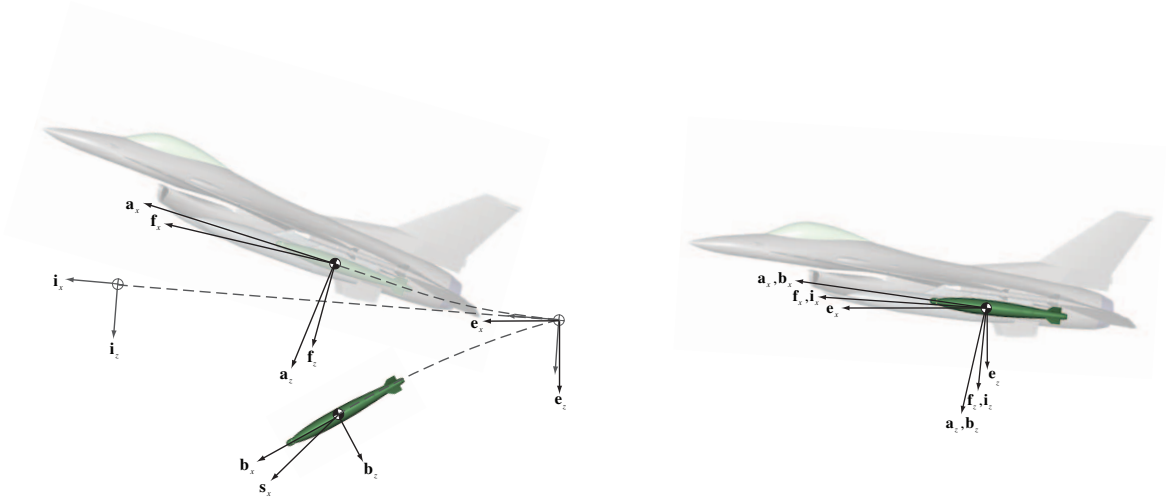

A Moment after Release, $t > 0$ B Moment of Release, $t = 0$

Figure 2-3. Definition of earth, inertial, and flight axes.

Atmospheric Wind Axis $W\{\mathbf{w}_x, \mathbf{w}_y, \mathbf{w}_z\}$. The Atmospheric Wind Axis $W\{\mathbf{w}_x, \mathbf{w}_y, \mathbf{w}_z\}$ is established in the Atmospheric Wind Reference Frame W. For the purposes of store separation, the atmospheric winds surrounding the aircraft at release are assumed to be monolithic (uniform) and moving at a constant velocity relative to the surface of the earth. The particular velocity of the wind is rarely important since only the motion of the store relative to the wind and relative to the aircraft is of interest. The monolithic assumption allows the wind to be modeled as an idealized rigid body and represented by a reference frame. The assumed constant translational velocity also qualifies the atmospheric wind frame as a suitable inertial reference frame, a fact that will be useful in deriving the so-called wind axis equations of motion. The atmospheric wind axis $W\{\mathbf{w}_x, \mathbf{w}_y, \mathbf{w}_z\}$ is aligned with the earth axis $E\{\mathbf{e}_x, \mathbf{e}_y, \mathbf{e}_z\}$ with the origin of the atmospheric wind axis O_W moving at a constant velocity relative to the origin of the earth axis O_E, where the magnitude of the velocity is defined by the atmospheric winds. If the atmospheric winds are assumed to be identically zero, then the atmospheric wind axis and earth axis are coincident.

Store Wind Axis $S\{\mathbf{s}_x, \mathbf{s}_y, \mathbf{s}_z\}$. The Store Wind Axis $S\{\mathbf{s}_x, \mathbf{s}_y, \mathbf{s}_z\}$ is established in the Store Wind Reference Frame. The store wind axis is quite different from the previously defined atmospheric wind axis. The origin of the store wind axis O_S is coincident with the store CG throughout the trajectory. The velocity of the store relative to the local wind reference frame determines the orientation of the store wind axis. The velocity and orientation of the store wind axis with respect to the atmospheric wind axis is essential for determining the aerodynamic forces acting on the store during flight. The $\mathbf{s}_x$ direction rotates to maintain alignment with the store velocity vector. The $\mathbf{s}_z$ direction is perpendicular to $\mathbf{s}_x$ and positive in the downward direction. The $\mathbf{s}_y$ direction is defined by $\mathbf{s}_y = \mathbf{s}_z \times \mathbf{s}_x$. The store wind axis is shown graphically in Figure 2-4.

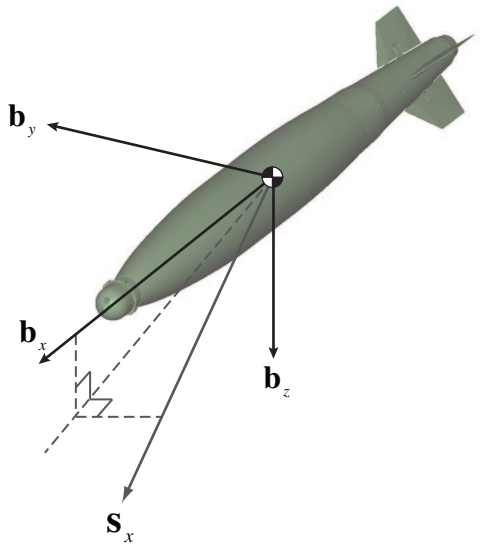

Figure 2-4. Definition of store wind axis coordinate system.

So far, seven reference frames and associated coordinate systems have been introduced. In practice, several more coordinate systems are needed to model store separation including the suspension, carriage, pylon, reference, and grid axis systems. For missiles, the aeroballistic coordinate system is usually introduced. And for wind tunnel testing and flight test data reduction, a multitude of additional coordinate systems

are needed. However, for the purposes of deriving the store separation equations of motion relative to a maneuvering aircraft, these seven definitions will suffice.

2.2.2 Coordinate Free Equations of Motion

Using reference frames as a physical entity representing an idealized rigid body, the equations of motion for a flight vehicle can be derived in a coordinate free manner without the associated algebraic complexities. Once the coordinate free equations of motion have been developed, they can be implemented in any suitable coordinate system(s).

Let $t = 0$ be defined at the instant the store begins to move relative to the aircraft (the moment of release). Also, let the position of the center of mass of the store at the moment of release be defined as the point O_B . It is assumed that the store is acted on by a uniform gravitational field so the center of mass (CM) and the center of gravity (CG) are coincident. The position of the Store CG relative to an inertially fixed point at any time $t > 0$ is defined as $\mathbf{r}_B$. Note that $\mathbf{r}_B$ is a vector that represents a physical entity, the existence of which is not dependent on a particular coordinate system. In preparation for the use of Euler's Laws, it is necessary to differentiate the position $\mathbf{r}_B$ to get the velocity of the store CG as seen by an observer in the inertial reference frame. The expression is shown in Equation (2–1) where the left superscript ${}^I[\ ]$ denotes a derivative as seen by an observer fixed in an inertial reference frame.

$$ {}^I\mathbf{v}_B = \frac{{}^I d}{dt}\mathbf{r}_B \tag{2–1} $$

Similarly, the acceleration of the store CG is shown in Equation (2–2).

$$ {}^I\mathbf{a}_B = \frac{{}^I d}{dt}{}^I\mathbf{v}_B \tag{2–2} $$

Applying Eulers 1st Law (a generalization of Newtons 1st Law to a rigid body) provides the first vector equation of motion for the translational dynamics, Equation (2–3).

$$ \mathbf{F} = m{}^I\mathbf{a}_B \tag{2–3} $$

In Equation (2–3), **F** is the total gravitational, contact, and aerodynamic force acting on the vehicle and m is the mass of the store, assumed to be constant for the duration of the trajectory (this assumption can be relaxed for missiles expelling propellant, but here it is assumed the change in mass is negligible over the relatively short time period of interest during store separation).

Eulers Law is only valid for the velocity and acceleration relative to an inertial reference frame. However, in determining an expression for the velocity and acceleration of the store CG, the most concise form that is consistent with the measurements obtained from a body-fixed measurement system is desirable. When the velocity of the store CG is expressed in any suitable body-fixed coordinate system, the acceleration is more concisely determined using the rotational time derivative [17] or transport theorem [18]. The angular velocity of the store body frame relative to the inertial reference frame is defined as ${}^{I}\boldsymbol{\omega}^{B}$. The acceleration can be expressed as shown in Equation (2–4).

$$ {}^{I}\mathbf{a}_{B} = \frac{{}^{B}d}{dt}{}^{I}\mathbf{v}_{B} + \left({}^{I}\boldsymbol{\omega}^{B} \times {}^{I}\mathbf{v}_{B}\right) \tag{2–4} $$

Rewriting Eulers 1st law results in the final coordinate-free form of the translational equations of motion for a flight vehicle as shown in Equation (2–5).

$$ \mathbf{F} = m\left[\frac{{}^{B}d}{dt}{}^{I}\mathbf{v}_{B} + \left({}^{I}\boldsymbol{\omega}^{B} \times {}^{I}\mathbf{v}_{B}\right)\right] \tag{2–5} $$

Considering the rotational equations of motion, the moment of inertia tensor referenced to the store CG and expressed in a body-fixed coordinate system is defined as $\mathbf{I}_{B}^{B}$. Again, the moment of inertia tensor represents a physical quantity and is therefore coordinate free. Once expressed in a particular coordinate system, the representation of the moment of inertia tensor will take on a conventional matrix form. The moment of inertia tensor can be used to define the angular momentum of the store frame relative to the inertial frame as shown in Equation (2–6).

$$ {}^{I}\mathbf{H}_{B} = \mathbf{I}_{B}^{B} \cdot {}^{I}\boldsymbol{\omega}^{B} \tag{2–6} $$

Applying Eulers 2nd Law, the following coordinate-free result is obtained.

$$\mathbf{M} = \frac{{}^{I}d}{dt}{}^{I}\mathbf{H}_{B} = \frac{{}^{I}d}{dt}\left(\mathbf{I}_{B}^{B} \cdot {}^{I}\boldsymbol{\omega}^{B}\right) \tag{2–7}$$

In Equation (2–7), $\mathbf{M}$ is the total moment acting on the store due to aerodynamic and contact forces (the moment due to the gravitational field is neglected since the gravitational field is assumed to be uniform).

Again, it is desirable to express all quantities in a coordinate system fixed to the body. This implies that the most efficient way to evaluate the time derivative with respect to the inertial frame is to apply the transport theorem, as shown in Equation (2–8).

$$\mathbf{M} = \frac{{}^{I}d}{dt}\left(\mathbf{I}_{B}^{B} \cdot {}^{I}\boldsymbol{\omega}^{B}\right) = \frac{{}^{B}d}{dt}\left(\mathbf{I}_{B}^{B} \cdot {}^{I}\boldsymbol{\omega}^{B}\right) + {}^{I}\boldsymbol{\omega}^{B} \times \left(\mathbf{I}_{B}^{B} \cdot {}^{I}\boldsymbol{\omega}^{B}\right) \tag{2–8}$$

For this derivation, it is assumed that the moment of inertia tensor is constant when expressed in any body-fixed coordinate system. This assumption is not necessarily the case for many applications in store separation due to deploying fins or moving control surfaces. The difficulty in modeling such effects is not primarily the complexity of the equations of motion, which are tractable, but in modeling the complexity of the aerodynamic effects of changing store configurations. At least one effort has been made to take the aerodynamic and inertial changes into consideration [14]. For simplicity of the current development, the inertia properties will be assumed constant. This is considered a justified assumption due to (1) the short time duration of interest for store separation (approximately 1 sec) and (2) the relatively minor effect on the equations of motion due to inherently small mass of the control surfaces compared to the store itself. The assumption could be relaxed without affecting the validity of Chapters 3 through 6, but the additional complexity is not warranted for this study.

Given the constancy of the moment of inertia tensor and linear properties of the time derivative, Eulers 2nd law can finally be expressed as shown in Equation (2–9).

$$\mathbf{M} = \frac{{}^{I}d}{dt}\left(\mathbf{I}_B^B \cdot {}^{I}\boldsymbol{\omega}^B\right) = \left(\mathbf{I}_B^B \cdot \frac{{}^{B}d}{dt}{}^{I}\boldsymbol{\omega}^B\right) + {}^{I}\boldsymbol{\omega}^B \times \left(\mathbf{I}_B^B \cdot {}^{I}\boldsymbol{\omega}^B\right) \tag{2–9}$$

It is noted that the time derivative ${}^{B}d{}^{I}\boldsymbol{\omega}^B/dt$ in Equation (2–9) is efficiently evaluated since the angular velocity is expressed in a coordinate system fixed in the body reference frame.

2.2.3 Standard Body-Axis Equations of Motion

The coordinate-free equations of motion derived in Section 2.2.2 are applicable to a wide range of dynamic systems, including any rigid body in free fall. In this section, the application begins to get specific to flight vehicles as the coordinate systems of interest are selected. The derivation of the standard body axis equations of motion is accomplished by expressing the coordinate-free equations in the body axis $B\{\mathbf{b}_x, \mathbf{b}_y, \mathbf{b}_z\}$. The body axis equations are the most frequently used form of the equations of motion in store separation analysis. The derivation can be separated into translational dynamics, rotational dynamics, translational kinematics, and rotational kinematics.

2.2.3.1 Translational dynamics

To apply Eulers 1st Law, it is necessary to specify a coordinated form of the vector quantities defined in Section 2.2.2. For simplicity, generalized coordinates for the velocity and angular acceleration are introduced [20]. Equation (2–10) provides the velocity of the store CG as seen by an observer fixed in an inertial reference frame and measured in a coordinate system fixed to the body. The scalar components ${}^{I}u_B^B$, ${}^{I}v_B^B$, and ${}^{I}w_B^B$ in Equation (2–10) represent the generalized velocity coordinates of the body ($[\,]_B$) frame relative to the inertial (${}^{I}[\,]$) frame, expressed in the body ($[\,]^B$) frame.

$${}^{I}\mathbf{v}_B = {}^{I}u_B^B\,\mathbf{b}_x + {}^{I}v_B^B\,\mathbf{b}_y + {}^{I}w_B^B\,\mathbf{b}_z \tag{2–10}$$

Equation (2–11) gives the time derivative of the velocity as seen by an observer in the body frame, where the "dot" notation (e.g. ${}^{I}\dot{u}_B^B$) is short hand for the scalar time derivative.

$$\frac{{}^{B}d}{dt}{}^{I}\mathbf{v}_B = {}^{I}\dot{u}_B^B\,\mathbf{b}_x + {}^{I}\dot{v}_B^B\,\mathbf{b}_y + {}^{I}\dot{w}_B^B\,\mathbf{b}_z \tag{2–11}$$

Similarly, Equation (2–12) gives the angular velocity, where the scalar components ${}^{I}p_B^B$, ${}^{I}q_B^B$, ${}^{I}r_B^B$ represent the generalized angular velocity coordinates of the body ($[\,]_B$) frame relative to the inertial (${}^{I}[\,]$) frame, expressed in the body ($[\,]^B$) frame.

$${}^{I}\boldsymbol{\omega}^B = {}^{I}p_B^B\,\mathbf{b}_x + {}^{I}q_B^B\,\mathbf{b}_y + {}^{I}r_B^B\,\mathbf{b}_z \tag{2–12}$$

The time derivative of the angular velocity in the body frame immediately follows.

$$\frac{{}^{B}d}{dt}{}^{I}\boldsymbol{\omega}^B = {}^{I}\dot{p}_B^B\,\mathbf{b}_x + {}^{I}\dot{q}_B^B\,\mathbf{b}_y + {}^{I}\dot{r}_B^B\,\mathbf{b}_z \tag{2–13}$$

The translation and angular velocities can also be written in a compact matrix notation, as shown in Equations (2–14a) and (2–14b).

$$\left[{}^{I}\mathbf{v}_B\right]^B = \left[{}^{I}u_B^B, {}^{I}v_B^B, {}^{I}w_B^B\right]^T \tag{2–14a}$$

$$\left[{}^{I}\boldsymbol{\omega}^B\right]^B = \left[{}^{I}p_B^B\,, {}^{I}q_B^B, {}^{I}r_B^B\,\right]^T \tag{2–14b}$$

The quantities $\left[{}^{I}\mathbf{v}_B\right]^B$ and $\left[{}^{I}\boldsymbol{\omega}^B\right]^B$ are the matrix representation of the vectors ${}^{I}\mathbf{v}_B$ and ${}^{I}\boldsymbol{\omega}^B$ in the body axis. The matrix representation is a convenient form for programming the equations and gives rise to a self-defining naming convention that is particularly useful in developing a computer simulation [21].

The translational equations of motion include the total force $\mathbf{F}$, which accounts for the gravitational, contact, and aerodynamic forces applied to the store during separation, with the resulting vector equation shown in Equation (2–15).

$$\mathbf{F} = \mathbf{F}_G + \mathbf{F}_C + \mathbf{F}_A \tag{2–15}$$

Equation (2–15) is coordinate free, but must be parameterized in a particular coordinate system to be used further. The contact and aerodynamic forces are suitably expressed in a body-fixed coordinate system.

$$\mathbf{F}_C = F_{C_x}\,\mathbf{b}_x + F_{C_y}\,\mathbf{b}_y + F_{C_z}\mathbf{b}_z \tag{2–16}$$

$$\mathbf{F}_A = F_{A_x}\,\mathbf{b}_x + F_{A_y}\,\mathbf{b}_y + F_{A_z}\mathbf{b}_z \tag{2–17}$$

The gravitational force is expressed in an earth fixed coordinate system, as shown in Equation (2–18).

$$\mathbf{F}_G = F_G\mathbf{g} = mg\,\mathbf{e}_z \tag{2–18}$$

The orientation of the store body axis with respect to the inertial axis is given by the standard (yaw-pitch-roll) Euler rotation sequence and the corresponding transformation matrix, as shown in Equation (2–19).

$$[T]^{BI} = \left[T\left(\phi_B^I\right)\right]^{BY}\left[T\left(\theta_B^I\right)\right]^{YX}\left[T\left(\psi_B^I\right)\right]^{XI} \tag{2–19}$$

The quantities $\psi_B^I, \theta_B^I, \phi_B^I$ are the yaw, pitch, and roll angles of the store body frame with respect to the inertial frame and the frames X and Y are intermediate reference frames. The rotations correspond to three simple rotations about the z, y, and x axes (a so-called 3-2-1 rotation). The expanded transformation matrix is shown in (2–20), where the trigonometric terms sin and cos have been abbreviated as s and c, respectively.

$$\begin{aligned}
[T]^{BI} &= \begin{bmatrix} 1 & 0 & 0 \\ 0 & \cos\phi_B^I & \sin\phi_B^I \\ 0 & -\sin\phi_B^I & \cos\phi_B^I \end{bmatrix}\begin{bmatrix} \cos\theta_B^I & 0 & -\sin\theta_B^I \\ 0 & 1 & 0 \\ \sin\theta_B^I & 0 & \cos\theta_B^I \end{bmatrix}\begin{bmatrix} \cos\psi_B^I & \sin\psi_B^I & 0 \\ -\sin\psi_B^I & \cos\psi_B^I & 0 \\ 0 & 0 & 1 \end{bmatrix} \\
&= \begin{bmatrix} \mathrm{c}\psi_B^I\,\mathrm{c}\theta_B^I & \mathrm{c}\theta_B^I\,\mathrm{s}\psi_B^I & -\mathrm{s}\theta_B^I \\ \mathrm{c}\psi_B^I\,\mathrm{s}\phi_B^I\,\mathrm{s}\theta_B^I - \mathrm{c}\phi_B^I\,\mathrm{s}\psi_B^I & \mathrm{c}\phi_B^I\,\mathrm{c}\psi_B^I + \mathrm{s}\phi_B^I\,\mathrm{s}\psi_B^I\,\mathrm{s}\theta_B^I & \mathrm{c}\theta_B^I\,\mathrm{s}\phi_B^I \\ \mathrm{s}\phi_B^I\,\mathrm{s}\psi_B^I + \mathrm{c}\phi_B^I\,\mathrm{c}\psi_B^I\,\mathrm{s}\theta_B^I & \mathrm{c}\phi_B^I\,\mathrm{s}\psi_B^I\,\mathrm{s}\theta_B^I - \mathrm{c}\psi_B^I\,\mathrm{s}\phi_B^I & \mathrm{c}\phi_B^I\,\mathrm{c}\theta_B^I \end{bmatrix}
\end{aligned} \tag{2–20}$$

In the most general case, the inertial axis is oriented with respect to the earth axis through the flight path angle of the aircraft at $t = 0$, defined as γ_I^E , which is always constant throughout the simulation, regardless of the aircraft maneuver. The bank angle of the aircraft at $t = 0$, defined as ϕ_I^E , is also used to define the orientation of the inertial axis relative to the earth axis and becomes important in defining the direction of gravity. The heading angle of the aircraft at $t = 0$ is immaterial from a store separation perspective due to the flat earth assumption. A graphical depiction of the earth-to-inertial transformation is shown in Figure 2-5. The earth-to-inertial transformation matrix is given in Equation (2–21).

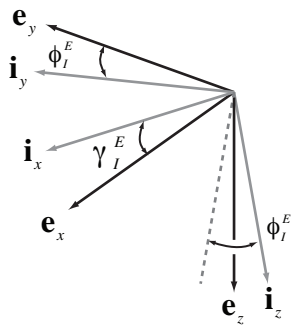

Figure 2-5. Earth-to-inertial axis transformation.

$$
\begin{aligned}
[T]^{IE} &= \begin{bmatrix} 1 & 0 & 0 \\ 0 & \cos\phi_I^E & \sin\phi_I^E \\ 0 & -\sin\phi_I^E & \cos\phi_I^E \end{bmatrix} \begin{bmatrix} \cos\gamma_I^E & 0 & -\sin\gamma_I^E \\ 0 & 1 & 0 \\ \sin\gamma_I^E & 0 & \cos\gamma_I^E \end{bmatrix} \\
&= \begin{bmatrix} \cos\gamma_I^E & 0 & -\sin\gamma_I^E \\ \sin\gamma_I^E \sin\phi_I^E & \cos\phi_I^E & \cos\gamma_I^E \sin\phi_I^E \\ \cos\phi_I^E \sin\gamma_I^E & -\sin\phi_I^E & \cos\gamma_I^E \cos\phi_I^E \end{bmatrix}
\end{aligned}
\tag{2–21}
$$

Using the combined transformations $[T]^{BE} = [T]^{BI}[T]^{IE}$, the orientation of the gravity vector in the body axis is given as shown in Equations (2–22) and (2–23a) through (2–23c).

$$[\mathbf{F}_G]^B = [T]^{BE}\,[\mathbf{F}_G]^E = [T]^{BI}\,[T]^{IE}\,[\mathbf{F}_G]^E \tag{2–22}$$

$$\begin{aligned}\mathbf{F}_G \cdot \mathbf{b}_x = &- mg(\cos\gamma_I^E \cos\phi_I^E \sin\theta_B^I + \cos\psi_B^I \cos\theta_B^I \sin\gamma_I^E \\ &- \cos\gamma_I^E \cos\theta_B^I \sin\phi_I^E \sin\psi_B^I)\end{aligned} \tag{2–23a}$$

$$\begin{aligned}\mathbf{F}_G \cdot \mathbf{b}_y = &\; mg(\sin\gamma_I^E(\cos\phi_B^I \sin\psi_B^I - \cos\psi_B^I \sin\phi_B^I \sin\theta_B^I) \\ &+ \cos\gamma_I^E \sin\phi_I^E(\cos\phi_B^I \cos\psi_B^I + \sin\phi_B^I \sin\psi_B^I \sin\theta_B^I) \\ &+ \cos\gamma_I^E \cos\phi_I^E \cos\theta_B^I \sin\phi_B^I)\end{aligned} \tag{2–23b}$$

$$\begin{aligned}\mathbf{F}_G \cdot \mathbf{b}_z = &- mg(\sin\gamma_I^E(\sin\phi_B^I \sin\psi_B^I + \cos\phi_B^I \cos\psi_B^I \sin\theta_B^I) \\ &+ \cos\gamma_I^E \sin\phi_I^E(\cos\psi_B^I \sin\phi_B^I - \cos\phi_B^I \sin\psi_B^I \sin\theta_B^I) \\ &- \cos\gamma_I^E \cos\phi_B^I \cos\phi_I^E \cos\theta_B^I)\end{aligned} \tag{2–23c}$$

Returning to Eulers 1st Law applied to a flight vehicle, Equation (2–5), and combining Equations (2–16), (2–17), (2–18), and (2–22) results in the three scalar translational equations of motion shown in Equations (2–24a) through (2–24c). Substitution of the scalar products is straightforward using Equations (2–23a) through (2–23c).

$$F_{C_x} + F_{A_x} + \mathbf{F}_G \cdot \mathbf{b}_x = \; m\,{}^I\dot{u}_B^B + m\left({}^I q_B^B\,{}^I w_B^B - {}^I r_B^B\,{}^I v_B^B\right) \tag{2–24a}$$

$$F_{C_y} + F_{A_y} + \mathbf{F}_G \cdot \mathbf{b}_y \; = \; m\,{}^I\dot{v}_B^B - m\left({}^I p_B^B\,{}^I w_B^B - {}^I r_B^B\,{}^I u_B^B\right) \tag{2–24b}$$

$$F_{C_z} + F_{A_z} + \mathbf{F}_G \cdot \mathbf{b}_z = m\,{}^I\dot{w}_B^B + m\left({}^I p_B^B\,{}^I v_B^B - {}^I q_B^B\,{}^I u_B^B\right) \tag{2–24c}$$

Equations (2–24a) through (2–24c) represent the general case when the aircraft bank angle and flight path angle are non-zero at the moment of release. Two simplified cases are also of interest. First, when the aircraft is in wings-level flight ($\phi_I^E = 0$), the gravity vector expressed in the body axis is given by Equation (2–25). The resulting

translational equations of motion are given by Equations (2–26a) through (2–26c).

$$[\mathbf{F}_G]^B = mg \begin{bmatrix} -(\,c\gamma_I^E\, s\theta_B^I + c\psi_B^I\, c\theta_B^I\, s\gamma_I^E) \\ (\,s\gamma_I^E(\,c\phi_B^I\, s\psi_B^I - c\psi_B^I\, s\phi_B^I\, s\theta_B^I) + c\gamma_I^E\, c\theta_B^I\, s\phi_B^I) \\ -(\,s\gamma_I^E(\,s\phi_B^I\, s\psi_B^I + c\phi_B^I\, c\psi_B^I\, s\theta_B^I) - c\gamma_I^E\, c\phi_B^I\, c\theta_B^I) \end{bmatrix} \tag{2–25}$$

$$F_{C_x} + F_{A_x} - mg(\,c\gamma_I^E\, s\theta_B^I + c\psi_B^I\, c\theta_B^I\, s\gamma_I^E) = m\,({}^I\dot{u}_B^B + {}^I q_B^B\, {}^I w_B^B - {}^I r_B^B\, {}^I v_B^B) \tag{2–26a}$$

$$F_{C_y} + F_{A_y} + mg(\,s\gamma_I^E(\,c\phi_B^I\, s\psi_B^I - c\psi_B^I\, s\phi_B^I\, s\theta_B^I) + c\gamma_I^E\, c\theta_B^I\, s\phi_B^I) = m\,({}^I\dot{v}_B^B - {}^I p_B^B\, {}^I w_B^B - {}^I r_B^B\, {}^I u_B^B) \tag{2–26b}$$

$$F_{C_z} + F_{A_z} - mg(\,s\gamma_I^E(\,s\phi_B^I\, s\psi_B^I + c\phi_B^I\, c\psi_B^I\, s\theta_B^I) - c\gamma_I^E\, c\phi_B^I\, c\theta_B^I) = m\,({}^I\dot{w}_B^B + {}^I p_B^B\, {}^I v_B^B - {}^I q_B^B\, {}^I u_B^B) \tag{2–26c}$$

Second, when the inertial axes are aligned with the earth axes (e.g. the aircraft is in straight, wings-level flight at $t = 0$), the constants $\gamma_I^E = \phi_I^E = 0$, and the gravity force expressed in body axes reduces to the matrix representation given by Equation (2–27).

$$[\mathbf{F}_G]^B = mg \begin{bmatrix} -\sin\theta_B^I \\ \cos\theta_B^I \sin\phi_B^I \\ \cos\phi_B^I \cos\theta_B^I \end{bmatrix} \tag{2–27}$$

In this special case, the scalar translational equations of motion reduce to the following classical form for a flight vehicle [22], as shown in Equations (2–28a) through (2–28c).

$$F_{C_x} + F_{A_x} - mg\sin\theta_B^I = m\,{}^I\dot{u}_B^B + m({}^I q_B^B\, {}^I w_B^B - {}^I r_B^B\, {}^I v_B^B) \tag{2–28a}$$

$$F_{C_y} + F_{A_y} + mg\cos\theta_B^I \sin\phi_B^I = m\,{}^I\dot{v}_B^B - m({}^I p_B^B\, {}^I w_B^B - {}^I r_B^B\, {}^I u_B^B) \tag{2–28b}$$

$$F_{C_z} + F_{A_z} + mg\cos\phi_B^I \cos\theta_B^I = m\,{}^I\dot{w}_B^B + m({}^I p_B^B\, {}^I v_B^B - {}^I q_B^B\, {}^I u_B^B) \tag{2–28c}$$

Note that even though the form of the Equations (2–28a) through (2–28c) is identical to the classical form, the meaning of the dynamic motion variables is different. The translational velocities are defined relative to a moving inertial reference frame, so the velocities are identically zero at the moment of release even though the store is moving relative to the surrounding air mass (and the surface of the earth). This distinction becomes important when determining the aerodynamic forces and moments.

2.2.3.2 Translational kinematics

The position vector of the store CG with respect to the origin of the inertial axis system is given by $\mathbf{r}_B$, which is conveniently expressed in inertial coordinates.

$$\mathbf{r}_B = {}^I x_B^I \, \mathbf{i}_x + {}^I y_B^I \, \mathbf{i}_y + {}^I z_B^I \, \mathbf{i}_z \tag{2–29}$$

The time derivative of the position vector as seen by an observer fixed in the inertial reference frame gives the velocity of the store with respect to the inertial frame, expressed in inertial axes.

$${}^I\mathbf{v}_B = \frac{{}^I d\mathbf{r}_B}{dt} = {}^I \dot{x}_B^I \, \mathbf{i}_x + {}^I \dot{y}_B^I \, \mathbf{i}_y + {}^I \dot{z}_B^I \, \mathbf{i}_z \tag{2–30}$$

The quantity ${}^I\mathbf{v}_B$ was defined in Equation (2–10) to be ${}^I\mathbf{v}_B = {}^I u_B^B \, \mathbf{b}_x + {}^I v_B^B \, \mathbf{b}_y + {}^I w_B^B \, \mathbf{b}_z$ and since both expressions represent the same physical quantity, the expressions must be equivalent.

$${}^I\mathbf{v}_B = {}^I \dot{x}_B^I \, \mathbf{i}_x + {}^I \dot{y}_B^I \, \mathbf{i}_y + {}^I \dot{z}_B^I \, \mathbf{i}_z = {}^I u_B^B \, \mathbf{b}_x + {}^I v_B^B \, \mathbf{b}_y + {}^I w_B^B \, \mathbf{b}_z \tag{2–31}$$

Using the body-to-inertial transformation matrix in Equation (2–20), the two expressions can be evaluated in the same coordinate system, shown in vector form in (2–32) and matrix form in (2–33).

$$\left[{}^I\mathbf{v}_B\right]^I = \left[\bar{T}\right]^{BI} \left[{}^I\mathbf{v}_B\right]^B = \left[T\right]^{IB} \left[{}^I\mathbf{v}_B\right]^B \tag{2–32}$$

$$\begin{bmatrix} {}^{I}\dot{x}_B^I \\ {}^{I}\dot{y}_B^I \\ {}^{I}\dot{z}_B^I \end{bmatrix} = [T]^{IB} \begin{bmatrix} {}^{I}u_B^B \\ {}^{I}v_B^B \\ {}^{I}w_B \end{bmatrix} \tag{2–33}$$

Equation (2–33) can be expressed as three scalar kinematic differential equations for the translational equations of motion, which apply regardless of the aircraft maneuver at release.

$$\begin{aligned} {}^{I}\dot{x}_B^I =& {}^{I}w_B^B(\sin\phi_B^I \sin\psi_B^I + \cos\phi_B^I \cos\psi_B^I \sin\theta_B^I) \\ & - {}^{I}v_B^B(\cos\phi_B^I \sin\psi_B^I - \cos\psi_B^I \sin\phi_B^I \sin\theta_B^I) + {}^{I}u_B^B \cos\psi_B^I \cos\theta_B^I \end{aligned} \tag{2–34a}$$

$$\begin{aligned} {}^{I}\dot{y}_B^I =& {}^{I}v_B^B(\cos\phi_B^I \cos\psi_B^I + \sin\phi_B^I \sin\psi_B^I \sin\theta_B^I) \\ & - {}^{I}w_B^B(\cos\psi_B^I \sin\phi_B^I - \cos\phi_B^I \sin\psi_B^I \sin\theta_B^I) + {}^{I}u_B^B \cos\theta_B^I \sin\psi_B^I \end{aligned} \tag{2–34b}$$

$${}^{I}\dot{z}_B^I = {}^{I}w_B^B \cos\phi_B^I \cos\theta_B^I - {}^{I}u_B^B \sin\theta_B^I + {}^{I}v_B^B \cos\theta_B^I \sin\phi_B^I \tag{2–34c}$$

In order to determine the proximity of the store with respect to the aircraft, the translational kinematics must also account for the aircraft maneuver relative to the inertial frame. This derivation is continued in Section 2.2.5.

2.2.3.3 Rotational dynamics

Euler's 2nd Law for a rigid body applied to a flight vehicle has been previously given in Equation (2–9). In order to carry the above operations further, the moment of inertia tensor $\mathbf{I}_B^B$ must be expressed in coordinate form as shown in Equation (2–35).

$$\mathbf{I}_B^B = I_{xx}\,\mathbf{b}_x \otimes \mathbf{b}_x + I_{yy}\,\mathbf{b}_y \otimes \mathbf{b}_y + I_{zz}\,\mathbf{b}_z \otimes \mathbf{b}_z + I_{xz}\,\mathbf{b}_x \otimes \mathbf{b}_z + I_{zx}\,\mathbf{b}_z \otimes \mathbf{b}_x \tag{2–35}$$

In Equation (2–35), I_{xx}, I_{yy}, I_{zz} are the moments of inertia, $I_{xz} = I_{zx}$ is the product of inertia. The remaining products of inertia are zero, $I_{xy} = I_{yx} = I_{yz} = I_{zy} = 0$, due to symmetry of the flight vehicle in the x–z plane. The expressions $\mathbf{b}_i \otimes \mathbf{b}_j$ for $i, j = x, y, z$ represent the dyadic product between to basis vectors $\mathbf{b}_i$ and $\mathbf{b}_j$. The assumption of symmetry of the flight vehicle is not strictly necessary and the derivation could be continued without the assumption, albeit with more lengthy expressions. However,

nearly all stores are symmetric or nearly symmetric in the *x*–*z* plane, so the assumption is made for the sake of simplicity in the resulting equations of motion. The choice of the body axis as the preferred coordinate system is crucial since the body frame is the only frame in which the moment of inertia tensor is constant. The moment of inertia tensor can also be represented as a matrix quantity, as shown in Equation (2–36).

$$\left[\mathbf{I}_B^B\right] = \begin{bmatrix} I_{xx} & 0 & -I_{xz} \\ 0 & I_{yy} & 0 \\ -I_{xz} & 0 & I_{zz} \end{bmatrix} \tag{2–36}$$

Given the dyadic representation in Equation (2–35) with prior results for ${}^{I}\boldsymbol{\omega}^{B}$ and ${}^{B}d{}^{I}\boldsymbol{\omega}^{B}/dt$ in Equations (2–13) and (2–13), Eulers 2nd Law for a flight vehicle can be written as three scalar differential equations of motion shown in Equation (2–37a) through (2–37c).

$$M_{C_x} + M_{A_x} = {}^{I}\dot{p}_B^B I_{xx} - {}^{I}\dot{r}_B^B I_{xz} + ({}^{I}q_B^B)({}^{I}r_B^B)(I_{zz} - I_{yy}) - ({}^{I}q_B^B)({}^{I}p_B^B) I_{xz} \tag{2–37a}$$

$$M_{C_y} + M_{Ay} = {}^{I}\dot{q}_B^B I_{yy} + ({}^{I}p_B^B)({}^{I}r_B^B)(I_{xx} - I_{zz}) - \left(({}^{I}p_B^B)^2 - ({}^{I}r_B^B)^2\right) I_{xz} \tag{2–37b}$$

$$M_{C_z} + M_{A_z} = {}^{I}\dot{r}_B^B I_{zz} - {}^{I}\dot{p}_B^B I_{xz} + ({}^{I}p_B^B)({}^{I}q_B^B)(I_{yy} - I_{xx}) + ({}^{I}q_B^B)({}^{I}r_B^B) I_{xz} \tag{2–37c}$$

2.2.3.4 Rotational kinematics

The angular velocity of the store relative to the inertial frame is expressed in terms of the generalized coordinates ${}^{I}p_B^B$, ${}^{I}q_B^B$, ${}^{I}r_B^B$, as shown in Equation (2–38).

$${}^{I}\boldsymbol{\omega}^{B} = {}^{I}p_B^B\,\mathbf{b}_x + {}^{I}q_B^B\,\mathbf{b}_y + {}^{I}r_B^B\,\mathbf{b}_z \tag{2–38}$$

The body-to-inertial transformation matrix, shown in Equation (2–39) and expanded in Equation (2–40), gives the angular orientation of the store relative to the inertial axis as a series of three consecutive rotations, where X and Y are intermediate reference frames.

$$[T]^{BI} = \left[T\left(\phi_B^I\right)\right]^{BY}\left[T\left(\theta_B^I\right)\right]^{YX}\left[T\left(\psi_B^I\right)\right]^{XI} \tag{2–39}$$

$$[T]^{BI} = \begin{bmatrix} 1 & 0 & 0 \\ 0 & c\phi_B^I & s\phi_B^I \\ 0 & -s\phi_B^I & c\phi_B^I \end{bmatrix} \begin{bmatrix} c\theta_B^I & 0 & -s\theta_B^I \\ 0 & 1 & 0 \\ s\theta_B^I & 0 & c\theta_B^I \end{bmatrix} \begin{bmatrix} c\psi_B^I & s\psi_B^I & 0 \\ -s\psi_B^I & c\psi_B^I & 0 \\ 0 & 0 & 1 \end{bmatrix} \tag{2–40}$$

The angular velocity can also be expressed as the combination of three simple rotational velocities about the corresponding axes. Since ${}^I\boldsymbol{\omega}^B$ represents a physical quantity, these expressions must be equivalent, as shown in vector form in Equation (2–41) and matrix form in Equation (2–42).

$${}^I\boldsymbol{\omega}^B = \dot{\psi}_B^I \mathbf{x}_z + \dot{\theta}_B^I \mathbf{y}_y + \dot{\phi}_B^I \mathbf{b}_x = {}^I p_B^B \mathbf{b}_x + {}^I q_B^B \mathbf{b}_y + {}^I r_B^B \mathbf{b}_z \tag{2–41}$$

$$\left[{}^I\boldsymbol{\omega}^B\right]^B = \dot{\psi}_B^I \left[T\left(\phi_B^I\right)\right]^{BY} \left[T\left(\theta_B^I\right)\right]^{YX} \begin{bmatrix} 0 \\ 0 \\ 1 \end{bmatrix} + \dot{\theta}_B^I \left[T\left(\phi_B^I\right)\right]^{BY} \begin{bmatrix} 0 \\ 1 \\ 0 \end{bmatrix} + \dot{\phi}_B^I \begin{bmatrix} 1 \\ 0 \\ 0 \end{bmatrix} \tag{2–42}$$

Equating the two sets of expressions results in three scalar kinematic differential equations, given in Equations (2–43a) through (2–43c).

$${}^I p_B^B = \dot{\phi}_B^I - \dot{\psi}_B^I \sin(\theta_B^I) \tag{2–43a}$$

$${}^I q_B^B = \dot{\psi}_B^I \cos\theta_B^I \sin\phi_B^I + \dot{\theta}_B^I \cos(\phi_B^I) \tag{2–43b}$$

$${}^I r_B^B = \dot{\psi}_B^I \cos\theta_B^I \cos\phi_B^I - \dot{\theta}_B^I \sin(\phi_B^I) \tag{2–43c}$$

2.2.3.5 Collected body-axis equations of motion

The translational and rotational relationships above result in twelve first order differential equations of motion corresponding to the rigid store six degrees of freedom. The equations of motion can be written in state-space form suitable for analysis using modern control methods or integration with a numerical ordinary differential equation (ODE) solver. The twelve differential equations previously derived can be expressed in state space form by solving for the individual scalar derivatives. The results are collected below. These results reflect equations corresponding to a flight path angle and bank angle identically equal to zero at release, rendering a simplified expression for the

gravity vector in body coordinates. Furthermore, it is understood that these equations are valid in the body axis and representing motion variables relative to an inertial axis. As such, the superscript notation has been omitted. For this special case, the results are consistent with the equations presented in the predominant flight dynamics literature [17, 22, 23].

Translational Kinematics

$$\dot{x} = w(\,\mathrm{s}\phi\,\mathrm{s}\psi + \,\mathrm{c}\phi\,\mathrm{c}\psi\,\mathrm{s}\theta) - v(\,\mathrm{c}\phi\,\mathrm{s}\psi - \,\mathrm{c}\psi\,\mathrm{s}\phi\,\mathrm{s}\theta) + u\,\mathrm{c}\psi\,\mathrm{c}\theta \tag{2-44a}$$

$$\dot{y} = v(\,\mathrm{c}\phi\,\mathrm{c}\psi + \,\mathrm{s}\phi\,\mathrm{s}\psi\,\mathrm{s}\theta) - w(\,\mathrm{c}\psi\,\mathrm{s}\phi - \,\mathrm{c}\phi\,\mathrm{s}\psi\,\mathrm{s}\theta) + u\,\mathrm{c}\theta\,\mathrm{s}\psi \tag{2-44b}$$

$$\dot{z} = w\,\mathrm{c}\phi\,\mathrm{c}\theta - u\,\mathrm{s}\theta + v\,\mathrm{c}\theta\,\mathrm{s}\phi \tag{2-44c}$$

Rotational Kinematics

$$\dot{\phi} = p + (q\sin\phi + r\cos\phi)\tan\theta \tag{2-45a}$$

$$\dot{\theta} = q\cos\phi - r\sin\phi \tag{2-45b}$$

$$\dot{\psi} = (q\sin\phi + r\cos\phi)\sec\theta \tag{2-45c}$$

Translational Dynamics

$$\dot{u} = (F_x - mg\,\mathrm{s}\theta - mqw + mrv)/m \tag{2-46a}$$

$$\dot{v} = (F_y + mpw - mru + mg\,\mathrm{c}\theta\,\mathrm{s}\phi)/m \tag{2-46b}$$

$$\dot{w} = (F_z - mpv + mqu + mg\,\mathrm{c}\phi\,\mathrm{c}\theta)/m \tag{2-46c}$$

Rotational Dynamics

$$\dot{p} = \left(I_{xz}M_z + I_{zz}M_x + I_1 qr + I_2 pq\right)/\left(I_{xx}I_{zz} - I_{xz}^2\right) \tag{2-47a}$$

$$I_1 := \left(I_{yy}I_{zz} - I_{xz}^2 - I_{zz}^2\right) \qquad I_2 := \left(I_{xx}I_{xz} - I_{xz}I_{yy} + I_{xz}I_{zz}\right)$$

$$\dot{q} = \left(M_y - I_{xz}p^2 + I_{xz}r^2 - I_{xx}pr + I_{zz}pr\right)/I_{yy} \tag{2-47b}$$

$$\dot{r} = \left(I_{xz}M_x + I_{xx}M_z + I_3 qr + I_4 pq\right)/\left(I_{xx}I_{zz} - I_{xz}^2\right) \tag{2-47c}$$

$$I_3 := \left(I_{xz}I_{yy} - I_{xx}I_{xz} - I_{xz}I_{zz}\right) \qquad I_4 := \left(I_{xz}^2 + I_{xz}^2 - I_{xx}I_{yy}\right)$$

2.2.4 Wind-Axis Equations

The choice of a suitable inertial axis is important for expressing the physical laws that govern rigid body motion but the inertial axis alone is not sufficient for describing the forces acting on a vehicle in flight. Rather, the aerodynamic forces and moments are determined by the vehicle motion relative to the surrounding air mass. In traditional flight dynamics literature, the wind-axis origin is located at the CG of the flight vehicle (and thus translates with the vehicle tracing out the trajectory of the CG over time), but rotates relative to the vehicle to maintain constant alignment with the velocity vector. However, by convention in store separation analysis, the wind reference frame is used to denote the atmosphere surrounding the aircraft at the time of release. Here, the symbol W denotes the reference frame affixed to the atmospheric wind that is assumed to be uniform and moving at a constant velocity with respect to the earth frame. The symbol S will be used to denote the store wind-axis, which is fixed at the store CG and aligned with the store velocity vector, in a manner consistent with the predominant flight dynamics literature.

The velocity of the store relative to the wind reference frame is shown in Equation (2–48), where ${}^{W}V_B$ is the magnitude of the velocity and the unit vector $\mathbf{s}_x$ is defined by the direction of the store velocity.

$$ {}^{W}\mathbf{v}_B = {}^{W}V_B\,\mathbf{s}_x \tag{2–48} $$

The orientation of the velocity vector with respect to the store body axis is given by the two Cartesian incidence angles, α_s and β_s . To determine the transformation matrix relating the store body axis and the store wind axis, it is convenient to introduce the intermediate reference frame X (which supersedes any previously defined intermediate reference frames). The rotation of the intermediate frame with respect to the body frame is given by Equation (2–49), where α_s is the store angle-of-attack.

$$[T]^{XB} = \begin{bmatrix} \cos\alpha_s & 0 & \sin\alpha_s \\ 0 & 1 & 0 \\ -\sin\alpha_s & 0 & \cos\alpha_s \end{bmatrix} \tag{2–49}$$

The rotation of the store wind-axis with respect to the intermediate frame is given by Equation (2–50), where β_s is the store angle-of-sideslip.

$$[T]^{SX} = \begin{bmatrix} \cos\beta_s & \sin\beta_s & 0 \\ -\sin\beta_s & \cos\beta_s & 0 \\ 0 & 0 & 1 \end{bmatrix} \tag{2–50}$$

The transformation for the store wind-axis with respect to the body axis is given by the corresponding compound transformation, as shown in Equation (2–51).

$$[T]^{SB} = [T]^{SX}\,[\bar{T}]^{BX} = \begin{bmatrix} \cos\alpha_s\cos\beta_s & \sin\beta_s & \cos\beta_s\sin\alpha_s \\ -\cos\alpha_s\sin\beta_s & \cos\beta_s & -\sin\alpha_s\sin\beta_s \\ -\sin\alpha_s & 0 & \cos\alpha_s \end{bmatrix} \tag{2–51}$$

The magnitude of the store velocity relative to the wind, ${}^{W}V_B$, and the Cartesian incidence angles, α_s and β_s , play an important role in characterizing the aerodynamic forces and moments for the store in far-field (freestream) conditions. If the body-axis equations of motion are solved, the velocity and incidence angles can be determined as ancillary equations. Alternatively, the translational equations of motion can be expressed in the wind-axis and solved directly. The first method is the most common in store separation analysis but the second method will become particularly valuable for trajectory optimization. Both approaches are briefly considered here.

2.2.4.1 Ancillary equations

The generalized velocities, ${}^{I}u_B^B, {}^{I}v_B^B, {}^{I}w_B^B$, represent the components of the velocity of the vehicle with respect to the inertial reference frame, which is itself moving at a

constant velocity determined by the aircraft velocity at the instant of release. It is also valuable to define a set of generalized velocities ${}^{W}u_B^B, {}^{W}v_B^B, {}^{W}w_B^B$, which represent the velocity of the store frame ($[\ ]_B$) with respect to the atmospheric wind frame (${}^{W}[\ ]$), expressed in the store body axis ($[\ ]^B$). When the velocity of the store with respect to the inertial frame, ${}^{I}\mathbf{v}_B = {}^{I}u_B^B\,\mathbf{b}_x + {}^{I}v_B^B\,\mathbf{b}_y + {}^{I}w_B^B\,\mathbf{b}_z$, is known from the solution of the body-axis differential equations, and the velocity of the inertial frame relative to the wind, ${}^{W}\mathbf{v}_I = {}^{W}u_I^I\,\mathbf{i}_x$, is known from the initial conditions, the velocity of the store relative to the wind can be readily determined. The vector form is given by Equation (2–52).

$$ {}^{W}\mathbf{v}_B = {}^{I}\mathbf{v}_B + {}^{W}\mathbf{v}_I \tag{2–52} $$

Equation (2–52) can be written in matrix form using the transformation matrix $[T]^{BI}$.

$$ \left[{}^{W}\mathbf{v}_B\right]^B = \left[{}^{I}\mathbf{v}_B\right]^B + [T]^{BI}\left[{}^{W}\mathbf{v}_I\right]^I \tag{2–53} $$

Expanding the matrix equation results in three scalar equations.

$$ \begin{bmatrix} {}^{W}u_B^B \\ {}^{W}v_B^B \\ {}^{W}w_B^B \end{bmatrix} = \begin{bmatrix} {}^{I}u_B^B + {}^{W}u_I^I \cos\psi_B^I \cos\theta_B^I \\ {}^{I}v_B^B - {}^{W}u_I^I(\cos\phi_B^I \sin\psi_B^I - \cos\psi_B^I \sin\phi_B^I \sin\theta_B^I) \\ {}^{I}w_B^B + {}^{W}u_I^I(\sin\phi_B^I \sin\psi_B^I + \cos\phi_B^I \cos\psi_B^I \sin\theta_B^I) \end{bmatrix} \tag{2–54} $$

Finally, the magnitude of the velocity, ${}^{W}V_B$, is given by the Euclidean norm.

$$ {}^{W}V_B = \sqrt{\left({}^{W}u_B^B\right)^2 + \left({}^{W}v_B^B\right)^2 + \left({}^{W}w_B^B\right)^2} \tag{2–55} $$

To determine the incidence angles using the generalized velocities, expand the matrix equation $\left[{}^{W}\mathbf{v}_B\right]^S = [T]^{SB}\left[{}^{W}\mathbf{v}_B\right]^B$ as shown in Equation (2–56).

$$ \begin{bmatrix} {}^{W}V_B \\ 0 \\ 0 \end{bmatrix} = \begin{bmatrix} \cos\alpha_s \cos\beta_s & \sin\beta_s & \cos\beta_s \sin\alpha_s \\ -\cos\alpha_s \sin\beta_s & \cos\beta_s & -\sin\alpha_s \sin\beta_s \\ -\sin\alpha_s & 0 & \cos\alpha_s \end{bmatrix} \begin{bmatrix} {}^{W}u_B^B \\ {}^{W}v_B^B \\ {}^{W}w_B^B \end{bmatrix} \tag{2–56} $$

Using these three scalar equations, the corresponding expressions for α_s and β_s can be determined. Note that ${}^{W}u_B^B = 0$ results in $\alpha_s = 90$ deg for any ${}^{W}w_B^B \neq 0$, whereas ${}^{W}V_B = 0$ results in β_s being undefined.

$$\alpha_s = \tan^{-1}\left({}^{W}w_B^B \;/\; {}^{W}u_B^B\right) \tag{2–57}$$

$$\beta_s = \sin^{-1}\left({}^{W}v_B^B \;/\; {}^{W}V_B\right) \tag{2–58}$$

2.2.4.2 Wind-axis equations of motion

The translation equations of motion can also be derived using the translational and angular velocities expressed in the store wind axis. The velocity of the store with respect to the atmospheric wind is given by Equation (2–59).

$${}^{W}\mathbf{v}_B = {}^{W}V_B\,\mathbf{s}_x \tag{2–59}$$

Since the wind is assumed to be monolithic (uniform), the wind is treated as an idealized rigid body and can be represented by a reference frame. Furthermore, since the wind is assumed to be moving at a constant translational velocity with respect to the earth, the wind reference frame is a suitable inertial reference frame for the purpose of store separation. As such, Eulers 1st law can be applied. Applying the transport theorem to achieve a compact set of differential equations, the acceleration of the store body with respect to the wind frame is given by Equation (2–60).

$$\frac{{}^{W}d}{dt}{}^{W}\mathbf{v}_B = \frac{{}^{S}d}{dt}{}^{W}\mathbf{v}_B + \left({}^{W}\boldsymbol{\omega}^S \times {}^{W}\mathbf{v}_B\right) \tag{2–60}$$

The angular velocity of the store wind frame with respect to the wind reference frame is given by the vector addition of the intermediate body frame.

$${}^{W}\boldsymbol{\omega}^S = {}^{W}\boldsymbol{\omega}^B + {}^{B}\boldsymbol{\omega}^S \tag{2–61}$$

Since the wind frame is an inertial reference frame (albeit moving with a different translational velocity than the primary inertial reference frame), the angular velocity

of the body relative to the wind frame is equivalent to the angular velocity of the body relative to the primary inertial frame (e.g. the angular velocity of the wind frame with respect to the primary inertial frame is zero – indeed, if this were not the case the wind frame would not qualify as an inertial reference frame).

$$ {}^{W}\boldsymbol{\omega}^{B} = {}^{I}\boldsymbol{\omega}^{B} \tag{2–62} $$

The angular velocity of the store wind axis relative to the store body axis is given by the addition of two simple angular velocities, as shown in Equation (2–63).

$$ {}^{B}\boldsymbol{\omega}^{S} = -\dot{\alpha}\mathbf{x}_{y} + \dot{\beta}\,\mathbf{s}_{z} \tag{2–63} $$

The vector expression in Equation (2–63) can be written in matrix form using the transformation matrix between the intermediate reference frame X and the store wind axis.

$$ \left[{}^{B}\boldsymbol{\omega}^{S}\right]^{S} = -\dot{\alpha}\,[T]^{SX}\begin{bmatrix}0\\1\\0\end{bmatrix} + \dot{\beta}\begin{bmatrix}0\\0\\1\end{bmatrix} \tag{2–64} $$

Expressing the vector in the store wind coordinate system gives the angular velocity in a consistent form, as shown in Equation (2–65).

$$ {}^{B}\boldsymbol{\omega}^{S} = -\dot{\alpha}\sin\beta\,\mathbf{s}_{x} - \dot{\alpha}\cos\beta\,\mathbf{s}_{y} + \dot{\beta}\,\mathbf{s}_{z} \tag{2–65} $$

Using the transformation matrix for the store wind axis with respect to the store body axis, the angular velocity of the store wind axis relative to the atmospheric wind axis can be written in matrix form as Equation (2–66).

$$ \left[{}^{W}\boldsymbol{\omega}^{S}\right]^{S} = [T]^{SB}\left[{}^{I}\boldsymbol{\omega}^{B}\right]^{B} + \left[{}^{B}\boldsymbol{\omega}^{S}\right]^{S} \tag{2–66} $$

Expanding the matrix equation gives the following three scalar differential equations.

$$\left[{}^{W}\boldsymbol{\omega}^{S}\right]^{S} = \begin{bmatrix} {}^{I}q_B^B \sin\beta_s - \dot{\alpha}_s \sin\beta_s + {}^{I}p_B^B \cos\alpha_s \cos\beta_s + {}^{I}r_B^B \cos\beta_s \sin\alpha_s \\ {}^{I}q_B^B \cos\beta_s - \dot{\alpha}_s \cos\beta_s - {}^{I}p_B^B \cos\alpha_s \sin\beta_s - {}^{I}r_B^B \sin\alpha_s \sin\beta_s \\ \dot{\beta}_s + {}^{I}r_B^B \cos\alpha_s - {}^{I}p_B^B \sin\alpha_s \end{bmatrix} \tag{2–67}$$

To express the equations of motion in the store wind axis, the gravity vector must be properly coordinated using the transformation matrices $[T]^{SB}$ and $[T]^{BI}$.

$$\mathbf{F}_G = mg\,[T]^{SB}\,[T]^{BI}\,\mathbf{i}_z \tag{2–68}$$

For the sake of brevity, it has been assumed that the aircraft flight path angle at release is zero and as a consequence the inertial axis is aligned with the earth axis. Relaxing this assumption introduces a third transformation matrix, $[T]^{IE}$, which significantly lengthens the resulting equations without fundamentally changing the derivation. Expanding the matrix equation above gives the gravity vector expressed in the store wind axis coordinate system.

$$\mathbf{F}_G = mg \begin{bmatrix} \mathrm{s}\beta_s\,\mathrm{c}\theta_B^I\,\mathrm{s}\phi_B^I - \mathrm{c}\alpha_s\,\mathrm{c}\beta_s\,\mathrm{s}\theta_B^I + \mathrm{c}\beta_s\,\mathrm{c}\phi_B^I\,\mathrm{s}\alpha_s\,\mathrm{c}\theta_B^I \\ \mathrm{c}\beta_s\,\mathrm{c}\theta_B^I\,\mathrm{s}\phi_B^I + \mathrm{c}\alpha_s\,\mathrm{s}\beta_s\,\mathrm{s}\theta_B^I - \mathrm{c}\phi_B^I\,\mathrm{s}\alpha_s\,\mathrm{s}\beta_s\,\mathrm{c}\theta_B^I \\ \mathrm{s}\alpha_s\,\mathrm{s}\theta_B^I + \mathrm{c}\alpha_s\,\mathrm{c}\phi_B^I\,\mathrm{c}\theta_B^I \end{bmatrix} \tag{2–69}$$

Ignoring any contact forces between the aircraft and store and treating the atmospheric wind frame as an inertial reference frame, Eulers 1st Law can be written as shown in Equation (2–70), where $\mathbf{F}_A$ is the aerodynamic force expressed in the store wind axis.

$$\mathbf{F}_A + \mathbf{F}_G = m\left[\frac{{}^{S}d}{dt}{}^{W}\mathbf{v}_B + {}^{W}\boldsymbol{\omega}^{S} \times {}^{W}\mathbf{v}_B\right] \tag{2–70}$$

The aerodynamic force is typically parameterized in terms of Lift (F_L), Drag (F_D), and Side force (F_Y), as shown in Equation (2–71).

$$\mathbf{F}_A = -F_{D_W}\mathbf{s}_x + F_{Y_W}\mathbf{s}_y - F_L\mathbf{s}_z \tag{2–71}$$

The drag and side force in the store wind axis are related to the conventionally defined drag and side force (in the stability axis) by Equations (2–72) and (2–73).

$$F_{D_W} = F_D \cos\beta_s - F_Y \sin\beta_s \tag{2–72}$$

$$F_{Y_W} = F_Y \cos\beta_s + F_D \sin\beta_s \tag{2–73}$$

Finally, the translational differential equations of motion expressed in the store wind axis are given as Equations (2–74a) through (2–74c).

$$\begin{aligned} F_{D_W} = &- \dot{V}_B^W m - mg\cos\alpha_s\cos\beta_s\sin\theta_B^I + mg\sin\beta_s\cos\theta_B^I\sin\phi_B^I + \\ &mg\cos\beta_s\cos\phi_B^I\sin\alpha_s\cos\theta_B^I \end{aligned} \tag{2–74a}$$

$$\begin{aligned} F_{Y_W} = &\, mV_B^W(\dot{\beta}_s + {}^I r_B^I\cos\alpha_s - {}^I p_B^I\sin\alpha_s) - mg\cos\beta_s\cos\theta_B^I\sin\phi_B^I - \\ &mg\cos\alpha_s\sin\beta_s\sin\theta_B^I + mg\cos\phi_B^I\sin\alpha_s\sin\beta_s\cos\theta_B^I \end{aligned} \tag{2–74b}$$

$$\begin{aligned} F_L = &- mV_B^W(\dot{\alpha}_s\cos\beta_s - {}^I q_B^I\cos\beta_s + {}^I p_B^I\cos\alpha_s\sin\beta_s + {}^I r_B^I\sin\alpha_s\sin\beta_s) + \\ &mg\sin\alpha_s\sin\theta_B^I + mg\cos\alpha_s\cos\phi_B^I\cos\theta_B^I \end{aligned} \tag{2–74c}$$

Equations (2–74a) through (2–74c) can be put into state-space form by solving for the time derivatives, $\dot{V}_B^W$, $\dot{\alpha}_s$, and $\dot{\beta}_s$, as shown in Equations (2–75a) through (2–75c).

$$\dot{V}_B^W = - F_{D_W} + g\left(\mathrm{c}\phi_B^I\,\mathrm{c}\theta_B^I\,\mathrm{s}\alpha_s\,\mathrm{c}\beta_s + \mathrm{s}\phi_B^I\,\mathrm{c}\theta_B^I\,\mathrm{s}\beta_s - \mathrm{s}\theta_B^I\,\mathrm{c}\alpha_s\,\mathrm{c}\beta_s\right) \tag{2–75a}$$

$$\begin{aligned} \dot{\alpha}_s = &- \frac{F_L}{mV_B^W\,\mathrm{c}\beta_s} + {}^I q_B^B - \tan\beta_s\left({}^I p_B^B\,\mathrm{c}\alpha_s + {}^I r_B^B\,\mathrm{s}\alpha_s\right) \\ &+ \frac{g}{V_B^W\,\mathrm{c}\beta_s}\left(\mathrm{c}\phi_B^I\,\mathrm{c}\theta_B^I\,\mathrm{c}\alpha_s + \mathrm{s}\theta_B^I\,\mathrm{s}\alpha_s\right) \end{aligned} \tag{2–75b}$$

$$\begin{aligned} \dot{\beta}_s = &\frac{F_{Y_W}}{mV_B^W} + {}^I p_B^B\,\mathrm{s}\alpha_s - {}^I r_B^B\,\mathrm{c}\alpha_s + \frac{g}{V_B^W}\,\mathrm{c}\beta_s\,\mathrm{s}\phi_B^I\,\mathrm{c}\theta_B^I \\ &+ \frac{\mathrm{s}\beta_s}{V_B^W}\left(g\,\mathrm{c}\alpha_s\,\mathrm{s}\theta_B^I - g\,\mathrm{s}\alpha_s\,\mathrm{c}\phi_B^I\,\mathrm{c}\theta_B^I\right) \end{aligned} \tag{2–75c}$$

Combined with the 12 state space equations in the body axis, the differential equations are now 15 in number. However, only 12 of these equations are independent.

When necessary, the translational wind-axis equations of motion are used in lieu of the translational body-axis equations of motion. The choice of one system over another is driven by the particular application.

The 15 differential equations presented thus far are sufficient for determining the store motion relative to the inertial reference frame and atmospheric wind frame. For store separation, the primary interest is in the store motion relative to the aircraft, which is achieved through an algebraic extension to the equations of motion.

2.2.5 Position and Velocity of the Store Relative to the Aircraft

In the simplest case, the aircraft is assumed to be flying in uniform unaccelerated flight (such as a constant climb or dive angle or straight and level) and is therefore aligned with the inertial axis. The equations of motion derived in Sections 2.2.3 and 2.2.4 apply immediately, e.g. the aircraft-relative trajectory is identical to the inertial trajectory. However, in the more general case, the aircraft is maneuvering during the release, resulting in motion of the aircraft relative to the inertial reference frame. The motion may be arbitrary in the sense that the aircraft moves along any allowable trajectory, or the motion may be simplified by assuming a specific maneuver, such as a pull-up or push-over. If the motion is indeed arbitrary, it is assumed that the aircraft trajectory is known a priori. In other words, simulation of the aircraft trajectory is not considered. Regardless, the equations of motion of the store relative to the inertial reference frame are unmodified. Determining the position and velocity of the store relative to the aircraft, an essential step prior to aerodynamic modeling of the nonuniform flow field, is more involved.

The flight axis orientation is determined by the aircraft velocity vector throughout the trajectory. The position of the store relative to the flight axis is given by the vector relationship shown in Equation (2–76).

$$ {}^{F}\mathbf{r}_{B} = {}^{I}\mathbf{r}_{B} - {}^{I}\mathbf{r}_{F} \tag{2–76} $$

Similarly, the velocity is given by Equation (2–77).

$$ {}^{F}\mathbf{v}_B = {}^{I}\mathbf{v}_B - {}^{I}\mathbf{v}_F \tag{2–77} $$

In Equations (2–76) and (2–77), ${}^{I}\mathbf{r}_B = {}^{I}x_B^I\ \mathbf{i}_x + {}^{I}y_B^I\ \mathbf{i}_y + {}^{I}z_B^I\ \mathbf{i}_z$ and , ${}^{I}\mathbf{v}_B = {}^{I}\dot{x}_B^I\ \mathbf{i}_x + {}^{I}\dot{y}_B^I\ \mathbf{i}_y + {}^{I}\dot{z}_B^I\ \mathbf{i}_z$ are the position and velocity of the store CG relative to the inertial axis (given by simulation). Similarly, ${}^{I}\mathbf{r}_F = {}^{I}x_F^I\ \mathbf{i}_x + {}^{I}y_F^I\ \mathbf{i}_y + {}^{I}z_F^I\ \mathbf{i}_z$ and ${}^{I}\mathbf{v}_F = {}^{I}\dot{x}_F^I\ \mathbf{i}_x + {}^{I}\dot{y}_F^I\ \mathbf{i}_y + {}^{I}\dot{z}_F^I\ \mathbf{i}_z$ are the position and velocity of the flight axis origin relative to the inertial axis (given by the problem statement). The angular velocity of the store relative to the aircraft is given by the coordinate free expression shown in Equation (2–78), where ${}^{I}\boldsymbol{\omega}^B = {}^{I}p_B^B\ \mathbf{b}_x + {}^{I}q_B^B\ \mathbf{b}_y + {}^{I}r_B^B\ \mathbf{b}_z$ is the store angular velocity relative to the inertial frame and ${}^{I}\boldsymbol{\omega}^F = {}^{I}p_F^F\ \mathbf{f}_x + {}^{I}q_F^F\ \mathbf{f}_y + {}^{I}r_F^F\ \mathbf{f}_z$ is the flight axis angular velocity relative to the inertial frame.

$$ {}^{F}\boldsymbol{\omega}^B = {}^{I}\boldsymbol{\omega}^B - {}^{I}\boldsymbol{\omega}^F \tag{2–78} $$

In matrix form, the angular velocity of the store relative to the aircraft is shown in Equation (2–79), where $[T]^{BF}$ is the transformation matrix that represents the orientation of the store with respect to the flight axis, as shown in Equation (2–80).

$$ \left[{}^{F}\boldsymbol{\omega}^B\right]^B = \left[{}^{I}\boldsymbol{\omega}^B\right]^B - [T]^{BF}\left[{}^{I}\boldsymbol{\omega}^F\right]^F \tag{2–79} $$

$$ [T]^{BF} = [T]^{BI}\left[\bar{T}\right]^{FI} \tag{2–80} $$

The matrix $[T]^{FI}$ is determined using a 3-2-1 Euler rotation in a manner similar to $[T]^{BI}$.

$$ [T]^{FI} = \begin{bmatrix} 1 & 0 & 0 \\ 0 & \cos\phi_F^I & \sin\phi_F^I \\ 0 & -\sin\phi_F^I & \cos\phi_F^I \end{bmatrix} \begin{bmatrix} \cos\theta_F^I & 0 & -\sin\theta_F^I \\ 0 & 1 & 0 \\ \sin\theta_F^I & 0 & \cos\theta_F^I \end{bmatrix} \begin{bmatrix} \cos\psi_F^I & \sin\psi_F^I & 0 \\ -\sin\psi_F^I & \cos\psi_F^I & 0 \\ 0 & 0 & 1 \end{bmatrix} \tag{2–81} $$

Equations (2–76) through (2–81) are applicable in any maneuvering aircraft simulation, provided that the aircraft motion relative to the common inertial frame is

known or can be determined. However, the generality of these relationships are seldom required. Nearly all store separation simulations can be modeled using simplifying assumptions, including (1) straight and level flight, (2) steady climb or dive, (3) steady pull-up or push-over. Each of these maneuvers is steady (so the aircraft velocity and angle of attack are constant) and confined to the pitch-plane (so the lateral translational and angular velocities are zero), resulting in significant simplifications of Equations (2–76) through (2–81).

2.2.5.1 Straight and level flight

When the aircraft if flying straight and level during release, the flight axis is coincident with the inertial axis, resulting in the relationships shown in Equations (2–82) and (2–83).

$$ {}^{I}\mathbf{r}_F = {}^{I}\mathbf{v}_F = {}^{I}\boldsymbol{\omega}^F = 0 \tag{2–82} $$

$$ [T]^{FI} = \begin{bmatrix} 1 & 0 & 0 \\ 0 & 1 & 0 \\ 0 & 0 & 1 \end{bmatrix} \tag{2–83} $$

It is clear that the simulation results ${}^{I}\mathbf{r}_B$, ${}^{I}\mathbf{v}_B$, ${}^{I}\boldsymbol{\omega}_B$, and $[T]^{BI}$ are used directly to relate the position, velocity, and orientation of the store relative to the aircraft. In effect, the aircraft itself is used as an inertial reference frame. This is the simplest form of relative motion and the most commonly used approach in store separation trajectory prediction.

2.2.5.2 Steady climb or dive

The orientation of the inertial reference frame with respect to the earth is determined by the flight path angle of the aircraft at the instant the store is released. When the aircraft is in a steady climb or dive, the flight path angle remains constant. As a result, the flight axis remains coincident with the inertial axis throughout the trajectory. Once again, the simulation results ${}^{I}\mathbf{r}_B$, ${}^{I}\mathbf{v}_B$, ${}^{I}\boldsymbol{\omega}_B$, and $[T]^{BI}$ are used directly to relate the position, velocity, and orientation of the store relative to the aircraft. Note that the

simulation results will in general be different from the case of straight and level flight, due to the orientation of the gravity force acting on the store.

2.2.5.3 Constant load factor maneuver

A wings-level constant load factor pitch-plane maneuver can be idealized as a circular arc in a plane normal to the local earth horizontal [21]. The idealized motion of the aircraft leads to a closed-form solution for the flight axis motion relative to the inertial axis. The straightforward derivation is presented by Keen [21] and the results are included in this section.

Since the aircraft motion is assumed to be a circular arc with constant forward velocity, the acceleration of the flight axis relative to the inertial axis is given by Equation (2–84), where ${}^{I}az_F^F$ is the normal acceleration, N_Z is the load factor (for normal straight and level flight $N_Z = 1$) and g is the local acceleration of gravity.

$$ {}^{I}\mathbf{a}_F = {}^{I}az_F^F \, \mathbf{f}_z = (1 - N_Z)\, g \, \mathbf{f}_z \tag{2–84} $$

The angular velocity of the flight axes with respect to the inertial axes is given by Equation (2–85), where ${}^{I}q_F^F$ is the flight axis pitch rate and ${}^{W}u_I^I$ is the x-component of the velocity of the inertial axis relative to the wind axis (equivalent to the aircraft airspeed at release).

$$ {}^{I}\boldsymbol{\omega}^F = {}^{I}q_F^F \, \mathbf{f}_y = -\frac{{}^{I}az_F^F}{{}^{W}u_I^I} \, \mathbf{f}_y \tag{2–85} $$

Due to the planar motion, the orientation of the flight axes relative to the inertial axes is given by direct integration of the pitch rate.

$$ \theta_F^I = \int_0^t {}^{I}q_F^F \, dt = {}^{I}q_F^F \, t \tag{2–86} $$

The orientation is easily represented using a simple transformation matrix.

$$[T]^{FI} = \left[T\left(\theta_F^I\right)\right]^{FI} = \begin{bmatrix} \cos\theta_F^I & 0 & -\sin\theta_F^I \\ 0 & 1 & 0 \\ \sin\theta_F^I & 0 & \cos\theta_F^I \end{bmatrix} \tag{2–87}$$

Using the normal acceleration and pitch rate of the constant load factor maneuver, the apparent radius of curvature is as shown in Equation (2–88).

$$R = \frac{{}^I az_F^F}{\left({}^I q_F^F\right)^2} \tag{2–88}$$

The radius of curvature can be used to determine the position and velocity of the flight axes relative to the inertial axes, as shown in Equations (2–89) and (2–90).

$$\begin{aligned} {}^I\mathbf{r}_F &= {}^I x_F^I\, \mathbf{i}_x + {}^I y_F^I\, \mathbf{i}_y + {}^I z_F^I\, \mathbf{i}_z \\ {}^I x_F^I &= -{}^W u_I^I t - R\sin\theta_F^I \\ {}^I y_F^I &= 0 \\ {}^I z_F^I &= R\left(1-\cos\theta_F^I\right) \end{aligned} \tag{2–89}$$

$$\begin{aligned} {}^I\mathbf{v}_F &= {}^I u_F^I\, \mathbf{i}_x + {}^I v_F^I\, \mathbf{i}_y + {}^I w_F^I\, \mathbf{i}_z \\ {}^I u_F^I &= -{}^W u_I^I\left(1-\cos\theta_F^I\right) \\ {}^I w_F^I &= -{}^W u_I^I \sin\theta_F^I \\ {}^I v_F^I &= 0 \end{aligned} \tag{2–90}$$

Equations (2–84) through (2–90) provide a full specification of the flight axes motion with respect to the inertial axes for a constant load factor maneuver. Since the differential equations provide the motion of the store relative to the inertial axes, the position, orientation, and velocity of the store relative to the flight axis are readily determined.

2.3 Aerodynamic Modeling

The equations of motion for store separation are a formidable set of differential equations due primarily to the algebraic complexity and nonlinear coupling, but the approximate solution to this system of equations is readily obtained using standard numerical solvers. On the other hand, the aerodynamic modeling which is necessary to inform the equations of motion is substantially more difficult. Aerodynamics of flight vehicles is a major study in and of itself, and store separation complicates the matter by considering mutually interfering aerodynamics between the store and aircraft. The nonuniform interference flow field requires that the aerodynamic loads on the store take into account the location and orientation of the store relative to the aircraft. Aerodynamic coefficients are used to model the forces and moments acting on the store in flight and the delta-coefficient methodology is used to account for the spatial varying aerodynamics caused by the nonuniform interference flow field. These methods are well established in the flight dynamics community in general, and the store separation community in particular.

2.3.1 Aerodynamic Coefficients

The aerodynamic forces and moments arise from air pressure acting on the surface of the store. The pressure distribution is a function of the flow field (and varies with location in a nonuniform flow field) as well as the motion of the store through the surrounding air mass. In practice, the pressure distribution is modeled as a single force/moment set acting at the store center of gravity. These dimensional forces and moments are represented by the terms F_{A_i} and M_{A_i} , $i = x, y, z$, in Equations (2–34a) through(2–34c) and (2–37a) through (2–37c).

The aerodynamic forces and moments are non-dimensionalized based on the size of the flight vehicle and the dynamic pressure of the airflow. In a wind tunnel, forces and moments are usually measured and analyzed in the body axis, giving rise to the so-called “body axis coefficients”: C_X or C_A , C_Y , C_Z or C_N , C_l , C_m and C_n. Additionally,

the forces and moments are physically related to the magnitude and direction of the store velocity relative to the air, giving rise to the "wind axis coefficients": C_D , C_Y , C_L. Note that the moment coefficients are the same for both systems. Both systems are used prevalently in practice. Body axis coefficients are used exclusively to quantify the aerodynamic interference between the store and aircraft, but wind-axis coefficients are useful for building physical intuition and for automatic control system design.

The non-dimensional force coefficients are related to the dimensional aerodynamic forces and scaled by the dynamic pressure, q_∞, and reference area, S_{ref}.

$$C_i = \frac{F_i}{q_\infty S_{ref}} \text{ for } i = X, Y, Z, L, D \tag{2–91}$$

Similarly, the non-dimensional moment coefficients are scaled by the dynamic pressure, reference area, and reference length, l_{ref} , as shown in Equation (2–92). In general, the reference area and reference length may be different between coefficients. However, most stores are axisymmetric or nearly so and the parameters are the same for all force and moment coefficients.

$$C_i = \frac{M_i}{q_\infty S_{ref} l_{ref}} \text{ for } i = l, m, n \tag{2–92}$$

Conversion between the body axis and wind axis force coefficients is dependent on the store angle of attack and readily obtained from the transformation matrix in Equation (2–93).

$$\begin{bmatrix} C_D \\ C_Y \\ C_L \end{bmatrix} = \begin{bmatrix} \cos\alpha_s & 0 & \sin\alpha_s \\ 0 & 1 & 0 \\ -\sin\alpha_s & 0 & \cos\alpha_s \end{bmatrix} \begin{bmatrix} -C_X \\ C_Y \\ -C_Z \end{bmatrix} \tag{2–93}$$

Various methods are used to determine the value of the aerodynamic coefficients for a particular flight condition and trajectory of a flight vehicle, including analytical, numerical, and empirical methods. Analytical methods based on first principles will prove to be too simplistic for most store separation problems. Numerical methods,

including CFD, are widely used to estimate aerodynamic coefficients for store separation, but require sufficient computational resources. Empirical methods, based primarily on wind tunnel data and accomplished using a delta-coefficient methodology, provide a direct source for rapidly generating store separation trajectories for identification and control applications. In Chapter 3, system identification will be used to introduce a semi-empirical formulation of the aerodynamic coefficients. The semi-empirical classification is due to a postulated analytical form of the equations completed with parameters estimated from empirical data.

2.3.2 Delta-Coefficient Methodology

The aerodynamic loads acting on the store are due primarily to three identifiable physical contributions, including (1) the local flow velocity combined with the position and orientation of the store, (2) the translational velocity of the store through the flow field, and (3) the rotational velocity of the store through the flow field [21]. Physically, these contributions are interrelated and inseparable. Computational Fluid Dynamics has the advantage of treating these effects in a physically meaningful way by solving for the flow field surrounding the store during the trajectory and integrating the pressure distribution directly to obtain the aerodynamic loads. In contrast, when wind tunnel and analytical methods are applied, the effects are necessarily determined separately and subsequently combined to estimate the total aerodynamic loads. Experience has shown that this build-up approach is sufficiently accurate for most applications in store separation.

In general, the aerodynamic loads on a flight vehicle in uniform flow depend nonlinearly on present and past values of airspeed, angles of incidence, linear and angular accelerations, control surface deflections, unsteady flow properties, viscous forces, compressibility effects, atmospheric properties, and other physical factors [24]. For a store in the vicinity of the aircraft, each of these effects is complicated by the variation of the flow field in space and time. A full description of the aerodynamic

loads is not practical and in practice is not necessary. Rather, a variety of simplifying assumptions are introduced.

1. The aerodynamic effects are assumed to be separable (uncoupled) allowing superposition to be used to determine the total aerodynamic loads. This is a practical assumption that is not rigorously justified but is usually necessary to make the problem tractable.

2. The flow is quasi-steady, which implies that the flow field reaches a steady state instantaneously after changes in the boundary conditions. This assumption limits the aerodynamic loads to dependency on the present values of the independent variables, ignoring the effect of past values of the independent variables. Some nonlinear effects, such as hysteresis, are neglected under this assumption.

3. The atmosphere surrounding the aircraft is uniform and unaltered by the presence of the aircraft and store. This implies that the atmospheric properties (pressure, temperature, density) are constant and that local atmospheric winds are monolithic with a constant translational velocity. This assumption is reasonable, due to the short duration of a typical store separation event (approximately 1 second).

4. The aircraft is in a steady-state flight condition and the corresponding flow around the aircraft is steady (e.g. not time-variant). This assumption allows use of wind-tunnel measurements that are time-averaged values, equivalent to mean flow components when turbulent fluctuations are present. This assumption is justified when (a) the length scales of the turbulence are significantly smaller than the length scale of the store, and (b) the frequencies of the turbulence are significantly higher than the frequencies of store motion, as is the case in most circumstances. As a notable exception, large-scale variations in flow field properties caused by cavity aerodynamics for weapons bays have been suspected to cause significant variations in store trajectories [25, 26]. However, current store separation wind tunnel test methodologies are insufficient for modeling these effects. CFD remains the primary methodology for dealing with unsteady flow effects on store separation. The F-16 case study used in this research is a “clean” configuration with a store released from a wing station in straight and level flight, so turbulence is not expected to be a significant issue.

These primary assumptions allow a considerable reduction in the complexity of the aerodynamic modeling. When the assumptions above are imposed, the store aerodynamic loads are a function of the aircraft velocity and orientation, the position and orientation of the store relative to the aircraft, and the translational and rotational velocity of the store relative to the aircraft. In functional form, the non-dimensional

force or moment coefficients can be written as a nonlinear function of the independent parameters.

$$C_i(t) = f\left(M, \alpha_A, \beta_A; \mathbf{r}_{B/A}(t), \boldsymbol{\psi}_{B/A}(t), {}^{A}\mathbf{v}_B(t), {}^{A}\boldsymbol{\omega}^{B}(t), \boldsymbol{\delta}(t)\right) \tag{2–94}$$

In Equation (2–94), C_i represents any of the aerodynamic coefficients, M is the aircraft Mach number, and α_A and β_A are the aircraft incidence angles (each assumed constant throughout the trajectory consistent with a steady state flight condition). The time-dependent parameters $\mathbf{r}_{B/A}(t)$, $\boldsymbol{\psi}_{B/A}(t)$, ${}^{A}\mathbf{v}_B(t)$, ${}^{A}\boldsymbol{\omega}^{B}(t)$, and $\boldsymbol{\delta}(t)$, are the position, orientation, velocity, and angular velocity of the store relative to the aircraft and the control surface deflections, respectively.

Even with the prior simplifications, the above functional form is too complicated to be of practical use. Given sufficient resources, current quasi-static wind tunnel test methodologies are capable of capturing the aerodynamic dependencies on $\mathbf{r}_{B/A}(t)$ and $\boldsymbol{\psi}_{B/A}(t)$. This is accomplished by placing the store at a matrix of predetermined positions and attitudes in the vicinity of the aircraft and recording the time-averaged aerodynamic loads (the resulting data set is referred to as grid data). However, the dependencies on ${}^{A}\mathbf{v}_B(t)$ and ${}^{A}\boldsymbol{\omega}^{B}(t)$ would require a dynamic rig capable of perturbing the store (in the vicinity of the aircraft) at scaled velocities representative of those encountered in flight. Fortunately, the translational and rotational velocities of the store near the aircraft are relatively small, and the aerodynamic dependencies on the dynamic parameters ${}^{A}\mathbf{v}_B(t)$ and ${}^{A}\boldsymbol{\omega}^{B}(t)$ can be adequately approximated using a uniform flow field (e.g neglecting the aircraft interference). Thus, the aerodynamic effects are decomposed into contributions from a uniform and nonuniform flow field. Note that this limitation does not apply to CFD methods, and the dynamic interference effects could in principle be estimated using CFD.

The independent parameters $\mathbf{r}_{B/A}(t)$ and $\boldsymbol{\psi}_{B/A}(t)$ represent six quantities (namely, three positions $x_{B/A}, y_{B/A}, z_{B/A}$ and three rotations $\psi_B^A, \theta_B^A, \phi_B^A$) that may take on a range

of values during any given trajectory. To establish a wind tunnel database with sufficient coverage for all six parameters is prohibitively expensive. For instance, if each variable were evaluated at ten different values, the database would require 10^6 distinct data points. This complexity is compounded by the various aircraft configurations and flight conditions. Clearly, a more efficient approach is required.

Typically, spatial variations with $y_{B/A}$ are neglected to reduce the parameter space and confine the aerodynamic interference effects to the *x*–*z* plane aligned with the store at carriage. Variations with $x_{B/A}$ and $z_{B/A}$ are combined into a single radial direction $r_{B/A}$ projecting vertically downward and slightly aft of the release point, with the radial direction chosen to be representative of the aft translation of the store during separation due to aerodynamic drag. Measurements along this radial direction are accomplished using a quasi-static sweep that economically captures the aerodynamic features over a fine mesh of discrete values. The yaw and pitch attitudes, ψ_B^A and θ_B^A , are decoupled from the roll attitude, ϕ_B^A , requiring far fewer combined orientations (and implicitly neglecting interactions with the roll angle, a limitation that is partially corrected using an offline approximation). The net result of these practical reductions is a significantly smaller parameter space. However, even with this reduced parameter space, a sufficient number of data points are prohibitively expensive to obtain in a costly wind-tunnel test.

Typically, the final predetermined grid values selected for the angular orientations ψ_B^A , θ_B^A , and ϕ_B^A , are too sparse to be used independently, i.e. the grid data collected are insufficient to adequately describe the aerodynamics of the store near the aircraft. Rather, in a manner similar to the dynamic parameters, the aerodynamic dependencies on the store position and orientation are decomposed further into uniform and nonuniform contributions. The uniform flow contributions are independent of the aircraft and rapidly achieved over a larger range and finer increments of independent parameters. The nonuniform flow contributions are then added as an incremental correction due to the presence of the aircraft. This so-called delta-coefficient approach

(first developed by Bamber [27] and further documented by Morgret [28]) provides an efficient and economical way to map the spatially variant aerodynamic characteristics.

The decomposition of the aerodynamic contributions is assumed to be independent and superposition is used to determine the cumulative aerodynamic loads. Thus, the total aerodynamic coefficient is given by an initial freestream (FS) estimate, plus corrections for the dynamic effects due to translational (TRANS) and rotational (ROT) velocities, the aircraft interference or grid (GR) data, and the uniform flow control (C) effect. The aerodynamic model is represented by superposition of individual contributions, as shown in Equation (2–95).

$$C = C_{FS} + \Delta C_{GR} + \Delta C_{DD} + \Delta C_C \tag{2–95}$$

These contributions are frequently determined using separate aerodynamic tables obtained from wind tunnel testing, tabulated as a function of multiple independent parameters. In functional form, the coefficient is determined by the relationship shown in Equation (2–96), where ${}^{I}p_B^B$,${}^{I}q_B^B$, and ${}^{I}r_B^B$ are the rotational velocities relative to the inertial wind frame and δ_e ,δ_a , and δ_r are the elevator, aileron, and rudder deflections, respectively.

$$\begin{aligned} C =& C_{FS}\left(M, \alpha_S, \beta_S\right) + \Delta C_G\left(r_{B/A}, \psi_B^A, \theta_B^A, \phi_B^A\right) \\ &+ \Delta C_{ROT}\left({}^{I}p_B^B, {}^{I}q_B^B, {}^{I}r_B^B\right) + \Delta C_C\left(\delta_e, \delta_a, \delta_r\right) \end{aligned} \tag{2–96}$$

Note that the translational velocities of the store relative to the wind, ${}^{W}u_B^B$, ${}^{W}v_B^B$, and ${}^{W}w_B^B$ are implicit in the computation of α_s and β_s, using the ancillary wind axis equations developed in the previous section. Thus, the term ΔC_{TRANS} is quite naturally accounted for through $C_{FS}\left(M, \alpha_s, \beta_s\right)$.

The primary rationale for using the delta-coefficient method, as opposed to direct interpolation of measured grid data, is that a relatively small freestream database

can be leveraged efficiently to extend the range of applicability of a grid database [28]. The freestream data is often available at a finer resolution, and sometimes with increased accuracy due to a separate large-scale freestream wind tunnel test, so the delta-coefficient method provides a significant improvement in modeling accuracy and efficiency. The delta-coefficient method has been used successfully for many years within the store separation community and experience has shown it to be quite reliable when sufficient grid data are available and flow conditions are not too dissimilar from freestream conditions [28].

2.3.3 Representative Case Study

The discussion in Section 2.3 on aerodynamic modeling for store separation is clarified by consideration of a particular representative example. The case study selected highlights many of the modeling precedents discussed thus far and provides a solid framework for investigating system identification and trajectory optimization techniques.

2.3.3.1 Freestream data

The representative freestream data were collected at the Arnold Engineering Development Center (AEDC) test facility in the 4T transonic wind tunnel [29]. The Aerodynamic Wind Tunnel 4T is a closed-loop, continuous-flow, variable-density tunnel with a Mach number range from 0.05 to 2.0. The test section is 4 ft square and 12.5 ft long with perforated walls to reduce boundary layer effects. The test was accomplished using a $1/20^{\text{th}}$ scale store model and includes Mach numbers ranging from 0.8 to 1.2 and store incidence angles (α_s and β_s) ranging from -40 to +40 degrees. The aerodynamic forces and moments were measured with a 0.188-in diameter, sting-mounted, strain-gauged moment balance. The freestream wind tunnel test was accomplished in June 2009 and is documented in AEDC-TR-09-F-19 [1].

The freestream data were collected in a series of angle of attach sweeps (i.e. alpha sweeps) at fixed sideslip angles (i.e. fixed beta). Figure 2-6 shows a snapshot of a series of alpha sweeps at multiple sideslip angles.

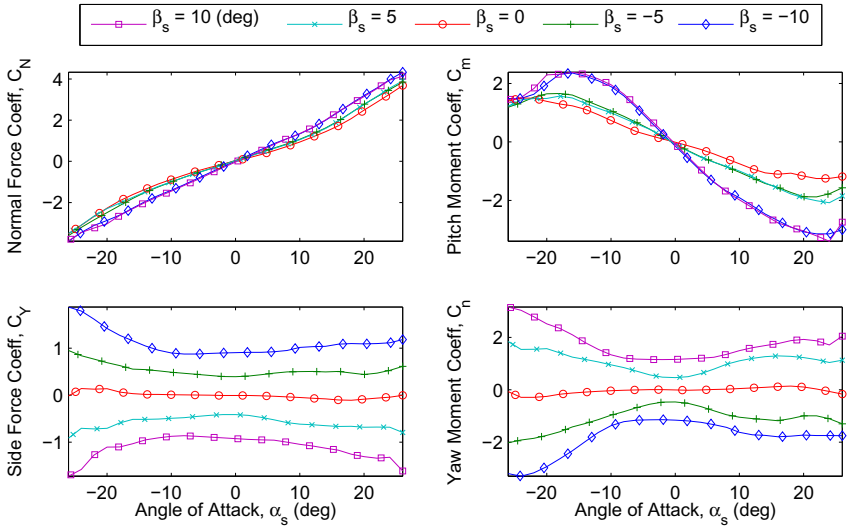

Figure 2-6. Freestream aerodynamic coefficients vs. angle of attack at fixed sideslip angle for a representative $1/20^{th}$ scale model at Mach 0.8.

The representative store is nearly axisymmetric and the symmetry is apparent in the collected freestream data, especially in the lateral side force and yawing moment measurements, C_Y and C_n . The relationship between C_N and α_s demonstrates an increasing normal force at higher angles of attack consistent with physical intuition. The linearity of the $C_N - \alpha_s$ curve over a relatively large range of α_s is an interesting and beneficial feature for subsequent application of system identification. The negative slope of the pitching moment coefficient over a range of α_s, especially near $\alpha_s = 0$, is indicative of a negative pitch moment derivative, $C_{m_\alpha} < 0$, a classical condition necessary (but not sufficient) for static longitudinal stability.

It is clear that the freestream data are well behaved and consistent over the range of independent variables presented thus far. However, separation-induced transients may drive the store well beyond the linear range of aerodynamics. Therefore the freestream data are collected at a wide range of α_s and β_s . Figure 2-7 shows the alpha

sweeps extended to the full +/- 40 deg range with 2 deg increments, with fixed beta values from -40 to +40 deg at 20 deg increments. The coarseness of the fixed beta values is chosen for clarity; the database includes beta values over the entire +/- 40 deg range at 5 deg increments.

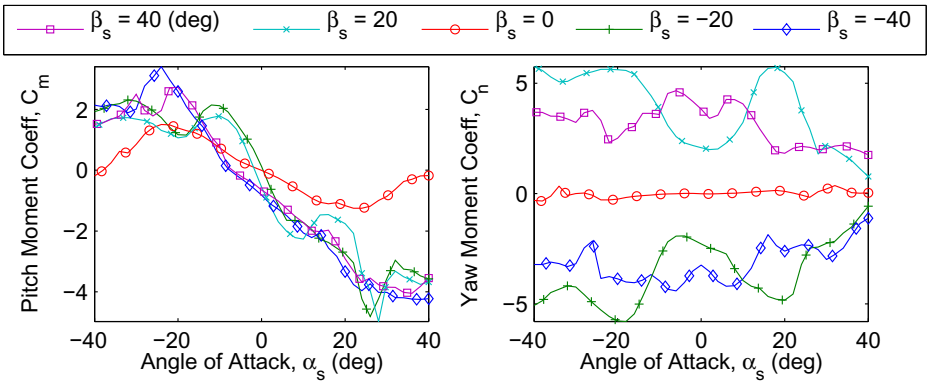

Figure 2-7. Pitching and Yawing moment coefficient vs. angle of attack for a representative $1/20^{th}$ scale model at Mach 0.8 for full range of angle of attack and sideslip angle.

It is clear that the full range of α_s and β_s include significant nonlinearities and simplistic analytical models are not feasible. Rather, the freestream data similar to those in Figure 2-7 are collected into a freestream database suitable for further analysis and interpolation during simulation.

2.3.3.2 Grid data

The freestream data are used to determine the store aerodynamics in uniform flow applicable to far-field conditions. In the proximity of the aircraft, the aerodynamics are spatially variant due to the nonuniform flow field. The aerodynamic interference is modeled using the delta-coefficients described in Section 2.3.2. The delta-coefficients are determined online during the wind tunnel test by measuring the total forces and moments acting on the store in proximity to the aircraft, and then subtracting off the interpolated freestream coefficients for the same flight conditions and incidence angles. Measurement of the grid data requires a dual-support structure in the wind tunnel, to

articulate both the aircraft and the store independently (the aircraft remains stationary during the vertical sweep of the store). The inverted aircraft wind tunnel model and metric store are shown in Figure 2-8.

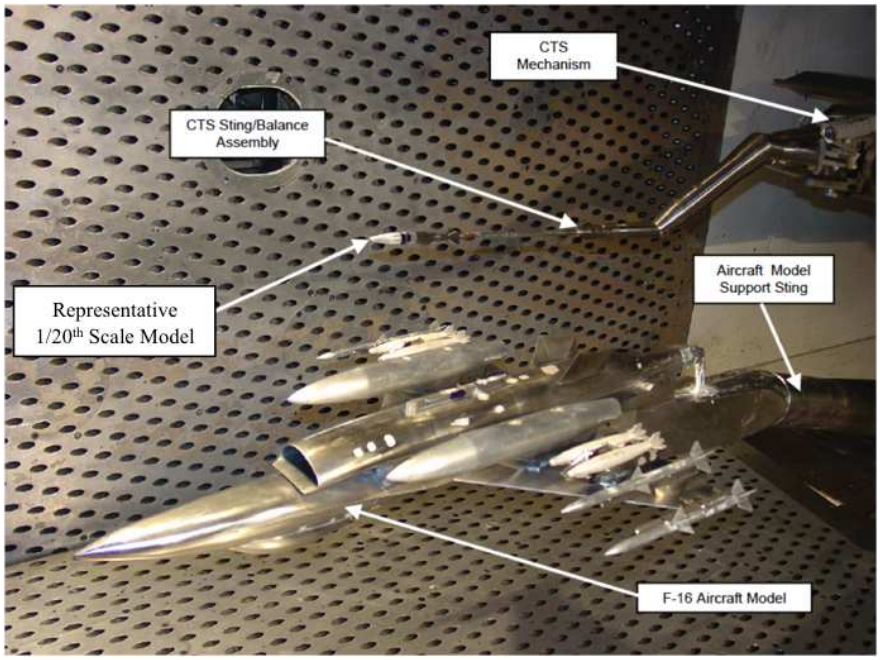

Figure 2-8. Dual support mechanism for F-16 store separation wind tunnel test. Excerpt from AEDC-TR-09-F-19 [1].

The grid data are collected as a function of the store position and attitude relative to the aircraft (3 dimensions), as well as the flight conditions and aircraft angle-of-attack, for a total of 5 independent variables for each aircraft configuration. Typically, the Mach number and aircraft angle-of-attack are held constant throughout the simulated trajectory, so a three-dimensional interpolation is sufficient for determining the aerodynamic coefficients of interest. Figure 2-9 shows a snapshot of representative grid data delta-coefficients for the representative $1/20^{th}$ scale model.

The grid data presented in Figure 2-9 illustrate the variation in the pitching and yawing moment delta coefficients with vertical position. For illustration, the pitching moment variation is shown for various fixed pitch angles and the yawing moment variation is shown for various yaw angles. The collected data include every combination

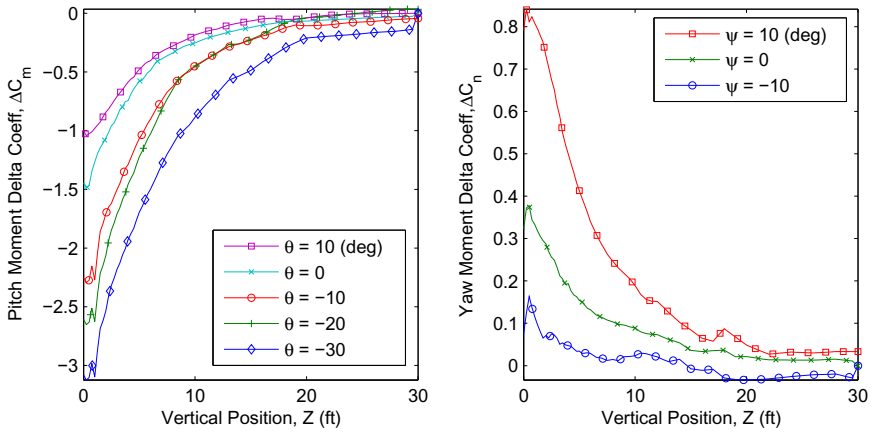

Figure 2-9. Aerodynamic pitching moment and yawing moment delta coefficients vs. vertical store position for various pitch and yaw angles, for a representative $1/20^{th}$ scaled model at Mach 0.8.

of the 5 discrete pitch angles and 3 discrete yaw angles, for a combination of 15 distinct attitudes. Each attitude is held constant throughout the vertical sweep. The vertical sweep is conducted slowly, so that the data at each discrete z-location represent quasi-static, time-averaged data. The collected data are organized by position and attitude in a database suitable for further analysis or multi-dimensional interpolation.

The most prominent feature of the grid data shown in Figure 2-9 is the consistent decay of the delta-coefficients with increasing distance from the aircraft. For this particular application the aircraft influence is negligible ($\Delta C_G = 0$) beyond 30 feet, indicating a uniform flow field in which the store aerodynamics can be modeled using only freestream data. For comparison, Figure 2-10 shows similar data collected at Mach 1.2.

Again, the influence of the aircraft flow field on the store aerodynamics is negligible beyond 30 ft. However, rather than a consistent decay, there is a significant perturbation in the coefficients between 10 and 20 feet below the aircraft. This level of complexity in the flow field is not unusual and demonstrates the importance of a high-resolution database for store separation modeling and simulation.

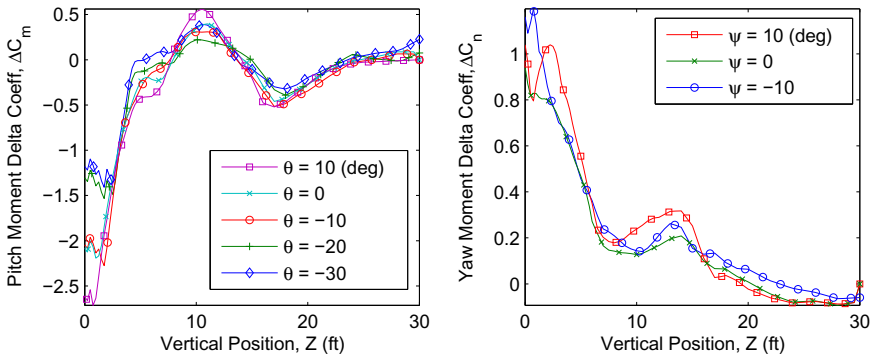

Figure 2-10. Aerodynamic pitching moment and yawing moment delta coefficients vs. vertical store position for various pitch and yaw angles, for a representative $1/20^{th}$ scaled model at Mach 1.2.

For a larger aircraft, the vertical position at which the spatial variation is negligible will be different, but the trends will be similar. The universality of the delta-coefficient decay in far-field conditions is an important feature useful for data quality checking and a characteristic that will be exploited in the application of system identification methods to modeling spatially variant aerodynamics.

2.4 Flight Test Validation

In order to make the store separation problem tractable, a variety of assumptions have been introduced up to this point. A few of these assumptions are related to the kinematics and dynamics, but most are related to the aerodynamic characteristics. Some of these assumptions are justified by examining the nature of the problem (and have an insignificant effect on the result) and some are necessary to make the solution accessible using practical methods (and may have a significant effect on the result that is difficult to quantify). Given the variety of assumptions that have been proposed, the question faced is one of accuracy: is the proposed methodology sufficiently accurate to characterize the store trajectory during separation?

The most direct answer to this question comes from comparison to flight test data. Flight testing provides a dependable way to validate the simulation, and simulation provides an effective way of reducing flight testing. As such, an iterative approach

to flight testing and simulation validation has proven to be an effective method for accomplishing store separation analyses.

2.4.1 Flight Test Data Reduction

The two primary sources of data for store separation flight test validation are photogrammetric and telemetry data. Photogrammetric data are obtained from high-speed video cameras mounted on the aircraft in locations that minimize flow field disturbance and provide multiple perspectives for observing the motion of the store relative to the aircraft. Photogrammetric data are used initially for qualitative assessment of the store trajectory, but specialized tracking software is also used to determine a quantitative description of the store trajectory [30].

Telemetry data are obtained from an inertial measurement unit (IMU) attached to the store and transmitted to an independent ground station during separation. The Spectrum Sensors & Controls 65210A six degree-of-freedom (6DOF) inertial measurement unit provides tri-axial acceleration and angular rate measurements. The self-contained IMU with a built-in FM transmitter provides simultaneous sampling at up to 42,500 samples/sec with reconfigurable output range and filter frequency. These data can be used to completely reconstruct the store separation trajectory and analyze the trajectory relative to the aircraft [31, 32].

2.4.1.1 Trajectory reconstruction

The purpose of trajectory reconstruction is to utilize the measured rates and accelerations to estimate the remaining state variables. Recognizing the presence of measurement noise, the trajectory reconstruction process could be accomplished using non-deterministic state estimation methods, such as Kalman filtering or optimal smoothing. However, deterministic methods based on kinematic relationships typically provide sufficient accuracy over the short time interval of interest for store separation purposes.

The IMU attached to the store measures the store angular rates in the body axis, which are equivalent to the generalized angular velocities shown in Equation (2–97).

$$ {}^{I}\boldsymbol{\omega}^{B} = {}^{I}p_B^B\,\mathbf{b}_x + {}^{I}q_B^B\,\mathbf{b}_y + {}^{I}r_B^B\,\mathbf{b}_z \tag{2–97} $$

The measured body rates can be used to determine the orientation of the store relative to the inertial reference frame by solving for the Euler angles using the kinematic differential equations in state space form.

$$ \begin{bmatrix} \dot{\phi}_B^I \\ \dot{\theta}_B^I \\ \dot{\psi}_B^I \end{bmatrix} = \begin{bmatrix} {}^{I}p_B^B + {}^{I}r_B^B \cos\phi_B^I \tan\theta_B^I + {}^{I}q_B^B \tan\theta_B^I \sin\phi_B^I \\ {}^{I}q_B^B \cos\phi_B^I - {}^{I}r_B^B \sin\phi_B^I \\ ({}^{I}r_B^B \cos\phi_B^I + {}^{I}q_B^B \sin\phi_B^I)\sec\theta_B^I \end{bmatrix} \tag{2–98} $$

These three scalar nonlinear equations are coupled and must be solved simultaneously using a differential equation solver, such as a 4th order Runge Kutta algorithm. Note that the kinematic relationships have a singularity at $\theta_B^I = \pm 90 deg$, which corresponds to a straight climb or dive. This situation rarely arises in store separation, but nonetheless quaternion relationships can be used instead for a more robust method of determining the Euler angles [33].

Once the orientation of the store body axis with respect to the inertial axis is available, the translational kinematics can be considered. Recall that the position of the store CG relative to the origin of the inertial axis system is given by $\mathbf{r}_B$. Similarly, let the position of the telemetry IMU center of navigation relative to the inertial axis system be denoted by $\mathbf{r}_T$. Then the position of the store CG relative to the IMU is denoted by $\mathbf{r}_{B/T}$. The three vectors are related by Equation (2–99).

$$ \mathbf{r}_B = \mathbf{r}_T + \mathbf{r}_{B/T} \tag{2–99} $$

Taking the derivative of the above expression, as seen by an observer fixed in the inertial reference frame gives Equation (2–100).

$$\frac{{}^{I}d\mathbf{r}_{B}}{dt} = \frac{{}^{I}d\mathbf{r}_{T}}{dt} + \frac{{}^{I}d\mathbf{r}_{B/T}}{dt} \tag{2–100}$$

The term $\mathbf{r}_{B/T}$ is fixed in body coordinates (assuming the CG is fixed) and known from pre-flight measurements. The derivative is most efficiently evaluated using the transport theorem.

$$\frac{{}^{I}d\mathbf{r}_{B}}{dt} = \frac{{}^{I}d\mathbf{r}_{T}}{dt} + \frac{{}^{B}d\mathbf{r}_{B/T}}{dt} + {}^{I}\boldsymbol{\omega}^{B} \times \mathbf{r}_{B/T} \tag{2–101}$$

Note that the term ${}^{B}d\mathbf{r}_{B/T}/dt = 0$ since the position of the CG relative to the IMU is constant. Also note that the derivative of $\mathbf{r}_{B}$ is equivalent to the velocity of the store CG, ${}^{I}d\mathbf{r}_{B}/dt = {}^{I}\mathbf{v}_{B}$. With these simplifications, Equation (2–101) can be rewritten as shown in Equation (2–102).

$${}^{I}\mathbf{v}_{B} = {}^{I}\mathbf{v}_{T} + {}^{I}\boldsymbol{\omega}^{B} \times \mathbf{r}_{B/T} \tag{2–102}$$

Introducing the acceleration of the store CG as ${}^{I}\mathbf{a}_{B}$, taking the time derivative of Equation (2–102) and simultaneously applying the transport theorem gives the result shown in Equation (2–103), where ${}^{I}\boldsymbol{\alpha}^{B}$ is the angular acceleration of the store relative to the inertial axis. The angular acceleration is determined by numerical differentiation (with appropriate smoothing) of the measured angular rates.

$${}^{I}\mathbf{a}_{B} = {}^{I}\mathbf{a}_{T} + {}^{I}\boldsymbol{\alpha}^{B} \times \mathbf{r}_{B/T} + {}^{I}\boldsymbol{\omega}^{B} \times \left({}^{I}\boldsymbol{\omega}^{B} \times \mathbf{r}_{B/T}\right) \tag{2–103}$$

Equation (2–103) provides a coordinate-free expression for the acceleration of the store CG when the translational and rotational accelerations are known from measurements. Since the measurements are necessarily made in the body axis, equation (2–103) is typically evaluated in the body axis. The resulting accelerations are easily transformed from the body axis to the inertial axis using a coordinate transformation.

$$\left[{}^{I}\mathbf{a}_{B}\right]^{I} = [T]^{IB}\left[{}^{I}\mathbf{a}_{B}\right]^{B} \tag{2–104}$$

Once the accelerations are expressed in the inertial axis, the acceleration due to gravity can be accounted for, depending on the type of accelerometers used (some accelerometers measure absolute acceleration, others measure changes in acceleration). The velocity and position of the store in inertial coordinates can be determined via direct integration of the transformed accelerations.

$$ {}^{I}\mathbf{v}_{B}(t) = \int_{0}^{t} {}^{I}\mathbf{a}_{B}(t)\, dt \tag{2–105} $$

$$ \mathbf{r}_{B}(t) = \int_{0}^{t} {}^{I}\mathbf{v}_{B}(t) dt \tag{2–106} $$

Once the trajectory reconstruction is accomplished, a complete description of the store trajectory during separation is available, providing a valuable resource for further analysis including determination of an aircraft-relative trajectory and investigation of the in-flight aerodynamic characteristics.

2.4.1.2 Trajectory analysis

The inertial trajectory determined from trajectory reconstruction is mathematically equivalent to an inertial trajectory generated via simulation. Therefore, once the reconstructed trajectory is quantified in inertial coordinates, the store motion relative to the aircraft can be determined using the mathematical relationships described in Section 2.2.5 for (1) an arbitrary aircraft maneuver or (2) a steady-state aircraft trajectory including (a) straight and level flight, (b) steady climb or dive, or (c) steady pull-up or push-over. The resulting aircraft-relative trajectory is suitable for qualitative comparison to photogrammetric data obtained from cameras fixed to the aircraft.

Once the twelve state variables have been estimated using the trajectory reconstruction process, the 6DOF equations of motion can be used to relate the observed motion to the corresponding aerodynamic forces responsible for the motion. Returning to the translational and rotational equations of motion given by Equations (2–28) and (2–37), it is apparent that when the store motion is known a priori, determining the aerodynamic

forces and moments can be accomplished algebraically, a process sometimes referred to as reverse dynamics. Thus, flight test data can be used directly to estimate the aerodynamic forces and moments acting on the store during separation. This provides a valuable resource for validating the separation characteristics and aerodynamic models. Consideration of a particular example will provide increased clarity to the trajectory reconstruction and trajectory analysis procedures.

2.4.2 Flight Test Results

Two representative cases were selected for comparison of simulation and flight test data including one release at Mach 0.9 / 550 KCAS and another at Mach 1.2 / 600 KCAS. Both flight tests were accomplished in a wings-level, steady, unaccelerated flight condition. The inert, unguided, instrumented separation test vehicle was equipped with an high-quality inertial measurement unit. The measured 6DOF telemetry data for the Mach 1.2 release is shown in Figure 2-11.

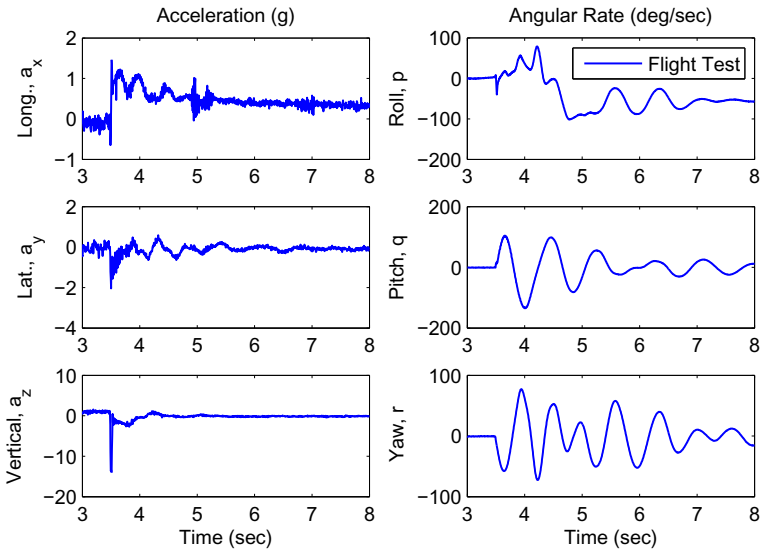

Figure 2-11. Measured 6DOF telemetry data for F-16 Separation Flight Test 4535 (Mach 1.2 / 600 KCAS).

The telemetry data shown includes the translational accelerations a_x, a_y, a_z and angular velocities, p, q, r, corresponding to scalar components of the inertial vectors $\left[{}^{I}\mathbf{a}_{B}\right]^{B}$ and $\left[{}^{I}\boldsymbol{\omega}^{B}\right]^{B}$, respectively. The large peak in vertical acceleration (a_z)

at approximately 3.5 seconds is the ejection force and represents the start of the separation event (redefined as $t = 0$ for subsequent plots). The inherent stability of the store is evident from the telemetry data in that the separation-induced transients diminish after about 5 seconds of flight time, driving the store toward a steady-state flight condition. However, it is difficult to visualize the nature of the store trajectory near the aircraft using only the telemetry data. The trajectory reconstruction process provides a more direct analysis. The reconstructed trajectory, along with a wind tunnel based simulation, is shown in Figure 2-12.

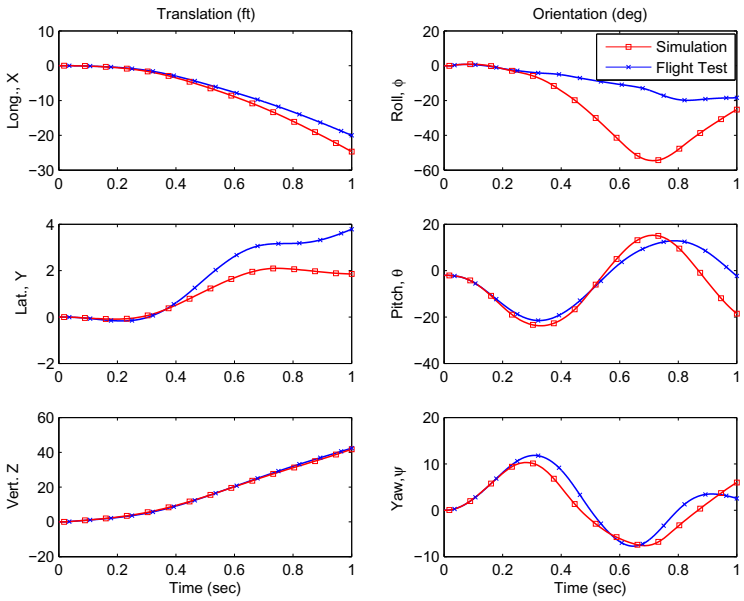

Figure 2-12. Reconstructed flight test trajectory comparison with wind tunnel based simulation for F-16 Separation Flight Test 4535 (Mach 1.2 / 600 KCAS).

The flight test trajectory in inertial coordinates (X, Y, Z corresponding to the scalar components of $[\mathbf{r}_B]^I$ and ϕ, θ, ψ corresponding to ϕ_B^I , θ_B^I , ψ_B^I) was determined using the trajectory reconstruction process described in Section 2.4.1.1. The simulated trajectory was determined using the wind tunnel based methods discussed in Section 2.3. The comparison shows excellent agreement for the primary degrees of freedom of interest (namely, pitch angle and vertical translation). A notable deviation in roll is

apparent from the comparison. This deviation is not unusual for store separation and is due to a combination of large uncertainties in wind tunnel measurements due to an exceedingly small roll moment measurement and a low roll-axis moment of inertia of the full-scale store (thus, the trajectory is sensitive to a variable that is difficult to measure accurately). For the nearly axisymmetric store used in this analysis, the deviation in roll angle between flight and simulation does not present a problem. Figure 2-13 shows a similar trend for flight test data at Mach 0.9 / 550 KCAS.

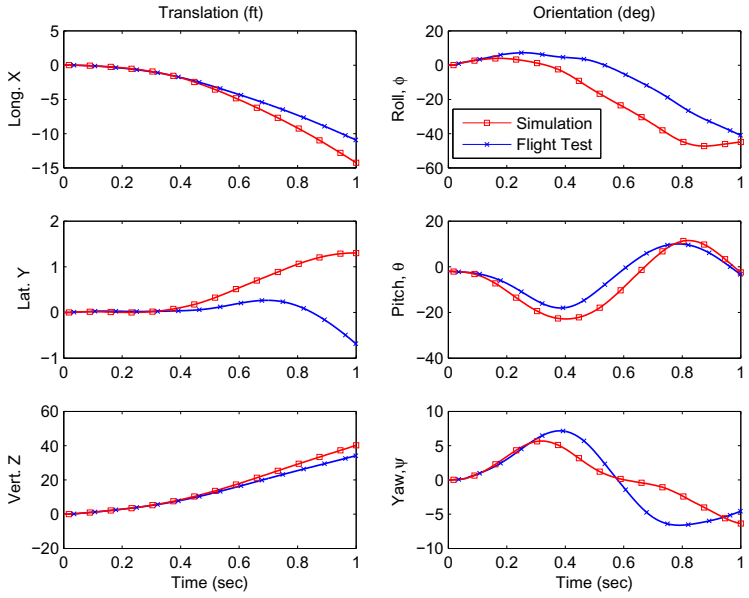

Figure 2-13. Reconstructed flight test trajectory comparison with wind tunnel based simulation for F-16 Separation Flight Test 2265 (Mach 0.9 / 550 KCAS).

The flight test and simulation trajectory comparison for the Mach 0.9 release indicates similar results to the Mach 1.2 release. Both trajectories are characterized by a slight nose-down pitch angle near the aircraft – a near-ideal separation trajectory. Recovery to a small nose-up pitch angle is evident in both cases, again indicating the inherent longitudinal stability of the store. Figure 2-14 shows a visual comparison of the flight and simulation trajectories for the Mach 1.2 release. The similarity between the flight test and simulated trajectories and the characteristic motion of the store near the aircraft is evident from the visualization.

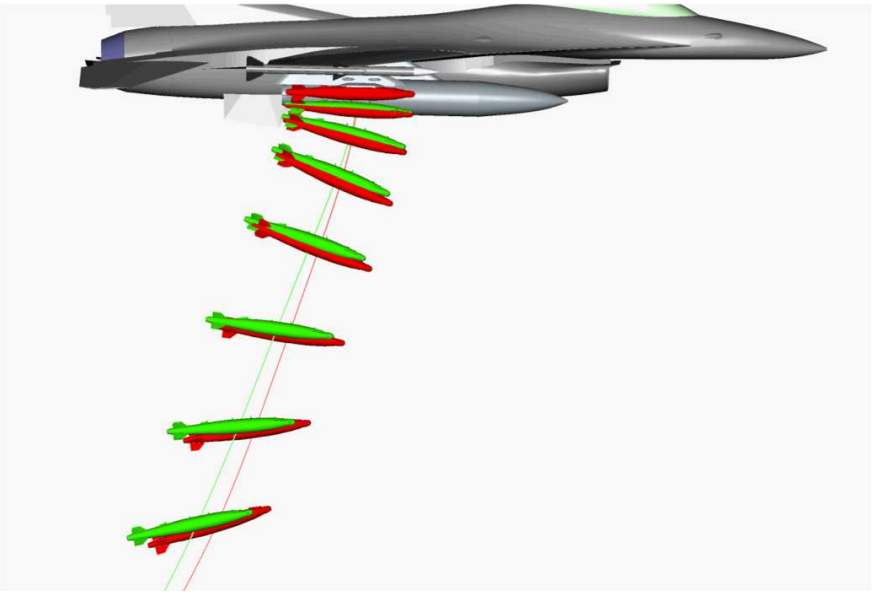

Figure 2-14. Visual comparison of flight test and wind tunnel based simulation trajectories for F-16 Separation Flight Test 4535 (Mach 1.2 / 600 KCAS).

For both cases, the agreement between the flight test and simulated trajectory is very strong, supporting the wind tunnel based trajectory prediction methodology. Considering the comparison of estimated aerodynamic coefficients from the flight test trajectories with wind tunnel predictions for an equivalent prescribed trajectory provides further validation of the aerodynamic modeling approach. Figures 2-15 and 2-16 show the aerodynamic comparison for both flight tests.

The flight test aerodynamic coefficients were determined as part of the trajectory reconstruction process. It is important to note that (1) the estimates are noisy due to the numerical differentiation, despite significant smoothing of the measured data and (2) that the ejector forces are included in the aerodynamic coefficients for the first 50 msec of the trajectory. For comparison, the wind tunnel based aerodynamic coefficients were determined using the delta-coefficient methodology for the prescribed flight test trajectory. The agreement between the flight test and wind tunnel aerodynamic coefficients is strong in both cases. The deviation in the axial force coefficient, C_A, is expected due to the difficulty of measuring axial force in the wind tunnel for a small-scale

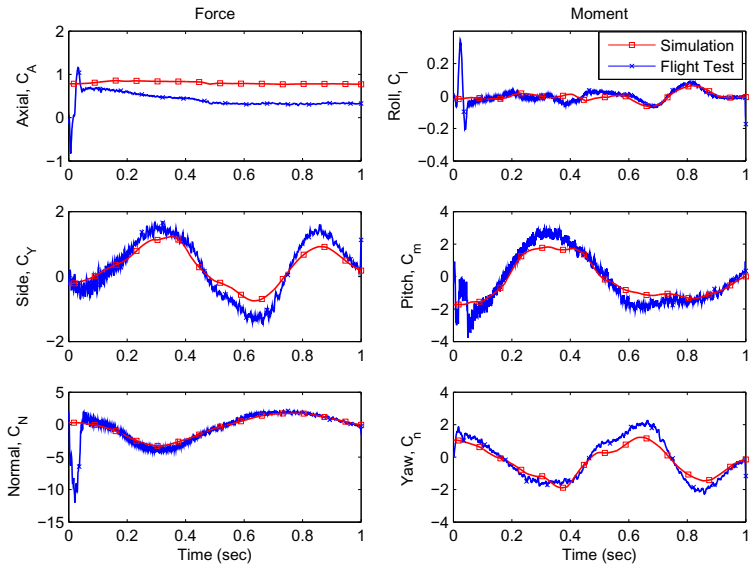

Figure 2-15. Comparison of flight test and wind tunnel aerodynamic coefficients for F-16 Separation Flight Test 4535 (Mach 1.2 / 600 KCAS).

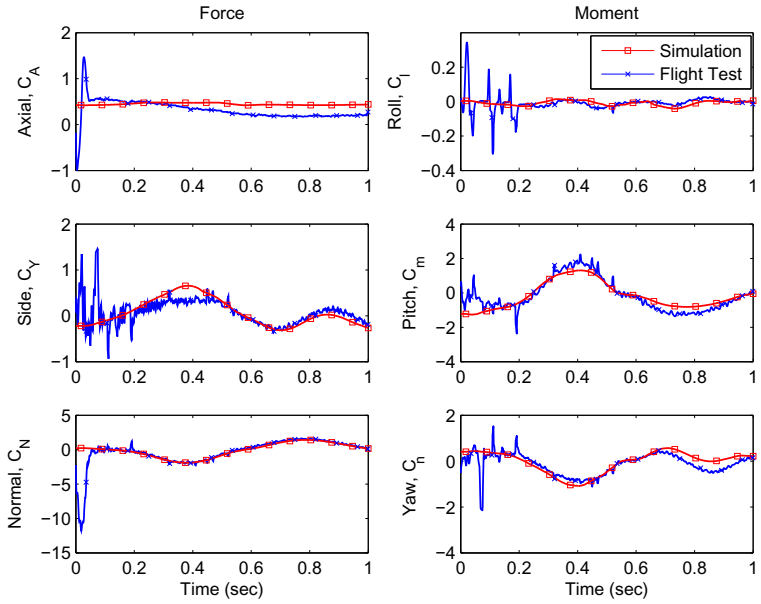

Figure 2-16. Comparison of flight test and wind tunnel aerodynamic coefficients for F-16 Separation Flight Test 2265 (Mach 0.9 / 550 KCAS).

model. Fortunately, the axial force has only a minute effect on the overall trajectory. It is unclear if the high frequency perturbations in the flight test data early in the trajectory (less than 0.25 sec) are due to noise in the measurement (perhaps structural vibration

from the ejection) or turbulent aerodynamics. Regardless, the time-averaged nature of the wind tunnel data is clearly evident when compared to measured flight test data. Despite these differences, the simulation results show a strong correlation with flight test, further validating the trajectory prediction methodology, providing a valuable resource for further analysis and control system design.

2.5 Chapter Summary

The purpose of this chapter is to summarize mathematical modeling of store separation in order to provide a framework for the remaining developments in system identification and trajectory optimization. Store separation is an inter-disciplinary field leveraging concepts from aerospace, mechanical and systems engineering. Rigid body dynamics, aerodynamics, wind tunnel testing and flight test validation were presented to provide the necessary background for implementing system identification and trajectory optimization for guided store separation. The store separation equations of motion were derived, using a set of reference frames and coordinate systems unique to store separation, and the equations were extended to determine an aircraft-relative trajectory for multiple types of aircraft maneuvers. The well-established delta-coefficient method was presented as an extension to traditional aerodynamic modeling for flight dynamics. Representative wind tunnel data were included to clarify the aerodynamic modeling approach. Finally, flight test trajectory reconstruction from inertial measurements was considered and representative flight test data were presented. Comparisons of the flight test data to wind tunnel based modeling and simulation were presented to validate the proposed methodology. Although the agreement with flight test is not perfect, the model presented here is sufficiently representative to use as a foundation for system identification and trajectory optimization.

CHAPTER 3
SYSTEM IDENTIFICATION

3.1 Overview

The purpose of system identification in the context of guided store separation is to develop a parametric model that describes the spatially variant aerodynamics of a store during separation. This model can be used to assess the major contributors affecting separation characteristics, determine the trajectory of the store given prescribed initial conditions, perform trajectory optimization, and design a control system using linear and nonlinear control techniques. This chapter provides a brief description of relevant techniques in system identification, followed by application of system identification methods to determine a parametric model for the spatially variant aerodynamics of a store during separation.

3.1.1 System Identification

System identification (SID) is the process of determining an adequate mathematical model, usually containing differential equations, with unknown parameters that have to be determined indirectly from measured experimental data [34]. Practically, SID encompasses a wide range of activities including mathematical modeling, designing suitable experiments, collecting measurements, performing diagnostics and statistical analysis, and validating identified models. System identification is closely related to parameter estimation (or parameter identification), but the two disciplines are not the same. SID involves a range of activities necessary to determine an adequate model for an experimental system, whereas parameter estimation is a class of statistical techniques that use measured data to estimate the parameters within a postulated model. Thus, parameter estimation is a subset of system identification.

The purpose of SID is to use experimental measurements, postulated physical relationships, and statistical inferences to determine a mathematical model that adequately describes the physical system of interest over a specified domain of

operation. SID is a broad discipline and has been applied in many areas including biology, medicine, chemical processes, economics, geology, materials, civil and mechanical engineering, and flight dynamics [34]. System identification, in the broadest sense, is an inverse approach to modeling cause-and-effect dynamic systems using observed input-output relationships.

System identification is well documented in the technical literature. The survey paper by Astrom and Eykhoff [35] and several notable textbooks including those by Eykhoff [36], Goodwin and Payne [37], Ljung [38], Schweppe [39], Sage and Melsa [40], Hsia [41] and Norton [42] are good starting points. Additionally, the proceedings from the International Federation on Automatic Control (IFAC) Symposia on Identification and System Parameter Estimation on three-year intervals from 1967 to present provide a rich resource for further investigation.

3.1.2 Flight Vehicle System Identification

Flight vehicle system identification consists of the specialization of general SID techniques to a variety of flight vehicles including aircraft, helicopters, and missiles. The flight characteristics of these vehicles are determined by the dynamic relationships described by the equations of motion combined with aerodynamic and propulsive forces and moments acting on the vehicle. The rigid body aircraft equations of motion are well known and closely related to the store separation equations of motion derived in Section 2.2.3.5. Propulsive forces are generally characterized in a ground test environment with corrections for in-flight performance. Therefore, SID of flight vehicles reduces to using measured data to determine the model structure for the aerodynamic forces and moments and to estimate of the unknown parameters contained in the model [24].

Wind tunnel testing and computational fluid dynamics (CFD) are common sources for quantifying aerodynamic characteristics of the flight vehicle early in the design phase and throughout the life cycle. In most cases, wind tunnel testing and CFD provide a more cost effective way to characterize the aerodynamics in comparison

to flight testing, but each method has significant limitations (such as scaling effects and dynamic limitations for wind tunnel testing and computational resources and error propagation for CFD). SID provides a way to characterize the aerodynamics using in-flight measurements for the actual flight vehicle in operational conditions. System identification (1) provides an important independent source of validation for wind tunnel testing and CFD, (2) provides a means of testing flight conditions and maneuvers that are not easily reproduced in a ground test environment, (3) provides a way to expand the flight envelope for existing flight vehicles, (4) provides a means of verification for specification compliance, and (5) provides a reliable source of aerodynamic modeling for automatic control system design [24]. Ideally, each of the three primary resources for aerodynamic modeling: wind tunnel testing, computational fluid dynamics, and system identification, are used in a coherent fashion to produce a comprehensive and reliable model of flight vehicle aerodynamics.

Although flight vehicle SID is appropriately categorized as a specialized application of SID, the use of in-flight measurements to determine aerodynamic parameters long preceded the advent of SID as a technical discipline. One of the first approaches for obtaining static and dynamic aerodynamic parameters from flight data was given by Milliken [43] in 1947. A few years later, Greenberg [44] and Shinbrot [45] established more general and rigorous methods for determining aerodynamic parameters from transient maneuvers.

With the introduction of digital computers in the 1960s and 1970s, flight vehicle SID became a tremendous field of research with much rapid advancement. Pioneering contributions were made by individuals such as Taylor and Iliff [46], Mehra [47], Stepner and Mehra [48], and Gerlach [49]. These early contributions were primarily in the area of developing various parameter and state estimation techniques. Introduction of highly maneuverable and unstable aircraft presented many challenges to the theory and practice of system identification, many of which were addressed by Klein [50] and Klein

and Murphy [51]. With a growing reliance on system identification for aircraft certification and control system design combined with a desire to reduce the extent of flight testing, research in optimal maneuver design was pursued by Mulder [52], Mehra [53, 54], and Morelli [55, 56]. Several useful technical references for aircraft system identification have been published, including an extensive bibliography compiled by Iliff and Maine [57], and broad survey papers by Klein [58, 59], and Hamel and Jategaonkar [60]. Padfield [61] and Hamel and Kaletka [62] have provided similar reference articles for rotorcraft system identification.

With multiple options for input design and parameter estimation techniques well in hand, current research trends are focused on model structure determination for nonlinear and time-variant aerodynamic phenomenon, including high-alpha flight [63], unsteady aerodynamics [64], wake vortex encounter [65, 66], ground effect [67] and other configuration changes [68]. The interest in SID for adaptive control systems has also led the development of various recursive parameter estimation techniques [38, 69], including recursive least squares and extended Kalman filtering with state augmentation [34]. The application of SID to store separation pursued in this research is properly understood in this context to be an extension of these burgeoning techniques to a nonlinear and, in this case, spatially variant aerodynamic modeling problem.

The urgent desire to reduce flight testing, combined with the increasing reliability and versatility of computational fluid dynamics has given rise to a promising endeavor to apply system identification techniques to CFD modeling. CFD can be used directly to estimate linear and nonlinear aerodynamic characteristics but these applications have traditionally been limited to stationary flight conditions. However, the computational power needed to perform dynamic maneuvers in a virtual environment is now technically feasible and increasingly available, closing the gap between traditional flight mechanics methods and computational methods. Promising results have been documented by Dean and Morton [70, 71] Green [72], Bodkin [73], and Clifton [74]. It is recognized

that whereas conventional SID is applied to the actual flight vehicle, CFD-based SID provides a model of a model, e.g. a parametric model or reduced order model. However, the CFD-based parametric model has many beneficial uses that may dramatically reduce the extent of full-scale flight tests, resulting in cost and schedule savings [70]. Furthermore, many of the inaccuracies that arise from flight testing (such as measurement error, state estimation, atmospheric turbulence, control system coupling, collinearity among state variables, etc) are no longer limitations within a computational environment. Though modeling inaccuracies are inherent in computational methods, the trade-off between modeling and flight-test limitations levels the playing field between the two approaches, providing further credibility to CFD-based SID. As CFD flow solvers continue to advance in sophistication and accuracy with simultaneous advancement of large scale computing capability, CFD-based SID will become increasingly relevant for flight dynamics and control.

Application of CFD-based SID to store separation is of particular interest. System identification requires execution of dynamic maneuvers that are physically impossible or at least immensely impractical for a store in the vicinity of an aircraft. However, such maneuvers are easily accomplished in a computational environment, providing the capability of parametric modeling using SID in a flow field environment that is otherwise difficult to describe analytically. Although this research emphasizes wind tunnel based SID, the transfer of these methodologies to a CFD environment should be straightforward.

3.1.3 Store Separation System Identification

The application of system identification to aerodynamic modeling for store separation leads to a parametric model that describes the spatially variant aerodynamics of the store during separation. Offline wind tunnel based trajectory simulations provide a virtual environment for accomplishing maneuvers necessary to perform system identification in an exploratory fashion due to the rapid computation of trajectories on

any modern personal computer. Store separation SID is a procedure that includes (1) model postulation, (2) input design, (3) model structure determination, (4) parameter estimation, and (5) model validation. For the purpose of this research, the postulated model is a multivariate polynomial with spatially variant coefficients. The model structure is dependent on the input and flight conditions and is determined using multivariate orthogonal decomposition. The input is defined using a multisine dynamic optimization algorithm. Parameter estimation is accomplished using the equation error method and model validation is accomplished by comparing predicted results with independent simulations. These concepts are discussed in detail in Section 3.2. The application of these techniques to determine a parametric model for store separation is one of the primary contributions of this research.

3.2 Identification Methods

The core activities of system identification are primarily model structure determination and parameter estimation. In practice, flight vehicle SID encompasses a much broader range of activity. According to Klein and Morelli [24], flight vehicle SID includes model postulation, experiment design, data compatibility analysis, model structure determination, parameter and state estimation, collinearity diagnostics, and model validation. An in-depth development of each of these areas is provided by Klein and Morelli and similar developments are provided by Jategaonkar [34]. When applying SID to store separation in a virtual environment, the process is slightly modified and in some ways simpler. Experiment design requires consideration of instrumentation requirements, which are not relevant for simulation-based study. Rather, the experiment design step reduces to input design, which is an area of paramount importance for simulation-based studies where shorter duration maneuvers are highly desirable. Data compatibility analysis is driven by the need to synthesize measurements from various instrumentation systems (typically the aircraft air data system and inertial measurement system) and again this step is omitted for simulated trajectory solutions.

State estimation is a necessary tool for flight testing since many of the state variables are not measured directly and even those that are measured directly are corrupted by noise. State estimation techniques (usually a Kalman filter variant) provide a way to reconstruct the flight path with optimal estimates of the true state given assumed measurement error characteristics. In a simulation environment, the states are specified and recorded with numerical precision; all states are known and measurement noise is not incurred. Finally, in flight testing, the state variables are inherently related through dynamic and kinematic relationships and in some cases the variables are nearly linearly dependent, causing significant problems for identifiability.[1] In such cases, collinearity diagnostics are necessary to determine the accuracy of the parameter estimation by considering the correlation among the input variables. In a simulation environment, the input is more freely selected and the inputs can be chosen to be mutually orthogonal, providing maximum information content in the input signal and eliminating collinearity among input variables.

With the above simplifications, the store separation SID procedure is reduced to the following steps: model postulation, input design, model structure determination, parameter estimation, and model validation. These procedures are discussed in more detail in Sections 3.2.1 through 3.2.4.

3.2.1 Input Design

The task of input design is to determine a suitable reference trajectory from which parameter estimation can be accomplished. The objective is to design an input that will excite the dynamic system so that the data contain sufficient information for accurate

[1] The concept of identifiability is closely related to controllability and observability. Identifiability, as the name suggests, quantifies the ability to determine the influence of a given input on a specified output. When two are more inputs are perfectly correlated, the influence of each input on the observed output becomes impossible to identify mathematically.

modeling. It is also desirable to maximize the information in the input signal in order to reduce the duration of the trajectory. Several types of input commonly used in aircraft system identification include an impulse, step, square wave, doublet, multistep, and frequency sweep [24]. These signals find wide application in aircraft system identification due primarily to the ease of implementation. However, these inputs generally require long duration maneuvers to generate sufficient modeling results. Alternatively, multisine inputs produce a favorable input signal for simulation-based system identification with rich information content over a relatively short time interval.

The multisine input is a sum of sinusoids with various frequencies, amplitudes, and phase angles, optimized to provide the maximum information content over a specified range of frequency and amplitude [24]. The Schroeder sweep is one such maneuver consisting of a summation of multiple harmonic cosine terms [75]. Previous work has shown that the Schroeder sweep provides an input with good frequency content and low peak factor [76]. The peak factor is a measure of the ratio of maximum input amplitude to input energy contained in the signal. Inputs with low peak factors are efficient in the sense of providing good frequency content without large amplitudes in the time domain [76]. Modifications of the Schroeder sweep have been investigated and applied in a variety of situations [77, 78]. Multisine inputs are difficult for a pilot to create manually, but have found strong support in applications involving simulation where the primary interest is in an information-rich input signal with compact duration [79, 80]. Morelli developed an extension of the Schroeder sweep input design method to include multiple orthogonal inputs with optimized peak factors [76]. The corresponding technique was implemented in the Matlab® toolbox System Identification Programs for Aircraft (SIDPAC®), also developed by Morelli [81]. The multisine input method can generate an arbitrary number of multiple inputs that are mutually orthogonal and adhere to a uniform power spectrum, providing an excellent framework for simulation-based system identification. The development proposed by Morelli is summarized here.

Each multisine input $\mathbf{u}_j$ is comprised of a set of summed harmonic sinusoids with individual phase lags ϕ_K , as shown in Equation (3–1), where M is the total number of harmonic frequencies, T is the time length of the excitation, and A_K and ϕ_K are the amplitude and phase angles to be chosen for each of the harmonic components.

$$\mathbf{u}_j = \sum_{k=1}^{M} A_k \cos\left(\frac{2\pi k\,\mathbf{t}}{T} + \phi_K\right) \tag{3–1}$$

The phase angles are chosen using a simplex optimization algorithm to produce a low peak factor PF, defined by Equation (3–2).

$$PF\,(\mathbf{u}_j) = \frac{[\max(\mathbf{u}_j) - \min(\mathbf{u}_j)]/2}{\sqrt{(\mathbf{u}_j^T\mathbf{u}_j)/N}} \tag{3–2}$$

When the input excitation $\mathbf{u}_j$ oscillates symmetrically about zero, the peak factor can be expressed in terms of the norms $\|\mathbf{u}_j\|_\infty$ and $\|\mathbf{u}_j\|_2$.

$$PF\,(\mathbf{u}_j) = \frac{[\max(\mathbf{u}_j) - \min(\mathbf{u}_j)]/2}{2\,\mathrm{rms}(\mathbf{u}_j)} = \frac{\|\mathbf{u}_j\|_\infty}{\|\mathbf{u}_j\|_2} \tag{3–3}$$

The term $\|\mathbf{u}_j\|_\infty/\|\mathbf{u}_j\|_2$ is referred to as the crest factor in signal processing literature and is a measure of the peak to average ratio. A single sinusoidal component from the summation in Equation (3–1) has $PF = \sqrt{2}$. The relative peak factor, defined by Equation (3–4), is a measure of the peak factor relative to a single sinusoid.

$$RPF\,(\mathbf{u}_j) = \frac{[\max(\mathbf{u}_j) - \min(\mathbf{u}_j)]}{2\sqrt{2}\,\mathrm{rms}(\mathbf{u}_j)} = \frac{PF\,(\mathbf{u}_j)}{\sqrt{2}} \tag{3–4}$$

The relative peak factor is a measure of efficiency of an input for parameter estimation purposes, in terms of the amplitude range of the input signal divided by the measure of the signal energy [76]. Lower relative peak factors are desirable for parameter estimation where the objective is to excite the system without driving it too far away from the nominal operating point [76]. In many cases, the postulated model is linear (or slightly nonlinear) and keeping the aircraft near the operating condition is an essential feature for valid input design. In the case of simulation-based

system identification, a low relative peak factor also implies an information-rich signal, covering the desired input range in a short time period. Furthermore, the orthogonal multisine input allows multiple inputs to be excited simultaneously while preserving good identifiability between the output and input signals due to the orthogonality of the inputs. This is compared to conventional square-wave and frequency-sweep inputs, which are executed sequentially to avoid correlation in the input variables, greatly extending the duration of the maneuver. By comparison, it is apparent that (1) conventional inputs are ideal for manual implementation in aircraft with sufficiently long maneuver durations, and (2) multisine inputs are ideal for computer simulation with compact maneuvers and good energy content.

Figure 3-1 shows a multisine input signal for two orthogonal inputs generated using the SIDPAC® function $\mathrm{mkmsswp}$. The frequency range specified is from 0 to 5 Hz, the duration is 5 seconds, and the amplitude is +/- 5. The inputs are representative of control surface deflections during a particular maneuver.

Parameter estimation involves developing a mathematical relationship between the specified input and observed output. Therefore, it is important to use an input signal that sufficiently covers the input space of interest. Figure 3-2 shows an alternative view of in the same two input signals, called a regressor map, which can be used to visualize the coverage of the input space. From Figure 3-2, it is apparent that the multsine input provides good coverage of the entire space with emphasis near the boundaries and corners. This particular feature is beneficial for capturing nonlinearities in the observed data and useful for predicting values within the input space.

3.2.2 Model Structure Determination

The postulated model for store separation SID includes a multivariate polynomial with constant coefficients for uniform flow contributions combined with a multivariate polynomial with spatially variant coefficients for the nonuniform flow contribution. The postulated model is general in the sense that it could be applied to any aircraft/store

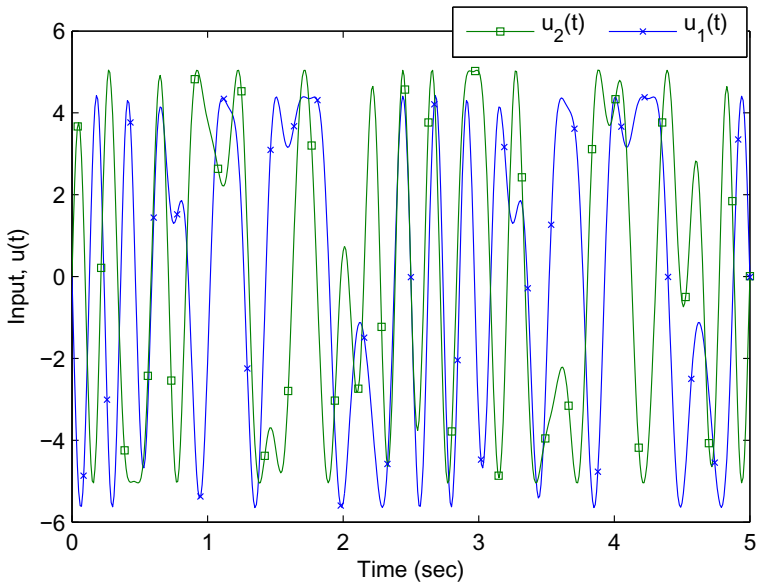

Figure 3-1. Multisine excitation for two orthogonal inputs from 0 to 5 Hz with amplitude range from +/- 5.

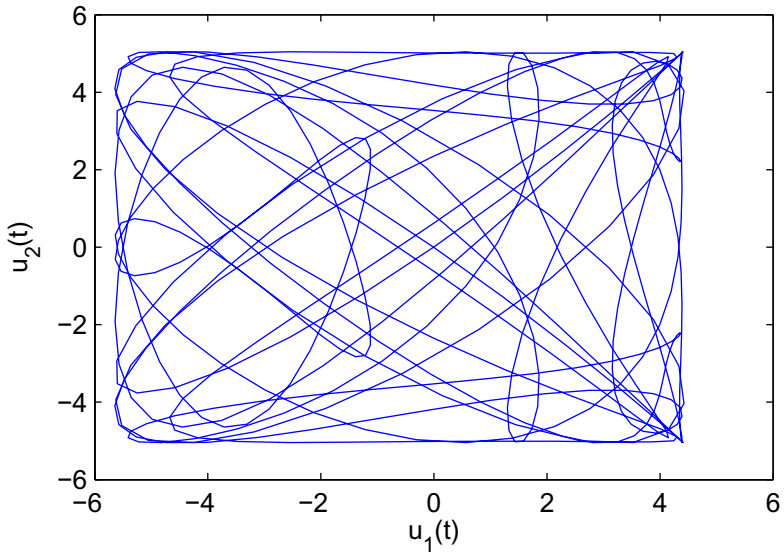

Figure 3-2. Regressor map for the multisine inputs shown in Figure 3-1.

configuration or to an individual store/aircraft in a variety of flight conditions and configurations, but to be of practical use the model must be completely specified. In other words, model postulation is suitable for a generic description of nonlinear

aerodynamics, but model structure determination and parameter estimation are necessary to finalize the model for a particular application of interest.

In general, the goal of model structure determination is to find a compact model that still has adequate complexity to capture the nonlinear functional dependencies between the independent and dependent variables [82]. Keeping the number of terms in the model low is an essential feature that improves the identifiability of the parameters in the model, resulting in a more accurate model with good predictive capability [82]. In this research, the model terms are determined using multivariate orthogonal polynomial functions based on a procedure proposed by Morelli [4] and implemented in the Matlab® toolbox SIDPAC®.

The proposed technique uses multivariate orthogonal modeling functions generated directly from the measured data to determine a compact nonlinear model structure. The orthogonal models are then transformed back into the original regressor space to determine a multivariate polynomial valid for modeling nonlinear aerodynamics. The final model is a finite multivariate power series expansion for the dependent variable in terms of the independent variables.

Determining the model structure in the transformed orthogonal coordinates provides several advantages over traditional iterative or ad hoc methods (such as stepwise regression). First, each transformed regressor is mutually orthogonal to all other regressors, eliminating any difficulties that arise from correlated inputs. Second, the estimate of each parameter within the model is decoupled from the estimates of all other parameters. This decoupling provides a way to assess the contribution of each individual model term independently of any other term in the model, resulting in a straightforward method for determining the most significant terms in the model. In general, the more terms present in the model, the better the model will fit the measured data. However, at some point, the explanatory power of the model is exhausted and the remaining increases in accuracy are due completely to over-parameterizing the

model and "fitting the noise" in the measured data. Obviously, a trade-off between goodness-of-fit and the number of parameters in the model is necessary. Orthogonal functions provide a means for achieving this trade-off in a structured fashion by selecting the model that minimizes the predicted squared error.

Model structure determination begins with a vector of measured dependent variable values consolidated as an N-dimensional vector $\mathbf{y}$.

$$\mathbf{y} = [y_1, y_2, ..., y_N]^T \tag{3–5}$$

The measured values are modeled by a linear combination of mutually orthogonal modeling functions, $\mathbf{p}_j$, $j = 1, 2, ..., n$. Each $\mathbf{p}_j$ is itself an N-dimensional vector, which is in general a function of the independent variables $\mathbf{x}_i$, $i = 1, 2, ..., m$. The independent variables can be consolidated into a regressor matrix.

$$\mathbf{X} = [\mathbf{x}_1, \mathbf{x}_2, ..., \mathbf{x}_m] \quad \mathbf{X} \in \mathbb{R}^{Nxm} \tag{3–6}$$

Similarly, the values of orthogonal functions can be written as a transformed regressor matrix, as shown in Equation (3–7), where it is understood that $\mathbf{P} = \mathbf{P}(\mathbf{X})$.

$$\mathbf{P} = [\mathbf{p}_1, \mathbf{p}_2, ..., \mathbf{p}_n] \quad \mathbf{P} \in \mathbb{R}^{Nxn} \tag{3–7}$$

A method for determining $\mathbf{P}(\mathbf{X})$ using Graham-Schmidt orthogonalization is presented by Morelli [24]. The dependent variable $\mathbf{y}$ can be expressed as a linear combination of the orthogonal modeling functions, as shown in Equation (3–8), where a_j ($j = 1, 2, ..., n$) are constants yet to be determined and ϵ is a vector of modeling errors.

$$\mathbf{y} = a_1\mathbf{p}_1 + a_2\mathbf{p}_2 + ... + a_n\mathbf{p}_n + \epsilon \tag{3–8}$$

In matrix form, equation (3–8) can be written as Equation (3–9), where $\mathbf{a} = [a_1, a_2, ..., a_N]^T$.

$$\mathbf{y} = \mathbf{P}\mathbf{a} + \epsilon \tag{3–9}$$

The goal is to determine the values of $\mathbf{a}$ which minimize the least squares cost function.

$$J = (\mathbf{y} - \mathbf{Pa})^T (\mathbf{y} - \mathbf{Pa}) \tag{3–10}$$

It will be shown in the Section 3.2.3 that the least squares estimate $\hat{\mathbf{a}}$ is given by Equation (3–11).

$$\hat{\mathbf{a}} = \left[\mathbf{P}^T\mathbf{P}\right]^{-1}\mathbf{P}^T\mathbf{y} \tag{3–11}$$

The matrix inversion $\left[\mathbf{P}^T\mathbf{P}\right]^{-1}$ is the source of difficulty for parameter estimation problems with correlated inputs. For the inverse to exist, the vectors $\mathbf{p}_j$ must be independent. Highly correlated inputs therefore result in an ill-conditioned matrix, significantly weakening the accuracy of the parameter estimates. However, for the case of mutually orthogonal modeling functions, the following important property exists.

$$\mathbf{p}_i^T\mathbf{p}_j = 0\,, \quad i \neq j, \quad i\,, j \;=\; 1,\, 2,\, \ldots,\, n \tag{3–12}$$

As a result, the matrix $\mathbf{P}^T\mathbf{P}$ is diagonal, the matrix inversion is trivialized, and the least squares parameter estimates are decoupled. Following Equation (3–11), the least squares parameter estimates are determined as a set of scalar equations.

$$a_j = \left(\mathbf{p}_j^T\mathbf{y}\right)/\left(\mathbf{p}_j^T\mathbf{p}_j\right) \quad j \;=\; 1,\, 2,\, \ldots,\, n \tag{3–13}$$

For the purposes of model structure determination, the result shown in Equation (3–13) is significant. In essence, the determination of the j^{th} parameter estimate has been decoupled from all other terms in the model. Only the dependent variable measurements and a single orthogonal vector are required to determine each parameter estimate. This allows each parameter to be determined uniquely regardless of the other parameters under consideration. Furthermore, the estimated cost function can be written as Equation (3–14).

$$\hat{J} = \mathbf{y}^T\mathbf{y} - \sum_{j=1}^{n}\left(\mathbf{p}_j^T\mathbf{y}\right)^2\Big/\left(\mathbf{p}_j^T\mathbf{p}_j\right) \tag{3–14}$$

The second term in this expression is always positive and it is therefore apparent that each orthogonal function will necessarily reduce the least squares cost function. More importantly, the quantitative reduction in the cost function can be determined independently for each orthogonal function, providing a means of selecting the most significant terms first and eliminating the least significant terms altogether.

Equation (3–14) indicates that the cost function will continue to be reduced as long as terms are added to the model. Intuitively, there must be a limit to the physically meaningful terms that explain the functional dependencies in the data. As such, the number of orthogonal modeling terms are chosen to minimize the predicted squared error, defined by [83] and shown in Equation (3–15).

$$PSE = \frac{\hat{J}}{N} + \sigma_o^2 \frac{n}{N} \tag{3–15}$$

The maximum estimate of the variance is given by Equation (3–16), where $\bar{y}$ is simply the average value of the independent variable measurements.

$$\sigma_o^2 = \frac{1}{N} \sum_{i=1}^{N} (y_i - \bar{y})^2 \tag{3–16}$$

The first term in the PSE (Equation (3–15)) represents the mean square fit error, and will always be reduced as the number of the terms in the model increases. The second term is a product of the maximum variance in the data and a ratio of the number of terms in the model with the number of measurements in the data. Therefore, the second term represents a penalty for over-fitting the data. Since the first term is guaranteed to decrease with each additional term, and the second term is always positive and guaranteed to increase with each additional term, the PSE is guaranteed to have a true global minimum. Further details on the statistical properties of the PSE metric, including justification for its use in modeling problems is documented by Barron [83]. The number of terms in the model is selected to achieve a minimum PSE, resulting in a model that is sufficiently complex to capture the functional dependencies

in the measured data and sufficiently compact to provide parameter identifiability and predictive capability. Examples using multivariate orthogonal functions will be considered in Sections 3.3.

3.2.3 Parameter Estimation

The most commonly applied parameter estimation techniques can be broadly classified into three categories: 1) equation error, 2) output error, and 3) filter error methods [60]. The choice of a particular method is generally dictated by the model structure and by the assumed characteristics of the measurement and process noise inherent in the system.

The output error method is a nonlinear optimization method that has been most widely used for aircraft parameter estimation [60]. The key feature of the output error method is the capability to account for the measurement noise inherent in flight-test data using the principle of maximum likelihood. In the output error method, model parameters are adjusted iteratively to minimize the error between the measured output and the model-estimated responses [34], hence the name “output error”. Thus, the nonlinear equations of motion are evaluated during each iteration resulting in a nonlinear optimization problem. A comprehensive description of the output error method with several examples is provided by Jategaonkar [34] and Morelli [24].

The output error method allows for measurement error in the dependent variables but assumes perfect measurement of the state variables. In flight-test applications, the state measurements are also corrupted by error. Particularly in situations with significant atmospheric turbulence, the output error method may yield poor estimates of the model parameters [34]. In such cases, the filter error method is more reliable. The filter error method accounts for both measurement noise and process noise (such as turbulence) by considering a stochastic system. As a consequence, a suitable state estimator is required to propagate the states. The state estimation is performed using a Kalman filter or an Extended Kalman Filter (EKF), depending on the linearity of the postulated

model. Filter error methods represent the most general approach to aircraft parameter estimation. Although the filter error method is substantially more complex than the output error method, the method is applicable to a wider variety of aircraft identification problems, including parameter estimation for nonlinear aerodynamic models in the presence of turbulence. The filter error method was first proposed by Balakrishnan [84], with pioneering developments by Mehra [85] and Iliff [86] in the 1970s. A comprehensive description of the filter error method with several examples is provided by Jategaonkar [34] and Morelli [24].

The third parameter estimation technique commonly used in SID is the equation error method. Synthesis of the aerodynamic forces and moments acting on a flight vehicle through Taylor series expansion leads to a model that is linear in the parameters (though it may be nonlinear in the state variables). The equation error method, based on classical regression techniques, is ideally suited for parameter estimation of multivariate polynomial models. The equation error method is the simplest of the three mainstream parameter estimation methods, but it may lead to least accurate estimates in the presence of significant measurement noise. Thus practical implementation of the equation error method relies on smooth flight-test conditions, quality flight-test instrumentation, and post-flight trajectory reconstruction.

For simulation-based system identification, these limitations are not of concern. In a simulation environment the states are known with numerical precision and the measurement noise is limited to the noise present in the CFD or wind tunnel database. Furthermore, the equation error method provides a great deal of flexibility in modeling structures and lends itself nicely to model structure determination methods, such as the multivariate orthogonal polynomial previously described. The equation error method does not rely on the temporal arrangement of the flight-test data, allowing multiple flight-test maneuvers to be concatenated together for a single estimation problem or alternatively a large scale maneuver to be decomposed into smaller locally valid models

(a process referred to as data partitioning) [34]. Finally, even for nonlinear equations of motion and nonlinear multivariate polynomials, the equation error method remains a linear estimation problem solved efficiently in a single pass using linear algebraic methods.

The equation error method is fundamentally based on the well-known least squares technique, which is briefly considered here. As a result of the postulated aerodynamic model for a store in uniform flow, the aerodynamic coefficients represented by the response variable $y(t)$ can be expressed as a linear combination of variables, as shown in Equation (3–17), where $\xi_1, \xi_2, ..., \xi_n$ are in general nonlinear combinations of the state variables (e.g. $\alpha, \beta, \alpha^2, \alpha\beta$ etc.).

$$y(t) = \theta_0 + \theta_1\xi_1(t) + \theta_2\xi_2(t) + ... + \theta_n\xi_n(t) \tag{3–17}$$

Despite the potential nonlinear relationship between the response variable and the state variables, the model equation for $y(t)$ is linear in the parameters $\theta_0, \theta_1, ..., \theta_n$. The model equation can be written in more compact form as shown in Equation (3–18).

$$\mathbf{y} = \mathbf{X}\boldsymbol{\theta} \tag{3–18}$$

In Equation (3–18), $\mathbf{y} = [\ y(1)\ \ y(2)\ \ ...\ \ y(N)\ ]^T$ is an $N \times 1$ vector, $\boldsymbol{\theta} = [\ \theta_0\ \ \theta_1\ \ ...\ \ \theta_n\ ]^T$ is an $n_p \times 1$ vector with the number of parameters $n_p = n + 1$, and $\mathbf{X} = [\ 1\ \ \xi_1\ \ ...\ \ \xi_n\ ]^T$ is an $N \times n_p$ matrix. The response variables are not known precisely. Rather, the measurement equation is given by Equation (3–19), where $\mathbf{z} = [\ z(1)\ \ z(2)\ \ ...\ \ z(N)\ ]^T$ and $\boldsymbol{\upsilon} = [\ \nu(1)\ \ \nu(2)\ \ ...\ \ \nu(N)\ ]^T$ are both $N \times 1$ vectors and $\boldsymbol{\nu}$ are the measurement errors.

$$\mathbf{z} = \mathbf{X}\boldsymbol{\theta} + \boldsymbol{\upsilon} \tag{3–19}$$

The best estimator of the parameters $\boldsymbol{\theta}$ in a least-squares sense comes from minimizing the sum of squared differences between the measurements and the model.

The associated cost function can be written as Equation (3–20).

$$J(\boldsymbol{\theta}) = \frac{1}{2}(\mathbf{z} - \mathbf{X}\boldsymbol{\theta})^T(\mathbf{z} - \mathbf{X}\boldsymbol{\theta}) \tag{3–20}$$

The parameter estimate $\hat{\boldsymbol{\theta}}$ that minimizes the cost function must satisfy Equation (3–21), which can be simplified to Equation (3–22).

$$\frac{\partial J}{\partial \boldsymbol{\theta}} = -\mathbf{X}^T\mathbf{z} + \mathbf{X}^T\mathbf{X}\hat{\boldsymbol{\theta}} = \mathbf{0} \tag{3–21}$$

$$\mathbf{X}^T\left(\mathbf{z} - \mathbf{X}\hat{\boldsymbol{\theta}}\right) = \mathbf{0} \tag{3–22}$$

Provided that the required inverse exists, Equation (3–22) can be solved to yield the least squares estimator.

$$\hat{\boldsymbol{\theta}} = \left(\mathbf{X}^T\mathbf{X}\right)^{-1}\mathbf{X}^T\mathbf{z} \tag{3–23}$$

Thus, given the measurements $\mathbf{z}$ and a matrix of postulated regressors $\mathbf{X}$, the parameters $\boldsymbol{\theta}$ that minimize the residual error $\boldsymbol{\nu}$ can be determined directly. The mathematical simplicity of Equation (3–23) is the primary advantage of the equation error method and the principle feature that leads to a variety of applications and modeling flexibility. Examples using the equation error method applied to store separation system identification will be presented in Section 3.3.

3.2.4 Model Postulation

For store separation, the established delta coefficient methodology (2.3.2) provides a solid starting point for application of system identification methods. Using the superposition approach inherent in the delta-coefficient methodology, the functional form of the aerodynamic coefficients is shown in Equation (3–24).

$$C = C_{FS} + \Delta C_{TRANS} + \Delta C_{ROT} + \Delta C_G + \Delta C_C \tag{3–24}$$

The four separate terms in Equation (3–24) result from four distinct types of wind tunnel testing, providing a logical framework for the functional expression. It is also

noted that the freestream, rotational, and control terms: C_{FS}, ΔC_{ROT} , and ΔC_C, are all determined in a uniform flow environment, whereas the grid data correction, ΔC_G, is determined from a nonuniform flow. This dichotomy suggests another way to formulate the aerodynamic coefficients as shown in Equation (3–25a), where C_U represents the uniform flow contribution to the total aerodynamic coefficient and ΔC_{NU} represents the nonuniform correction. It is intuitive and convenient to apply system identification to each of these terms separately and recombine the expressions to determine the total aerodynamic coefficient.

$$C = C_U + \Delta C_{NU} \tag{3–25a}$$

$$C_U = C_{FS}\left(M, \alpha_S, \beta_S\right) + \Delta C_{ROT}\left({}^W p_B^B, {}^W q_B^B, {}^W r_B^B\right) + \Delta C_C\left(\delta_e, \delta_a, \delta_r\right) \tag{3–25b}$$

$$\Delta C_{NU} = \Delta C_G\left(r_{B/A}, \psi_B^A, \theta_B^A, \phi_B^A\right) \tag{3–25c}$$

3.2.4.1 Uniform flow contribution

Due to the assumption of a quasi-steady flow field, the functional form of the uniform flow contribution is amenable to a Taylor series expansion. The expansion can be represented by a multivariate polynomial that is linear in the parameters but potentially nonlinear in the state variables. The general nonlinear form of the Taylor series expansion is conveniently expressed using matrix notation, as shown in Equation (3–26).

$$C_{i_U} = \mathbf{X}\left(\alpha_s, \beta_s, p, q, r, \delta\right)\boldsymbol{\beta} \tag{3–26}$$

In Equation (3–26), $\mathbf{X} \in \mathbb{R}^{1\times N}$ is a matrix of regressors composed of linear and nonlinear functions of the original state variables, and $\boldsymbol{\beta} \in \mathbb{R}^{N\times 1}$ is a matrix of constant coefficients, composed in part of conventional aerodynamic derivatives. For simplicity, it has also been assumed that the variation in the coefficient with respect to Mach number and velocity is negligible over the interval of interest (approximately 1 sec).

Given the postulated model in Equation (3–26), several methods exist that may be used to determine a suitable model structure **X** and model coefficients β . In this research, the regressors were determined using multivariate orthogonal polynomials and the coefficients were determined using ordinary least squares, as discussed in 3.2.3. An example using this approach is presented in Section 3.3.

3.2.4.2 Non-uniform flow contribution

The nonuniform flow field is characterized in wind tunnel testing by measuring aerodynamic forces and moments acting on the store at multiple discrete locations within the flow field. At any one location, the nonuniform correction can be formulated as shown in Equation (3–27).

$$\Delta C_{NU}\left(z = const\right) = \Delta C_{NU}\left(\psi, \theta, \phi\right) \tag{3–27}$$

A Taylor series expansion can be applied appropriately, where it is recognized that the expansion is carried out at a particular stationary location within the flow field. Intuitively, the expansions at each location within the flow field can be formulated in a nonlinear continuous fashion, resulting in a multivariate polynomial model with spatially variant coefficients. The general nonlinear form of this model can be conveniently expressed in matrix notation, as shown in Equation (3–28).

$$\Delta C_{NU}\left(z, \psi, \theta, \phi\right) = \mathbf{E}\left(\psi, \theta, \phi\right) \begin{bmatrix} c_0(z) & c_1(z) & \dots & c_{n-1}(z) \end{bmatrix}^T \tag{3–28}$$

The model structure $\mathbf{E}\left(\psi, \theta, \phi\right) \in \mathbb{R}^{1\times n}$ is composed of linear and nonlinear combinations of the Euler angles and can be determined using multivariate orthogonal polynomials. The model coefficients $c_0(z)$, $c_1(z)$, $c_{n-1}(z)$, etc. represent spatially variant terms and require further consideration.

3.2.4.3 Spatial variation

Identification of a nonuniform delta-coefficient model consists of two interrelated tasks, including (1) determination of the model structure in the state variables and

(2) determination of the spatially variant coefficients. In this research, the model structure is determined using multivariate orthogonal polynomials in a manner similar to the freestream model. The functional form of the spatially variant coefficients is specified by considering the dominant characteristics of diminishing nonuniform flow field aerodynamics and the parameters within the functional form are estimated using nonlinear least squares. The result is a compact parametric model that can be used to represent the spatially variant aerodynamics of store during separation for a variety of applications.

The diminishing nature of the nonuniform delta coefficient as the store separates from the aircraft provides an important boundary condition for the spatially variant coefficients in Equation (3–28). Under the quasi-steady and uniform atmosphere assumptions posited in Chapter 2, there always exists a distance between the aircraft and store at which the aircraft flow field effect on the store is negligible. This physical realization can be expressed mathematically by considering the limit as $z \rightarrow \infty$, i.e. one can be assured that the limiting value of the nonuniform delta coefficient is zero, as shown in Equation (3–29).

$$\lim_{z \to \infty} \Delta C_{NU} = 0 \tag{3–29}$$

Given the multivariate polynomial model postulated in Equation (3–28), it is evident that each term in the model is independent. Therefore, Equation (3–29) implies that each coefficient in the model will approach zero independently, as shown in Equation (3–30), where n is the number of terms in the model.

$$\lim_{z \to \infty} c_i(z) = 0 \quad i = 1, \ldots, n \tag{3–30}$$

This guiding criterion is based on the physical principle that as the distance between the aircraft and store increases without bound, the effect of the aircraft flow field on the store aerodynamics becomes negligible. In practice, it is reasonable to

expect the effect of the aircraft on the store aerodynamics to become small at a vertical distance equivalent to 1-2 lengths of the aircraft.

One particular mathematical expression that meets the boundary condition expressed in Equation (3–30) is the exponential function, $e^{-\varphi z}$ where the rate of decay, φ, needs to be estimated using measured data. However, the exponential function is monotonically decreasing. For complex flow fields, one can be assured that the aircraft effect will diminish as the distance between the aircraft and store becomes large, but there is no assurance that this decrease will be monotonic. For example, one might expect that the flow field effect would become more significant as a store passes through a shock or expansion wave during supersonic flight. A postulated model that satisfies Equation (3–30) and allows a non-monotonic curvature is given by an exponential-polynomial product, as shown in Equation (3–31).

$$c_i(z) = e^{-\varphi z}\left(\eta_0 + \eta_1 z + \eta_2 z^2 + \ldots + \eta_m z^m\right) \tag{3–31}$$

Equation (3–31) represents a nonlinear equation for single model coefficient with unknown parameters φ, η_0, η_1,… , η_m that must be estimated from measured data.

The nonuniform delta coefficient can be written as a matrix equation, as shown in Equation (3–32).

$$\Delta C_{NU}(z,\psi,\theta,\phi) = \mathbf{E}(\psi,\theta,\phi)\begin{bmatrix} c_0(z) & c_1(z) & \ldots & c_{n-1}(z) \end{bmatrix}^T \tag{3–32}$$

The model structure is a matrix composed of linear and nonlinear regressors, as shown in Equation (3–33).

$$\mathbf{E}(\psi,\theta,\phi) = \begin{bmatrix} \xi_1 & \xi_2 & \ldots & \xi_n \end{bmatrix} \qquad \mathbf{E} \in \mathbb{R}^{1\times n} \tag{3–33}$$

Using the postulated form of the spatially variant model coefficients given in Equation (3–31), the model coefficients can also be written in a general matrix form, as

shown in Equation (3–34) and further condensed in Equation (3–35).

$$c_i(z) = e^{-\varphi_i z}\left(\begin{bmatrix} \eta_0 & \eta_1 & \dots & \eta_m \end{bmatrix}\begin{bmatrix} 1 & z & \dots & z^m \end{bmatrix}^T\right) \tag{3–34}$$

$$c_i(z) = e^{-\varphi_i z}\left(\boldsymbol{\eta}_i \mathbf{Z}_i\right) \tag{3–35}$$

In Equation (3–35), $\mathbf{Z}_i = [\ 1 \quad z \quad \dots \quad z^m\ ]^T$ is a $p \times 1$ vector and $\boldsymbol{\eta}_i = [\ \eta_0 \quad \eta_1 \quad \dots \quad \eta_m\ ]$ is a $1 \times p$ vector, where $p = m + 1$. If it is further presumed that the model structure within the polynomial portion of each model term is held fixed, then $\mathbf{Z} = \mathbf{Z}_i \in \mathbb{R}^{p\times 1}$ for $i = 1, \dots, n$. Consequently, the vectors $\boldsymbol{\eta}_i$ can be combined into an $n \times p$ matrix.

$$\boldsymbol{\eta} = \begin{bmatrix} \boldsymbol{\eta}_1^T & \boldsymbol{\eta}_2^T & \dots & \boldsymbol{\eta}_n^T \end{bmatrix}^T \qquad \boldsymbol{\eta} \in \mathbb{R}^{n\times p} \tag{3–36}$$

The matrix product in Equation (3–35) results in an $n \times 1$ vector.

$$\boldsymbol{\eta}\mathbf{Z} \in \mathbb{R}^{n\times 1} \tag{3–37}$$

Furthermore, the scalar exponential functions of z can be written as a matrix exponential, as shown in Equation (3–38).

$$e^{-\Phi z} = \begin{bmatrix} e^{-\phi_1 z} & \cdots & 0 \\ \vdots & \ddots & \vdots \\ 0 & \cdots & e^{-\phi_n z} \end{bmatrix} \qquad \boldsymbol{\Phi} \in \mathbb{R}^{n\times n} \tag{3–38}$$

Combining the results from Equation (3–37) and (3–38), the matrix product in Equation (3–39) corresponds to the original coefficient matrix.

$$e^{-\Phi z}\boldsymbol{\eta}\,\mathbf{Z} = \begin{bmatrix} c_0(z) & c_1(z) & \dots & c_{n-1}(z) \end{bmatrix}^T \in \mathbb{R}^{n\times 1} \tag{3–39}$$

Consider the original form of Equation (3–32). Using the result in Equation (3–39), the nonuniform delta coefficient can be written in the compact parametric form shown in Equation (3–40).

$$\Delta C_{NU}(z, \psi, \theta, \phi) = \mathbf{E}(\psi, \theta, \phi)\, e^{-\Phi z}\boldsymbol{\eta}\mathbf{Z}(z) \tag{3–40}$$

Equation (3–40) is significant. Given sufficient wind tunnel or CFD data, this compact parametric model is a suitable candidate for modeling the spatially variant aerodynamics of a store during separation. The terms $\mathbf{E}(\psi, \theta, \phi)$ and $\mathbf{Z}(z)$ are matrices composed of the original state variables. The components of the matrix $\mathbf{E}(\psi, \theta, \phi)$ are determined using multivariate orthogonal polynomials and the components of $\mathbf{Z}(z)$ are chosen by the analyst for the particular application at hand (a cubic polynomial including z, z^2 and z^3 is generally sufficient). The terms $\mathbf{\Phi}$ and $\boldsymbol{\eta}$ are constant matrices determined using nonlinear least squares estimation. Thus, all four terms are readily determined and quantified using the SID techniques discussed in Section 3.2.

Returning to Equation (3–26), the uniform flow contribution to the aerodynamic coefficient can also be expressed in matrix form, where $\mathbf{X}$ is a matrix of regressors and $\boldsymbol{\beta}$ is a constant vector. The general matrix form for the total aerodynamic coefficient is given by Equation (3–41).

$$C = \mathbf{X}(\alpha_S, \beta_S, p, q, r, \delta)\,\boldsymbol{\beta} + \mathbf{E}(\psi, \theta, \phi)\, e^{-\Phi z}\boldsymbol{\eta}\mathbf{Z}(z) \tag{3–41}$$

Of particular importance is the nature of the exponential term, $e^{-\Phi z}$. During a safe separation, the variable z is always positive and monotonically increasing. Therefore, provided that the matrix $\mathbf{\Phi}$ is positive definite, the exponential term will continually diminish as z increases, and the aerodynamic coefficient will approach the freestream value, as shown in Equation (3–42).

$$\lim_{z\to\infty}\left(\mathbf{X}\boldsymbol{\beta} + \mathbf{E}\, e^{-\Phi z}\boldsymbol{\eta}\mathbf{Z}\right) = \mathbf{X}\boldsymbol{\beta} \quad \Rightarrow \quad \lim_{z\to\infty}\left(C_U + \Delta C_{NU}\right) = C_U \tag{3–42}$$

Equation (3–41) can be considered as a candidate model for any store in a continuous spatially varying flow field for which time-averaged wind tunnel or CFD data are available. The accuracy of the model in reproducing the source data will be dependent on the complexities of the flow field and the expertise of the analyst. An

extended example will provide greater clarification in the application and utility of this parametric model.

3.3 Example: Store Separation

The system identification approach discussed in Section 3.2 is first applied to determine a parametric freestream model, valid for a store in far-field, uniform flow conditions; see Section 3.3.1. Next, the nonuniform delta coefficient is modeled using system identification to determine a spatially variant parametric model; see Section 3.3.2. The freestream and delta coefficient models for this example are based completely on wind tunnel data, but in principle could also be determined using CFD. Finally, in Section 3.3.3 the two models are combined to estimate the total aerodynamic forces and moments and the cumulative model is compared to flight-test data with favorable results.

3.3.1 Freestream System Identification

Modeling the aerodynamic characteristics of a store in far-field, uniform (freestream) flight conditions is straightforward using established system identification techniques. This section presents simulated results used for model identification, and provides validation of the parametric freestream model.

3.3.1.1 Simulated maneuver

In the typical application of flight vehicle SID, the inputs are specified and the response of the vehicle is measured in flight. However, this approach may result in correlation between state variables and low information content in the aircraft response, requiring long duration maneuvers. In a simulation environment, direct manipulation of the state and control inputs results in a more efficient maneuver with improved identifiability [49, 70]. Multisine inputs can be used to generate orthogonal signals for the desired state and control inputs and the kinematic equations of motion can be used to maintain physical relationships between state variables. For the current application, the air incidence angles were specified using multisine inputs, the angular body rates were

computed using kinematic relationships, the velocity of the store relative to the air was held constant, and the position of the store CG was held fixed (i.e. the store is pinned at a stationary location but free to rotate, conceptually similar to a wind tunnel test).

The kinematic relationships between the time derivative of the Euler angles and the angular rates can be extracted from the conventional rigid aircraft equations of motion [24]. For the special case of a pinned store CG, the roll orientation is specified such that $\theta = \alpha_s$, $\psi = -\beta_s$ and $\phi := 0$. As a result the kinematic relationship reduces to the expressions in Equation (3–43).

$$\begin{bmatrix} p & q & r \end{bmatrix}^T = \begin{bmatrix} \dot{\beta}_s \sin\alpha_s & \dot{\alpha}_s & -\dot{\beta}_s \cos\alpha_s \end{bmatrix}^T \tag{3–43}$$

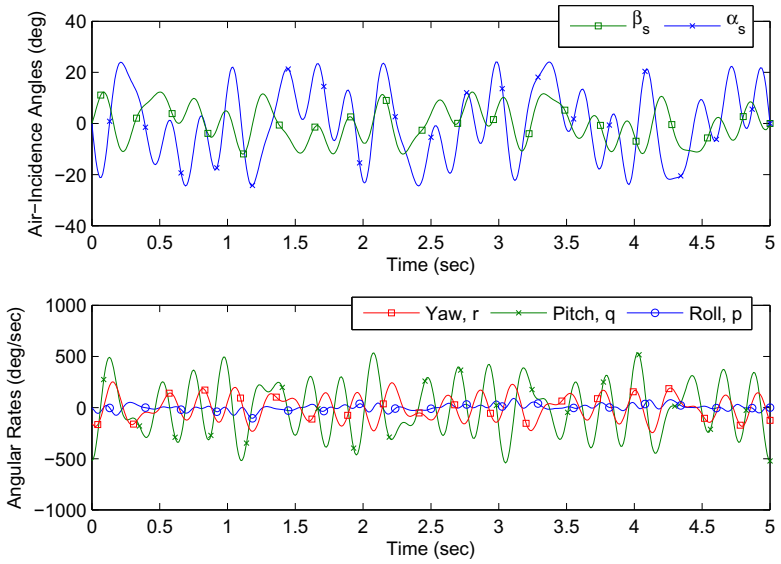

Figure 3-3. Definition of a training maneuver with multisine inputs for (top) air-incidence angles and (bottom) angular rates computed using kinematic relationships.

The top portion of Figure (3-3) shows the specified air incidence angles of the store in uniform flow, generated as orthogonal multisine inputs with a frequency range of 0-5 Hz and an amplitude range of ± 20 deg for α_s and ± 10 for β_s. The bottom portion of Figure (3-3) shows the angular rates computed using the kinematic relationships in (3–43).

With all twelve state variables specified, the aerodynamic coefficients for the prescribed trajectory can be determined with the same interpolation methods used for a conventional 6DOF simulation. Multivariate orthogonal polynomials are used to determine a suitable model structure that minimizes the predicted squared error and the ordinary least squares approach is used to estimate the model parameters. The results for the pitching moment coefficient, C_m, and the normal force coefficient, C_N, are shown in Figure (3-4).

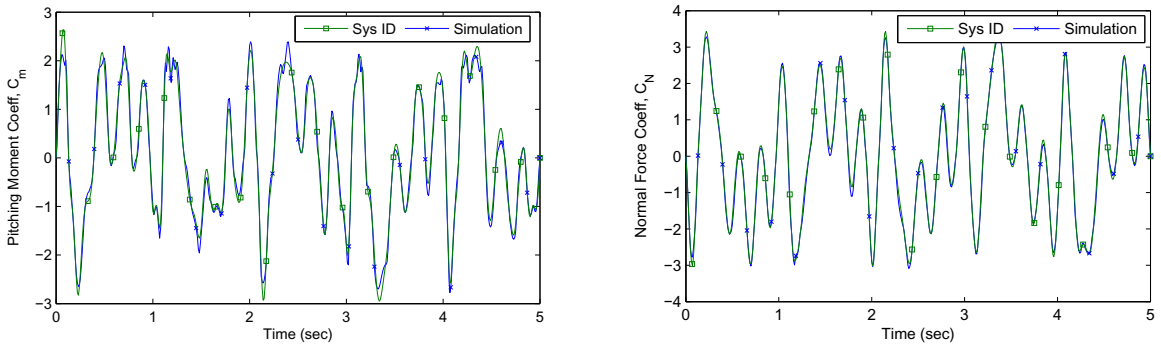

A Pitching Moment B Normal Force

Figure 3-4. Aerodynamic coefficient comparison between simulation and system identification results for a store in freestream flight conditions at Mach 0.9 / 550 KCAS / 4800 ft.

The results from simulation and the predicted response for C_m and C_N are in good agreement over a range of output values, with R-squared values of $R^2 = 98.5\%$ and $R^2 = 99.7\%$, respectively. The identified multivariate polynomial models, a 4th order model for C_m and 3rd order model for C_N , are given by Equations (3–44) and (3–45).

$$C_m = -4.94\alpha - 74\hat{q} - 94.71\alpha\beta^2 + 2.44\alpha^2 + 10.07\alpha^3 - 77.75\alpha^2\beta^2 \quad (3\text{–}44)$$

$$C_N = 5.25\alpha + 45.656\alpha\beta^2 + 7.90\alpha^3 \quad (3\text{–}45)$$

Similar results were obtained for side force ($R^2 = 99.1\%$) and yaw moment ($R^2 = 97.3\%$) coefficients. The axial force ($R^2 = 84.9\%$) and roll moment ($R^2 = 91.2\%$) coefficients have lower prediction accuracy due in part to a greater measurement

uncertainty. Fortunately, the trajectory prediction is less sensitive to these coefficients. Overall, the multivariate polynomials with constant coefficients characterize the freestream aerodynamics quite well. It should be noted that these models are valid for the range of ± 20 deg for α_s and ± 10 for β_s, commensurate with the prescribed maneuver. Though the models may be evaluated outside of this range, the accuracy of the prediction quickly degrades. If a larger range is necessary, the input maneuver can be redesigned, though model predictive accuracy may degrade if the input design is too large. Alternatively, the system identification process can be applied over a neighboring range of input values (say, 30 ± 10 deg for α_s) to identify a complementary model. The complementary models can then by synthesized in a simulation environment.

3.3.1.2 Model validation

The predictive quality of the model can be evaluated in multiple ways; two particular comparisons are examined here. First, comparison of the model to the static freestream database from which it is derived is considered. Second, comparison with a similar but independent maneuver is considered.

A static freestream model can be recovered by setting all dynamic terms in the model to zero. For this application, this implies that $\hat{p} = \hat{q} = \hat{r} = 0$. The resulting model is readily deduced from Equations (3–44) and (3–45). It should be noted that the recovered static model is not necessarily identical to the model that would have been estimated if $\hat{p} = \hat{q} = \hat{r} = 0$ from the beginning. However, it is close enough to demonstrate the validity of the dynamic model in this restricted sense. The results for the static pitching moment coefficient, C_m , and the static normal force coefficient, C_N, are shown in Figure (3-5). Again, the results are favorable.

The predictive quality of the model is further justified by considering a similar but independent maneuver. Figure (3-6) shows air incidence angles generated using a multisine input with a frequency range of 0-3 Hz and an amplitude range of +/- 20 deg for α_s and +/- 10 for β_s (top). Figure (3-6) shows a comparison of the resulting

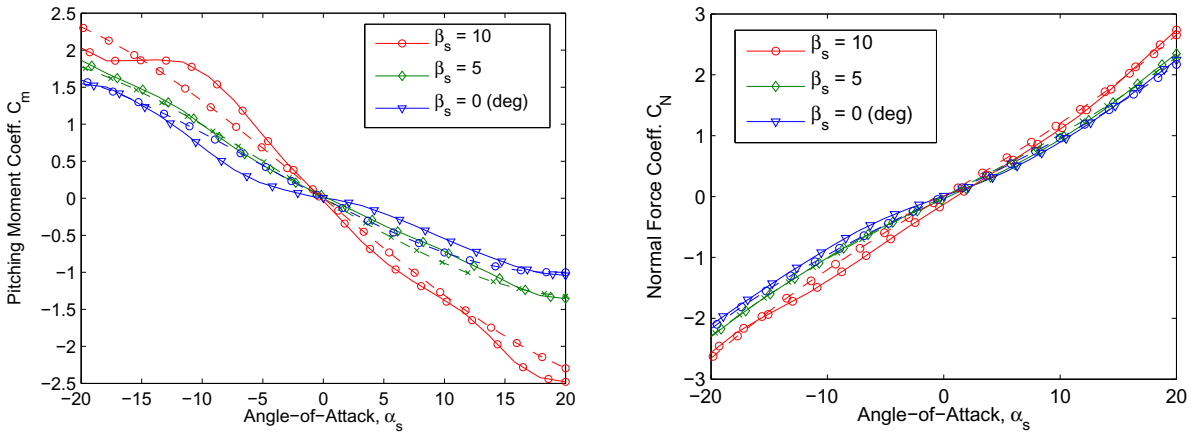

A Pitching Moment B Normal Force

Figure 3-5. Static aerodynamic coefficient comparison between interpolated wind tunnel data (solid lines) and system identification results (dashed lines) for a store in freestream flight conditions at Mach 0.9 / 550 KCAS / 4800 ft.

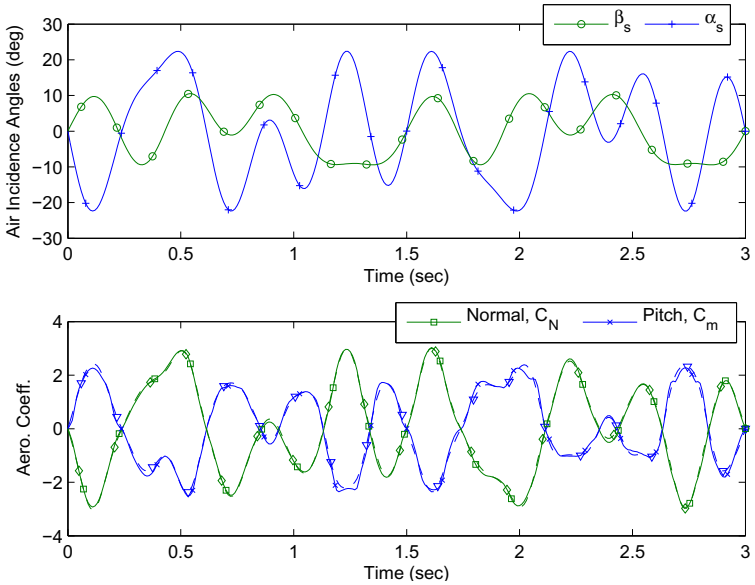

Figure 3-6. Validation results showing an independent maneuver and aerodynamic coefficient comparison between interpolated wind tunnel data (solid lines) and system identification results (dashed lines) for freestream flight conditions at Mach 0.9 / 550 KCAS / 4800 ft.

pitching moment and normal force coefficients along the trajectory (bottom). The system identification model is shown to agree favorably with the simulation results, indicating good predictive quality for an independent trajectory.

3.3.2 Spatially Variant System Identification

Identification of a constant parameter model for aerodynamics of a store in a uniform flow field is a straightforward, as shown in Section 3.3.1. Modeling the aerodynamics of a store in a nonuniform flow field is more involved due to the spatially variant terms in the model. This section describes the use of a piecewise-continuous maneuver to determine a spatially variant aerodynamic model and validation of the model against an independent simulated maneuver.

3.3.2.1 Piecewise-continuous maneuver

System identification of the store in freestream conditions included specification of a maneuver followed by model structure determination and parameter estimation using multivariate orthogonal polynomials. For the piecewise-continuous approach to modeling the spatially variant aerodynamics, the freestream modeling approach is simply repeated at multiple stationary locations within the nonuniform flow field and the results are combined to determine a suitable multivariate polynomial model with spatially variant coefficients.

The same maneuver used for freestream system identification, shown in Figure (3-3), is used at each stationary location within the nonuniform flow field. It should be noted that the freestream aerodynamic coefficients are parameterized in terms of the air incidence angles α_s and β_s , the non-dimensional angular rates $\hat{p}, \hat{q}, \hat{r}$, and optionally the control surface deflections $\delta_a, \delta_e, \delta_r$. In contrast, the delta coefficients are parameterized in terms of the distance along the vertical direction from the aircraft, z, and the orientation of the store relative to the aircraft, ψ, θ, ϕ. Since each maneuver is conducted at a stationary position within the nonuniform flow field, $\theta = \alpha_s$, $\psi = -\beta_s$, and $\phi = 0$. Therefore, the maneuver specified in Figure (3-3) can be used directly. All other state variables are specified using the relationships specified in 3.3.1.1. A non-zero roll angle is corrected for using a coordinate transformation during simulation. This approach neglects the interaction between the aircraft flow field and the store roll

angle, an adequate approximation for a store that is nearly axisymmetric. A slightly more sophisticated “rolled delta coefficient” approach can be used when the store is not axisymmetric [3], but the additional complexity is unwarranted for this example.

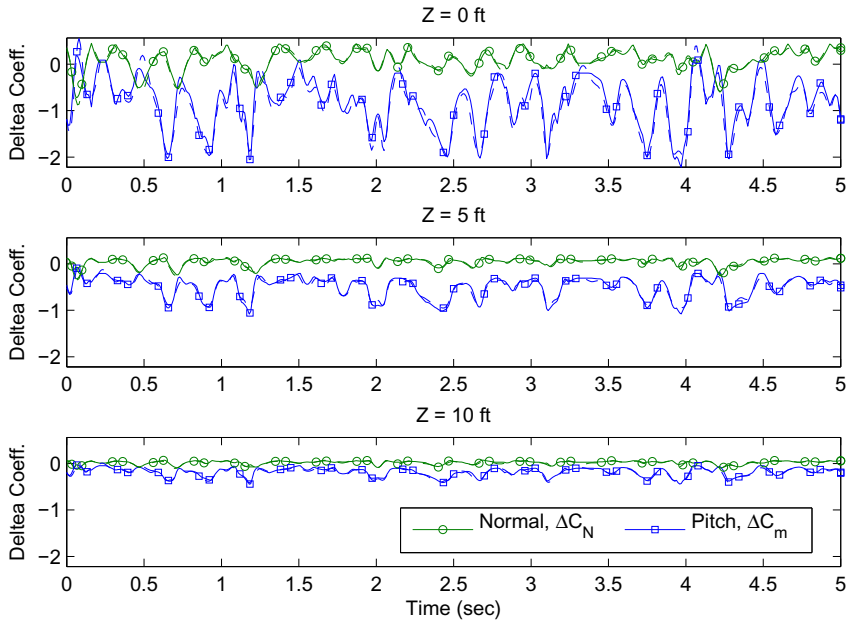

Figure 3-7. Comparison of simulation (solid) and system identification (dashed) results for aerodynamic pitching moment and normal force delta coefficients at (a) z=0ft, (b) z=5ft, and (c) z=10ft.

Figure (3-7) compares simulation and system identification results for the pitching moment and normal force delta coefficients at three representative stationary positions in the nonuniform flow field. The ordinate axis scale in Figure (3-7) is held fixed to emphasize the diminishing value of the delta coefficient as the vertical distance increases. The results indicate that the identified model matches the training data well at each stationary position within the flow field.

The identified model equations for the pitching moment delta coefficient are shown in Equations (3–46) through (3–48), as are the R-squared values for each position. The model structure was determined using multivariate orthogonal polynomials for the first maneuver ($z = 0$) and held fixed for all remaining positions. The coefficients were

determined using ordinary least squares estimation.

$$\begin{aligned}\Delta C_m(z=0) = &-1.02+2.83\theta+16.24\psi^2+9.7\psi\theta-11.41\theta^3-0.53\psi-20.82\psi^2\theta \\ &-40.22\psi\theta^3+131.00\psi^2\theta^2-2.31\theta^2, \quad R^2(z=0)=93.2\%\end{aligned} \tag{3–46}$$

$$\begin{aligned}\Delta C_m(z=5) = &-0.47+1.16\theta+1.47\psi^2+3.85\psi\theta-3.64\theta^3-0.42\psi-8.56\psi^2\theta \\ &-6.86\psi\theta^3+58.89\psi^2\theta^2-1.48\theta^2, \quad R^2(z=5)=95.4\%\end{aligned} \tag{3–47}$$

$$\begin{aligned}\Delta C_m(z=10) = &-0.18+0.51\theta+0.95\psi^2+1.20\psi\theta-1.55\theta^3-0.06\psi-4.86\psi^2\theta \\ &-1.81\psi\theta^3+26.06\psi^2\theta^2-0.53\theta^2, \quad R^2(z=5)=94.3\%\end{aligned} \tag{3–48}$$

Equations (3–46) through (3–48) are three discrete models that may be represented by a continuous model with spatially variant coefficients, as shown in Eqn. (3–49).

$$\begin{aligned}\Delta C_m(z\geq 0) = &\, c_0(z)+c_1(z)\theta+c_2(z)\psi^2+c_3(z)\psi\theta+c_4(z)\theta^3+c_5(z)\psi+c_6(z)\psi^2\theta \\ &+c_7(z)\psi\theta^3+c_8(z)\psi^2\theta^2+c_9(z)\theta^2 \qquad \bar{R}^2=90.1\%\end{aligned} \tag{3–49}$$

Each of the spatially variant coefficients in Equation (3–50) can further be modeled by a nonlinear exponential-polynomial product, as discussed in Section 3.2.4.3 and shown in Equation (3–50), where n is the number of terms in the model and m is the order of the polynomial in z. For the pitching moment delta coefficient model in Equation (3–49), $n=10$ and $m=3$.

$$c_i(z) = e^{-\phi z}\left(\eta_0+\eta_1 z+\eta_2 z^2+\ldots+\eta_m z^m\right) \qquad i=1\ldots n \tag{3–50}$$

The pitching moment delta coefficient model now consists of eleven equations including Equation (3–49) and ten nonlinear equations represented by Equation (3–50). These eleven equations may be written in a concise matrix form, as shown in Equation (3–51), where ΔC_{NU} represents any of the nonuniform flow field delta coefficients. A similar model may be identified for the normal force delta coefficient, as well as the four remaining delta coefficients.

$$\Delta C_{NU}(z,\psi,\theta,\phi) = \mathbf{E}(\psi,\theta,\phi)\, e^{-\Phi z}\boldsymbol{\eta}\mathbf{Z}(z) \tag{3–51}$$

The spatial variation of the model terms for the pitching moment and normal force delta coefficient models is shown in Figure (3-8). The solid lines represent numerical results; the dashed lines are parameterized using Equation (3–51). The curves shown in Figure (3-8) have been scaled by the standard error of each parameter. As a result, the magnitude of each parameter is indicative of the relative importance within the model. The legend entries in Figure (3-8) list the parameters in order of decreasing statistical significance.

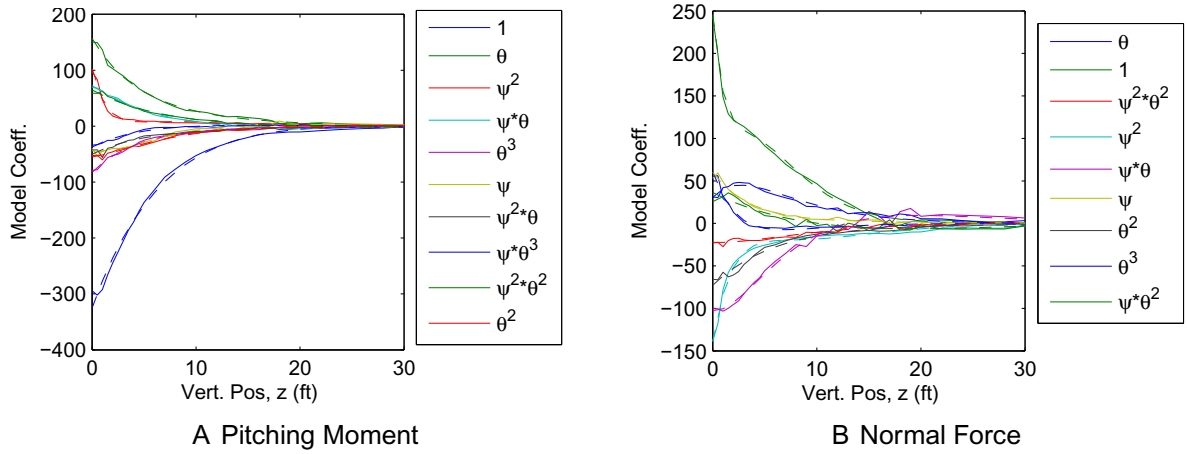

Figure 3-8. Spatial variation of model parameters at Mach 0.9 / 550 KCAS / 4800 ft.

Figure (3-9) shows similar results for a supersonic flight condition. Again, the model structure was determined using a maneuver near carriage and model parameters were estimated using ordinary least squares at each discrete position in the flow field. The magnitude of the scaled model coefficients is representative of the influence each term has on the result, and the legend entries are listed in decreasing order of statistical significance. The solid lines in Figure (3-9) represent the discrete numerical results and the dashed lines are the parameterized result in the form of Equation (3–51). The supersonic flow field is more complex, and as a result the parameterized model is not as accurate as the subsonic case. However, the parametric model still captures the salient features of the training data. Consideration of an independent maneuver and comparison to flight-test data will further justify the predictive capability of the model.

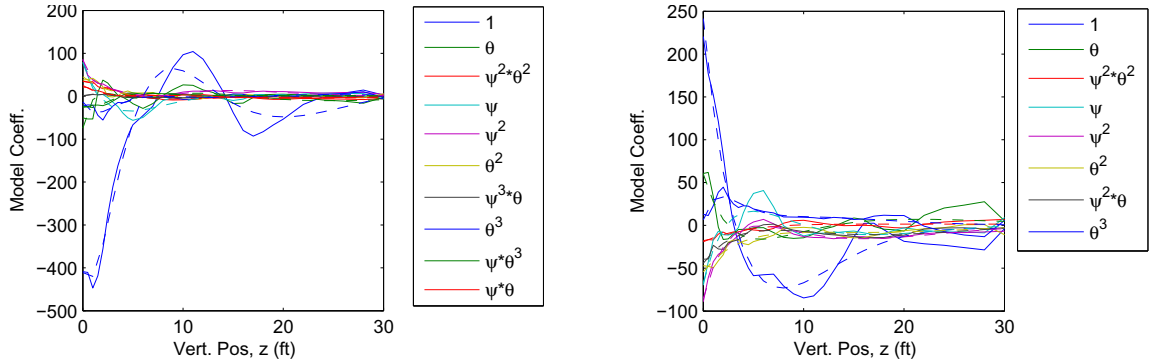

A Pitching Moment B Normal Force

Figure 3-9. Spatial variation of model parameters at Mach 0.9 / 550 KCAS / 4800 ft.

3.3.2.2 Model validation

Model validation is considered by application of the identified model to an independent simulation. Figure (3-10) shows a simulated trajectory created using orthogonal multisine inputs for the store orientation with respect to the aircraft, based on a frequency range of 0-3 Hz and an amplitude range of ± 20 deg for θ and ± 10 for ψ. The vertical position varies continuously from 0 to 30 ft linearly throughout the 3 sec trajectory. The solid lines in the lower portion of Figure (3-10) represent the pitching moment and normal force delta coefficients obtained from conventional simulation for the prescribed trajectory. The dashed lines represent the parameterized model derived from piecewise continuous system identification. It is apparent that the parametric model is an adequate representation of the wind tunnel delta coefficients. The subsonic results are slightly more accurate, as expected based on the relative complexities of the individual flow fields. However, in both cases, the system identification results capture the salient features of the spatially variant aerodynamics.

3.3.3 Flight Test Comparison

The freestream and spatially variant parametric models introduced in Section 3.3.1 and 3.3.2 have been shown to adequately represent the wind tunnel source data on which the models are based. Further confidence in the predictive capability of the combined aerodynamic model can be gained by comparison to actual flight-test data.

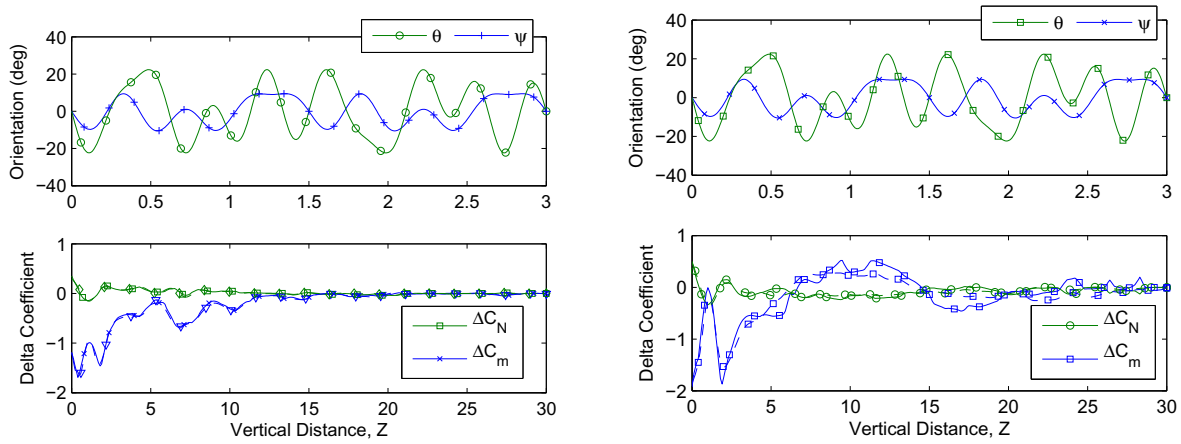

A Mach 0.9 / 550 KCAS / 4800 ft

B Mach 1.2 / 600 KCAS / 1800 ft

Figure 3-10. Validation results showing pitching moment and normal force delta coefficient comparison between simulation and system identification for an independent maneuver.

In this section, comparison between simulation, parametric modeling, and flight-test data indicate the parametric model adequately characterizes the store separation aerodynamics and may be useful for trajectory prediction. Other applications, including sensitivity analysis, trajectory optimization, and control system design, are also possible given the validated parametric model.

3.3.3.1 Trajectory comparison

Figure (3-11) shows a comparison between flight-test data, conventional 6DOF simulation using a wind tunnel database, and 6DOF simulation using a parametric model. Results are shown in Figure (3-11A) for flight test 2265 (Mach 0.90 / 552 KCAS / 4820 ft) and Figure (3-11B) for flight test 4535 (Mach 1.19 / 595 KCAS / 17900 ft). In both cases, the trajectory prediction determined using the identified parametric model closely matches the conventional simulation and flight-test results, especially in the primary motion variables: vertical translation, z , and pitch angle, θ.

3.3.3.2 Aerodynamic comparison

The reconstructed trajectory can be used, along with the equations of motion, to estimate the full-scale aerodynamic forces and moments acting on the store during

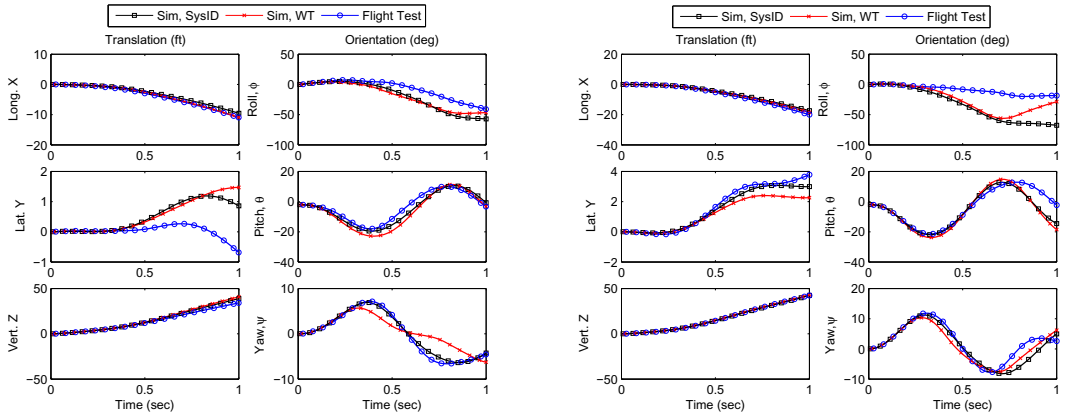

A Mach 0.90 / 552 KCAS / 4820 ft

B Mach 1.19 / 595 KCAS / 17900 ft

Figure 3-11. Trajectory comparison between flight test, conventional simulation, and simulation with system identification.

separation. These estimates can be compared to wind tunnel estimates evaluated along the flight-test trajectory for a more direct assessment of the aerodynamic model. Figure (3-12) shows a comparison between the estimated full-scale aerodynamic coefficients and (1) simulated coefficients using conventional methods and (2) simulated coefficients using parametric modeling. Again, both types of simulation closely resemble the flight-test data. In particular, the parametric model is observed to match flight test with nearly the same level of accuracy as conventional methods.

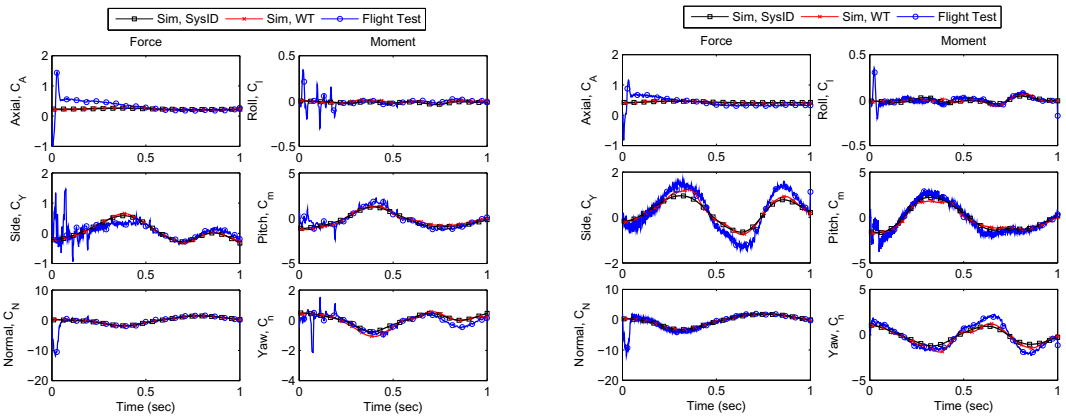

A Mach 0.90 / 552 KCAS / 4820 ft

B Mach 1.19 / 595 KCAS / 17900 ft

Figure 3-12. Aerodynamic comparison between flight test, conventional simulation, and simulation with system identification.

3.4 Example: Planar Store Separation

Store separation is often dominated by vertical translation and pitch attitude. In most cases, lateral translation and yaw attitude are fairly benign and of secondary interest. For instructive purposes, consideration of a store confined to the vertical *x*–*z* plane during separation maintains the primary scope of interest and considerably reduces the complexity of the parametric model.

The system identification approach described in Section 3.3 can also be used to determine a simplified parametric model describing the longitudinal aerodynamics of a store confined to the vertical plane. In Section 3.3 the objective was to construct a parametric model that could adequately capture the salient features of six dimensional wind tunnel database for application to trajectory prediction and flight test matching. A simplified planar model provides a reduced order model that retains the essential features of the more complex model, but in a simple compact expression. This simplified parametric model will be used extensively in Chapters 4 and 5 to illustrate the application of optimal control theory to store separation. The full six dimensional aerodynamic model will be considered in Chapter 6.

For planar store separation, the dominant effect of the nonuniform flow field is on the pitching moment. As such, consider the following spatially variant quasi-linear aerodynamic model.

$$C_A = C_{A_0} = constant \tag{3–52}$$

$$C_N = C_{N_\alpha}\alpha + C_{N_{\delta_e}}\delta_e \tag{3–53}$$

$$C_m = C_{m_\alpha}\alpha + C_{m_q}\hat{q} + C_{m_{\delta_e}}\delta_e + e^{-(\mu z)}\left(\eta_0 + \eta_1 z\right) \tag{3–54}$$

The variable δ_e is the elevator control surface deflection, the only input of interest for dynamics limited to the *x*–*z* plane. The variable $\hat{q}$ is the non-dimensional pitch rate introduced for unit consistency. The variables C_{N_α}, C_{A_0}, C_{m_α}, and C_{m_q} are the classical aerodynamic derivatives in the body axis. The variables $C_{N_{\delta_e}}$ and $C_{m_{\delta_e}}$ are

the classical control derivatives. The aerodynamic and control derivatives can be estimated using freestream system identification. The exponential-polynomial form $\Delta C_m(z) = e^{-(\mu z)}(\eta_0 + \eta_1 z)$ is a special case of the more general parametric model presented in Section 3.3. The constants μ, η_0, and η_1 can be estimated using spatially variant system identification. The final result is a simplified quasi-linear aerodynamic model that can be used to investigate guidance and control of a store during separation.

The following example is based on a store aerodynamic database at Mach 0.8 / 10kft. The longitudinal input is shown in Figure 3-13. The angle of attack α_s was specified as a multisine input using an amplitude of ± 5 deg, a frequency range of $0 - 5$ Hz, and a duration of $t = 5$ seconds. The pitch rate q was computed using the kinematic relationship for pitch rate and angle of attack. For the case of planar motion with a pinned center of gravity, $q = \dot{\alpha}_s$. Finally, the elevator control surface deflection δ_e was specified using an orthogonal multisine input with the same amplitude, frequency range, and duration as the angle of attack.

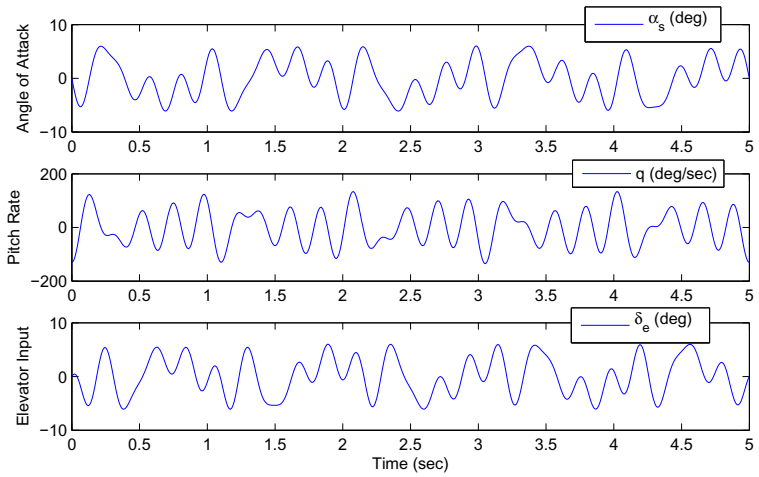

Figure 3-13. Angle of attack, pitch rate, and elevator input for planar system identification.

The freestream simulation results for the pitching moment and normal force are shown in Figure 3-14. The aerodynamic coefficients were determined using interpolation of the freestream wind tunnel database along the trajectory shown in Figure 3-13. The

system identification results were determined using the equation error method described in Section 3.2.4.1. Some discrepancies between the model and the data are evident, as one might expect given the simple linear structure of the aerodynamic model. However, for this limited range of angle of attack, $|\alpha_s| \leq 5$ deg, the linear model adequately captures the freestream aerodynamic characteristics. The normal force and pitching moment derivatives were estimated to be $C_{N_\alpha} = 4.56$ rad^{-1} and $C_{m_\alpha} = -3.38$ rad^{-1}, respectively. The pitching moment damping derivative is known from the wind tunnel test report to be $C_{m_q} = -74$ rad^{-1}. The negative value of C_{m_α} for small α_s is indicative of the inherent longitudinal stability of the store.

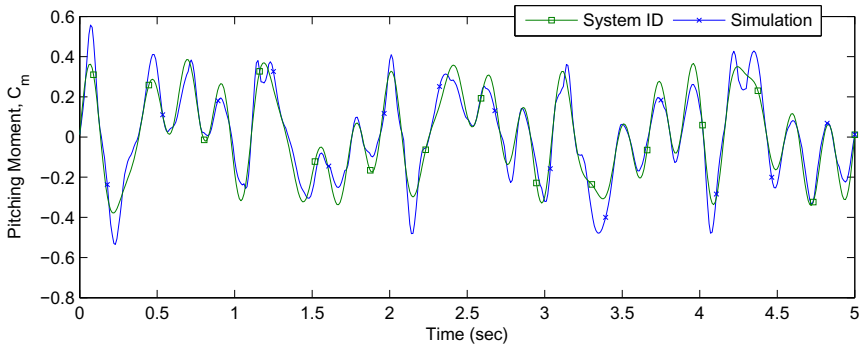

A Pitching Moment

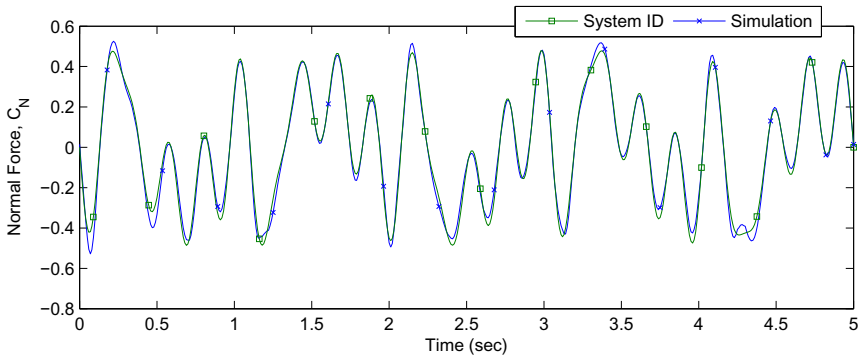

B Normal Force

Figure 3-14. Planar aerodynamic coefficient comparison between simulation and system identification for a store in freestream flight conditions at Mach 0.8 / 10 kft.

Figure 3-15 shows simulation results for the pitching moment and normal force control increment. Again, the simulation results were determined using an aerodynamic database and the system identification results were determined using the equation error

method. The normal force and pitching moment control derivatives were estimated to be $C_{N_{\delta_e}} = 2.09$ rad^{-1} and $C_{m_{\delta_e}} = -8.16$ rad^{-1}, respectively.

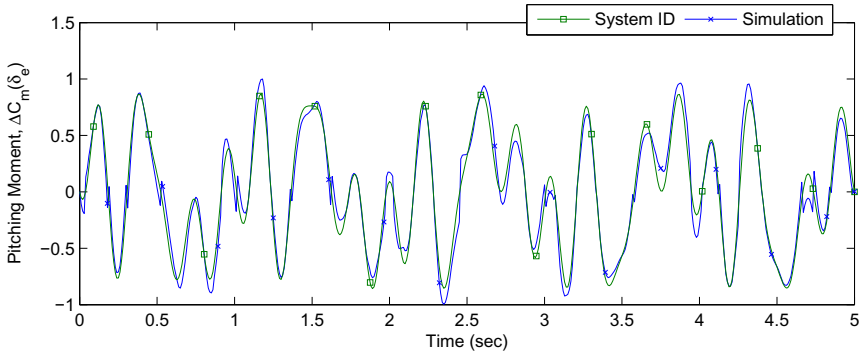

A Pitching Moment

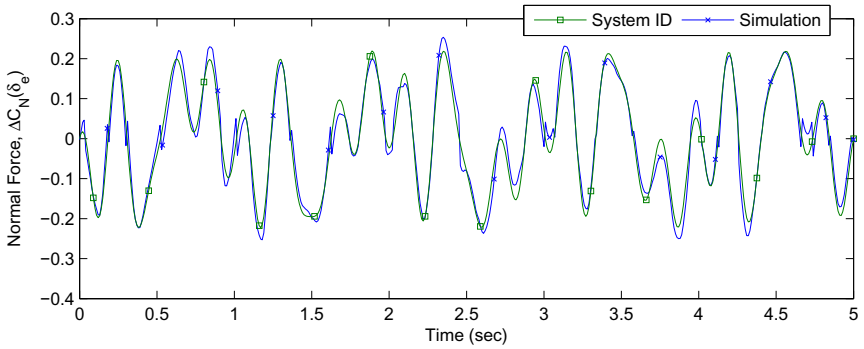

B Normal Force

Figure 3-15. Planar aerodynamic control effect comparison between simulation and system identification for a store in freestream flight conditions at Mach 0.8 / 10 kft.

Finally, Figure 3-16 shows the pitching moment delta coefficient $\Delta C_m(z)$. The figure includes data extracted from the wind tunnel database for a nominal yaw angle of $\psi_B^A = 0$. The wind tunnel data show the measured delta coefficient for increasingly nose-down pitch attitudes. The pitch attitude is held constant throughout the vertical sweep. The delta coefficients converge to zero at about 30 feet below the aircraft, indicating the aircraft effect is no longer significant. The nonlinear exponential-polynomial product is also shown.

The constants μ, η_0 and η_1 were determined using the spatially variant system identification technique described in Section 3.2.4.2. The figure indicates that the

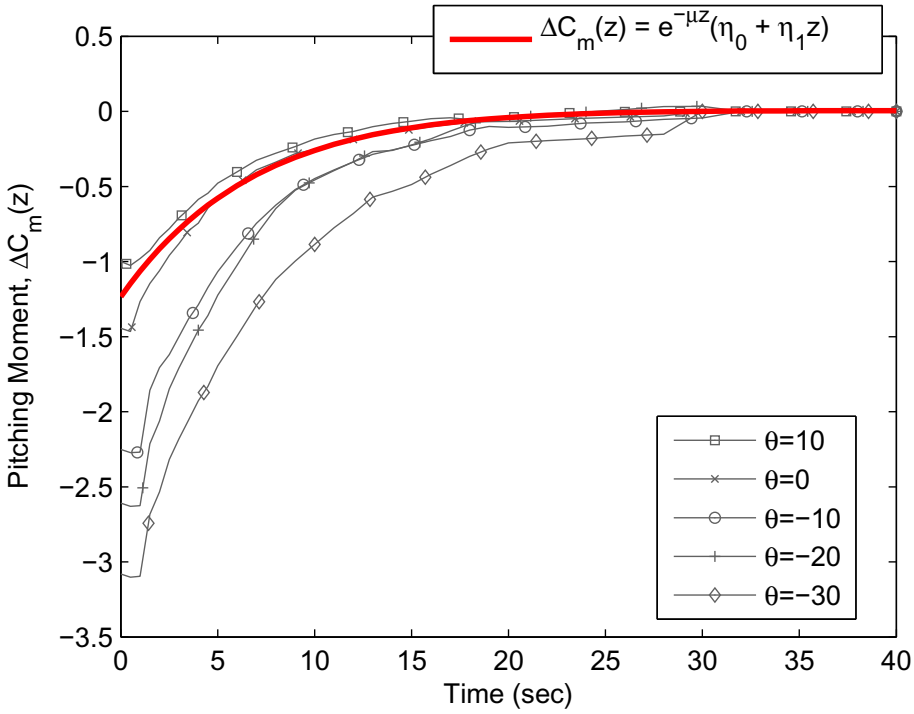

Figure 3-16. Pitching moment delta coefficient for simplified parametric model using system identification.

parametric model closely resembles the grid data for a pitch angle between $0 < \theta_B^A < 10$ deg. This result is consistent with the training maneuver, which is based on a pitch angle between $-5 < \theta_B^A < 5$ deg. The spatially variant parameters are summarized in Table 3-1, along with the freestream derivatives.

Table 3-1. Parameters used in planar store separation aerodynamic model.

Aerodynamic Derivatives	Control Derivatives	Spatially Variant Parameters
$C_{N_\alpha} = 4.56$ rad^{-1}	$C_{m_{\delta_e}} = -8.16$ rad^{-1}	$\mu = 0.115$
$C_{M_\alpha} = -3.38$ rad^{-1}	$C_{N_{\delta_e}} = 2.09$ rad^{-1}	$\eta_0 = -1.23$
$C_{M_q} = -74$ rad^{-1}		$\eta_1 = 0.042$ ft^{-1}
$C_{A_0} = 0.201$		

The compact aerodynamic model in Equations (3–52) through (3–54) can be used in conjunction with the three degree-of-freedom equations of motion to simulate the separation of a store confined to the vertical *x*–*z* plane. This reduced order model

is useful for design and analysis of potential control strategies, as will be shown in Chapters 4 and 5.

3.5 Chapter Summary

The purpose of this chapter is to show that the existing aerodynamic data can be represented as a parametric model using system identification techniques. The parametric model offers the advantage of representing the store separation aerodynamics in analytical form, suitable for trajectory prediction, sensitivity analysis, trajectory optimization, and control system design.

The parametric model is expected to be nonlinear and spatially variant due to the complexity of the nonuniform flow field surrounding the aircraft during flight. The modeling task is decomposed into two complementary models: a freestream model for the uniform flow contribution and a delta-coefficient model for the nonuniform flow contribution. The freestream aerodynamic model is based on a multivariate polynomial with constant coefficients, the model structure is identified using orthogonal polynomials, and the coefficients are estimated using ordinary least squares. The delta coefficient model is based on a multivariate polynomial with spatially variant coefficients. The spatially variant coefficients are given a particular exponential-polynomial form based on physical considerations and known boundary conditions. The unknown parameters are estimated using nonlinear least squares. The result is a compact nonlinear parametric model that is a suitable candidate for any store separation problem where time-averaged aerodynamic data are available.

The proposed parametric modeling approach is applied to a representative example. The example includes small-scale wind tunnel data and full-scale flight-test data for a representative store separating from the F-16 aircraft at both subsonic and supersonic conditions. In all cases considered, the parametric model adequately represented the underlying wind tunnel data and accurately reproduced the flight-test results. As such, the validated model is considered suitable for further analysis,

including trajectory optimization and control system design. Specifically, development of a store separation guidance and control system using the models discussed herein is considered in Chapter 6.

CHAPTER 4
TRAJECTORY OPTIMIZATION

4.1 Overview

Trajectory optimization is the process of determining control and state histories for a dynamic system in order to minimize (or maximize) a measure of performance while satisfying prescribed boundary conditions and/or path constraints [87]. Trajectory optimization is closely related to Optimal Control Theory, and indeed, the terms are often used interchangeably. The dynamic system is generally modeled in the time domain using a state space representation. The measure of performance represents a metric or combination of metrics (e.g. time, energy, control effort, deviation from a desired operating condition, etc.) that quantify the desired performance of the system. The boundary conditions include limitations on the initial and/or final state of the dynamic system, as well as limits on the control (e.g. actuator limits, control saturation). Path (or state) constraints are used to exclude trajectories that violate a predetermined range or type of undesirable motion. Each of these components are stated with mathematical precision and combined to create an optimal control problem.

From an historical point of view, the advent of optimal control theory arose from the stringent requirements on aerospace systems [88]. Such systems are inherently nonlinear, they are subject to various constraints (fuel, thrust, acceleration, etc.), and they are greatly benefited by optimization due to high operational costs. Prominent applications of optimal control to aerospace systems include orbit transfer and rendezvous [89], optimal guidance and control to direct the powered flight of a missile [90], control of a re-entry vehicle [91, 92], maximum range of a missile [89], and automatic landing of an aircraft [93]. A prominent contribution of optimal control theory came from a study published by Bryson [94]. In this groundbreaking work, Bryson presented the optimal flight path for a supersonic fighter to climb to a desired altitude in minimum time and a companion solution for a fighter to achieve maximum

altitude, a capability of intense interest during the cold-war era in which the results were obtained. The solutions were paired with actual flight test results that closely matched the predicted trajectories. The non-intuitive but realistically demonstrated results helped optimal control theory gain traction among practitioners. This classic problem is still used as a clear illustration of the capability of optimal control [95].

More recently optimal control techniques have been used to solve spacecraft orientation and navigation problems with minimum time and/or fuel consumption [96, 97], flight control of a reusable reentry vehicle [91, 92], multiple spacecraft cooperative formation [98, 99], and time-optimal UAV flight through an urban environment [100, 101]. Also of particular relevance are the numerous studies considering flight path trajectory optimization through non-uniform wind fields, such as wind-corrected flight path planning for micro-air vehicles [102], minimum-time flight paths through high-altitude atmospheric winds [103, 104], optimal recovery from microburst wind shear [105, 106], and the maximum range trajectory of a glider in ground effect and wind shear [107]. Optimal control has also been successfully used in various other applications, including such diverse applications as motion planning for autonomous ground vehicles [108], quantum mechanics [109], and environmental and economic processes [110], to name just a few. Several excellent textbooks have also been written on the topic of optimal control, including those by Bryson [87, 111–113], Kirk [114], Athans and Falb [115] and Stengel [116].

The classical approach to solving an optimal control problem involves the use of Pontryagins minimum principle [117]. Pontryagins minimum principle (PMP) is fundamentally an extension and application of the calculus of variations to the optimal control problem [88]. This approach can be used to develop a set of differential equations that provide necessary (but not sufficient) conditions for local optimality. These necessary conditions can be used to find analytical solutions for a narrow range of optimal control problems, but in practice numerical methods are necessary

to approximate a solution. In more recent literature, numerical methods are used to approximate a solution more directly, but PMP still plays a key role in validating the necessary optimality conditions for the proposed solution [118, 119]. In this research, the classical indirect approach to optimal control is considered exclusively, due primarily to the greater computational efficiency and additional insight gained by analytical formulation of the optimality conditions. More detail about the numerical methods used in the course of this study are presented in Section 4.2.5.

4.2 Optimal Control

The objective of an optimal control problem is to determine an admissible control input that minimizes (or maximizes) the desired performance index subject to the specified boundary conditions and dynamic constraints. The solution using an indirect method is based on the calculus of variations. Ordinary calculus is predominantly concerned with the calculus of functions, characterized by the differential operator. Comparatively, the calculus of variations is concerned with the calculus of functionals, characterized by the variational operator.

4.2.1 First Order Optimality Conditions

The objective of an optimal control problem is to minimize the Bolza form of the cost functional

$$J = \Phi\big(\mathbf{x}(t_0), t_0, \mathbf{x}(t_f), t_f\big) + \int_{t_0}^{t_f} L\big(\mathbf{x}(t), \mathbf{u}(t)\big)\, dt \tag{4–1}$$

subject to the dynamic constraints

$$\dot{\mathbf{x}}(t) = \mathbf{f}\big(\mathbf{x}(t), \mathbf{u}(t)\big) \tag{4–2}$$

the inequality path and control constraints

$$\mathbf{C}\big(\mathbf{x}(t), \mathbf{u}(t)\big) \leq 0 \tag{4–3}$$

and the boundary conditions

$$\phi\big(\mathbf{x}(t_0), t_0, \mathbf{x}(t_f), t_f\big) = 0 \tag{4–4}$$

where $\mathbf{x}(t) \in \mathbb{R}^n$ is the state, $\mathbf{u}(t) \in \mathbb{R}^m$ is the control, $\mathbf{f} : \mathbb{R}^n \times \mathbb{R}^m \to \mathbb{R}^n$ is a system of ordinary differential equations, $\mathbf{C} : \mathbb{R}^n \times \mathbb{R}^m \to \mathbb{R}^s$ are the (optional) path and control constraints, $\phi : \mathbb{R}^n \times \mathbb{R} \times \mathbb{R}^n \times \mathbb{R} \to \mathbb{R}^q$ are the boundary conditions, and t is time. The Mayer cost is given by $\Phi : \mathbb{R}^n \times \mathbb{R} \times \mathbb{R}^n \times \mathbb{R} \to \mathbb{R}$ and the Lagrangian is $L : \mathbb{R}^n \times \mathbb{R}^m \to \mathbb{R}$.

The augmented cost functional is formed by multiplying the constraints with associated Lagrange multipliers and joining the product with the cost functional.

$$\begin{aligned} J_a =& \Phi\big(\mathbf{x}(t_0), t_0, \mathbf{x}(t_f), t_f\big) - \nu^T \phi\big(\mathbf{x}(t_0), t_0, \mathbf{x}(t_f), t_f\big) + \\ & \int_{t_0}^{t_f} \Big[L\big(\mathbf{x}(t), \mathbf{u}(t)\big) - \boldsymbol{\lambda}^T(t)\big(\dot{\mathbf{x}}(t) - \mathbf{f}\big(\mathbf{x}(t), \mathbf{u}(t)\big)\big) + \mu^T(t)\mathbf{C}\big(\mathbf{x}(t), \mathbf{u}(t)\big)\Big]\, dt \end{aligned} \tag{4–5}$$

where $\nu^T \in \mathbb{R}^q$, $\boldsymbol{\lambda}^T(t) \in \mathbb{R}^n$, and $\mu^T(t) \in \mathbb{R}^s$ are the Lagrange multipliers. The Hamiltonian is introduced in terms of the state $\mathbf{x}(t)$ and the costate $\boldsymbol{\lambda}^T(t)$ as a combination of the Lagrangian and augmented dynamic constraints.

$$H\big(\mathbf{x}(t), \mathbf{u}(t), \boldsymbol{\lambda}(t), \boldsymbol{\mu}(t)\big) := L\big(\mathbf{x}(t), \mathbf{u}(t)\big) + \boldsymbol{\lambda}^T(t)\mathbf{f}\big(\mathbf{x}(t), \mathbf{u}(t)\big) + \mu^T(t)\mathbf{C}\big(\mathbf{x}(t), \mathbf{u}(t)\big) \tag{4–6}$$

Using the Hamiltonian, the augmented cost functional can be written as follows.

$$\begin{aligned} J_a =& \Phi\big(\mathbf{x}(t_0), t_0, \mathbf{x}(t_f), t_f\big) - \nu^T \phi\big(\mathbf{x}(t_0), t_0, \mathbf{x}(t_f), t_f\big) + \\ & \int_{t_0}^{t_f} \Big[H\big(\mathbf{x}(t), \mathbf{u}(t), \boldsymbol{\lambda}(t), \boldsymbol{\mu}(t)\big) - \boldsymbol{\lambda}^T(t)\dot{\mathbf{x}}(t)\Big]\, dt \end{aligned} \tag{4–7}$$

The 1st order necessary conditions for an extremal trajectory are determined by taking the first variation of the augmented cost functional with respect to each free variable.

$$\begin{aligned}\delta J_a =& \frac{\partial \Phi}{\partial \mathbf{x}(t_0)}\delta \mathbf{x}_0 + \frac{\partial \Phi}{\partial t_0}\delta t_0 + \frac{\partial \Phi}{\partial \mathbf{x}(t_f)}\delta \mathbf{x}_f + \frac{\partial \Phi}{\partial t_f}\delta t_f \\ & - \delta \nu^T \phi - \nu^T \left(\frac{\partial \phi}{\partial \mathbf{x}(t_0)}\delta \mathbf{x}_0 + \frac{\partial \phi}{\partial t_0}\delta t_0 + \frac{\partial \phi}{\partial \mathbf{x}(t_f)}\delta \mathbf{x}_f + \frac{\partial \phi}{\partial t_f}\delta t_f \right) \\ & + \left(\left[H - \boldsymbol{\lambda}^T \dot{\mathbf{x}} \right]_{t=t_f} \right) \delta t_f - \left(\left[H - \boldsymbol{\lambda}^T \dot{\mathbf{x}} \right]_{t=t_0} \right) \delta t_0 \\ & + \int_{t_0}^{t_f} \left[\frac{\partial H}{\partial \mathbf{x}}\delta \mathbf{x} + \frac{\partial H}{\partial \mathbf{u}}\delta \mathbf{u} - \delta \lambda^T \left(\dot{\mathbf{x}} - \mathbf{f} \right) - \boldsymbol{\lambda}^T \delta \dot{\mathbf{x}} + \delta \mu^T \mathbf{C} \right] dt \end{aligned} \tag{4–8}$$

The term within the integral of Equation (4–8) containing $\delta \dot{\mathbf{x}}$ requires special treatment. Integrating by parts, the integral can be expanded as follows.

$$\int_{t_0}^{t_f} -\boldsymbol{\lambda}^T \delta \dot{\mathbf{x}} dt = -\boldsymbol{\lambda}^T(t_f)\delta \mathbf{x}(t_f) + \boldsymbol{\lambda}^T(t_0)\delta \mathbf{x}(t_0) + \int_{t_0}^{t_f} \dot{\boldsymbol{\lambda}}^T \delta \mathbf{x} dt \tag{4–9}$$

Furthermore, the terms $\delta \mathbf{x}(t_0)$ and $\delta \mathbf{x}(t_f)$ can be expanded to first order using the definition of a variation in a manner analogous to a Taylor series expansion.

$$\delta \mathbf{x}_0 = \delta \mathbf{x}(t_0) + \dot{\mathbf{x}}(t_0)\delta t_0 \tag{4–10}$$

$$\delta \mathbf{x}_f = \delta \mathbf{x}(t_f) + \dot{\mathbf{x}}(t_f)\delta t_f \tag{4–11}$$

Substituting these expressions into equation (4–8), cancelling terms involving $\dot{\mathbf{x}}(t_0)$ and $\dot{\mathbf{x}}(t_f)$, and factoring the variation of each free variable, the augmented cost functional is given by Equation (4–12).

$$\begin{aligned}\delta J_a =& \left(\frac{\partial \Phi}{\partial \mathbf{x}(t_0)} - \nu^T \frac{\partial \phi}{\partial \mathbf{x}(t_0)} + \boldsymbol{\lambda}^T(t_0) \right) \delta \mathbf{x}_0 + \left(\frac{\partial \Phi}{\partial \mathbf{x}(t_f)} - \nu^T \frac{\partial \phi}{\partial \mathbf{x}(t_f)} - \boldsymbol{\lambda}^T(t_f) \right) \delta \mathbf{x}_f \\ & + \left(\frac{\partial \Phi}{\partial t_0} - \nu^T \frac{\partial \phi}{\partial t_0} - H(t_0) \right) \delta t_0 + \left(\frac{\partial \Phi}{\partial t_f} - \nu^T \frac{\partial \phi}{\partial t_f} + H(t_f) \right) \delta t_f - \delta \nu^T \phi \\ & + \int_{t_0}^{t_f} \left[\left(\frac{\partial H}{\partial \mathbf{x}} + \dot{\boldsymbol{\lambda}}^T \right) \delta \mathbf{x} + \frac{\partial H}{\partial \mathbf{u}}\delta \mathbf{u} - \delta \boldsymbol{\lambda}^T \left(\dot{\mathbf{x}} - \mathbf{f} \right) + \delta \mu^T \mathbf{C} \right] dt \end{aligned} \tag{4–12}$$

In a manner analogous to ordinary calculus, the extremal condition is found by requiring $\delta J_a = 0$. However, each variation is independent, so for an extremal solution to exist each term in equation (4–12) must be zero individually. As a result, the following 1st order optimality conditions are obtained.

$$\dot{\mathbf{x}}^T = \frac{\partial H}{\partial \boldsymbol{\lambda}} \tag{4–13}$$

$$\dot{\boldsymbol{\lambda}}^T = -\frac{\partial H}{\partial \mathbf{x}} \tag{4–14}$$

$$\mathbf{0} = \frac{\partial H}{\partial \mathbf{u}} \tag{4–15}$$

$$\boldsymbol{\lambda}^T(t_0) = -\frac{\partial \Phi}{\partial \mathbf{x}(t_0)} + \nu^T \frac{\partial \phi}{\partial \mathbf{x}(t_0)} \tag{4–16}$$

$$\boldsymbol{\lambda}^T(t_f) = \frac{\partial \Phi}{\partial \mathbf{x}(t_f)} - \nu^T \frac{\partial \phi}{\partial \mathbf{x}(t_f)} \tag{4–17}$$

$$H(t_0) = \frac{\partial \Phi}{\partial t_0} - \nu^T \frac{\partial \phi}{\partial t_0} \tag{4–18}$$

$$H(t_f) = -\frac{\partial \Phi}{\partial t_f} + \nu^T \frac{\partial \phi}{\partial t_f} \tag{4–19}$$

Equations (4–13) and (4–14) represent a set of $2n$ coupled ordinary differential equations. The boundary conditions are given by equations (4–16) through (4–19). Depending on the specifications of the problem, one or more of these boundary conditions may not apply. However, the boundary conditions usually include specifications at the initial and terminal conditions. Thus, equations (4–13) and (4–14) can usually be classified as a set of $2n$ nonlinear, coupled ordinary differential equations with split boundary conditions, referred to as a Hamiltonian boundary value problem (HBVP). Finally, note that equation (4–15) can often be used to determine an explicit form for the optimal control in terms of the state and costate.

Using the complementary slackness condition, the Lagrange multiplier $\mu(t)$ is related to the dynamic constraint $\mathbf{C}\left(\mathbf{x}(t), \mathbf{u}(t)\right) \leq 0$, as shown in Equation (4–20).

$$\text{Lagrange multiplier } \mu(t): \begin{cases} \mu_i(t) = 0 & \text{if} \quad C_i\left(\mathbf{x}(t), \mathbf{u}(t)\right) < 0; \quad i = 1, \ldots, s \\ \mu_i(t) > 0 & \text{if} \quad C_i\left(\mathbf{x}(t), \mathbf{u}(t)\right) = 0; \quad i = 1, \ldots, s \end{cases} \tag{4–20}$$

The positivity of μ_i when $C_i = 0$ is interpreted such that improving the cost may only come from violating the constraint [113]. Furthermore, $\mu_i(t) = 0$ when $C_i < 0$ states that this constraint is inactive and can be ignored. In this case, the Hamiltonian reduces to the classical form given in equation (4–21).

$$H = L\left(\mathbf{x}(t), \mathbf{u}(t)\right) + \boldsymbol{\lambda}^T(t)\mathbf{f}\left(\mathbf{x}(t), \mathbf{u}(t)\right) \tag{4–21}$$

The constraint $\mathbf{C}\left(\mathbf{x}(t), \mathbf{u}(t)\right) \leq 0$ can be used to limit the components of the state or the control to predetermined hard limits. Stated another way, any trajectory that does not satisfy these constraints is inadmissible and will not satisfy the necessary conditions. Frequently, the hard limits can be replaced by "soft limits" imposed by penalizing the components of the state and control in the cost functional. When this is the case, the additional conditions required by the dynamic state and control inequality constraints may be omitted, and Equations (4–13) through (4–19) provide the necessary conditions for an extremal or stationary solution.

These conditions alone are not sufficient to conclude that the extremal trajectory is indeed a local optimal trajectory. In a manner analogous to ordinary function minimization, consideration of the second variation provides a sufficient condition to demonstrate that the stationary solution is also a local minimum solution. Further discussion of the necessary and sufficient conditions for optimality will be presented in Chapter 5, and it will be shown that in order for a neighboring optimal control to exist, the stationary solution must be a local minimum (i.e. the second variation is positive definite over the entire path). For now, a solution that satisfies equations (4–13) through

(4–19) may be said to be an extremal or stationary trajectory, which may or may not be an optimal trajectory.

4.2.2 Interpretation of the Costate

The necessary conditions presented in equations (4–13) through (4–19) introduce an additional set of differential equations referred to as the costate. The costate is a Lagrange multiplier that was introduced purely as a mathematical device to allow formulation of the minimization problem subject to the dynamic constraints. However, the costate can be related to the cost functional along a stationary path, as shown by Bryson and Ho [113].

$$\boldsymbol{\lambda}^T = -\frac{\partial L_{\min}}{\partial \mathbf{f}} \tag{4–22}$$

Hence, the costate can be interpreted as the sensitivity of the Lagrange cost functional to changes in the system dynamics evaluated along the extremal trajectory. This relationship provides meaningful insight into the optimal performance of the system, as discussed in Section 4.3.3.4.

4.2.3 Interpretation of the Hamiltonian

Consider the form of the Hamiltonian without inequality constraints given by equation (4–21), which can be written as functional form in equation (4–23).

$$H = H\left(\mathbf{x}(t), \mathbf{u}\left(\mathbf{x}(t), \boldsymbol{\lambda}^T(t)\right), \boldsymbol{\lambda}^T(t), t\right) = H\left(\mathbf{x}(t), \boldsymbol{\lambda}^T(t), t\right) \tag{4–23}$$

Taking the total derivative with respect to time yields equation (4–24).

$$\frac{dH}{dt} = \frac{\partial H}{\partial \mathbf{x}}\dot{\mathbf{x}} + \frac{\partial H}{\partial \boldsymbol{\lambda}}\dot{\boldsymbol{\lambda}} + \frac{\partial H}{\partial t} \tag{4–24}$$

Noting that the derivatives of the Hamiltonian with respect to the state and costate are given by the 1st order optimality conditions in equations (4–13) and (4–14), the total derivative can be stated as equation (4–25) and reduced to equation (4–26).

$$\frac{dH}{dt} = -\dot{\boldsymbol{\lambda}}^T\dot{\mathbf{x}} + \dot{\mathbf{x}}^T\dot{\boldsymbol{\lambda}} + \frac{\partial H}{\partial t} \tag{4–25}$$

$$\frac{dH}{dt} = \frac{\partial H}{\partial t} \tag{4–26}$$

In many cases, the Hamiltonian is not an explicit function of time, so equation (4–26) can be taken further to imply that the Hamiltonian is a constant.

$$\frac{dH}{dt} = \frac{\partial H}{\partial t} = 0 \quad \Rightarrow \quad H = const \tag{4–27}$$

The significance of Equation (4–27) is noteworthy. Equation (4–27) implies that when the Hamiltonian is not an explicit function of time, it must be constant along an extremal solution. Analytically, this result can frequently be used as an additional known value in solving optimal control problems. Numerically, the constancy of the Hamiltonian can be used as a quality check to ensure that an extremal solution has indeed been found.

4.2.4 Linear Quadratic Regulator

Recall that the cost functional is given in generic form by equation (4–1), restated here.

$$J = \Phi\left(\mathbf{x}(t_0), t_0, \mathbf{x}(t_f), t_f\right) + \int_{t_0}^{t_f} L\left(\mathbf{x}(t), \mathbf{u}(t)\right) dt \tag{4–28}$$

In Equation (4–28), $\Phi\left(\mathbf{x}(t_0), t_0, \mathbf{x}(t_f), t_f\right)$ is the endpoint or Mayer cost, and $L\left(\mathbf{x}(t), \mathbf{u}(t)\right)$ is the accumulated or Lagrange cost. In many applications, a quadratic cost functional is applied, as in equation (4–29).

$$J = \mathbf{x}^T(t_f) P \mathbf{x}(t_f) \; + \; \frac{1}{2} \int_{t_0}^{t_f} \left(\mathbf{x}^T Q \mathbf{x} \; + \; \mathbf{u}^T R \mathbf{u}\right) dt \tag{4–29}$$

The matrix $Q \in \mathbb{R}^{n \times n}$ is a positive semi-definite matrix ($Q \geq 0$) and $R \in \mathbb{R}^{m \times m}$ is a positive definite matrix ($R > 0$) chosen by the control designer to achieve favorable trajectory characteristics within suitable state and control limits. The quadratic cost functional is quite flexible and has an intuitive physical significance. The values of Q determine which state variables will be regulated to zero. The values of P penalize the

deviation from a desired end-state. The values of R determine the amount of control effort available to achieve the objective.

The quadratic cost functional is especially useful for dynamic systems represented by a linear time variant state space relationship.

$$\dot{\mathbf{x}} = A(t)\mathbf{x}(t) + B(t)\mathbf{u}(t) \tag{4–30}$$

Using equation (4–30), the Hamiltonian can be written as follows.

$$H = \tfrac{1}{2}\mathbf{x}^T Q\mathbf{x} + \tfrac{1}{2}\mathbf{u}^T R\mathbf{u} + \boldsymbol{\lambda}^T(t)A(t)\mathbf{x}(t) + \boldsymbol{\lambda}^T(t)B(t)\mathbf{u}(t) \tag{4–31}$$

The costate differential equations and optimal control condition are readily determined, as shown in equations (4–32) and (4–33).

$$\dot{\boldsymbol{\lambda}} = -\frac{\partial H}{\partial \mathbf{x}}^T = -Q\mathbf{x}(t) - A^T(t)\boldsymbol{\lambda}(t) \tag{4–32}$$

$$\mathbf{0} = \frac{\partial H}{\partial \mathbf{u}} = R\mathbf{u} + B^T(t)\boldsymbol{\lambda}(t) \tag{4–33}$$

Equation (4–33) can be solved to determine the optimal control in terms of the system parameters and the costate, as shown in (4–34).

$$\mathbf{u} = -R^{-1}B^T(t)\boldsymbol{\lambda}(t) \tag{4–34}$$

Suppose, due to the linearity of the system dynamics, that the costate can be written as a linear combination of the state variables. This is shown in equation (4–35), where $K(t)$ is an unknown matrix. The derivative of (4–35) is given by (4–36).

$$\boldsymbol{\lambda}(t) = K(t)\mathbf{x}(t) \tag{4–35}$$

$$\dot{\boldsymbol{\lambda}}(t) = \dot{K}(t)\mathbf{x}(t) + K(t)\dot{\mathbf{x}}(t) \tag{4–36}$$

Substituting in the expressions for $\dot{\mathbf{x}}$ and $\dot{\boldsymbol{\lambda}}$ and solving for $\dot{K}$ provides the following matrix differential Riccati equation.

$$\dot{K}(t) = -Q - A^T(t)K(t) - K(t)A(t) + R^{-1}B^T(t)K(t) \tag{4–37}$$

The Riccati equation is stable in backward time and can be solved using standard numerical differential equation solvers, such as a Runge Kutta method. The result is a set of time varying gains $K(t)$. As a result, the optimal control law can be written as a combination of the state variables as in Equation (4–38).

$$\mathbf{u} = -R^{-1}B^T(t)K(t)\mathbf{x}(t) \tag{4–38}$$

Notice that the costate equations are eliminated from the solution process and the boundary value problem is decoupled. The Riccati equation can be solved independently, allowing the control gains to be tabulated and stored offline. The optimal trajectory can be implemented real-time using the stored gains and full-state feedback. This result shares many commonalities with neighboring optimal control, and will be further considered in Chapter 5.

4.2.5 Numerical Methods

Numerical methods for optimal control can be classified as direct or indirect methods. Following the indirect method, the necessary conditions are derived from the calculus of variations and Pontryagin's minimum principle (PMP), resulting in a Hamiltonian boundary-value problem (HBVP). The differential equations posed by the HBVP necessarily include a subset of variables that are unstable, making numerical solutions difficult to obtain over long durations. Examples of indirect methods include shooting, multiple shooting [120], finite difference [121], and collocation [122]. The numerical difficulties with indirect methods, combined with the requirement to derive the optimality conditions in analytical form, have led to the development of alternative numerical methods that attempt to find an approximate solution directly.

In a direct method, the optimal control problem is transcribed into a finite-dimensional nonlinear programming problem (NLP), which can be solved using a variety of existing

software packages. Examples of direct methods include direct shooting methods [123] and direct collocation methods [124]. A subset of direct collocation methods referred to as *p-methods* or *pseudospectral methods* [125] have gained immense popularity in the optimal control community due to the diversity of problems that can be solved, favorable convergence properties, computational efficiency, and ease of problem statement when little is known about the optimal performance of the system. Full-featured software packages implementing pseudospectral methods are now available in commercial [119] and open source packages [125].

Collocation, a valuable numerical method for solving boundary value problems, involves representing the solution to the differential equation as a low-order polynomial over a mesh of specified sub-intervals. As a result, the differential equation is represented by a system of nonlinear algebraic equations that inherently satisfy the endpoint constraints and may be solved using a suitable computational algorithm. Whereas conventional numerical integration methods (e.g. Euler, Runge-Kutta, etc.) require propagation of the differential equations in time, collocation arrives at a solution over the entire interval simultaneously. This property largely mitigates the numerical difficulties associated with unstable modes of a HBVP. As such, collocation provides an efficient way to find a solution to an optimal control problem following either the indirect or direct approach.

The indirect approach requires analytical statement of the 1st order optimality conditions, but this also offers an advantage of additional insight into the optimal performance of the dynamic system. Additionally, the indirect approach using collocation generally results in a more accurate solution obtained with less computational resources [95]. Finally, the indirect method is assured to satisfy the first order optimality conditions and second order conditions may be used to verify the solution as a minimum (as opposed to a maximum, saddle, or singular solution).

For the current application to store separation trajectory optimization, the short duration of a store separation event (approximately 1 sec) makes the problem amenable to indirect methods and the physical insight gained from the 1st order optimality conditions is a valuable asset for store separation trajectory analysis. For these reasons, the emphasis in this research is on indirect methods. The numerical solutions presented herein are based on the Matlab® program bvp4c, which implements a three-stage Lobatto IIIa formula. The bvp4c algorithm provides an approximate solution that is fourth-order accurate and differentiable over the specified interval [126]. The optimal control solutions presented in Section 4.3.3 are solved exclusively using this method.

4.3 Optimal Store Separation

4.3.1 Performance Index

Successful store separation is a balance between two competing objectives. First, a successful store separation trajectory must be safe and not exhibit any threatening motion toward the aircraft. In some cases, lateral motion is the primary concern due to tight tolerances between the store and adjacent aircraft components or additional stores. However, in most cases, safe separation is dominated by the vertical translation of the store. If the store escapes the aircraft flow field with a monotonically increasing vertical velocity, then the trajectory is considered safe. If the store hesitates or begins to flyback to the aircraft, the trajectory is considered unsafe. Due to uncertainties in separation prediction methods and variations in store and aircraft properties, flight-testing of unsafe trajectories is usually avoided altogether.

In most cases, the store is launched from an ejector providing an initial vertical velocity. In order to flyback, the store must generate enough aerodynamic lift to first arrest the vertical velocity and then begin translation in an upward direction. Thus, flyback is always preceded by a significant duration at a positive angle of attack. For most stores, limiting the angle of attack can ensure a safe separation. The safety margin is increased when the angle of attack is negative throughout much of the trajectory,

generating aerodynamic forces in the direction of translation and accelerating the store away from the aircraft.

A second criterion for a successful separation is that the trajectory must be acceptable, i.e. the transitory effects of the separation must not compromise the ability of the store to achieve a specified mission. An unsafe trajectory cannot be acceptable, but a safe trajectory may be unacceptable. Therefore, safety is a subset of acceptability. In comparison to safety, it is generally more difficult to quantify and ensure acceptability. However, for the purpose of this investigation, acceptability can be adequately addressed by the following four necessary conditions.

1. The store total aerodynamic angle of attack should not exceed the specified range for which the store autopilot has been designed to function properly.
2. The angular rates and accelerations should not exceed the specified range for which the onboard instrumentation is sufficient to measure.
3. The control inputs should not exceed the specified capability of the control actuators.
4. The total aerodynamic loads should not exceed the safety margins for the structural integrity of the store and empennage.

A conceptual comparison of safe and acceptable trajectory characteristics is shown in Figure 4-1. In Figure 4-1A, the benign trajectory is safe and acceptable. In Figure 4-1B, the trajectory is unsafe due to flyback and therefore unacceptable. In Figure 4-1C, the trajectory is safe, but unacceptable due to over-rotation.

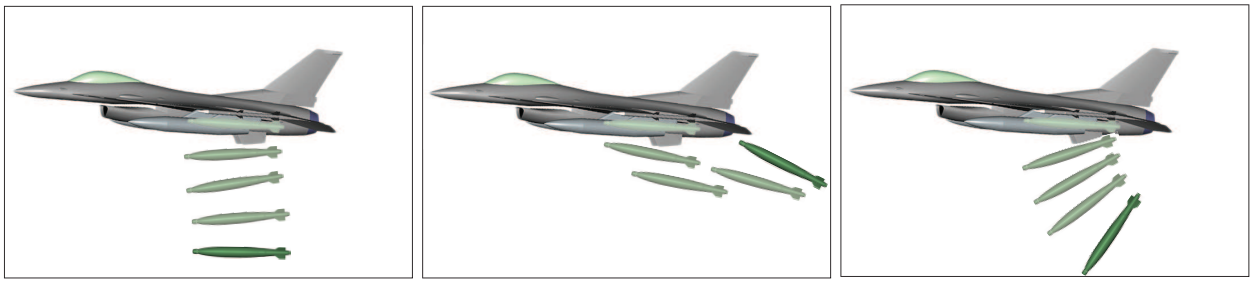

A Safe / Acceptable B Unsafe / Unacceptable C Safe / Unacceptable

Figure 4-1. Conceptual trajectories demonstrating safety and acceptability criteria.

Precise statement of the acceptability conditions requires consideration of a specific system. In general terms, acceptability can be achieved by keeping the total angle of attack and angular rates low and by limiting control effort. A narrow but useful sufficient condition for acceptability, especially in control system design, is to require the state and input be maintained within a certain predefined operating range over which the control system has been designed to function properly.

Finally, it is recognized that a separation autopilot is a transitional control system, intended to guide the store through the nonuniform flow field and transfer the control to the mission autopilot. As such, the objective of a separation autopilot is to safely drive the store to a near-equilibrium state at or before the transition to the mission autopilot. Therefore, it is desirable not only for certain components of the state to be near zero, but also for certain components of the derivative of the state to be near zero.

The following discussion can be summarized as the following sufficient condition for safe and acceptable store separation: minimize the total aerodynamic angle of attack and deviation from a near-equilibrium condition at the end-state subject to predefined limits on the state and control inputs. This objective can readily be achieved using a quadratic cost functional and control inequality constraints when necessary.

4.3.2 First Order Optimality Conditions

The general 1st order optimality conditions presented in Equations (4–13) through (4–19) can readily be applied to store separation. The state space representation of the store separation equations of motion are similar to the classical aircraft flight dynamics equations prevalent in the literature [17, 22, 23], and are described in detail in Chapter 2. In general form, the nonlinear differential equations are written as shown in equation (4–39).

$$\dot{\mathbf{x}}(t) = \mathbf{f}\left(\mathbf{x}(t), \mathbf{u}(t)\right) \tag{4–39}$$

Here, $\mathbf{x}(t) \in \mathbb{R}^n$ is the state with $n = 12$ and $\mathbf{u}(t) \in \mathbb{R}^m$ is the control with $m = 3$ for a full six degree-of-freedom (6DOF) model. The equations of motion are dependent on

the aerodynamic forces and moments, given in equations (4–40) and (4–41). In general, $\mathbf{C}_F \in \mathbb{R}^{N_F}$ and $\mathbf{C}_M \in \mathbb{R}^{N_M}$. In the 6DOF case, $N_F = N_M = 3$.

$$\mathbf{C}_F^T = [C_D, C_Y, C_L]^T = \frac{1}{q_\infty S}[D, Y, L]^T \tag{4–40}$$

$$\mathbf{C}_M^T = [C_l, C_m, C_n]^T = \frac{1}{q_\infty S\,\bar{c}}[M_X, M_Y, M_Z]^T \tag{4–41}$$

The aerodynamic forces and moments are themselves functions of the state and control inputs. In a very general sense, the equations of motion can be cast in the following functional form.

$$\dot{\mathbf{x}}(t) = \mathbf{f}\Big(\mathbf{x}(t), \mathbf{u}(t),\ \ \mathbf{C}_F^T\big(\mathbf{x}(t), \mathbf{u}(t)\big),\ \ \mathbf{C}_M^T\big(\mathbf{x}(t), \mathbf{u}(t)\big)\Big) \tag{4–42}$$

In the absence of inequality constraints, the Hamiltonian can be formed as equation (4–43).

$$H = L + \boldsymbol{\lambda}^T \mathbf{f}\Big(\mathbf{x}(t), \mathbf{u}(t),\ \ \mathbf{C}_F^T\big(\mathbf{x}(t), \mathbf{u}(t)\big),\ \ \mathbf{C}_M^T\big(\mathbf{x}(t), \mathbf{u}(t)\big)\Big) \tag{4–43}$$

Applying the optimality conditions from Section 4.2.1 gives the costate differential equation and the necessary condition for unconstrained optimal control.

$$\dot{\boldsymbol{\lambda}} = -\frac{\partial H}{\partial \mathbf{x}} = -\left[\frac{\partial L}{\partial \mathbf{x}} + \boldsymbol{\lambda}^T\left(\frac{\partial \mathbf{f}(\mathbf{x},\mathbf{u})}{\partial \mathbf{x}} + \frac{\partial \mathbf{f}(\mathbf{x},\mathbf{u})}{\partial \mathbf{C}_F}\frac{\partial \mathbf{C}_F}{\partial \mathbf{x}} + \frac{\partial \mathbf{f}(\mathbf{x},\mathbf{u})}{\partial \mathbf{C}_M}\frac{\partial \mathbf{C}_M}{\partial \mathbf{x}}\right)\right] \tag{4–44}$$

$$\frac{\partial H}{\partial \mathbf{u}} = \left[\frac{\partial L}{\partial \mathbf{u}} + \boldsymbol{\lambda}^T\left(\frac{\partial \mathbf{f}(\mathbf{x},\mathbf{u})}{\partial \mathbf{u}} + \frac{\partial \mathbf{f}(\mathbf{x},\mathbf{u})}{\partial \mathbf{C}_F}\frac{\partial \mathbf{C}_F}{\partial \mathbf{u}} + \frac{\partial \mathbf{f}(\mathbf{x},\mathbf{u})}{\partial \mathbf{C}_M}\frac{\partial \mathbf{C}_M}{\partial \mathbf{u}}\right)\right] = \mathbf{0} \tag{4–45}$$

Several of the derivatives in Equations (4–44) and (4–45) can be evaluated analytically using only the equations of motion without reference to the particular functional form of the aerodynamic coefficients. The first term inside the parentheses in each of equations (4–44) and (4–45) are Jacobian matrices similar to the canonical form of the state space representation for linear control theory.

$$\hat{A} := \frac{\partial \mathbf{f}(\mathbf{x},\mathbf{u})}{\partial \mathbf{x}} \in \mathbb{R}^{n\times n} \tag{4–46}$$

$$\hat{B} := \frac{\partial \mathbf{f}(\mathbf{x},\mathbf{u})}{\partial \mathbf{u}} \in \mathbb{R}^{n\times m} \tag{4–47}$$

Similarly, the derivatives of $\mathbf{f}(\mathbf{x}, \mathbf{u})$ with respect to the force and moment coefficients can be analytically determined as Jacobian matrices from the equations of motion.

$$\Gamma_{C_F} := \frac{\partial \mathbf{f}(\mathbf{x}, \mathbf{u})}{\partial \mathbf{C}_F} \in \mathbb{R}^{n \times N_F} \tag{4–48}$$

$$\Gamma_{C_M} := \frac{\partial \mathbf{f}(\mathbf{x}, \mathbf{u})}{\partial \mathbf{C}_M} \in \mathbb{R}^{n \times N_M} \tag{4–49}$$

The remaining four derivatives within the parentheses of Equations (4–44) and (4–45) can be recognized as the aerodynamic derivatives (Equations (4–50) and (4–51)) and control derivatives (Equations (4–52) and (4–53)), respectively.

$$C_{F_x} := \frac{\partial \mathbf{C}_F}{\partial \mathbf{x}} \in \mathbb{R}^{N_F \times n} \tag{4–50}$$

$$C_{M_x} := \frac{\partial \mathbf{C}_M}{\partial \mathbf{x}} \in \mathbb{R}^{N_M \times n} \tag{4–51}$$

$$C_{F_u} := \frac{\partial \mathbf{C}_F}{\partial \mathbf{u}} \in \mathbb{R}^{N_F \times m} \tag{4–52}$$

$$C_{M_u} := \frac{\partial \mathbf{C}_M}{\partial \mathbf{u}} \in \mathbb{R}^{N_M \times m} \tag{4–53}$$

These matrices may be determined analytically when the functional form of the aerodynamic dependencies on the state and control are known, usually as a result of system identification. Alternatively, these matrices may be evaluated numerically from tabulated values using finite differencing or an alternative numerical differentiation technique.

Using the notation above, the differential-algebraic equations describing the 1st order necessary conditions for an optimal store separation trajectory are given as follows.

$$\dot{\mathbf{x}}(t) = \mathbf{f}\left(\mathbf{x}(t), \mathbf{u}(t),\ \mathbf{C}_F\left(\mathbf{x}(t), \mathbf{u}(t)\right),\ \mathbf{C}_M\left(\mathbf{x}(t), \mathbf{u}(t)\right)\right) \tag{4–54}$$

$$\dot{\boldsymbol{\lambda}}(t) = -\left[\mathbf{L}_x + \boldsymbol{\lambda}^T\left(\hat{A}(t) + \Gamma_{C_F}(t) C_{F_x}(t) + \Gamma_{C_M}(t) C_{M_x}(t)\right)\right] \tag{4–55}$$

$$\frac{\partial H}{\partial \mathbf{u}} = \left[\mathbf{L}_u + \boldsymbol{\lambda}^T\left(\hat{B}(t) + \Gamma_{C_F}(t) C_{F_u}(t) + \Gamma_{C_M}(t) C_{M_u}(t)\right)\right] = \mathbf{0} \tag{4–56}$$

The quadratic cost functional introduces in Section 4.2.4 provides a flexible and intuitive starting point for many optimal control problems. The matrices P, Q, and R can be selected to drive the system to a specified end-state without expending too much control effort. For the purpose of store separation, it is desirable to minimize certain components of the end-state (for example, $\alpha(t_f)$ and $q(t_f)$) as well as certain components of the derivative of the end-state (for example, $\dot{\alpha}(t_f)$ and $\dot{q}(t_f)$). The quadratic cost function can be used to achieve this through careful selection of the state and control weighting factors. In this research, the scalar weighting factors corresponding to diagonal entries of P, Q, and R are denoted Q_α, P_q, R_{δ_e}, etc. Off-diagonal scalar weighting factors are not used herein.

$$J = \mathbf{x}^T(t_f)P\mathbf{x}(t_f) + \frac{1}{2}\int_{t_0}^{t_f}\left(\mathbf{x}^T Q\mathbf{x} + \mathbf{u}^T R\mathbf{u}\right)dt \tag{4–57}$$

Using the quadratic cost functional, the 1st order optimality conditions can be simplified even further and the optimal control can be determined explicitly. Note that the matrix R^{-1} is guaranteed to exist since R is positive definite.

$$\dot{\mathbf{x}}(t) = \mathbf{f}\left(\mathbf{x}(t), \mathbf{u}(t), \ \mathbf{C}_F\left(\mathbf{x}(t), \mathbf{u}(t)\right), \ \mathbf{C}_M\left(\mathbf{x}(t), \mathbf{u}(t)\right)\right) \tag{4–58}$$

$$\dot{\boldsymbol{\lambda}}(t) = -\left[Q\mathbf{x} + \boldsymbol{\lambda}^T\left(\hat{A}(t) + \Gamma_{C_F}(t)C_{F_x}(t) + \Gamma_{C_M}(t)C_{M_x}(t)\right)\right] \tag{4–59}$$

$$\mathbf{u}(t) = -R^{-1}\boldsymbol{\lambda}^T\left(\hat{B}(t) + \Gamma_{C_F}(t)C_{F_u}(t) + \Gamma_{C_M}(t)C_{M_u}(t)\right) \tag{4–60}$$

The initial conditions are specified by $\mathbf{x}(t_0) = \mathbf{x}_0$. The $2n$ boundary conditions are completed using the costate terminal values for the 1st order optimality conditions given by equation (4–17). In the absence of terminal constraints, the costate terminal conditions reduce to Equation (4–61).

$$\boldsymbol{\lambda}(t_f) = P\mathbf{x}(t_f) \tag{4–61}$$

Equations (4–58) through (4–61) represent a set of $2n$ nonlinear, coupled, algebraic-differential equations with split boundary conditions. Provided a solution can be found, the solution to this set of equations provides an extremal trajectory subject to the specified constraints and cost functional. The extremal trajectory is a candidate optimal trajectory, and may be shown to be at least locally optimal using the second variation of the cost functional, developed in Chapter 5.

4.3.3 Example: Planar Store Separation

Store separation is most often dominated by vertical translation and pitch attitude. In most cases, lateral translation and yaw attitude are fairly benign and of secondary interest. For instructive purposes, consideration of a store confined to the vertical $x - z$ plane during separation maintains the primary scope of interest and considerably reduces the complexity of the optimal control problem.

4.3.3.1 Model equations

For this simplified problem statement, the state space equations of motion, in mixed wind and body axes are given as equation (4–62).

$$\begin{bmatrix} \dot{V} \\ \dot{\alpha} \\ \dot{q} \\ \dot{\theta} \\ \dot{z} \end{bmatrix} = \begin{bmatrix} -D/m - g\sin\gamma \\ q - L/mV + g/V\cos\gamma \\ M/I_{yy} \\ q \\ -V\sin\gamma \end{bmatrix} \tag{4–62}$$

The components of the state, V(t), $\alpha(t)$, q(t), $\theta(t)$ and z(t), are the air-relative velocity, angle of attack, pitch rate, pitch angle, and vertical position, respectively. The flight path angle is given by $\gamma(t) = \theta(t) - \alpha(t)$ and the local acceleration of gravity is denoted by g. The variables L, D, and M represent the dimensional lift, drag, and pitching moment, respectively. Finally, I_{yy} is the pitch-axis moment of inertia and m is the

mass of the store. The analytical Jacobian matrices are evaluated directly, resulting in equations (4–63) through (4–66).

$$\frac{\partial \mathbf{f}(\mathbf{x},\mathbf{u})}{\partial \mathbf{x}} := \hat{A} = \begin{bmatrix} 0 & g\cos\gamma & 0 & -g\cos\gamma & 0 \\ q_\infty S C_L/mV^2 - g\cos\gamma/V^2 & g\sin\gamma/V & 1 & -g\sin\gamma/V & 0 \\ 0 & 0 & 0 & 0 & 0 \\ 0 & 0 & 1 & 0 & 0 \\ -\sin\gamma & V\cos\gamma & 0 & -V\cos\gamma & 0 \end{bmatrix} \tag{4–63}$$

$$\frac{\partial \mathbf{f}(\mathbf{x},\mathbf{u})}{\partial \mathbf{u}} := \hat{B} = \mathbf{0} \tag{4–64}$$

$$\frac{\partial \mathbf{f}(\mathbf{x},\mathbf{u})}{\partial \mathbf{C}_F} := \Gamma_{C_F} = \begin{bmatrix} 0 & -Sq_\infty/m \\ -Sq_\infty/mV & 0 \\ 0 & 0 \\ 0 & 0 \\ 0 & 0 \end{bmatrix} \tag{4–65}$$

$$\frac{\partial \mathbf{f}(\mathbf{x},\mathbf{u})}{\partial \mathbf{C}_M} := \Gamma_{C_M} = \begin{bmatrix} 0 \\ 0 \\ q_\infty S\,\bar{c}/I_{yy} \\ 0 \\ 0 \end{bmatrix} \tag{4–66}$$

4.3.3.2 Aerodynamic model

To proceed further, it is necessary to specify an explicit aerodynamic model for the store during separation; a simplistic spatially variant model based on wind tunnel data is chosen for illustration. A more complex multivariate nonlinear model could also be used within the framework presented here, at the expense of significantly more complex mathematical expressions. For planar store separation, the dominant effect of the

nonuniform flow field is on the pitching moment. As such, consider the following spatially variant quasi-linear aerodynamic model.

$$C_L = C_{L_\alpha}\alpha + C_{L_{\delta_e}}\delta_e \tag{4–67}$$

$$C_D = C_{D_0} + KC_L^2 + C_{D_{\delta_e}}\delta_e \tag{4–68}$$

$$C_m = C_{m_\alpha}\alpha + C_{m_q}\hat{q} + C_{m_{\delta_e}}\delta_e + e^{-(\mu z)}\left(\eta_0 + \eta_1 z\right) \tag{4–69}$$

The variable δ_e represents the elevator control surface deflection, the only input of interest for dynamics limited to the $x - z$ plane. The variable $\hat{q}$ is the non-dimensional pitch rate introduced for unit consistency. The variables C_{L_α}, C_{D_0}, C_{m_α}, and C_{m_q} represent the classical aerodynamic derivatives. The variables $C_{L_{\delta_e}}$, $C_{D_{\delta_e}}$, and $C_{m_{\delta_e}}$ represent the classical control derivatives. For the current example, the aerodynamic and control derivatives are constant and estimated using freestream wind tunnel data. The term $e^{-(\mu z)}\left(\eta_0 + \eta_1 z\right)$ is the only spatially variant contribution to the aerodynamic model. The exponential-polynomial form is seen as a special case of the more general parametric model presented in Chapter 3. The constants μ, η_0, and η_1 were estimated using a nonlinear least squares curve fit of representative wind tunnel data at a nominal pitch attitude. For this particular example, the values of the constants are provided in Table (4-1).

Table 4-1. Aerodynamic derivatives, control derivatives, and spatially variant parameters used in planar store separation aerodynamic model.

Aerodynamic Derivatives	Control Derivatives	Spatially Variant Parameters
$C_{L_\alpha} = 3.81$ rad^{-1}	$C_{M_{\delta_e}} = -8.24$ rad^{-1}	$\mu = 0.158$
$C_{M_\alpha} = -2.11$ rad^{-1}	$C_{L_{\delta_e}} = 2.21$ rad^{-1}	$\eta_0 = -0.953$
$C_{M_q} = -74$ rad^{-1}	$C_{D_{\delta_e}} = -0.22$ rad^{-1}	$\eta_1 = 0.064$ ft^{-1}
$C_{D_0} = 0.201$		
$K = 0.1856$		

4.3.3.3 Optimality conditions

Using the simplified aerodynamic model in Equations (4–67) through (4–69), the Jacobian matrices for the aerodynamic and control derivatives can be determined.

$$C_{F_x} = \begin{bmatrix} 0 & C_{L_\alpha} & 0 & 0 & 0 \\ 0 & 2KC_{L_\alpha}^2\alpha(t) & 0 & 0 & 0 \end{bmatrix} \tag{4–70}$$

$$C_{M_x} = \begin{bmatrix} 0 & C_{m_\alpha} & C_{m_q} & 0 & e^{-(\mu z)}\left(-\mu\left(\eta_0 + \eta_1 z\right) + \eta_1\right) \end{bmatrix} \tag{4–71}$$

$$C_{F_u} = \begin{bmatrix} C_{L_{\delta_e}} \\ C_{D_{\delta_e}} \end{bmatrix} \tag{4–72}$$

$$C_{M_u} = \begin{bmatrix} C_{m_{\delta_e}} \end{bmatrix} \tag{4–73}$$

As a result, the optimal control is given in terms of the costates and control derivatives, as shown in Equation (4–74).

$$u(t) = \delta_e(t) = -R^{-1}\left[\lambda_q(C_{m_{\delta_e}} q_\infty S\,\bar{c})/Iyy - \lambda_\alpha(C_{L_{\delta_e}} q_\infty S\,)/mV - \lambda_V(C_{D_{\delta_e}} q_\infty S)/m\right] \tag{4–74}$$

Equation (4–74) can be seen as a particular case of the optimal control for a linear time variant system: $u(t) = \delta_e(t) = -R^{-1}B(t)^T\boldsymbol{\lambda}(t)$. However, the nonlinear dynamics in the present case leads to a nonlinear relationship between the states and costates, so an optimal feedback control law is not forthcoming. It is assumed that the initial conditions are known, $\mathbf{x}(t_0) = \mathbf{x}_0$. For planar store separation, it is desirable to minimize the total angle of attack $\alpha(t)$ and the terminal conditions $\alpha(t_f)$ and $q(t_f)$. This is readily accomplished using the scalar values P_α, P_q, Q_α, and R_{δ_e}.

4.3.3.4 Results

Figure 4-2A shows an extremal trajectory for a particular set of initial conditions. The weighting factors were chosen to be $P_\alpha = P_q = Q_\alpha = 1$ and $R_{\delta_e} = 10$ with all other factors set to zero. The initial conditions are given in equation (4–75), corresponding to a

standard day release at Mach number of 0.8 and altitude of 10kft.

$$\mathbf{x}(t_0) := \begin{bmatrix} V = 861 ft/sec & \alpha = 5 deg & q = -50 deg/sec & \theta = 0 deg & z = 0 ft \end{bmatrix}^T \quad (4\text{–}75)$$

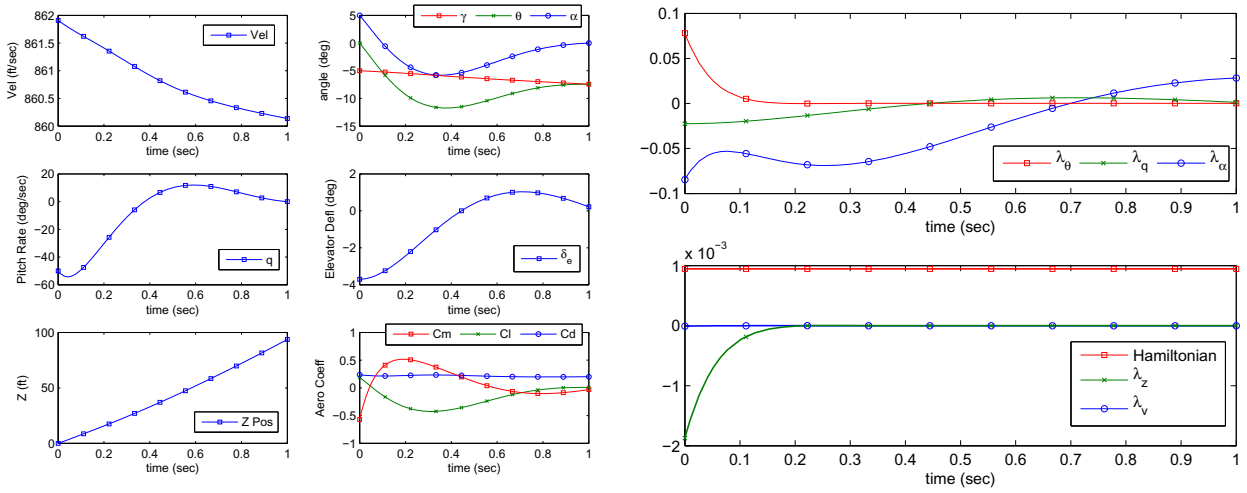

A Optimal Trajectory

B Hamiltonian and Costate

Figure 4-2. An extremal trajectory for planar store separation with weighting factors selected to minimize angle of attack.

The results shown in Figure 4-2A are representative of an ideal store separation trajectory. The initial pitch rate is nose-down, consistent with a desirable pitch rate imposed by the ejection forces. The initial angle of attack, $\alpha(0)$, is 5 deg, consistent with a large downward velocity and level attitude imposed by the ejection. The optimal control first drives the store pitch rate more negative, simultaneously bringing $\alpha(t)$ negative, and then gently begins a slightly underdamped pitch rate oscillation, driving $\alpha(t)$ and $q(t)$ to zero at the $t_f = 1$. The level slope of the $\alpha(t)$ and $q(t)$ curves further indicate that the derivatives $\dot{\alpha}(t_f)$ and $\dot{q}(t_f)$ are also near zero, consistent with the desired performance. The store exhibits benign motion throughout the trajectory and is in a near-equilibrium state at the transitional final time, $t_f = 1$.

The Hamiltonian and costate variables are shown in Figure 4-2B. The Hamiltonian is constant as expected for an extremal trajectory. The costate variables $\lambda_\alpha(t)$ and $\lambda_q(t)$

show the most significant variation. This variation is directly related to the dependence of the aerodynamic model on $\alpha(t)$ and $q(t)$, as well as the inclusion of $\alpha(t)$ and $q(t)$ in the cost functional.

Consider the costate variables $\lambda_z(t)$ and $\lambda_V(t)$. The norm $\|\lambda_V\| = 3.416E^{-5}$ is nearly zero and essentially constant throughout the trajectory, indicating a negligible sensitivity of the cost functional to changes in velocity. This is primarily due to the functional form of the aerodynamic model, which does not include any explicit dependence on $V(t)$ (the dependence is built-in to the wind tunnel data used in estimating the aerodynamic coefficients). The costate $\lambda_V(t)$ rapidly approaches zero and is essentially negligible after 200 msec. This indicates that the cost functional is only sensitive to the vertical location $z(t)$ early in the trajectory, nearest the aircraft. This conclusion is consistent with physical intuition and the exponential decay of the aerodynamic model.

The previous extremal trajectory was determined with the accumulated (Lagragian) cost on the angle of attack set to one, $Q_\alpha = 1$, with zero penalty for the pitch rate, $Q_q = 0$. As an alternative, consider the case where $Q_\alpha = 0$ and $Q_q = 1$, placing the emphasis on minimizing the pitch rate throughout the trajectory. The terminal cost $P_\alpha = P_q = 0$ remain unchanged. The resulting extremal trajectory is shown in Figure 4-3A and the Hamiltonian and costate variables are shown in Figure 4-3B.

In comparison with the trajectory shown in Figure 4-2A, it is clear that the pitch rate is reduced rapidly and converges to a constant value for the duration between 300msec and 900msec, striking a balance between the minimum pitch rate and the minimum control input. The rapid decrease in the pitch rate comes as the expense of control effort, marginally exceeding the linear operating range of the control model. Also note that the angle of attack remains slightly positive throughout the trajectory, another adverse characteristic. As such, the preferred design choice for this particular example is to omit the penalty on pitch rate and place the emphasis on the angle of attack and control effort. The resulting negative increase in pitch rate (see Figure 4-2A) is actually

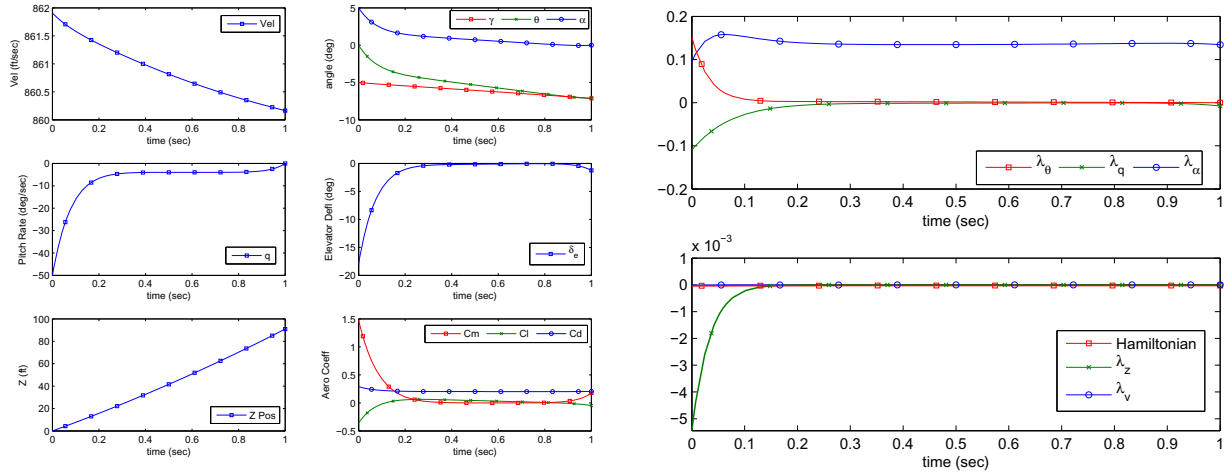

A Optimal Trajectory

B Hamiltonian and Costate

Figure 4-3. An extremal trajectory for planar store separation with weighting factors selected to minimize pitch rate.

advantageous from a safe separation perspective, and well beneath the angular rate limits required for an acceptable separation.

Each solution to the Hamiltonian BVP is dependent on the specified initial conditions, $\mathbf{x}(t_0) = \mathbf{x}_0$. As such, it is worthwhile to consider how changes in initial conditions affect changes in the extremal trajectory. Figure 4-4 shows a series of neighboring trajectories for a range of initial pitch rates from 0 deg/sec to -150 deg/sec in 50 deg/sec increments. The remaining initial conditions are held constant at the values prescribed in equation (4–75). The weighting factors are restored to the original values, $P_\alpha = P_q = Q_\alpha = 1$ and $R_{\delta_e} = 10$ with all other factors set to zero.

All of the trajectories in Figure 4-4 exhibit a similar trend. From a store separation perspective, a larger nose-down pitch rate is desirable since it drives the angle of attack more negative, resulting in increased safety with adequate acceptability margins. However, an overly aggressive negative initial pitch rate ($q < -150\,\mathrm{deg}/\mathrm{sec}$) results in an unacceptable trajectory, due to large elevator control deflection ($\delta_e = -10\,\mathrm{deg}$) and excessive angle of attack ($\alpha < -15\,\mathrm{deg}$), exceeding the linear range of the aerodynamic

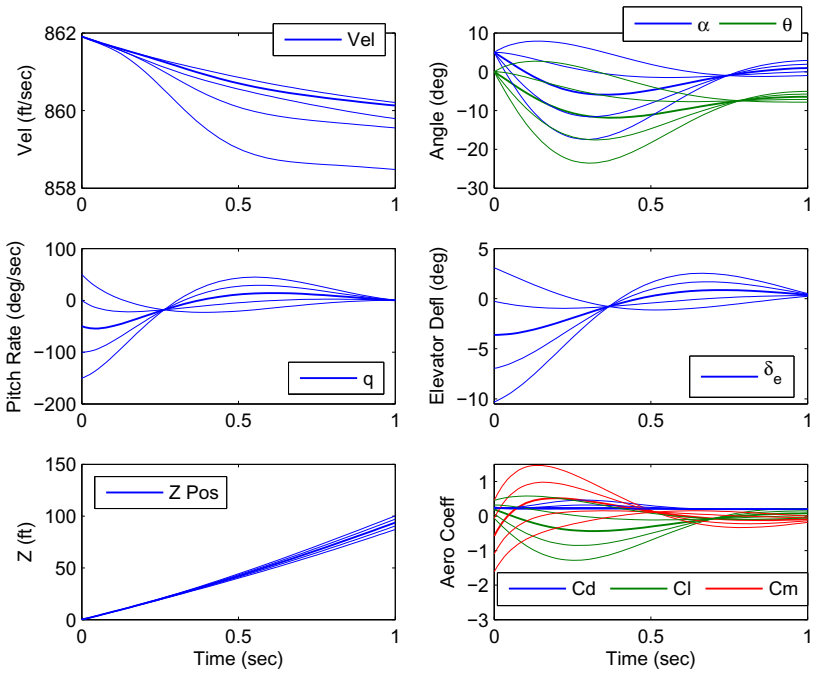

Figure 4-4. Series of neighboring extremal trajectories for varied initial pitch rates.

model. A pitch rate in the neighborhood of $-50 > q > -100\,\text{deg}/\text{sec}$ is the preferred range of initial pitch rate for this particular example.

Changes in the initial angle of attack also have a significant effect on the extremal trajectory. A series of neighboring extremal trajectories are shown in Figure 4-5, using a range of values for the initial angle of attack, $0 \leq \alpha(0) \leq 5\ \text{deg}$. The remaining initial conditions are the same as equation (4–75).

Note that the initial pitch angle is zero in all cases, $\theta(0) = 0\,\text{deg}$. Bering in mind that the initial pitch angle is fixed by the aircraft hardware at carriage, the initial angle of attack is not manipulated by reorienting the store, but by ejecting the store with increasing values of downward velocity. An initial $\alpha(0) = 0\,\text{deg}$ is equivalent to a gravity-release, i.e. zero ejection velocity. An initial $\alpha(0) = 5\,\text{deg}$ is equivalent to a large ejection velocity of $75 ft/\text{sec}$ (for the selected flight condition with $V = 861 ft/\text{sec}$). Note that a negative initial $\alpha(0) < 0$ for $\theta(0) = 0\,\text{deg}$ is impossible since it would physically require an initial vertical velocity in the upward direction, interfering with the aircraft

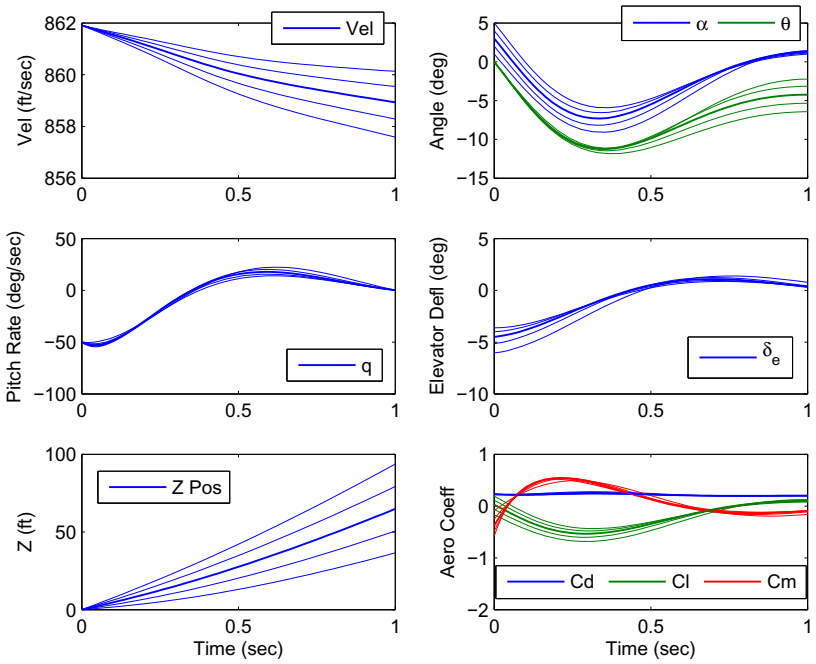

Figure 4-5. Series of neighboring optimal trajectories for varied initial angle of attack.

hardware. As a result of the varying $\alpha(0)$, the vertical translation curves in Figure 4-5 show a wide range of values. From a safety perspective, it is clearly desirable to move the store away from the aircraft as quickly as possible, indicating that a large initial $\alpha(0)$, is preferable (equivalent to a large vertical ejection velocity). However, the dramatic increase in vertical translation for large $\alpha(0)$, also results in a significant potential energy loss. For a store with a long-range mission, this may be unacceptable. The preferred initial angle of attack for this problem is in the range of $1 > \alpha(0) > 2\,\text{deg}$, equivalent to a quite realistic ejection velocity of $15 - 30 ft/\,\text{sec}$.

The preceding discussion demonstrates that there exists a range of initial conditions over which a candidate optimal trajectory can be found that satisfies safety and acceptability criteria. Knowledge of the preferred range of initial conditions can be used to specify ejector performance criteria. However, the exact initial conditions cannot be determined a priori and the optimal control clearly requires adjustment based on the initial conditions. This difficulty leads to the importance of considering a

feedback controller to account for the variations in the initial conditions as well as model inaccuracies and unmodeled disturbances. Neighboring optimal control provides the framework for implementing such a controller. This discussion will be continued in the Chapter 5 with the introduction of neighboring optimal control.

4.4 Chapter Summary

The purpose of this research is to investigate a store separation guidance and control system which explicitly accounts for the spatially variant aerodynamics of the store during separation and leverages the aerodynamic interaction between the store and aircraft to improve separation characteristics. This objective is accomplished, in part, using optimal control to determine a "best case" trajectory.

A candidate optimal trajectory for store separation is determined by solving a Hamiltonian boundary value problem, as specified by the 1st order optimality conditions in optimal control. The general optimality conditions are applied to a store during separation and the 1st order necessary conditions for optimal store separation are derived. A simplified example, namely planar store separation with a spatially-variant aerodynamic model, is considered to illustrate the use of these methods. The "open-loop" candidate optimal trajectory is a suitable starting point for consideration of "closed-loop" feedback using neighboring optimal control. This discussion is taken up in Chapter 5.

CHAPTER 5
NEIGHBORING OPTIMAL CONTROL

5.1 Overview

Previous studies have highlighted the use of active control to improve separation characteristics, primarily as a side benefit of demonstrating the use of a new CFD capability. The most significant documented contribution to controlled store separation comes from R.H. Nichols and A.G. Denny (Arnold Engineering Development Center) [5]. The authors present a case study for the numerical simulation of a non-thrusted ejector launched AIM-120C Advanced Medium Range Air-to-Air Missile (AMRAAM) in controlled separation from a wing station of the F-15E Strike Eagle. The results indicate a significant improvement of the separation characteristics with an active autopilot during separation.

C. A. Atwood (NASA Ames Research Center) made another notable contribution to controlled store separation [6]. Atwood demonstrated a CFD simulation of a canard-controlled store released from an open flow rectangular cavity at supersonic freestream conditions. Again, the simulation showed significant improvements in the separation characteristics using a basic pitch attitude controller, in comparison to the canard-fixed store.

In both of these studies, the emphasis was on demonstrating controlled separation with a high fidelity CFD simulation. As such, the investigation of the autopilot itself was limited. Remarkably, literature on investigation of a control system designed specifically for the nonuniform flow field encountered by a store during separation is void.

This research is focused on the development of a transitional guidance and control system, designed with the separation-induced transients in mind, to achieve the best case trajectory for a variety of flight conditions and configurations. In particular, the objective is to improve the separation characteristics of ejector-launched guided munitions using a separation autopilot to achieve an optimal trajectory with respect

to specified safety and acceptability performance metrics. The open-loop optimal trajectory is determined using classical optimal control theory, as shown in Chapter 4. Closed-loop feedback control is accomplished using neighboring optimal control, as developed here.

5.2 Neighboring Optimal Control

The first order optimality conditions discussed in Section 4.2.1 provide the necessary conditions for an extremal trajectory. The control is determined based on solution of the two point Hamiltonian boundary value problem and implicitly assumes perfect knowledge of the system operating in a disturbance-free environment. However, deterministic disturbances or variations in the initial conditions, terminal conditions, and system parameters alter the optimal state and control history, requiring computation of unique solution for each variation. Stated another way, the optimal control strategy is "open-loop", meaning the control is specified a priori and fixed regardless of perturbations that may affect the system during operation. In contrast, a "closed-loop" control law is more desirable as it accounts for variations in initial conditions and disturbances along the optimal path. Neighboring optimal control (NOC) provides a powerful approach for implementing feedback control along an optimal path by considering linear perturbations along the extremal solution. NOC relies on a locally linearized dynamic model in conjunction with a quadratic cost functional derived from the second variation of the original cost functional. The neighboring optimal solution is then approximated as the sum of the original optimal trajectory plus the linear-optimal solution [116].

Neighboring optimal control was first introduced in the early 1960's by Kelly [127] and Breakwell, Speyer and Bryson [128]. These early contributions were stated informally as an extension to the accessory minimum problem (AMP) and immediately gained traction as a convenient approach for implementing optimal control for a real world system [129] as well as a viable numerical method for solving open-loop optimal

control problems [128, 130]. Significant contributions to NOC in the presence of path and equality constraints were made by Jacobson [131], Lee [132], Pesch [133, 134], Hymas [135] and Fisher [136]. Similar contributions for NOC in the presence of parameter variations were provided by Lee [137], D'Souza [138], and Hull [139, 140]. Applications of NOC in the aerospace community include advanced launch systems [141], space shuttle guidance [134], hypersonic vehicle descent [142], flight vehicle guidance [143], and missile guidance against a maneuvering target [144], to name a few. Conventional nonlinear trajectory optimization problems require substantial computational resources to find an extremal solution, which typically prohibits a real-time implementation of optimal control. However, NOC is easily implemented and may be used to provide real-time optimal control in the presence of small disturbances [145–147]. Several applications for aircraft flight through nonlinear spatially-varying flow fields developed by Jardin and Bryson are also of particular interest due to conceptual similarity to guidance and control of a store during separation [148–150].

Current research trends in NOC include improvements in working with path and control constraints [145, 151], robust analysis for control of systems with uncertainties [152–154], implementation of real-time optimal control [146], and application to increasingly complex real world systems including air transportation management [103, 104, 147, 155], reusable launch vehicles [152, 154], and flight through adverse flowfield conditions [156]. In this context, store separation guidance and control is a challenging application of established principles in NOC. Additionally, the concept of infinite horizon neighboring optimal control (IHNOC) is introduced here to demonstrate how NOC can be constructed to provide continuation of the optimal control beyond the original open-loop finite-horizon solution.

5.2.1 Second Order Optimality Conditions

Consider the Bolza problem introduced in Section 4.2.1 with a cost functional given by Equation (5–1), dynamic constraints given by Equation (5–2), path and control

inequality constraints given by (5–3), and terminal constraints given by Equation (5–4), where it is assumed that the initial conditions, $\mathbf{x}(t_0)$, and final time, t_f, are specified.

$$J = \phi\big(\mathbf{x}(t_f)\big) + \int_{t_0}^{t_f} L\big(\mathbf{x}(t), \mathbf{u}(t)\big)\, dt \tag{5–1}$$

$$\dot{\mathbf{x}}(t) = \mathbf{f}\big(\mathbf{x}(t), \mathbf{u}(t)\big) \tag{5–2}$$

$$\mathbf{C}\big(\mathbf{x}(t), \mathbf{u}(t)\big) \leq 0 \tag{5–3}$$

$$\boldsymbol{\psi}\big(\mathbf{x}(t_f)\big) = 0 \tag{5–4}$$

The corresponding 1st order necessary conditions are determined by taking the first variation of the augmented cost functional with respect to each free variable, resulting in the Euler-Lagrange equations and transversality conditions. The Euler-Lagrange equations are given by Equations (5–5) and (5–6), and the transversality condition is given by Equation (5–7), where $H = L + \boldsymbol{\lambda}^T \mathbf{f}$ is the Hamiltonian.

$$\dot{\boldsymbol{\lambda}}^T = -\frac{\partial H}{\partial \mathbf{x}} \tag{5–5}$$

$$\mathbf{0} = \frac{\partial H}{\partial \mathbf{u}} \tag{5–6}$$

$$\boldsymbol{\lambda}^T(t_f) = \frac{\partial \phi}{\partial \mathbf{x}(t_f)} - \boldsymbol{\nu}^T \frac{\partial \boldsymbol{\psi}}{\partial \mathbf{x}(t_f)} \tag{5–7}$$

The state $\mathbf{x}(t)$ and costate $\boldsymbol{\lambda}(t)$ form a Hamiltonian system with split boundary conditions given by $\mathbf{x}(t_0)$ and $\boldsymbol{\lambda}(t_f)$, resulting in a two-point Hamiltonian boundary value problem (HBVP). The solution to the HBVP, denoted $(\mathbf{x}^*(t), \mathbf{u}^*(t))$, represents an extremal trajectory with open-loop control of the type encountered in Chapter 4.

Now, consider a small variation in the initial conditions given by $\delta\mathbf{x}(t_0)$. It is intuitive to expect that the extremal trajectory will also vary slightly by the amount $\delta\mathbf{x}(t)$. With the perturbed trajectory, the cost functional can be approximated to second order by Equation (5–8). It is noted that in order to satisfy the first order necessary conditions, the first variation in the cost functional is zero along the optimal path, $\delta J = 0$. This term is

consequently ommitted from Equation (5–8).

$$J\left[\mathbf{x}^*(t)+\delta\mathbf{x}(t)\right]=J\left[\mathbf{x}^*(t)\right]+\delta^2 J\left[\delta\mathbf{x}(t)\right] \tag{5–8}$$

From Equation (5–8) it is apparent that in order to minimize the original cost function along the perturbed trajectory, it is necessary to minimize $\delta^2 J$. The second variation of the augmented cost functional is obtained by expanding the original cost functional to second order and the constraints to first order, eliminating terms which are necessarily zero along the extremal trajectory [113]. The result is given by Equation (5–9), where the subscript notation indicates partial differentiation.

$$\begin{aligned}\delta^2 J_a = &\frac{1}{2}\left[\delta\mathbf{x}^T\left(\phi_{xx}+\left(\boldsymbol{\nu}^T\boldsymbol{\psi}_x\right)_x\right)\delta\mathbf{x}\right]_{t=t_f}+\\ &\frac{1}{2}\int_{t_0}^{t_f}\begin{bmatrix}\delta\mathbf{x}^T & \delta\boldsymbol{\lambda}^T\end{bmatrix}\begin{bmatrix}H_{xx} & H_{xu}\\ H_{ux} & H_{uu}\end{bmatrix}\begin{bmatrix}\delta\mathbf{x}\\ \delta\boldsymbol{\lambda}\end{bmatrix}dt\end{aligned} \tag{5–9}$$

Thus, the objective is to find a control variation $\delta\mathbf{u}(t)$, corresponding to variations in the state $\delta\mathbf{x}(t)$ and costate $\delta\boldsymbol{\lambda}(t)$, which minimizes the second variation of the cost functional. This minimization problem can be further constructed by linearizing the 1st order necessary conditions along the extremal trajectory, as shown in Equation (5–10) through (5–14).

$$\delta\dot{\mathbf{x}}(t)=\mathbf{f}_x\delta\mathbf{x}+\mathbf{f}_u\delta\mathbf{u} \tag{5–10}$$

$$\delta\dot{\boldsymbol{\lambda}}(t)=-H_{xx}\delta\mathbf{x}-\mathbf{f}_x^T\delta\boldsymbol{\lambda}-H_{xu}\delta\mathbf{u} \tag{5–11}$$

$$0=H_{ux}\delta\mathbf{x}+\mathbf{f}_u^T\delta\boldsymbol{\lambda}+H_{uu}\delta\mathbf{u} \tag{5–12}$$

$$\delta\boldsymbol{\lambda}^T(t_f)=\left[\left(\phi_{xx}+\left(\boldsymbol{\nu}^T\boldsymbol{\psi}_x\right)_x\right)\delta\mathbf{x}+\boldsymbol{\psi}_x^T\delta\boldsymbol{\nu}\right]_{t=t_f} \tag{5–13}$$

$$\delta\boldsymbol{\psi}=\left[\boldsymbol{\psi}_x\delta\mathbf{x}\right]_{t=t_f} \tag{5–14}$$

The variations $\delta\mathbf{x}$, $\delta\mathbf{u}$, and $\delta\boldsymbol{\lambda}$ are defined as perturbations along the optimal trajectory. In particular, $\delta\mathbf{x}=\mathbf{x}(t)-\mathbf{x}^*(t)$, $\delta\mathbf{u}=\mathbf{u}(t)-\mathbf{u}^*(t)$, and $\delta\boldsymbol{\lambda}=\boldsymbol{\lambda}(t)-\boldsymbol{\lambda}^*(t)$ are the variations in the state, control, and costate respectively.

Thus, for the neighboring optimal control problem, the objective is to minimize the cost functional given by Eq. (5–9) subject to the constraints given in Equations (5–10) through (5–14). Upon careful inspection, it becomes apparent that the problem statement is synonymous with the linear quadratic problem (LQP) considered in Section 4.2.4 and the established solution methodology can be applied directly to the NOC problem.

The optimal control problem statement and corresponding necessary conditions described in Equations (5–1) through (5–7) include both path/control inequality constraints and terminal constraints. To be considered an allowable trajectory, the NOC extremal trajectory must also satisfy these constraints. However, the presence of these constraints adds significant complexity to the mathematical explanation. Therefore, the NOC problem without path, control, or terminal constraints will be considered first in Section 5.2.2. Terminal constraints are considered in Section 5.2.3 and path/control inequality constraints are considered in Section 5.2.4.

It is noted that the NOC problem discussed thus far considers only perturbations in initial conditions. Since any point along the extremal path is a valid starting point, this development is directly applicable to disturbances along the extremal path. However, variations in the system parameters also result in perturbations of the extremal trajectory. The subject of NOC in the presence of parameter variations is addressed in Section 5.2.5.

Finally, it is important to note that the first order necessary conditions result in an extremal trajectory which may or may not be optimal. The second variation of the cost functional is analogous to the second derivative in calculus and can be used to establish sufficient conditions for optimality. This will be discussed in Section 5.2.6.

The theoretical development here has many practical applications. Application of NOC to store separation is considered in Section 5.3 with an extended example in Section 5.4. Application of NOC to a realistic case study is taken up in Chapter 6.

5.2.2 Neighboring Extremal

The 1st order necessary conditions for a neighboring extremal without terminal conditions are given by Equations (5–15) through (5–18).

$$\delta\dot{\mathbf{x}}(t) = \mathbf{f}_x\delta\mathbf{x} + \mathbf{f}_u\delta\mathbf{u} \tag{5–15}$$

$$\delta\dot{\boldsymbol{\lambda}}(t) = -H_{xx}\delta\mathbf{x} - \mathbf{f}_x^T\delta\boldsymbol{\lambda} - H_{xu}\delta\mathbf{u} \tag{5–16}$$

$$0 = H_{ux}\delta\mathbf{x} + \mathbf{f}_u^T\delta\boldsymbol{\lambda} + H_{uu}\delta\mathbf{u} \tag{5–17}$$

$$\delta\boldsymbol{\lambda}^T(t_f) = [\phi_{xx}\delta\mathbf{x}]_{t=t_f} \tag{5–18}$$

It should be noted that the end point cost $\phi(\mathbf{x}(t_f))$ is still present in the simplified problem so it is still possible to achieve an arbitrarily precise terminal condition when desired. The function $\phi(\mathbf{x}(t_f))$ is often referred to as a "soft" constraint, whereas $\psi(\mathbf{x}(t_f))$ is a "hard" constraint.

Equation (5–17) can be used to solve for the control variation explicitly provided that the matrix inverse H_{uu}^{-1} exists. The control variation is given by Equation (5–19).

$$\delta\mathbf{u} = -H_{uu}^{-1}\left(H_{ux}\delta\mathbf{x} + \mathbf{f}_u^T\delta\boldsymbol{\lambda}\right) \tag{5–19}$$

Note that when the Hamiltonian is linear in the control, the matrix $H_{uu} = 0$ and the inverse does not exist. In this case, the control must be determined using the minimum principle, often resulting in maximum control effort for the duration of the trajectory, a strategy referred to as "bang-bang" control [111, 114].

Substituting (5–19) into the differential equations (5–15) and (5–16) results in the linear system of equations (5–20) and (5–21), where the time-varying matrices $A(t)$, $B(t)$, and $C(t)$, given by Equations (5–22) through (5–24), are evaluated along the extremal path.

$$\delta\dot{\mathbf{x}} = A(t)\delta\mathbf{x} - B(t)\delta\boldsymbol{\lambda} \tag{5–20}$$

$$\delta\dot{\boldsymbol{\lambda}} = -C(t)\delta\mathbf{x} - A^T(t)\delta\boldsymbol{\lambda} \tag{5–21}$$

$$A(t) = \mathbf{f}_x - \mathbf{f}_u H_{uu}^{-1} H_{ux} \tag{5–22}$$

$$B(t) = \mathbf{f}_u H_{uu}^{-1} \mathbf{f}_u^T \tag{5–23}$$

$$C(t) = H_{xx} - H_{xu} H_{uu}^{-1} H_{ux} \tag{5–24}$$

The boundary condition $\delta\boldsymbol{\lambda}(t_f) = \phi_{xx}\delta\mathbf{x}$ from (5–19) suggests a particular form of perturbed costate as a linear combination of the perturbed state, as shown in Equation (5–25), with the corresponding boundary condition given by (5–26).

$$\delta\boldsymbol{\lambda}(t) = S(t)\delta\mathbf{x}(t) \tag{5–25}$$

$$S(t_f) = \phi_{xx} \tag{5–26}$$

Differentiation of (5–25) results in Equation (5–27). Substitution of (5–20) and (5–21) into (5–27) results in the differential Riccati Equation (5–28).

$$\delta\dot{\boldsymbol{\lambda}}(t) = \dot{S}(t)\delta\mathbf{x}(t) + S(t)\delta\dot{\mathbf{x}}(t) \tag{5–27}$$

$$\dot{S}(t) = -SA - A^T S + SBC - C \tag{5–28}$$

The Riccati equation, subject to the terminal condition (5–26), is stable in backward time and independent of the variations $\delta\mathbf{x}(t)$, $\delta\boldsymbol{\lambda}(t)$, and $\delta\mathbf{u}(t)$. As a result, once an extremal trajectory has been determined using the 1st order necessary conditions, the Riccati equation can be used to compute and store $S(t)$ along the extremal path.

Equation (5–25) can be used with $S(t)$ to eliminate the costate from the problem. Substitution of (5–25) into (5–19) provides the control variation $\delta\mathbf{u}(t)$.

$$\delta\mathbf{u} = -H_{uu}^{-1}\left(H_{ux} + \mathbf{f}_u^T S\right)\delta\mathbf{x} \tag{5–29}$$

Recalling the definition of the perturbed state and control, $\delta\mathbf{x} = \mathbf{x}(t) - \mathbf{x}^*(t)$ and $\delta\mathbf{u} = \mathbf{u}(t) - \mathbf{u}^*(t)$, where $\mathbf{x}^*(t)$ and $\mathbf{u}^*(t)$ represent the nominal extremal trajectory, Equation (5–29) can be expressed as (5–30) and (5–31).

$$\mathbf{u}(t) = \mathbf{u}^*(t) - K(t)\left(\mathbf{x}(t) - \mathbf{x}^*(t)\right) \tag{5–30}$$

$$K(t) = H_{uu}^{-1}\left(H_{ux} + \mathbf{f}_u^T S\right) \tag{5–31}$$

Equations (5–30) and (5–31) represent a Neighboring Optimal Feedback Law that can be used to correct for varying initial conditions or disturbances along the extremal path. The neighboring optimal control structure is shown graphically in Figure 5-1.

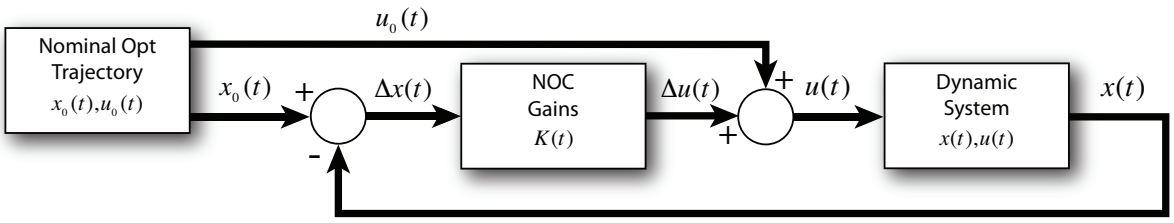

Figure 5-1. Neighboring Optimal Control block diagram.

Although the math is arduous, the final result is compact and easily implemented. The neighboring optimal control process is summarized as follows.

1. Using the 1st order optimality conditions, compute and store the nonlinear, open-loop, optimal trajectory for the given problem statement, $\mathbf{x}^*(t)$ and $\mathbf{u}^*(t)$.

2. Using the matrix Riccati equation, compute and store the feedback gains, $K(t)$ along the optimal path. If collocation is used, the Riccati equation can be solved commensurate with the open-loop optimal trajectory in step 1.

3. Using the stored matrix $K(t)$, the stored nominal optimal trajectory $\mathbf{x}^*(t)$ and $\mathbf{u}^*(t)$, and the estimates of the actual state $\mathbf{x}(t)$, determine the control $\mathbf{u}(t) = \mathbf{u}^*(t) + \delta\mathbf{u}$ during operation.

With the above synopsis, neighboring optimal control is seen to be a compact and efficient approach to implementing feedback control along an optimal path when deviations from the optimal path are expected to be small. Application of NOC to store separation is straightforward, resulting in a feedback control system which may be used to account for variations in initial conditions and flow field perturbations. Extension of the

neighboring optimal feedback law for prescribed terminal conditions, constrained control inputs, and parameter variations are discussed subsequently.

5.2.3 Neighboring Extremal with Terminal Constraints

The 1st order necessary conditions for an extremal trajectory with terminal constraints $\psi(\mathbf{x}(t_f)) = \mathbf{0}$ are given in Equations (5–10) through (5–14). The inclusion of terminal constraints affects the computation of a neighboring extremal in two primary ways including (1) modification of the boundary conditions for the Riccati equation and (2) modification of the feedback structure to include explicit dependence on the terminal conditions.

The boundary conditions on the variation of the costate and the variation of the terminal conditions are given in Equations (5–32) and (5–33). If the original terminal constraint $\psi(\mathbf{x}(t_f)) = \mathbf{0}$ is satisfied by the neighboring extremal, then $\delta\psi = \mathbf{0}$ as a consequence. However, in some cases it may be desirable to adjust the terminal constraints during operation. Therefore, $\delta\psi$ may be considered a user specified parameter and we seek a feedback control law with explicit dependence on the original terminal constraint and any specified perturbation $\delta\psi$.

$$\delta\boldsymbol{\lambda}^T(t_f) = \left[\left(\phi_{xx} + \left(\boldsymbol{\nu}^T\boldsymbol{\psi}_x\right)_x\right)\delta\mathbf{x} + \boldsymbol{\psi}_x^T\delta\boldsymbol{\nu}\right]_{t=t_f} \tag{5–32}$$

$$\delta\boldsymbol{\psi} = \left[\boldsymbol{\psi}_x\delta\mathbf{x}\right]_{t=t_f} \tag{5–33}$$

The boundary conditions in Equations (5–32) and (5–33) suggest a particular form for the variation in the costate $\delta\boldsymbol{\lambda}(t)$ and terminal conditions $\delta\boldsymbol{\psi}(t)$ as a linear combination of the variation in the state $\delta\mathbf{x}(t)$ and Lagrange multiplier $\delta\boldsymbol{\nu}$, as shown in Equations (5–34) and (5–35). The corresponding matrix boundary conditions given in (5–36) through (5–38).

$$\delta\boldsymbol{\lambda}(t) = S(t)\delta\mathbf{x}(t) + R(t)\delta\boldsymbol{\nu} \tag{5–34}$$

$$\delta\boldsymbol{\psi}(t) = R(t)^T\delta\mathbf{x}(t) + Q(t)\delta\boldsymbol{\nu} \tag{5–35}$$

$$S(t_f) = \left[\phi_{xx} + \left(\boldsymbol{\nu}^T \boldsymbol{\psi}_x\right)_x\right]_{t=t_f} \tag{5–36}$$

$$R(t_f) = \left[\boldsymbol{\psi}_x^T\right]_{t=t_f} \tag{5–37}$$

$$Q(t_f) = 0 \tag{5–38}$$

Differentiation of Equation (5–34) and substitution of Equations (5–20) and (5–21) results in the same differential Riccati equation as before, Equation (5–28), with the new boundary conditions specified in Equation (5–36). Taking note that $\delta\boldsymbol{\nu}$ is a constant vector and differentiating Equation (5–35) results in the differential equation (5–39).

$$0 = \dot{R}^T(t)\delta\mathbf{x}(t) + R^T(t)\delta\dot{\mathbf{x}}(t) + \dot{Q}(t)\delta\boldsymbol{\nu} \tag{5–39}$$

Substitution of Equation (5–20) for $\delta\dot{\mathbf{x}}(t)$ with subsequent factoring of the coefficients gives Equation (5–40).

$$0 = \left(\dot{R}^T + R^T\left(A - BS\right)\right)\delta\mathbf{x} + \left(\dot{Q} - R^T B R\right)\delta\boldsymbol{\nu} \tag{5–40}$$

Since the variations $\delta\mathbf{x}$ and $\delta\boldsymbol{\nu}$ are independent, both coefficients must be zero independently, giving two additional matrix differential equations.

$$\dot{R} = -\left(A^T - SB\right)R \tag{5–41}$$

$$\dot{Q} = R^T B R \tag{5–42}$$

The complete set of neighboring extremal differential equations and corresponding boundary conditions are summarized in Equations (5–43) through (5–45).

$$\dot{S}(t) = -SA - A^T S + SBC - C,\ S(t_f) = \left[\phi_{xx} + \left(\boldsymbol{\nu}^T \boldsymbol{\psi}_x\right)_x\right]_{t=t_f} \tag{5–43}$$

$$\dot{R} = -\left(A^T - SB\right)R,\ R(t_f) = \left[\boldsymbol{\psi}_x^T\right]_{t=t_f} \tag{5–44}$$

$$\dot{Q} = R^T B R,\ Q(t_f) = 0 \tag{5–45}$$

Equations (5–43) through (5–45) are a set of matrix differential equations with all necessary boundary conditions specified at the final time t_f. The equations are stable in

backward time and independent of the variations $\delta\mathbf{x}(t)$, $\delta\boldsymbol{\lambda}(t)$, and $\delta\mathbf{u}(t)$. As a result, the equations can be solved numerically along an extremal path yielding the time varying matrices $S(t)$, $R(t)$, and $Q(t)$.

Recall that the control variation is given by Equation (5–19), restated here for convenience.

$$\delta\mathbf{u} = -H_{uu}^{-1}\left(H_{ux}\delta\mathbf{x} + \mathbf{f}_u^T\delta\boldsymbol{\lambda}\right) \tag{5–46}$$

Substitution of $\delta\boldsymbol{\lambda} = S\delta\mathbf{x} + R\delta\boldsymbol{\nu}$ from Equation (5–34) gives the result shown in Equation (5–47).

$$\delta\mathbf{u} = -H_{uu}^{-1}H_{ux}\delta\mathbf{x} - H_{uu}^{-1}\mathbf{f}_u^T\left(S\delta\mathbf{x} + R\delta\boldsymbol{\nu}\right) \tag{5–47}$$

Equation (5–35) can be used to eliminate the dependence of the control on the Lagrage multiplier $\delta\boldsymbol{\nu}$, as shown in Equation (5–48).

$$\begin{aligned} \delta\boldsymbol{\psi} &= R^T\delta\mathbf{x} + Q\delta\boldsymbol{\nu} \\ \Rightarrow \delta\boldsymbol{\nu} &= Q^{-1}\left(\delta\boldsymbol{\psi} - R^T\delta\mathbf{x}\right) \end{aligned} \tag{5–48}$$

Substitution of this expression for $\delta\boldsymbol{\nu}$ into Equation (5–47) and subsequent factoring of the coefficients gives Equation (5–49).

$$\delta\mathbf{u} = -H_{uu}^{-1}\left(H_{ux} + \mathbf{f}_u^T S - \mathbf{f}_u^T RQ^{-1}R^T\right)\delta\mathbf{x} - H_{uu}^{-1}\mathbf{f}_u^T RQ^{-1}\delta\boldsymbol{\psi} \tag{5–49}$$

Equation (5–49) can be written concisely as a feedback law with time-varying gains $\Lambda_1(t)$ and $\Lambda_2(t)$.

$$\delta\mathbf{u} = -\Lambda_1(t)\delta\mathbf{x} - \Lambda_2(t)\delta\boldsymbol{\psi} \tag{5–50}$$

$$\Lambda_1(t) = H_{uu}^{-1}\left(H_{ux} + \mathbf{f}_u^T S - \mathbf{f}_u^T RQ^{-1}R^T\right) \tag{5–51}$$

$$\Lambda_2(t) = H_{uu}^{-1}\mathbf{f}_u^T RQ^{-1} \tag{5–52}$$

The feedback control law in Equation (5–50) shows an explicit dependence on the variation in the state (arising from perturbed initial conditions or disturbances along the extremal trajectory) and the variation in the terminal conditions (arising from a

user-specified change in terminal conditions from the nominal extremal solution). Some simplification results if $\delta\psi = 0$.

$$\delta\mathbf{u} = -H_{uu}^{-1}\left(H_{ux} + \mathbf{f}_u^T S - \mathbf{f}_u^T R Q^{-1} R^T\right)\delta\mathbf{x} \tag{5–53}$$

Recall that the neighboring optimal control law in the absence of terminal constraints is given by Equation (5–29), restated here as $\delta\hat{\mathbf{u}}(t)$.

$$\delta\hat{\mathbf{u}}(t) = -H_{uu}^{-1}\left(H_{ux} + \mathbf{f}_u^T S\right)\delta\mathbf{x} \tag{5–54}$$

The feedback law with terminal constraints from Equation (5–53) can be expressed as a combination of the control variation without terminal constraints, $\delta\hat{\mathbf{u}}(t)$, and an additional term due to terminal constraints, as shown in Equation (5–55).

$$\delta\mathbf{u} = \delta\hat{\mathbf{u}}(t) + H_{uu}^{-1}\mathbf{f}_u^T R Q^{-1} R^T \delta\mathbf{x} \tag{5–55}$$

In order for $\delta\mathbf{u}$ to exist and be finite, the matrix inverse $Q^{-1}(t)$ must also exist for $t \in [t_0, t_f]$. However, the boundary conditions specified in Equation (5–45) require that $Q(t_f) = 0$, which implies $Q^{-1}(t_f) = \infty$. As a result, $\delta\mathbf{u}(t) \to \infty$ as $t \to t_f$.

What at first seems like an inconvenient mathematical artifact actually alludes to an intuitive physical principle. Namely, to guarantee that the system arrives at an exact terminal condition $\psi(\mathbf{x}(t_f)) = 0$ in the presence of disturbances $\delta\mathbf{x}(t)$ requires an infinite amount of control. Stated another way, as the terminal condition is approached, an infinite amount of control is required over an infintely short period of time to reach the specified end state.

This problem is also manifest by examining the time-varying gains in Equations (5–51) and (5–52), which approach infinity near the terminal time.

$$\lim_{t \to t_f} \Lambda_1(t) = \Lambda_2(t) = \infty \tag{5–56}$$

The divergence of the time-varying gains near $t = t_f$ introduces a difficulty in using NOC with terminal constraints for realistic systems. This problem is well-known in the literature and a simple workaround is to bound the gains using a saturation function [128]. As a result, the gains are held constant over the final duration of the trajectory. Another alternative is to specify bounds on the control, in the form of an inequality constraint. The system will then naturally employ maximum control effort near the terminal conditions in order to come as close to the terminal condition as possible. Consideration of NOC in the presence of inequality constraints on the control is discussed next.

5.2.4 Neighboring Extremal with Path/Control Constraints

The optimal performance of many systems involves operation at or near a physical boundary. Examples include maximum control effort in a "bang-bang" control system and maximum acceleration to reach a target in minimum time. Interior constraints can be classified as (1) path constraints, (2) control constraints, or (3) path and control constraints. The constraints may be further classified as equality or inequality constraints, for a total of six possible problem types, each with a similar but distinct solution approach [111]. For a more in depth treatment, the reader is referred to literature that addresses neighboring optimal control with path and control constraints in detail [131–133, 136, 151]. The general solution approach, briefly considered here, consists of joining the constraints to the Hamiltonian using corresponding Lagrange multipliers.

Consider the path/control inequality constraint introduced in Equation (5–3).

$$\mathbf{C}\big(\mathbf{x}(t), \mathbf{u}(t)\big) \leq 0 \tag{5–57}$$

As discussed in Chapter 4, the path/control constraint can be joined to the Hamiltonian using the Lagrange multiplier $\boldsymbol{\mu}(t)$.

$$H\left(\mathbf{x}, \mathbf{u}, \boldsymbol{\lambda}, \boldsymbol{\mu}\right) = L\left(\mathbf{x}, \mathbf{u}\right) + \boldsymbol{\lambda}^T \mathbf{f}\left(\mathbf{x}, \mathbf{u}\right) + \boldsymbol{\mu}^T C\left(\mathbf{x}, \mathbf{u}\right) \tag{5–58}$$

Using the complementary slackness condition, the Lagrange multiplier $\boldsymbol{\mu}(t)$ is related to the value of the dynamic constraint $\mathbf{C}\left(\mathbf{x}(t), \mathbf{u}(t)\right) \leq 0$, as shown in Equation (5–59), where s is the number of constraints and the dimension of the vector $\mathbf{C}\big(\mathbf{x}, \mathbf{u}\big)$.

$$\text{Lagrange multiplier } \boldsymbol{\mu}(t): \begin{cases} \mu_i(t) = 0 & \text{if} \quad C_i\left(\mathbf{x}(t), \mathbf{u}(t)\right) < 0; \quad i = 1, \ldots, s \\ \mu_i(t) > 0 & \text{if} \quad C_i\left(\mathbf{x}(t), \mathbf{u}(t)\right) = 0; \quad i = 1, \ldots, s \end{cases} \tag{5–59}$$

The positive value of μ_i when $C_i = 0$ is interpreted such that improving the cost may only come from violating the constraint [113]. Furthermore, $\mu_i(t) = 0$ when $C_i < 0$ states that this constraint is inactive and can be ignored. In this case, the Hamiltonian reduces to the unconstrained form given in equation (5–60).

$$H\left(\mathbf{x}, \mathbf{u}, \boldsymbol{\lambda}\right) = L\left(\mathbf{x}, \mathbf{u}\right) + \boldsymbol{\lambda}^T \mathbf{f}\left(\mathbf{x}, \mathbf{u}\right) \tag{5–60}$$

Similarly, the Euler-Lagrange equations are dependent on the activity of the constraint inequality.

$$\dot{\boldsymbol{\lambda}}^T = -H_x = \begin{cases} -L_x - \boldsymbol{\lambda}^T \mathbf{f}_x - \boldsymbol{\mu}\mathbf{C}_x, & \mathbf{C} = 0 \\ -L_x - \boldsymbol{\lambda}^T \mathbf{f}_x, & \mathbf{C} < 0 \end{cases} \tag{5–61}$$

The necessary condition to determine the optimal control is given by Equation (5–62).

$$H_u = L_u + \boldsymbol{\lambda}^T \mathbf{f}_u + \boldsymbol{\mu}\mathbf{C}_u = 0 \tag{5–62}$$

When the constraint is inactive, $\boldsymbol{\mu}(t) = 0$ and $\mathbf{u}(t)$ is determined from $L_u + \boldsymbol{\lambda}^T \mathbf{f}_u = 0$ in the usual unconstrained manner. Otherwise, when the constraint is active, $\mathbf{u}(t)$ is determined from $\mathbf{C}(\mathbf{x}, \mathbf{u}) = 0$ and $\boldsymbol{\mu}(t)$ is determined from Equation (5–62). A simple check to ensure $\boldsymbol{\mu}(t) \geq 0$ is sufficient to verify the stationarity of the extremal along the constrained arc. When the inequality constraint does not include the control explicitly, e.g. $\mathbf{C} = \mathbf{C}(\mathbf{x})$, additional effort is needed to introduce the control through differentiation of $\mathbf{C}(\mathbf{x})$ and substitution of $\dot{\mathbf{x}}(t)$ until the control appears explicitly in the constraint

equation. This additional complexity is not necessary for the current application and only constraints of the form $\mathbf{C}(\mathbf{x}, \mathbf{u})$ will be considered herein.

This argument can be extended to NOC as follows. Consider the variation of the function $H_u(\delta\mathbf{x}, \delta\boldsymbol{\lambda}, \delta\mathbf{u}, \delta\boldsymbol{\mu}) = 0$, as shown in Equation (5–63).

$$\delta H_u(\delta\mathbf{x}, \delta\boldsymbol{\lambda}, \delta\mathbf{u}, \delta\boldsymbol{\mu}) = H_{ux}\delta\mathbf{x} + \mathbf{f}_u^T\delta\boldsymbol{\lambda} + H_{uu}\delta\mathbf{u} + \mathbf{C}_u^T\delta\boldsymbol{\mu} = 0 \tag{5–63}$$

When $\mathbf{C} < 0$, the variation $\delta\boldsymbol{\mu} = 0$ and the control can be determined in a manner identical to the unconstrained neighboring extremal. In the case that $\mathbf{C} = 0$, the constrained control $\mathbf{u}_c$ can be determined from the constraint and $\delta\mathbf{u} = \mathbf{u}_c - \mathbf{u}^*$ is also known. As such, the variation $\delta\boldsymbol{\mu}$ can be determined from Equation (5–63). The two possibilities are summarized in Equation (5–64).

$$\text{When: } \begin{cases} \mathbf{C} < 0, \quad \delta\boldsymbol{\mu} = 0, \quad \delta\mathbf{u} = -H_{uu}^{-1}\left(H_{ux} + \mathbf{f}_u^T S\right)\delta\mathbf{x} \\ \mathbf{C} = 0, \quad \delta\mathbf{u} = \mathbf{u}_c - \mathbf{u}^*, \quad \delta\boldsymbol{\mu} = -\mathbf{C}_u^{-T}\left[\left(H_{ux} + \mathbf{f}_u^T S\right)\delta\mathbf{x} + H_{uu}\delta\mathbf{u}\right] \end{cases} \tag{5–64}$$

The variation $\delta\boldsymbol{\mu}$ carries the same significance as the original multiplier $\boldsymbol{\mu}$ and the complementary slackness condition in Equation (5–59). Namely, a positive $\delta\boldsymbol{\mu}$ implies that the cost can only be improved by violating the constraints. Consequently, a simple check of $\delta\boldsymbol{\mu} \geq 0$ is sufficient to ensure the stationarity of the neighboring extremal along the constrained arc. These verifications are implicit to the numerical examples presented subsequently and when a constrained arc is encountered, it can be assumed by the reader that these qualifications have been met.

5.2.5 Neighboring Extremal with Parameter Variations

Consider a system that is dependent on a set of constant parameters $\boldsymbol{\theta}$, as shown in Equation (5–65).

$$\dot{\mathbf{x}}(t) = \mathbf{f}\left(\mathbf{x}, \mathbf{u}, \boldsymbol{\theta}, t\right) \tag{5–65}$$

It is assumed that the initial value of $\boldsymbol{\theta}$ is known and used in the solution of the nominal HBVP. The goal is to find a neighboring optimal feedback law that minimizes

the original cost functional to second order in the presence of disturbances $\delta\mathbf{x}(t_0)$ and parameter variations $\delta\boldsymbol{\theta}$. The development is similar to the discussion in Section 5.2.3. For the present discussion, it will be assumed that no terminal constraints have been specified, although extension to the case with terminal constraints is straightforward. For a more in depth treatment, the reader is referred to literature that addresses neighboring optimal control with parameters in detail [137, 138, 140].

The variation in the state and costate differential equations with parameter variations are given by Equations (5–66) and (5–67).

$$\delta\dot{\mathbf{x}}(t) = \mathbf{f}_x\delta\mathbf{x} + \mathbf{f}_u\delta\mathbf{u} + \mathbf{f}_\theta\delta\boldsymbol{\theta} \tag{5–66}$$

$$\delta\dot{\boldsymbol{\lambda}}(t) = -H_{xx}\delta\mathbf{x} - H_{xu}\delta\mathbf{u} - H_{x\theta}\delta\boldsymbol{\theta} - \mathbf{f}_x^T\delta\boldsymbol{\lambda} \tag{5–67}$$

The necessary condition for optimal control $H_u = 0$ followed by the resulting expression for the control variation $\delta\mathbf{u}$ is given by Equation (5–68).

$$\begin{aligned} 0 =& H_{ux}\delta\mathbf{x} + H_{uu}\delta\mathbf{u} + H_{u\theta}\delta\boldsymbol{\theta} + \mathbf{f}_u^T\delta\boldsymbol{\lambda} \\ \Rightarrow \delta\mathbf{u} =& -H_{uu}^{-1}\left(H_{ux}\delta\mathbf{x} + H_{u\theta}\delta\boldsymbol{\theta} + \mathbf{f}_u^T\delta\boldsymbol{\lambda}\right) \end{aligned} \tag{5–68}$$

Substitution of $\delta\mathbf{u}$ from Equation (5–68) into the differential equations (5–66) and (5–67) results in the following linear system of equations in terms of $\delta\mathbf{x}$, $\delta\boldsymbol{\lambda}$, and $\delta\boldsymbol{\theta}$.

$$\delta\dot{\mathbf{x}}(t) = A(t)\delta\mathbf{x} - B(t)\delta\boldsymbol{\lambda} + U(t)\delta\boldsymbol{\theta} \tag{5–69}$$

$$\delta\dot{\boldsymbol{\lambda}}(t) = -C(t)\delta\mathbf{x} - A^T(t)\delta\boldsymbol{\lambda} + V(t)\delta\boldsymbol{\theta} \tag{5–70}$$

The matrices $A(t)$, $B(t)$, and $C(t)$ are given by Equations (5–22) through (5–24) in Section 5.2.2. The matrices $U(t)$ and $V(t)$ are determined in a similar manner.

$$U(t) = \mathbf{f}_\theta - \mathbf{f}_u H_{uu}^{-1} H_{u\theta} \tag{5–71}$$

$$V(t) = H_{xu}H_{uu}^{-1}H_{u\theta} - H_{x\theta} \tag{5–72}$$

The terminal condition $\delta\boldsymbol{\lambda}(t_f) = \phi_{xx}\delta\mathbf{x}(t_f)$ suggests a particular form for the costate as a linear combination of the variation of the state $\delta\mathbf{x}(t)$ and the constant parameter vector $\delta\boldsymbol{\theta}$, as shown in Equation (5–73).

$$\delta\boldsymbol{\lambda}(t) = S(t)\delta\mathbf{x} + W(t)\delta\boldsymbol{\theta} \tag{5–73}$$

Differentiation of Equation (5–73) followed by substitution of $\delta\dot{\mathbf{x}}$ and $\delta\dot{\boldsymbol{\lambda}}$ results in the following matrix differential equations for $S(t)$ and $W(t)$. The corresponding boundary conditions are determined by comparison with $\delta\boldsymbol{\lambda}(t_f) = \phi_{xx}\delta\mathbf{x}(t_f)$.

$$\dot{S}(t) = -SA - A^T S + SBS - C, \quad S(t_f) = \phi_{xx} \tag{5–74}$$

$$\dot{W}(t) = V - A^T W - S(U - BW), \quad W(t_f) = 0 \tag{5–75}$$

Equations (5–74) and (5–75) are a set of matrix differential equations with all necessary boundary conditions specified at the final time t_f. The equations are stable in backward time and independent of the variations $\delta\mathbf{x}$, $\delta\mathbf{u}$, $\delta\boldsymbol{\lambda}$, and $\delta\boldsymbol{\theta}$. As a result, the equations can be solved numerically along an extremal path yielding the time varying matrices $S(t)$ and $W(t)$.

Recall that the neighboring optimal control law in the absence of parameter variations or terminal constraints is given by Equation (5–29), restated here as $\delta\hat{\mathbf{u}}(t)$.

$$\delta\hat{\mathbf{u}}(t) = -H_{uu}^{-1}\left(H_{ux} + \mathbf{f}_u^T S\right)\delta\mathbf{x} \tag{5–76}$$

The feedback law with parameter variations, which results from the substitution of (5–73) into (5–68), can be expressed as a combination of the control variation without parameter variations, $\delta\hat{\mathbf{u}}(t)$, and an additional term due to parameter variations, as shown in Equation (5–77).

$$\delta\mathbf{u} = \delta\hat{\mathbf{u}}(t) - H_{uu}^{-1}\left(H_{u\theta} + \mathbf{f}_u^T W(t)\right)\delta\boldsymbol{\theta} \tag{5–77}$$

Equation (5–77) represents a neighboring optimal feedback control law that minimizes the original cost function to second order in the presence of disturbances and parameter variations.

When the parameter variation $\delta\boldsymbol{\theta}$ is known or may be estimated during operation, NOC may be used to implement a feedback control law that is explicitly dependent on the perturbed parameters. However, when $\delta\boldsymbol{\theta}$ is unknown, the control variation is necessarily sub-optimal. Although the feedback control can still accommodate disturbances that result from applying the nominal open-loop (feed forward) control to the system with perturbed parameters, the feedback will not be optimal to second order and some additional cost will be incurred. Therefore, the use of NOC for a system with unknown parameter variations can be described as "near optimal", provided that the parameter variations remain small.

5.2.6 Sufficient Conditions for Optimality

The 1st order optimality conditions specify the necessary conditions for an extremal trajectory. However, an extremal trajectory that satisfies the necessary conditions may or may not be locally optimal. In order to demonstrate that the extremal trajectory is indeed a locally optimal trajectory, it is necessary to consider 2nd order sufficient conditions.

Whereas the 1st order necessary conditions require $\delta J_a = 0$, the 2nd order sufficient conditions for local optimality require $\delta^2 J_a > 0$ [113]. The 2nd variation of the augmented cost functional is given by Equation (5–78), which is the same cost functional used for solving the neighboring optimal control problem.

$$\begin{aligned}\delta^2 J_a = & \frac{1}{2}\left[\delta\mathbf{x}^T\left(\phi_{xx} + \left(\boldsymbol{\nu}^T\boldsymbol{\psi}_x\right)_x\right)\delta\mathbf{x}\right]_{t=t_f} + \\ & \frac{1}{2}\int_{t_0}^{t_f}\begin{bmatrix}\delta\mathbf{x}^T & \delta\boldsymbol{\lambda}^T\end{bmatrix}\begin{bmatrix}H_{xx} & H_{xu}\\ H_{ux} & H_{uu}\end{bmatrix}\begin{bmatrix}\delta\mathbf{x}\\ \delta\boldsymbol{\lambda}\end{bmatrix}dt\end{aligned} \tag{5–78}$$

The quadratic form of the cost functional ensures that if a neighboring extremal can be found, then $\delta^2 J_a > 0$. Thus, simply stated, the existence of a neighboring optimal solution is sufficient for ensuring the extremal path is indeed locally optimal.

The sufficient conditions for the existence of a neighboring extremal, which are synonymous with the sufficient conditions for local optimality, can be deduced from the mathematical development in the preceding sections. Rigorous developments are documented elsewhere [87, 113, 116]. Considering the more general case with terminal constraints, the sufficient conditions are summarized in Equations (5–79) through (5–81).

$$\text{Convexity Condition:} \quad H_{uu}(t) > 0 \quad \text{for} \quad t_0 \leq t \leq t_f \tag{5–79}$$

$$\text{Normality Condition:} \quad Q(t) < 0 \quad \text{for} \quad t_0 \leq t < t_f \tag{5–80}$$

$$\text{Jacobi Condition:} \quad S(t) - R(t)Q^{-1}(t)R^T(t) \quad \text{finite for} \quad t_0 \leq t < t_f \tag{5–81}$$

For the simplified case without terminal constraints, the sufficient conditions reduce to $H_{uu} > 0$ and $S(t)$ finite over the entire extremal trajectory. These conditions can be easily verified along the extremal path using the formulations developed in previous sections.

5.3 Store Separation Autopilot

Flight vehicles, such as aircraft and guided stores, use flight management systems (FMS) to achieve guidance and control throughout the flight profile. The pilot or FMS will frequently switch between autopilots that perform different functions, such as altitude hold, climb/descent, bank-to-turn, etc. In this context, a store separation autopilot is a transitional control system, designed to effectively transfer the store from release to a stable trimmed flight condition. The spatially variant aerodynamic characteristics are accounted for through the nominal optimal trajectory using the methods discussed in Chapter 4. Response to varying initial conditions and flow field disturbances are accounted for using full-state feedback based on neighboring optimal control techniques.

5.3.1 Feedback Using Neighboring Optimal Control

Application of neighboring optimal control to store separation is straight forward. A quadratic cost functional, given by Equation (5–82) is sufficient for this investigation, where Q is a constant positive semi-definite matrix $Q \geq 0$ and R is a constant positive definite matrix $R > 0$. The weighting matrices Q and R are chosen by the user to influence the magnitude of the state and control vector, respectively. The matrix $S_f \geq 0$ is specified by the user to achieve satisfactory terminal conditions.

$$J = \frac{1}{2}\mathbf{x}(t_f)^T S_f \mathbf{x}(t_f) + \frac{1}{2}\int_{t_0}^{t_f} \left(\mathbf{x}^T Q \mathbf{x} + \mathbf{u}^T R \mathbf{u}\right) dt \tag{5–82}$$

Using the quadratic cost functional, the 1st order optimality conditions without terminal constraints are stated in Equations (5–83) through (5–85).

$$\dot{\mathbf{x}}(\mathbf{t}) = \mathbf{f}\left(\mathbf{x}(t), \mathbf{u}(t)\right), \quad \mathbf{x}(t_0) \text{ specified} \tag{5–83}$$

$$\dot{\lambda}(\mathbf{t}) = -Q\mathbf{x}(t) - \mathbf{f}_x^T(t)\boldsymbol{\lambda}(t), \quad \boldsymbol{\lambda}(t_f) = S_f \mathbf{x}(t_f) \tag{5–84}$$

$$\mathbf{u}(t) = -R^{-1}\mathbf{f}_u^T(t)\boldsymbol{\lambda}(t) \tag{5–85}$$

Due to the difficulty of modeling store separation aerodynamics, it is desirable to isolate the aerodynamic terms appearing in the state equations $\dot{\mathbf{x}}(\mathbf{t}) = \mathbf{f}(\mathbf{x}, \mathbf{u})$. This allows the optimality equations developed herein to be used with a variety of aerodynamic models. Recognizing that the aerodynamic terms are also functions of the state and control, the state equations can be written in functional form as shown in Equation (5–86), where $C_F(\mathbf{x}, \mathbf{u})$ and $C_M(\mathbf{x}, \mathbf{u})$ are the aerodynamic force and moment coefficients, respectively.

$$\dot{\mathbf{x}}(\mathbf{t}) = \mathbf{f}\left(\mathbf{x}, \mathbf{C}_F(\mathbf{x}, \mathbf{u}), \mathbf{C}_M(\mathbf{x}, \mathbf{u})\right) \tag{5–86}$$

Using the notation in Equation (5–86), the Jacobian matrices in Equations (5–84) and (5–85) can be expanded as follows.

$$\mathbf{f}_x \triangleq \frac{\partial \mathbf{f}(\mathbf{x}, \mathbf{C}_F, \mathbf{C}_M)}{\partial \mathbf{x}} = \frac{\partial \mathbf{f}_0}{\partial \mathbf{x}} + \frac{\partial \mathbf{f}}{\partial \mathbf{C}_F}\frac{\partial \mathbf{C}_F}{\partial \mathbf{x}} + \frac{\partial \mathbf{f}}{\partial \mathbf{C}_M}\frac{\partial \mathbf{C}_M}{\partial \mathbf{x}} \tag{5–87}$$

$$\mathbf{f}_u \triangleq \frac{\partial \mathbf{f}(\mathbf{x}, \mathbf{C}_F, \mathbf{C}_M)}{\partial \mathbf{u}} = \frac{\partial \mathbf{f}_0}{\partial \mathbf{u}} + \frac{\partial \mathbf{f}}{\partial \mathbf{C}_F}\frac{\partial \mathbf{C}_F}{\partial \mathbf{u}} + \frac{\partial \mathbf{f}}{\partial \mathbf{C}_M}\frac{\partial \mathbf{C}_M}{\partial \mathbf{u}} \tag{5–88}$$

Equations (5–89) and (5–90) can be written more concisely using subscript notation to represent partial differentiation, where the notation $\mathbf{f}_{x_0}$ and $\mathbf{f}_{u_0}$ implies the derivative is taken while holding the aerodynamic coefficients constant.

$$\mathbf{f}_x = \mathbf{f}_{x_0} + \mathbf{f}_{C_F}\mathbf{C}_{F_X} + \mathbf{f}_{C_M}\mathbf{C}_{M_X} \tag{5–89}$$

$$\mathbf{f}_u = \mathbf{f}_{u_0} + \mathbf{f}_{C_F}\mathbf{C}_{F_U} + \mathbf{f}_{C_M}\mathbf{C}_{M_U} \tag{5–90}$$

The matrices $\mathbf{C}_{F_X}$ and $\mathbf{C}_{M_X}$ represent the aerodynamic stability derivatives, and the matrices $\mathbf{C}_{F_U}$ and $\mathbf{C}_{M_U}$ represent the aerodynamic control derivatives. These matrices may be determined analytically when a parametric form of the aerodynamic model is available, often as a result of system identification. Alternatively, they can be estimated numerically using finite differencing or an alternative numerical recipe.

Beginning with the necessary conditions in Equations (5–83) through (5–85), the linear differential equations for a neighboring extremal arise immediately from the results in Section 5.2.2 and are summarized in Equations (5–91) through (5–93).

$$\delta\dot{\mathbf{x}}(t) = \mathbf{f}_x\delta\mathbf{x} + \mathbf{f}_u\delta\mathbf{u} \tag{5–91}$$

$$\delta\mathbf{u}(t) = -R^{-1}\mathbf{f}_u^T S\delta\mathbf{x} \tag{5–92}$$

$$\dot{S}(t) = -S\mathbf{f}_x - \mathbf{f}_x^T S + S\mathbf{f}_u R^{-1}\mathbf{f}_u^T S - Q, \quad S(t_f) = S_f \tag{5–93}$$

Equations (5–91) through (5–93) are a compact set of differential equations that can be used to implement a Store Separation Autopilot that minimizes the original cost function to second order in the presence of disturbances along a predetermined

optimal trajectory. The matrix Riccati equation (5–93) is evaluated along the optimal trajectory to determine the feedback gains $K(t) = -R^{-1}\mathbf{f}_u^T S$ and the results are stored along with the nominal state and control, $x^*(t)$ and $u^*(t)$. The neighboring optimal control input can be determined real-time using feed forward of the nominal control plus feedback proportional to the deviation of the measured state from the reference trajectory, $\mathbf{u}(t) = \mathbf{u}^*(t) - K(t)\delta\mathbf{x}(t)$.

5.3.2 Infinite Horizon Neighboring Optimal Control

The aerodynamic characteristics of the store in the vicinity of the aircraft are inherently nonlinear. Aerodynamic nonlinearities appear through large flow field gradients near the aircraft as well as decay of the aircraft effects in far field conditions. Thus, the store transitions through a time (or spatially) variant nonlinear regime and rapidly approaches a trimmed freestream flight condition that can be adequately approximated by time invariant linear behavior. One approach to controlling the store in these two disparate flight regimes is to switch between a nonlinear time variant controller and a linear time invariant controller. Another approach is to design a single control system that accounts for the nonlinear flight regime and converges to a linear time invariant controller in far field conditions. The latter approach is adopted here in a process herein referred to as Infinite Horizon Neighboring Optimal Control.

The neighboring optimal feedback gains $K(t) = -R^{-1}\mathbf{f}_u^T S$ are determined in part by the solution to the matrix differential Riccati equation (5–94).

$$\dot{S}(t) = -S\mathbf{f}_x - \mathbf{f}_x^T S + S\mathbf{f}_u R^{-1}\mathbf{f}_u^T S - Q, \quad S(t_f) = S_f \tag{5–94}$$

The Jacobian matrices $\mathbf{f}_x$ and $\mathbf{f}_u$ are in general time-varying. For store separation, these matrices result from linearization along a predetermined trajectory and vary with time and/or distance from the aircraft due to the nonlinear aerodynamic characteristics. However, as the distance between the store and aircraft becomes large, the effect of the aircraft flow field becomes negligible and the Jacobian matrices converge to constant

freestream quantities, denoted here as F and G.

$$\lim_{t \to t_f} \mathbf{f}_x(t) \to F \tag{5–95}$$

$$\lim_{t \to t_f} \mathbf{f}_u(t) \to G \tag{5–96}$$

In this limiting case, the matrix differential Riccati equation (DRE) approaches a constant solution, resulting in an algebraic Riccati equation (ARE) with may be solved numerically to yield S_f.

$$0 = -S_f F - F^T S_f + S_f G R^{-1} G^T S_f - Q \tag{5–97}$$

The solution to the ARE can be used to determine the constant feedback gains $K_f = -R^{-1} G^T S_f$. The resulting linear time invariant control system is mathematically equivalent to a Linear Quadratic Regulator (LQR).

Returning to the original quadratic cost functional, restated here as Equation (5–98), it is apparent, with obvious forethought, that the matrix S_f is used to denote a user-specified weighting matrix that determines the end point (Mayer) cost.

$$J = \frac{1}{2}\mathbf{x}(t_f)^T S_f \mathbf{x}(t_f) + \frac{1}{2}\int_{t_0}^{t_f} \left(\mathbf{x}^T Q \mathbf{x} + \mathbf{u}^T R \mathbf{u}\right) dt \tag{5–98}$$

Choosing the Mayer cost to be consistent with the solution to the ARE results in time varying gain matrix that approaches a constant quantity as the system converges to a time invariant system. The time invariant gains can be used to maintain the system near the desired operating condition indefinitely.

$$\lim_{t \to t_f} K(t) \to K_f \tag{5–99}$$

In summary, Infinite Horizon Neighboring Optimal Control (IHNOC) consists of three sequential steps. First, optimal control theory is used to determine a nominal reference trajectory that optimizes a desired performance index for a dynamic system

with transitory nonlinear characteristics. Next, neighboring optimal control is used to implement a feedback control system that optimizes the original performance index to second order in the presence of disturbances along the optimal path. Finally, as the system approaches an operating condition that is adequately represented by a linear system model, the feedback controller converges to a linear time invariant regulator that may be used to keep the system near the desired operating condition indefinitely.

IHNOC provides a framework for designing a store separation autopilot that guides the store away from the aircraft along an optimal trajectory, responds in an optimal manner to disturbances along the nominal path, and converges to a time invariant linear feedback controller in far field conditions. An extended example demonstrating the efficacy of this approach is presented in Section 5.4 and a realistic case study is examined in Chapter 6.

5.4 Example: Planar Store Separation

Store separation is often dominated by vertical translation and pitch attitude. In most cases, lateral translation and yaw attitude are fairly benign and of secondary interest. For instructive purposes, consideration of a store confined to the vertical $x - z$ plane during separation maintains the primary scope of interest and considerably reduces the complexity of the optimal control problem. The example considered here is a continuation of the results discussed in Chapter 4. Extension of the approach to a full nonlinear six degree of freedom case study is taken up in Chapter 6.

5.4.1 Model Equations

The model equations for planar store separation were given in Section 4.3.3.1. The state space equations of motion in mixed wind and body axes are given in Equation (5–100).

$$\begin{bmatrix} \dot{V} \\ \dot{\alpha} \\ \dot{q} \\ \dot{\theta} \\ \dot{z} \end{bmatrix} = \begin{bmatrix} -D/m - g\sin\gamma \\ q - L/mV + g/V\cos\gamma \\ M/I_{yy} \\ q \\ -V\sin\gamma \end{bmatrix} \tag{5–100}$$

The components of the state, V(t), $\alpha(t)$, q(t), $\theta(t)$ and z(t), are the air-relative velocity, angle of attack, pitch rate, pitch angle, and vertical position, respectively. The flight path angle is given by $\gamma(t) = \theta(t) - \alpha(t)$ and the local acceleration of gravity is denoted by g. The variables L, D, and M represent the dimensional lift, drag, and pitching moment, respectively. Finally, I_{yy} is the pitch-axis moment of inertia and m is the mass of the store. The Jacobian matrices $\mathbf{f}_{x_0}$, $\mathbf{f}_{u_0}$, $\mathbf{f}_{C_F}$, and $\mathbf{f}_{C_M}$ can be evaluated analytically from the equations of motion and are provided in Section 4.3.3.1.

A simplistic spatially variant nonlinear aerodynamic model based on wind tunnel data has been selected to demonstrate the application of NOC to store separation. The model is the same model used in Section 4.3.3.2.

$$C_L = C_{L_\alpha}\alpha + C_{L_{\delta_e}}\delta_e \tag{5–101}$$

$$C_D = C_{D_0} + KC_L^2 + C_{D_{\delta_e}}\delta_e \tag{5–102}$$

$$C_m = C_{m_\alpha}\alpha + C_{m_q}\hat{q} + C_{m_{\delta_e}}\delta_e + e^{-(\mu z)}\left(\eta_0 + \eta_1 z\right) \tag{5–103}$$

The variable δ_e represents the elevator control surface deflection and $\hat{q}$ is the non-dimensional pitch rate introduced for unit consistency. The constants C_{L_α}, C_{D_0}, C_{m_α}, and C_{m_q} represent the classical aerodynamic derivatives. The constants $C_{L_{\delta_e}}$, $C_{D_{\delta_e}}$, and $C_{m_{\delta_e}}$ represent the classical control derivatives. For the current example, the aerodynamic and control derivatives are constant and estimated using freestream wind tunnel data and the system identification methods discussed in Chapter 3. The term $e^{-(\mu z)}\left(\eta_0 + \eta_1 z\right)$ is the only spatially variant contribution to the aerodynamic model. The

exponential-polynomial form is seen as a special case of the more general parametric model presented in Chapter 3. The constants μ, η_0, and η_1 were estimated using a nonlinear least squares curve fit of representative wind tunnel data at a nominal pitch attitude and are tabulated in Table (4-1). The Jacobian matrices $\mathbf{C}_{F_X}$, $\mathbf{C}_{M_X}$, $\mathbf{C}_{F_U}$, and $\mathbf{C}_{M_U}$ are readily determined from the aerodynamic model and provided in Section 4.3.3.1.

5.4.2 Neighboring Optimal Control

Figure 5-2 shows an open loop optimal trajectory and a neighboring optimal trajectory for the same initial conditions. The open loop trajectory was solved as an HBVP using the planar nonlinear equations of motion and simplified nonlinear aerodynamic model described in Section 5.4.1. The neighboring optimal trajectory was determined using the equations derived in Section 5.4 with a quadratic cost functional. The cost was selected such that $Q_\alpha = 10$ and $R_{\delta_e} = 10$ with all other weighting parameters set to zero, including $S_f = 0$. The results agree very closely as expected, indicating the NOC formulation is working well in the absence of any disturbances or parameter variations.

The solution $S(t)$ to the Riccati differential equation along the optimal trajectory is shown in Figure 5-3. Note that all of the Riccati gains converge to zero at $t = t_f$. This is consistent with the boundary condition resulting from the weighting matrix $S_f = 0$.

The corresponding control gains, $K(t) = -R^{-1}\mathbf{f}_u^T S(t)$, are shown in Figure 5-4. The various control gains differ by three orders of magnitude and the subplots in Figure 5-4 are organized by order of magnitude to enhance clarity. The largest gains are those associated with the state variables $\alpha(t)$, $\theta(t)$, and $q(t)$, as one might expect based on the specified cost parameters. Note that the control gains in Figure 5-4 also converge to zero at $t = t_f$, commensurate with $S_f = 0$.

The neighboring extremal in Figure 5-2 agrees well with the HBVP optimal trajectory with the same initial conditions. For the open loop trajectory, the HBVP must be solved again for each new set of initial conditions. However, NOC can be used to estimate

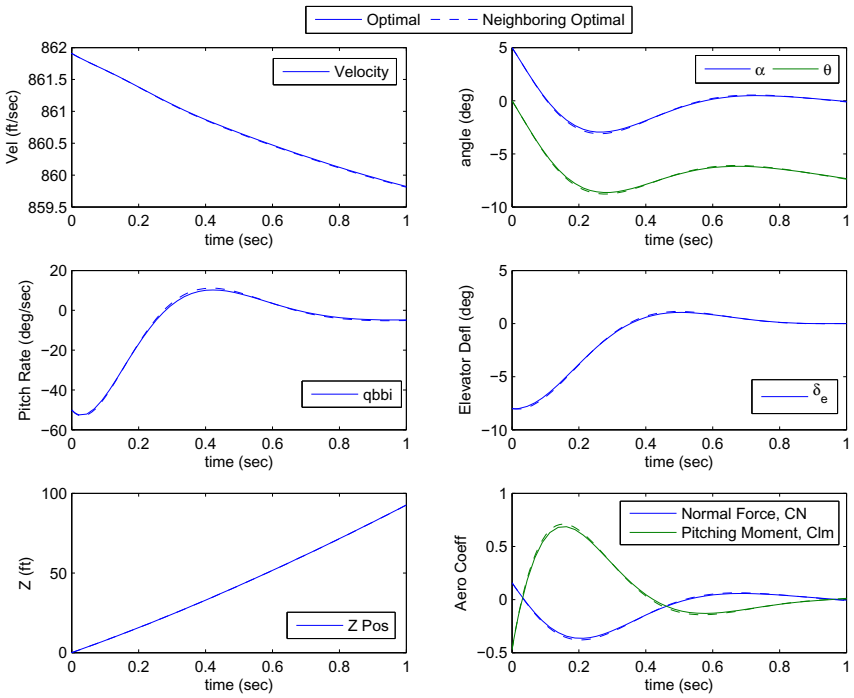

Figure 5-2. Optimal trajectory with neighboring optimal feedback control.

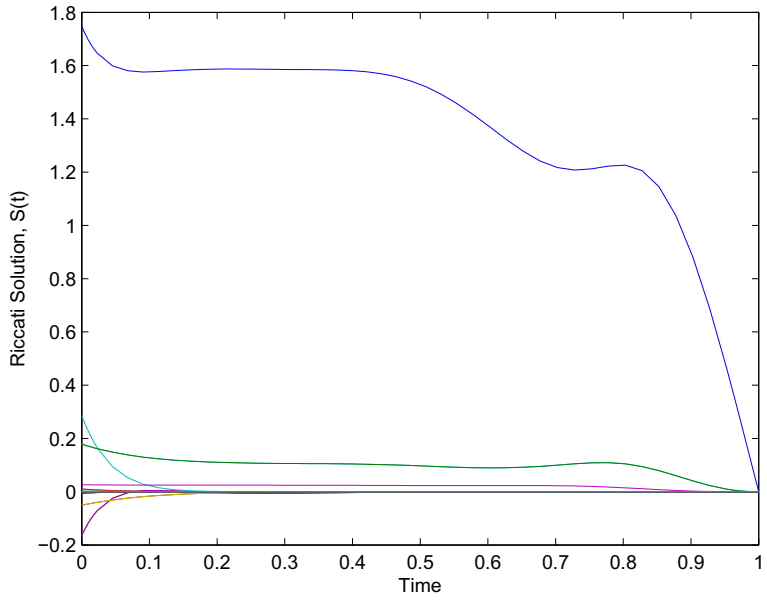

Figure 5-3. Solution to Riccati differential equation.

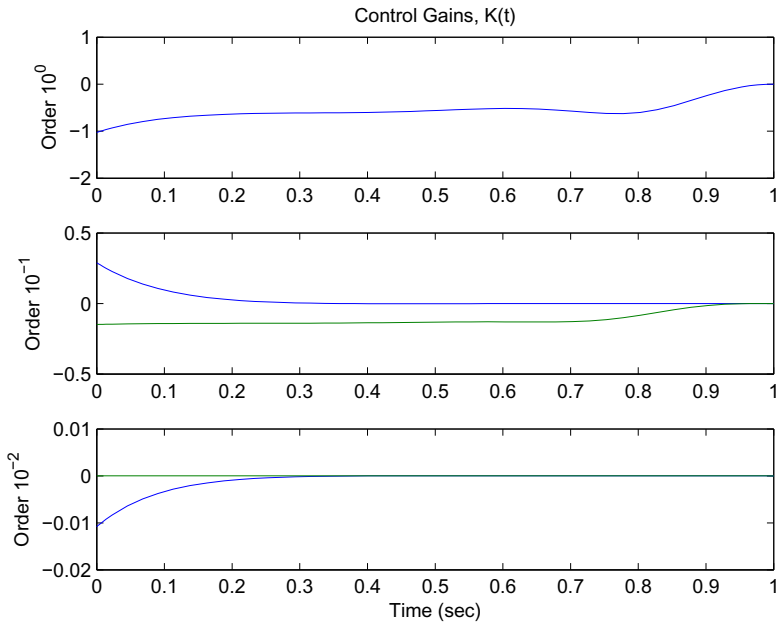

Figure 5-4. Neighboring optimal feedback gains.

a new optimal trajectory for each set of disturbances using only a single reference trajectory and stored gain matrix. Figure 5-5 shows a series of optimal trajectories computed for various initial pitch rates, $q(t_0) = -50 \pm 50$ deg/sec. The solutions were obtained with $Q_\alpha = 1$ and $R_{\delta_e} = 10$ and all other weighting parameters set to 0. The reduced weight Q_α was selected to avoid saturation of the control inputs.

The optimal solutions (solid lines) in Figure 5-5 were solved independently for each set of initial conditions. The first optimal solution, corresponding to $q(t_0) = -50$ deg/sec, was used as a reference trajectory for the remaining four NOC solutions. Note that each of the four NOC solutions agrees well with the true optimal solution for the specified initial conditions. Thus, the NOC formulation is adequately approximating the true optimal performance of the system in the presence of varying initial conditions.

Figure 5-6 shows a similar result for perturbations in $\alpha(t_0) = 5 \pm 2$ deg. Again, the neighboring optimal trajectories are adequate approximations of the true optimal trajectories, with some minor degradation at the extreme values. Despite the degradation, the performance of the neighboring optimal controller is excellent.

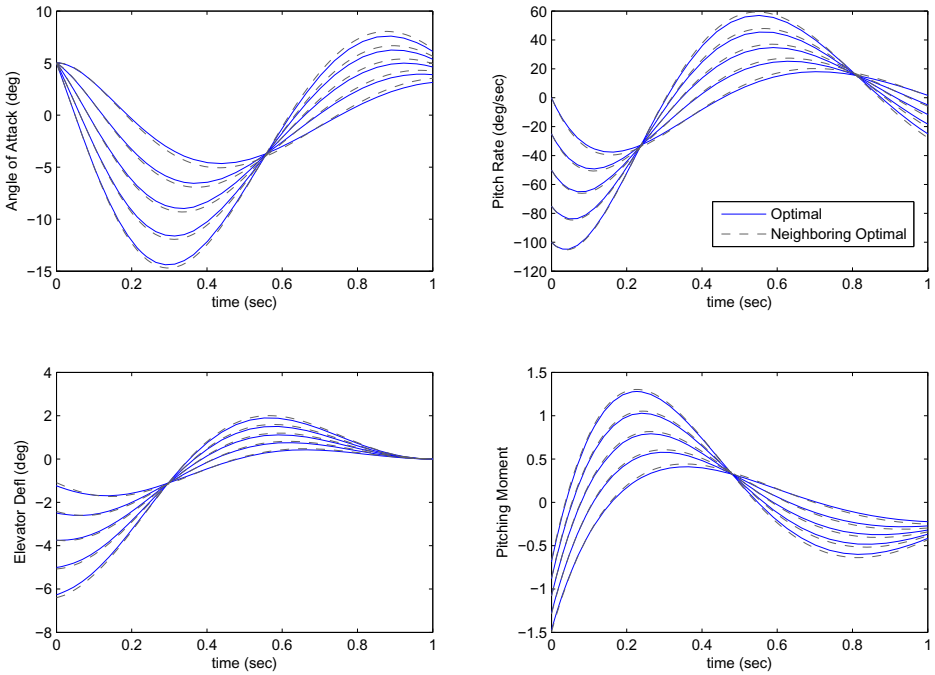

Figure 5-5. Optimal and neighboring optimal trajectories for varying initial pitch rate.

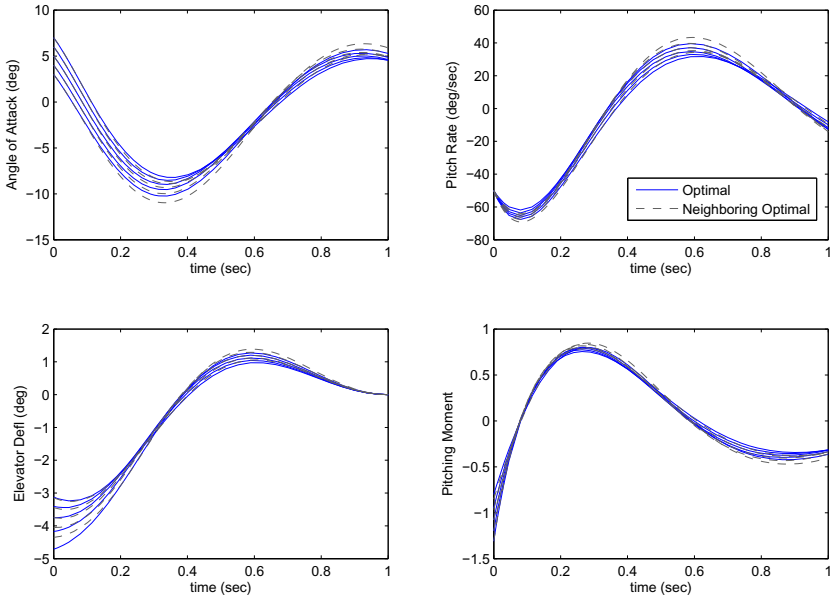

Figure 5-6. Optimal and neighboring optimal trajectories for varying initial angle of attack.

Figure 5-7 shows similar results for perturbations in both $q(t_0) = -50 \pm 50$ deg/sec and $\alpha(t_0) = 5 \pm 2$ deg. The results further demonstrate the performance of the neighboring optimal controller in the presence of large initial disturbances.

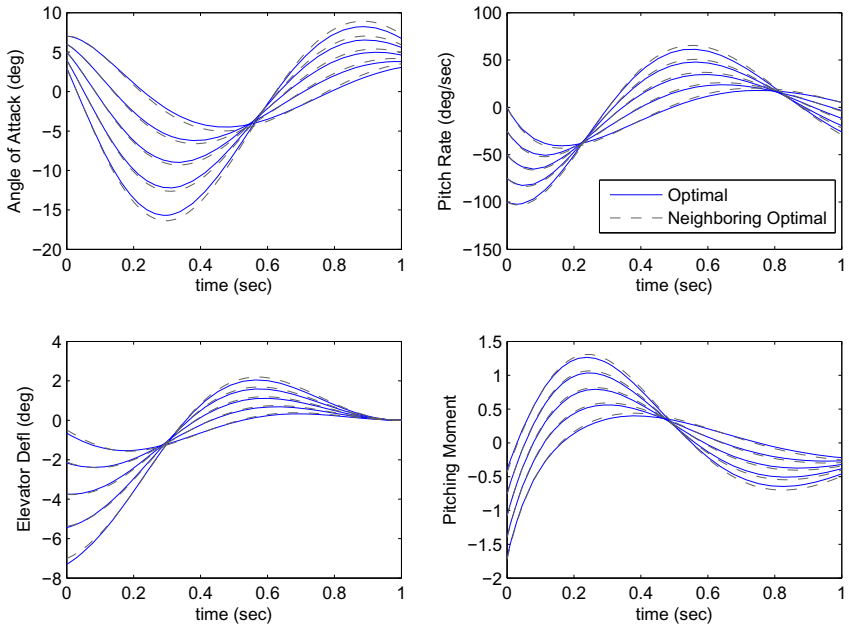

Figure 5-7. Optimal and neighboring optimal trajectories for varying initial pitch rate and initial angle of attack.

The consistency of the results presented in Figures 5-5 through 5-7 is indeed promising as a starting point. It is important to note that this example is based on an aerodynamic model that is linear by construction, with the exception of a single nonlinear spatially variant term. A full scale six degree of freedom aerodynamic model will necessarily be more complicated and one would expect that as the nonlinearities become stronger the effectiveness of the neighboring optimal controller will decrease.

The limitation of the neighboring optimal controller can be exposed by considering increasingly larger perturbations in initial conditions. For example, Figure 5-8 shows three trajectories for initial angle of attack $\alpha(t_0) = 5 \pm 5$ deg. The neighboring trajectories were computed using only the nominal optimal trajectory as a reference. The results

indicate that even though the NOC performs adequately, the neighboring trajectories differ substantially from the true optimal trajectories, especially at $\alpha(t_0) = 0$ deg.

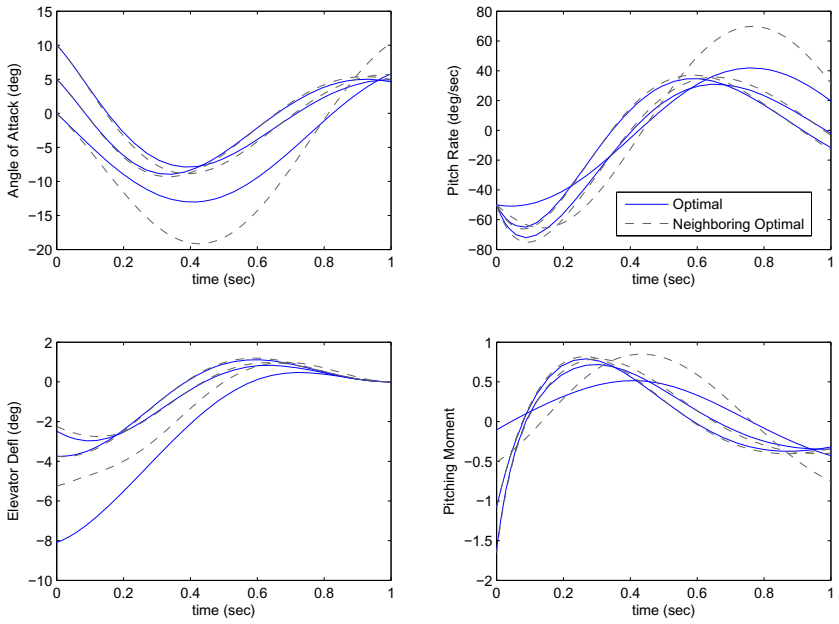

Figure 5-8. Optimal and neighboring optimal trajectories for large perturbations in initial angle of attack.

In comparison of the optimal and neighboring optimal solutions in Figure 5-8, two things are important to note. First, the range in initial $\alpha(t_0)$ is extensive. The initial pitch angle $\theta(t_0)$ has been held constant $\theta(t_0) = 0$ for all of the preceding comparisons. Thus, the change in angle of attack corresponds physically to a different initial vertical velocity. An initial $\alpha(t_0) = 0$ corresponds to zero vertical velocity, e.g. a gravity release. The nominal $\alpha(t_0) = 5$ deg corresponds to an ejection velocity of $75\ ft/sec$, or about $46g$ which is substantial. The maximum initial value of $\alpha(t_0) = 10\ deg$ corresponds to a $150\ deg/sec$ ejection velocity, or about $93g$, which far exceeds any realistic initial condition.

The second important note is that even in the most extreme conditions, the neighboring optimal controller performs well, driving the store to a benign flight condition in the desired time interval. The significant decrease in vertical velocity for $\alpha(t_0) = 0$

has the effect of immersing the store within the aircraft flow field for a longer duration, making the trajectory more sensitive to the nonlinear term in the aerodynamic model. As a result, the store experiences a stronger nose down pitching moment than the controller was designed for and the controller under compensates for the pitching moment, allowing the store to reach a larger nose down angle of attack. The reduced control corresponding to the reduced vertical velocity is actually advantageous, in that it increases the safety margin by allowing the aerodynamic effect to accelerate the store away from the aircraft, albeit at a higher cost than the true optimal solution.

The above discussion can be summarized as follows. For the simple quasi-linear aerodynamic model considered in this case, the initial conditions must be varied beyond reasonable limits in order to find a situation in which the neighboring optimal controller fails to adequately approximate the true optimal solution. Even in the most extreme cases, the performance of the neighboring optimal controller is stable and convergent and a significant improvement over the equivalent uncontrolled trajectory. However, the comparison does suggest that the performance of the neighboring optimal controller is limited in the presence of large deviations away from the nominal solution. This is consistent with the NOC theory developed in Section 5.2, which assumed small variations in the state $\delta\mathbf{x}(t)$ and control $\delta\mathbf{u}(t)$. In the presence of sufficiently large perturbations in initial conditions, the neighboring optimal control performance is marginal. Further investigation of the performance and limitations of the NOC formulation will be considered in Chapter 6.

5.4.3 Neighboring Optimal Control with Inequality Constraints

The equations for applying NOC to a problem with inequality constraints were discussed in Section 5.2.4. The constraints are adjoined to the augmented cost functional using the Lagrange multiplier $\boldsymbol{\mu}(t)$. The result is a set of two equations: one set is valid along an unconstrained arc, and the other is valid along the constrained arc. The difficulty arises at the junction points. Historically, this has been treated as

a multipoint boundary value problem, which may be solved using a multiple shooting algorithm that iterates to find the junction points. This feature introduces significant complexity to the numerical solution using sweep methods [131–133, 136].

Collocation methods result in an entirely different approach. With collocation, the equations are not swept forward or backward, but solved over the duration of the trajectory simultaneously. The boundary conditions are accounted for explicitly. As a result, a simple saturation function is all that is necessary to limit control authority. The equations in Section 5.2.4 can be used to verify that the resulting trajectory is an extremal.

In the previous section, the cost functional was specified in such a way to avoid saturation of the inputs. However, the store separation trajectory can be improved if the system is allowed to use full control authority when necessary. For the current example, the elevator deflection will be limited to $|\delta_e| \leq 10 \ deg$. The equations from Section 5.2.4 will be used to verify the stationarity of the resulting trajectory, restated in Equation (5–104).

$$\text{When: } \begin{cases} \mathbf{C} < 0, \quad \delta\boldsymbol{\mu} = 0, \quad \delta\mathbf{u} = -H_{uu}^{-1}\left(H_{ux} + \mathbf{f}_u^T S\right)\delta\mathbf{x} \\ \mathbf{C} = 0, \quad \delta\mathbf{u} = \mathbf{u}_c - \mathbf{u}^*, \quad \delta\boldsymbol{\mu} = -\mathbf{C}_u^{-T}\left[\left(H_{ux} + \mathbf{f}_u^T S\right)\delta\mathbf{x} + H_{uu}\delta\mathbf{u}\right] \end{cases} \tag{5–104}$$

Specifically, the control is first computed using $\delta\mathbf{u} = -H_{uu}^{-1}\left(H_{ux} + \mathbf{f}_u^T S\right)\delta\mathbf{x}$. If the inequality constraint is active (e.g. $|\mathbf{u}| = |\mathbf{u}^* + \delta\mathbf{u}| > 10 \ deg$), the control is limited to $10 \ deg$ and the Lagrange multiplier is $\delta\boldsymbol{\mu} = -\mathbf{C}_u^{-T}\left[\left(H_{ux} + \mathbf{f}_u^T S\right)\delta\mathbf{x} + H_{uu}\delta\mathbf{u}\right]$. A simple check to verify $\delta\boldsymbol{\mu} \geq 0$ is sufficient to ensure stationarity.

Figure 5-9 shows optimal and neighboring optimal trajectories with the elevator deflection constrained to $|\delta_e| \leq 10 \ deg$. The initial condition was specified as $\alpha(t_0) = 1 \ deg$, $q(t_0) = -50 \ deg/sec$. The cost was specified as $Q_\alpha = 10$ and $R_{\delta_e} = 1$, putting more emphasis on minimizing the angle of attack $\alpha(t)$ at the expense of more control effort.

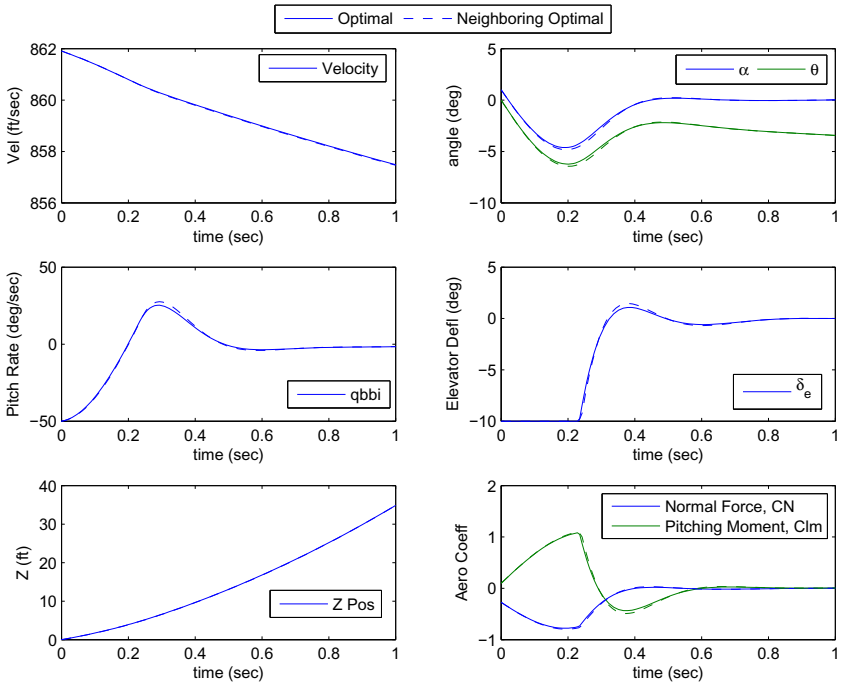

Figure 5-9. Optimal and neighboring optimal trajectories with constrained elevator deflection.

The constraint multiplier $\mu(t)$ for both the optimal and neighboring optimal trajectories is shown in Figure 5-10. During the constrained arc, the constraint multiplier is positive, indicating that a reduction in cost could only be accomplished by violating the constraint. During, the unconstrained arc, the constraint multiplier is zero to numerical precision, indicating the constraint is inactive. Note that the optimal and neighboring optimal constraint multipliers agree quite well for the same initial conditions, as expected.

Figure 5-11 shows a series of optimal and neighboring optimal trajectories for varying initial pitch rate. The reference trajectory was computed using an initial pitch rate of $q(t_0) = -50\ deg/sec$. The remaining two optimal trajectories were computed for increasingly negative values of initial pitch rate. The neighboring optimal trajectories, computing using the first trajectory as a reference, agree quite well with the true optimal trajectories.

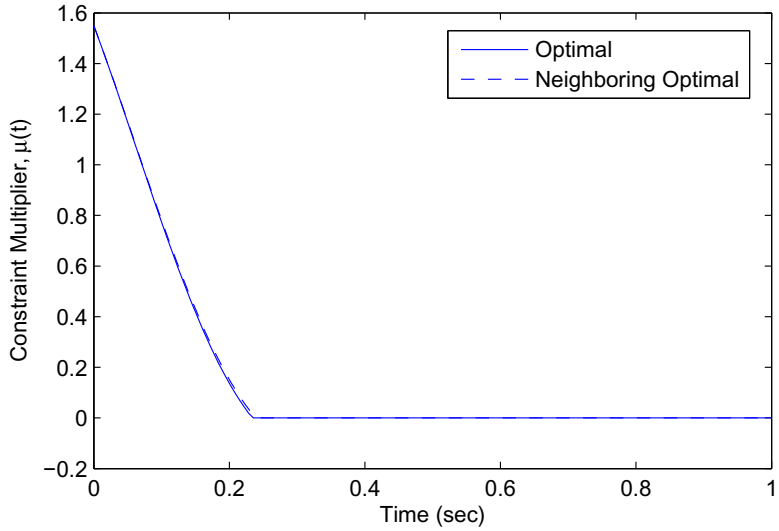

Figure 5-10. Constraint multiplier for optimal and neighboring optimal trajectories with constrained elevator deflection.

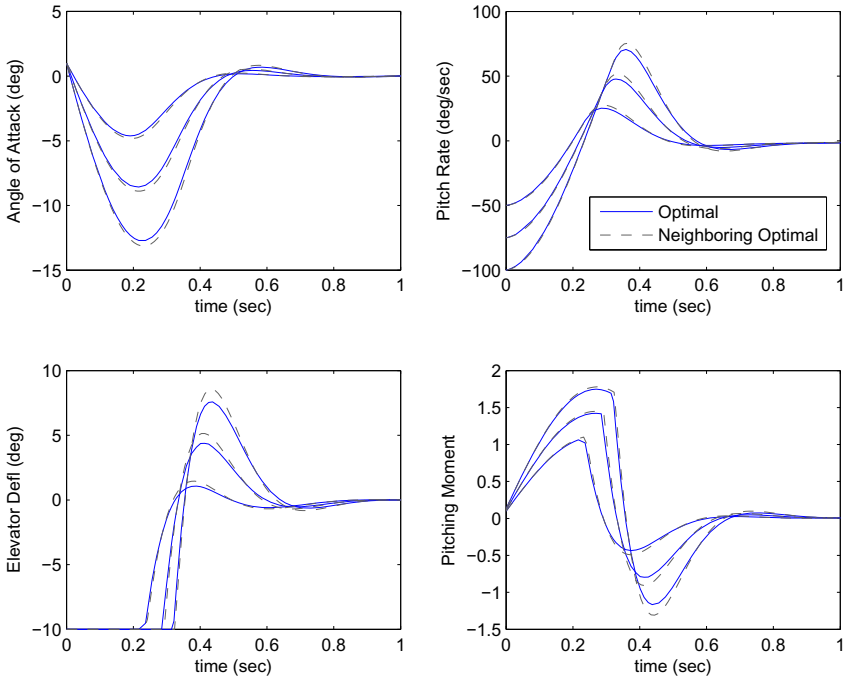

Figure 5-11. Optimal and neighboring optimal trajectories with constrained elevator deflection for varying initial pitch rate.

Figure 5-12 shows the constraint multipliers for the extremal trajectories shown in Figure 5-11. The positive value of the multiplier during the constrained arc indicates stationarity.

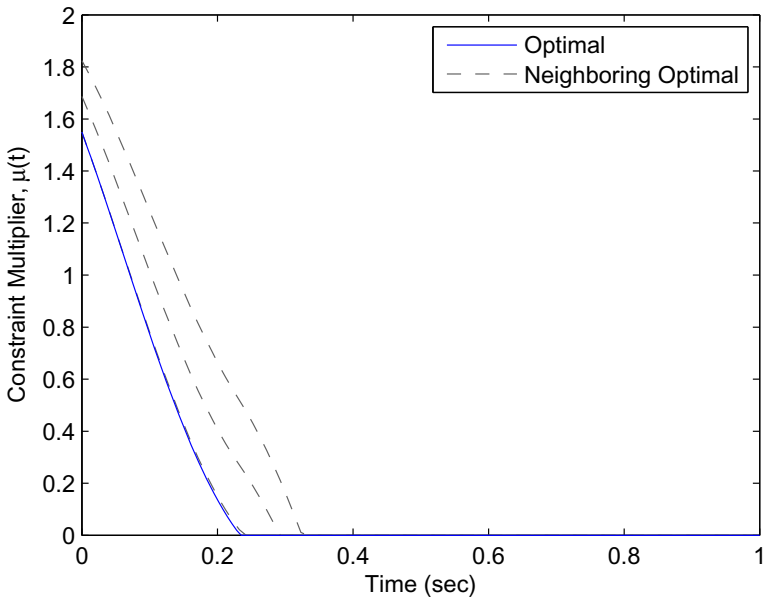

Figure 5-12. Constraint multiplier for optimal and neighboring optimal trajectories with constrained elevator deflection for varying initial pitch rate.

The results above indicate that the neighboring optimal controller adequately represents the optimal performance of the system even in the presence of constraints. However, constraints are inherently nonlinear the results are not always so exemplary. Figure 5-13 shows a series of optimal and neighboring optimal trajectories with varying initial pitch rate $q(t_0)$, with increasingly smaller initial values.

The reference optimal trajectory for $q(t_0) = -50\ deg/sec$ is identical to the trajectory shown previously in Figure 5-10. However, the agreement between the subsequent optimal and neighboring optimal trajectories is substantially different. The neighboring optimal controller is designed to minimize the angle of attack $\alpha(t)$ by using maximum control effort to counteract a significant nose down pitch rate near carriage. When the initial pitch rate is substantially reduced, the optimal trajectory changes dramatically resulting in large variations that degrade the accuracy of the neighboring optimal controller. Fortunately, the neighboring optimal controller is still stable and convergent and again biased toward an increased safety margin by driving the store nose down,

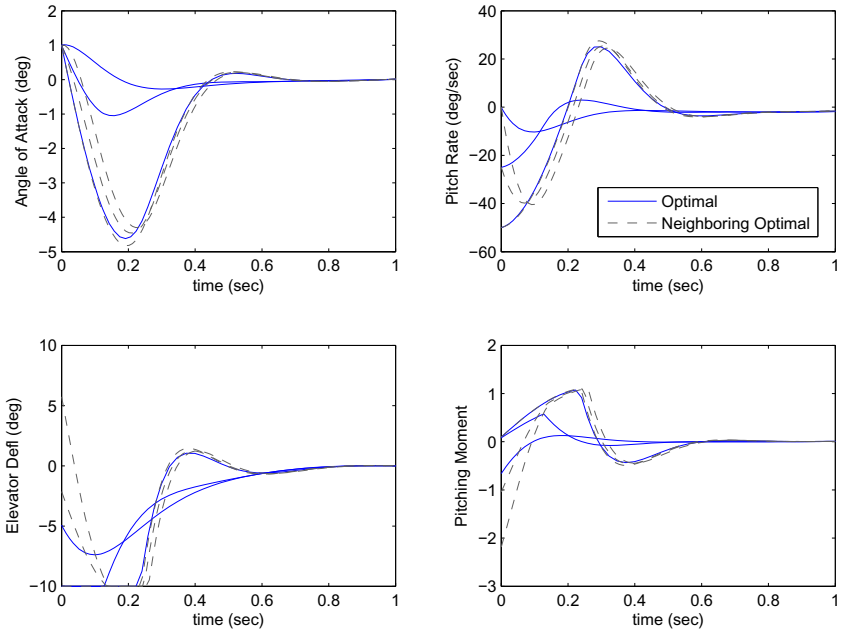

Figure 5-13. Optimal and neighboring optimal trajectories with constrained elevator deflection for varying initial pitch rate.

accelerating the store away from the aircraft, albeit at a higher cost than the true optimal solution.

Finally, Figure 5-14 shows an example with extremely adverse initial conditions. The reference optimal trajectory is the same as previous examples for $\alpha(t_0) = 1\ deg$ and $q(t_0) = -50\ deg/sec$. The perturbed initial conditions are $\alpha(t_0) = 0\ deg$ and $q(t_0) = 50\ deg/sec$. Physically, these initial conditions are equivalent to a gravity release (zero ejection velocity) with an initial nose up pitch rate, a potentially dangerous situation that may lead to the store flying back toward the aircraft. Therefore, this example is a "stress case" for the neighboring optimal controller.

Although there is a substantial difference between the optimal and neighboring optimal solutions for the perturbed initial conditions, the neighboring optimal controller performs quite well under these adverse conditions. The nose-up pitch rate is immediately arrested using maximum control effort. The neighboring extremal plunges much further

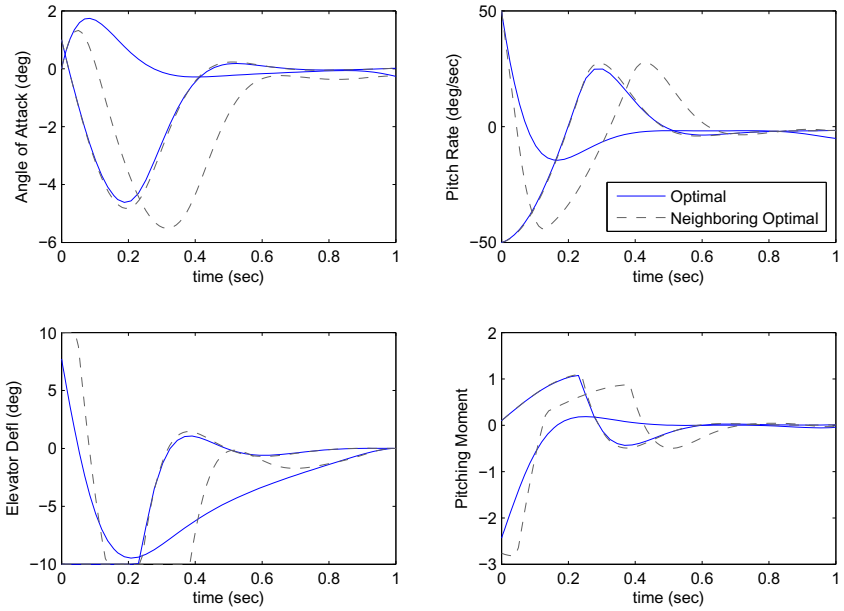

Figure 5-14. Optimal and neighboring optimal trajectories with constrained elevator deflection for extremely adverse initial conditions.

nose down than necessary, but still achieves an increasing safety margin in comparison with the optimal trajectory.

The above discussion can be summarized as follows. For the simple quasi-linear aerodynamic model considered in this case, neighboring optimal control in the presence of constraints adequately represents the true optimal performance when the constraints do not cause large disparity between the optimal and neighboring optimal solutions. However, even in the most adverse conditions considered, the neighboring optimal controller performed well, resulting in a safe and acceptable trajectory.

5.4.4 Neighboring Optimal Control with Terminal Cost

In all examples considered to this point, the terminal cost has been neglected, $S_f = 0$. The terminal cost can be used to achieve a desired terminal condition, focusing the control effort near the end of the trajectory. Figure 5-15 shows a reference optimal trajectory and a series of neighboring optimal trajectories for varying initial pitch rate. The Lagrange cost was specified as $Q_\alpha = 0$ and $R_{\delta_e} = 10$, which limits control effort

during the trajectory. The end point cost, or Mayer cost, was specified as $S_{f_\alpha} = 10$ to emphasize a minimal angle of attack at $t = t_f$.

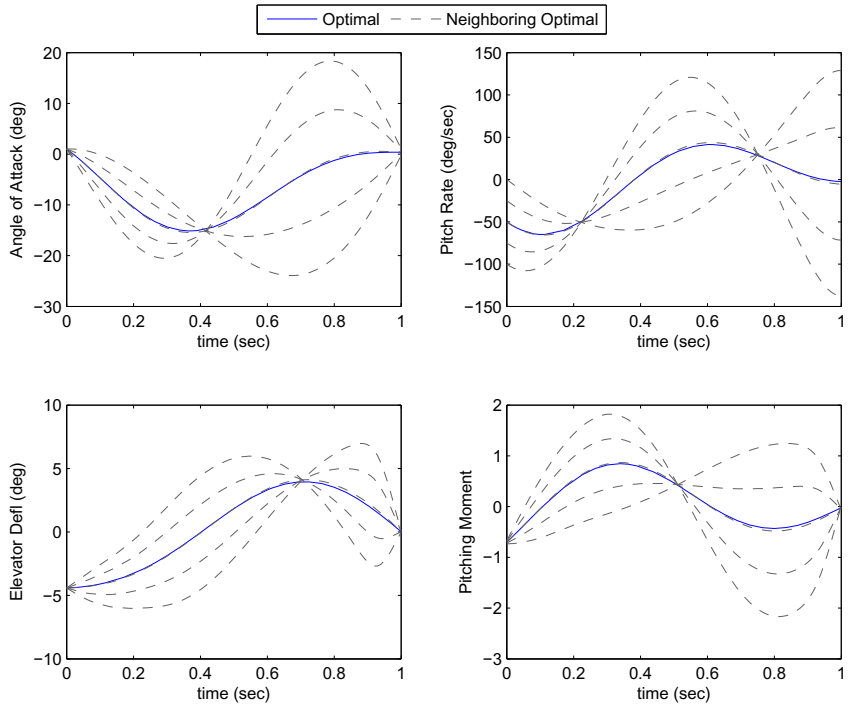

Figure 5-15. Optimal and neighboring optimal trajectories with terminal cost.

The solution $S(t)$ to the Riccati equation and the corresponding feedback gains $K(t) = -R^{-1}\mathbf{f}_u^T S(t)$ are shown in Figure 5-16. The Riccati gains are reduced to $1/100^{\text{th}}$ of the initial values during the mid section of the trajectory, commensurate with $Q = 0$. The gains that affect $\alpha(t_f)$ are increased near the end of the trajectory in order to minimize the end point cost.

Referring back to Figure 5-15, note the terminal condition $\alpha(t_f) \approx 0$ comes at the expense of a large variation in the terminal pitch rate $-150 < q(t_f) < 150\ deg/sec$. As a result, the store is far from a trimmed flight condition at $t = t_f$ and additional control would be necessary to capture the pitch rate. From this perspective, a non-zero cost on $\alpha(t)$, such as $1 \leq Q_\alpha \leq 10$, is preferable.

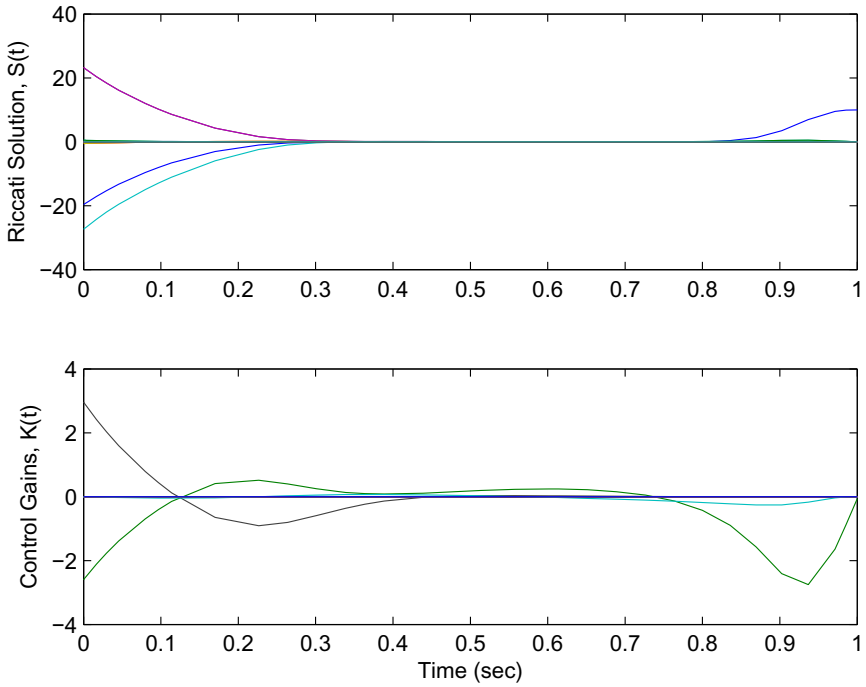

Figure 5-16. Solution to Riccati equation and feedback gains for neighboring optimal trajectories with terminal cost.

Finally, Figure 5-20 shows a series of neighboring trajectories for varying initial pitch rate with both Lagrange cost, $Q_\alpha = 1$ and $R_{\delta_e} = 10$, and Mayer cost, $S_{f_\alpha} = S_{f_q} = 1$. The trajectories terminate near a trimmed flight condition with $\alpha(t_f)$ and $q(t_f)$ near zero without excessive control effort. If more emphasis on $\alpha(t)$ is desired, a high weight on Q_α can be selected. In this case, the terminal conditions are very near zero and the end point cost can be omitted.

5.4.5 Neighboring Optimal Control with Terminal Constraints

The results with terminal cost from Section 5.4.4 can be extended to the case with terminal constraints. The solution is more involved, given the requirement of solving two additional matrix differential equations.

Figure 5-18 shows an optimal trajectory and several neighboring trajectories for varying initial pitch rate. In this case, the end point constraint was selected such that $\alpha(t_f) = 0$ and $q(t_f) = 0$.

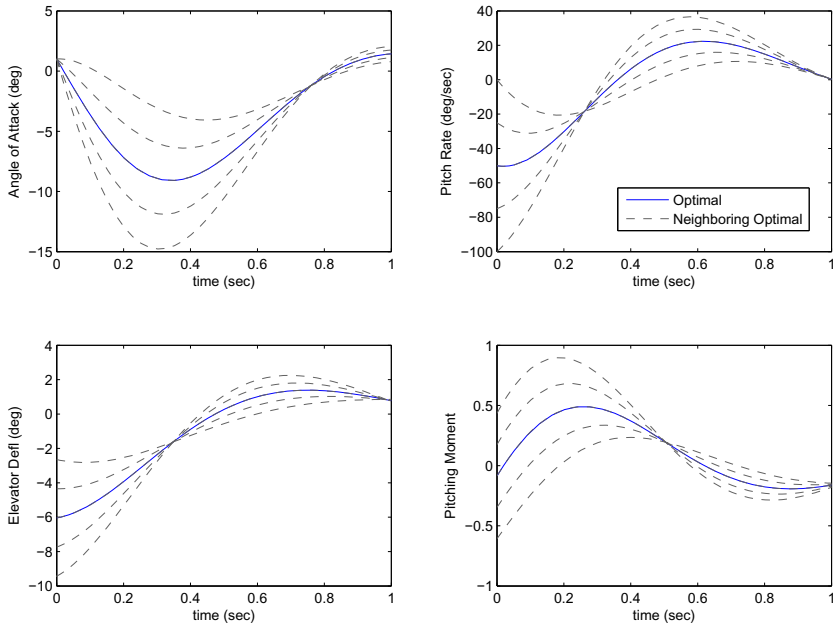

Figure 5-17. Optimal and neighboring optimal trajectories with cumulative and terminal cost.

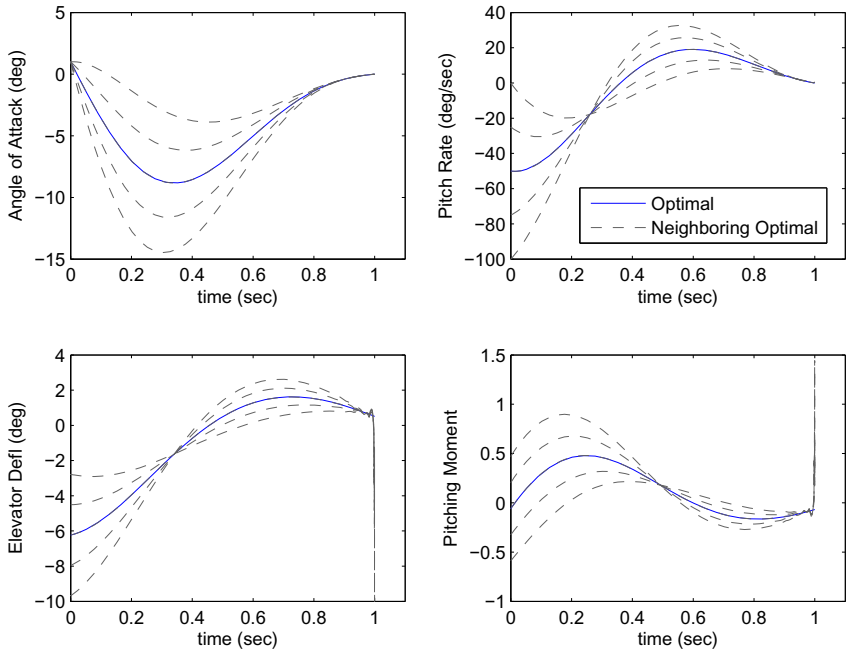

Figure 5-18. Optimal and neighboring optimal trajectories with terminal constraints.

It is clear that the trajectories converge to $\alpha(t_f) = 0$ and $q(t_f) = 0$ as desired. However, terminal constraints result in infinite gains near the end point, as suggested in Figure 5-18 by the sharp drop in elevator deflection at $t = t_f$.

The solution to the matrix differential equations are shown in Figure 5-19. The matrix $Q(t)$ converges to zero at $t = t_f$, giving rise to the infinite gains through the inverse $Q^{-1}(t_f)$. This is clearly an undesirable characteristic and of limited utility for store separation.

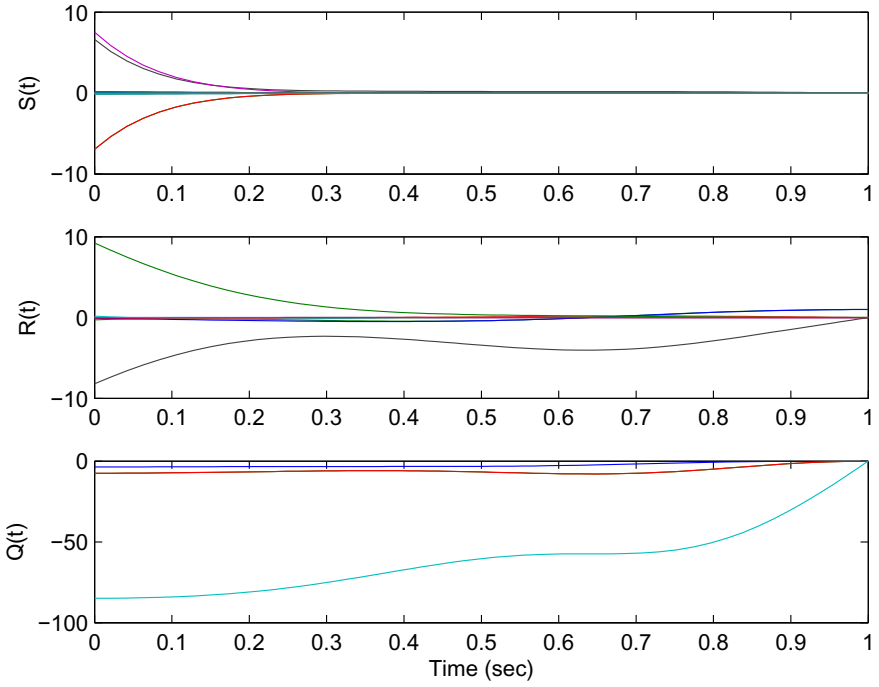

Figure 5-19. Solution to differential equations for neighboring optimal trajectories with terminal constraints.

Terminal constraints may be practically useful or absolutely necessary for some systems. For store separation, it is desirable to be near a trimmed flight condition at $t = t_f$, but it is not required to be at an exact flight condition. Given the additional complexity of infinite gains arising from terminal constraints, the end point cost is preferred over the end point constraint approach.

5.4.6 Infinite Horizon Neighboring Optimal Control

The previous sections considered neighboring optimal control with cumulative cost, end point cost, inequality constraints, and end point constraints. In each case, the HBVP is the same; the costs and constraints affect primarily the boundary conditions and the neighboring optimal differential equations. In all cases, the neighboring optimal feedback gains are time varying, but the gains change dramatically based on the boundary conditions.

In this section, the performance of the controller is extended beyond the final time $t = t_f$ used to solve the HBVP. In particular, the open loop optimal control problem is solved over the interval $t \in [t_0, t_f] = [0, 1]$, but the neighboring optimal feedback controller is used to control the system well beyond the open loop horizon. By judicious specification of the terminal cost, the boundary conditions are specified such that the neighboring optimal controller continues to respond to disturbances in an optimal manner indefinitely, i.e. over an infinite horizon.

This approach, herein referred to as infinite horizon neighboring optimal control (IHNOC), has significant practical value for transitional systems in general and store separation in particular. IHNOC is used to guide the store through a nonlinear flight regime to a trimmed flight condition. As the store approaches a trimmed flight condition, the controller converges to a linear time-invariant controller. The time-invariant controller, mathematically equivalent to a linear quadratic regulator, can be used to hold the store in a trimmed flight condition until transition to the mission autopilot is complete. This is clearly a desirable characteristic for many systems that exhibit nonlinearities. To the author's knowledge, this novel application of NOC to a system with transitional nonlinearities has not been documented elsewhere.

Figure 5-20 shows a series of optimal and neighboring optimal trajectories for varying initial pitch rate $q(t_0) = 0 \pm 50\ deg/sec$. The neighboring optimal trajectories are determined using a reference trajectory with $q(t_0) = 0\ deg/sec$. The agreement between

the optimal and neighboring optimal trajectories is good, despite the large variation in $q(t_0)$ and the control inequality constraints.

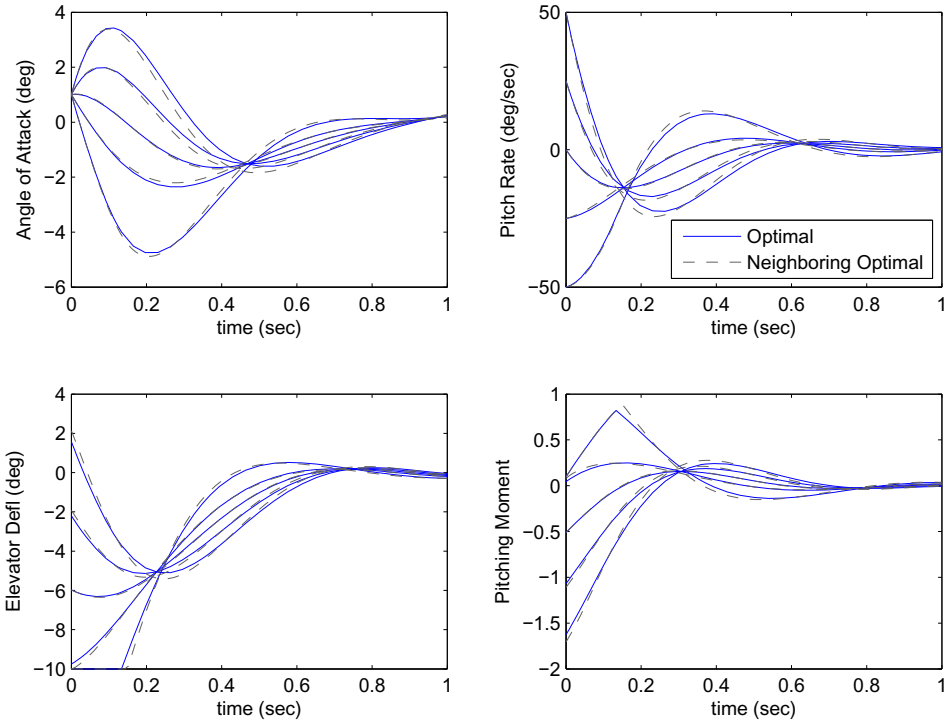

Figure 5-20. Optimal and neighboring optimal trajectories for varying initial pitch rate.

The extremal trajectories in Figure 5-20 are determined using a Lagrange cost of $Q_\alpha = R_{\delta_e} = 10$. The Mayer cost was specified as the positive definite solution of the algebraic Riccati equation (5–105), with the constant matrices F and G determined by Equation (5–106). The resulting Riccati solution and control gains are shown in Figure 5-21.

$$0 = -S_f F - F^T S_f + S_f G R^{-1} G^T S_f - Q \tag{5–105}$$

$$F = \lim_{t \to t_f} \mathbf{f}_x(t), \quad G = \lim_{t \to t_f} \mathbf{f}_u(t) \tag{5–106}$$

The time-varying structure of the control gains is evident from Figure 5-21. The gains begin at a maximum value at the initial time when the store is nearest the

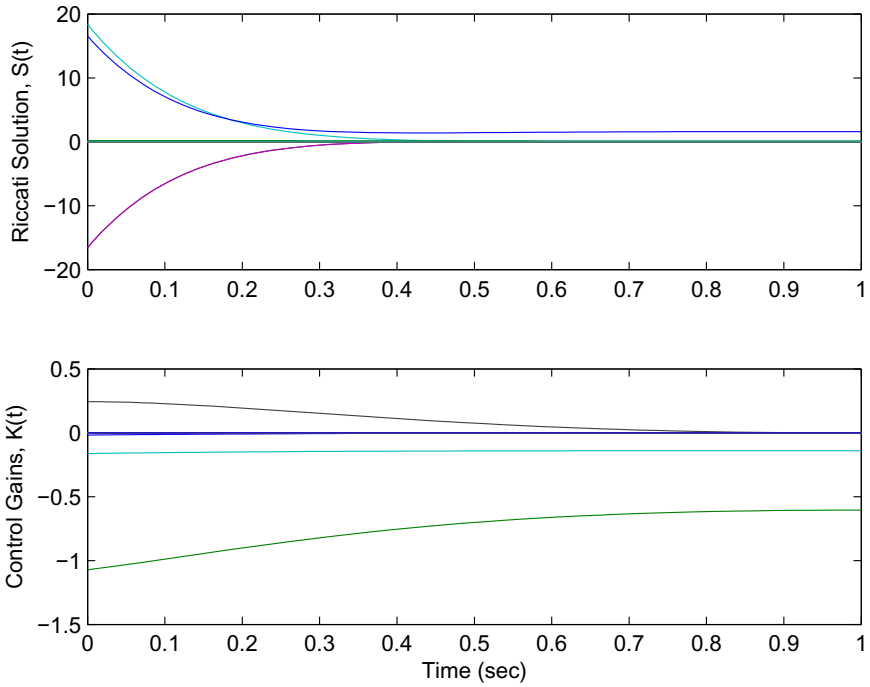

Figure 5-21. Solution to Riccati equation and feedback gains for neighboring optimal trajectories.

aircraft and converge rapidly to constant values as the aerodynamic nonlinearities become insignificant. The Riccati solution $S(t)$ and control gains $K(t)$ are constant after $0.9\ sec$, indicating the store is sufficiently far away from the aircraft that the aerodynamic interference is negligible.

Extension of IHNOC beyond $t_f = 1$ is trivial. The reference state $\mathbf{x}^*$, reference control $\mathbf{u}^*$ and feedback gains $K(t)$ are held constant at the terminal values for as long as the controller is active. Figure 5-22 shows the resulting series of trajectories. Note that the optimal trajectory is terminated at $t = t_f$, but the extremal trajectories continue smoothly to $t = 2$. All five simulations converge to the same trimmed flight condition, despite the large variations in initial conditions.

For comparison, Figure 5-23 shows a series of neighboring trajectories. The extremal trajectories are determined using a Lagrange cost of $Q_\alpha = Q_q = 1$ and $R_{\delta_e} = 10$, putting more emphasis on minimizing the pitch rate $q(t)$. The results are

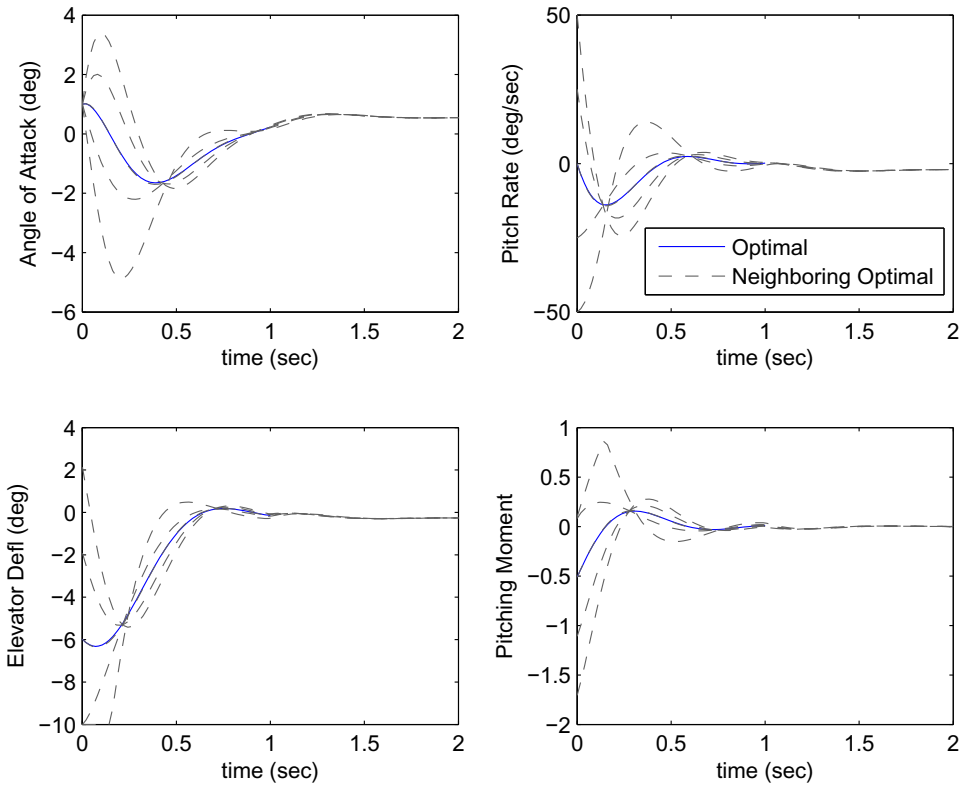

Figure 5-22. Optimal and neighboring optimal trajectories for varying initial pitch rate, extended beyond $t = t_f$.

consistent with the previous example. However, due to the additional cost placed on $q(t)$, the angle of attack $\alpha(t)$ is more dispersed at $t = t_f$ and does converge until $t = 2\ sec$. The results show how infinite horizon neighboring optimal control continues to operate in an optimal manner beyond the original finite horizon.

Finally, Figure 5-24 shows a series of neighboring trajectories with $Q_\alpha = R_{\delta_e} = 10$ and $Q_q = 0$. The initial conditions include variation in pitch rate $q(t_0) = -50 \pm 50\ deg/sec$ and angle of attack $\alpha(t_0) = 2 \pm 2\ deg$. The neighboring extremals are determined using the optimal trajectory with $\alpha(t_0) = 2\ deg$ and $q(t_0) = -50\ deg/sec$ as a reference trajectory. The results are again favorable, demonstrating convergence to a trimmed flight condition for a wide range of initial conditions.

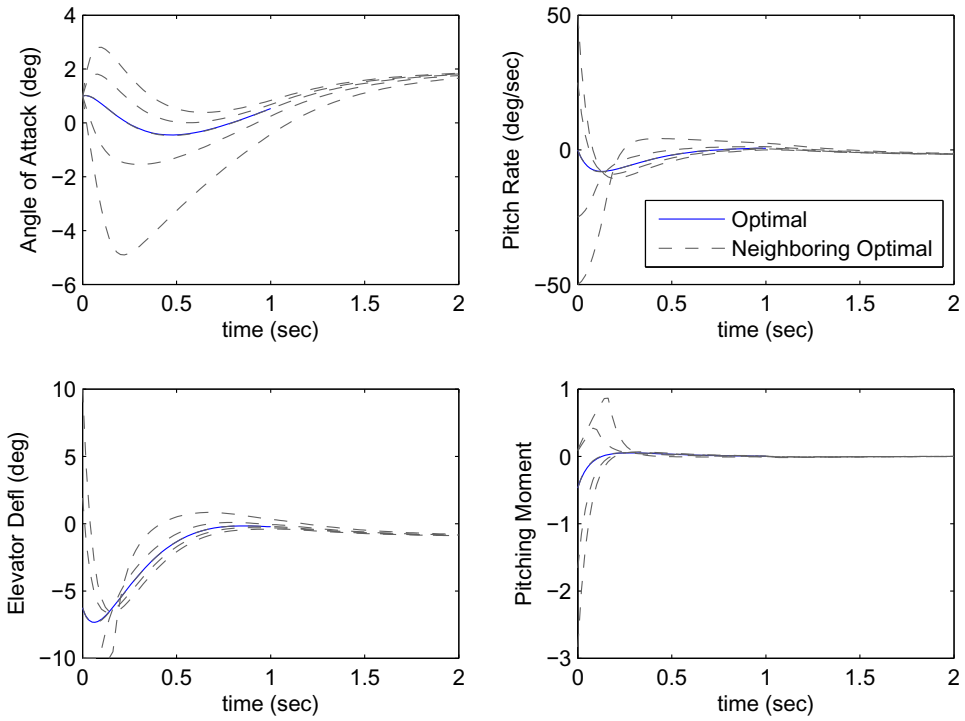

Figure 5-23. Optimal and neighboring optimal trajectories for varying initial pitch rate, with additional cost on $q(t)$.

5.4.6.1 Response to flow field disturbances

Neighboring optimal control is designed to correct for perturbations in the initial conditions $\delta\mathbf{x}(t_0)$. However, since any time is a valid "initial" time, NOC can also be used to correct for disturbances that happen along the optimal path. For store separation, turbulent air near the aircraft is of particular concern.

The study of aerodynamic turbulence is no small matter and a thorough analysis of turbulent effects on store separation is beyond the scope of this investigation. Rather, a more direct approach will be considered to demonstrate the performance of the controller in the presence of random disturbances.

The presence of random disturbances also changes the nature of the dynamic system from a deterministic system to a stochastic system. Methods for addressing optimal control in the presence of random disturbances are the subject of much

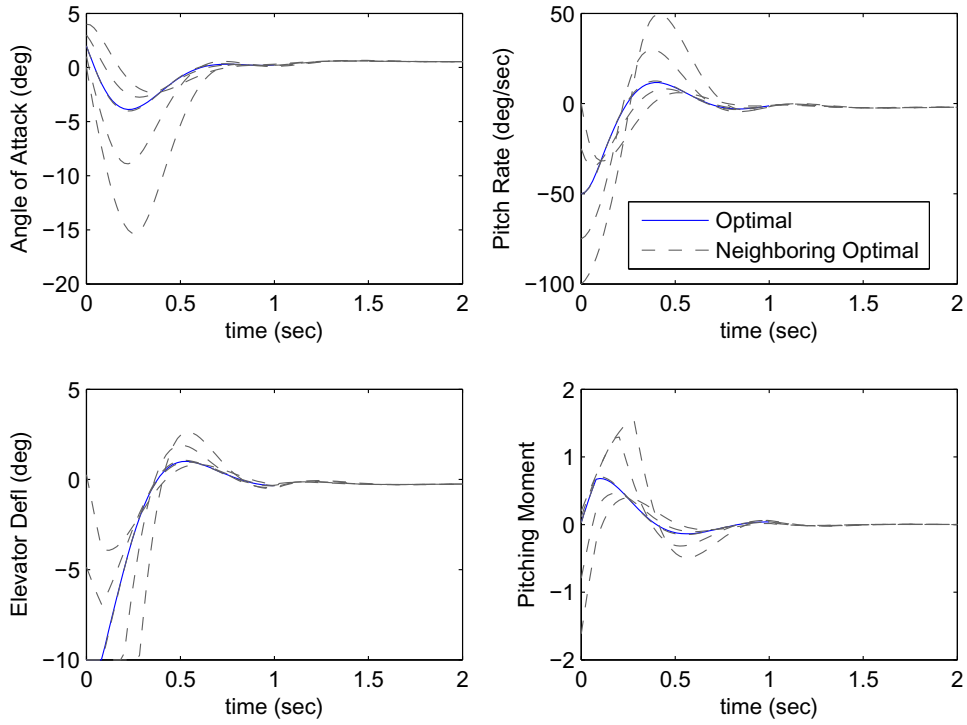

Figure 5-24. Optimal and neighboring optimal trajectories for varying initial pitch rate and initial angle of attack.

research [111, 113, 116]. For a linear time-varying stochastic system, a linear quadratic gaussian (LQG) controller may be utilized [113]. The LQG essentially combines a Kalman filter for state estimation and a LQR for control. Although such an approach would be a natural extension to this investigation, this is beyond the scope of the present work. This remains an area for continued research in store separation.

Figure 5-25 shows a snapshot of the longitudinal aerodynamic coefficients derived from store separation flight test 2265 (Mach 0.9 / 450 KCAS). The left most subfigures show the estimated aerodynamic coefficient based on inertial measurements, as well as a “smoothed” estimate. The smoothed estimate was determined using a 51-point moving average. The residuals for the three aerodynamic coefficients are shown on the right side of Figure 5-25. These residuals are assumed to include effects from aerodynamic turbulence, sensor noise, and structural vibration. No attempt will be made

to separate the effect of each source. Rather, the residuals will be used to introduce disturbances into the system, representative of the disturbances encountered in flight.

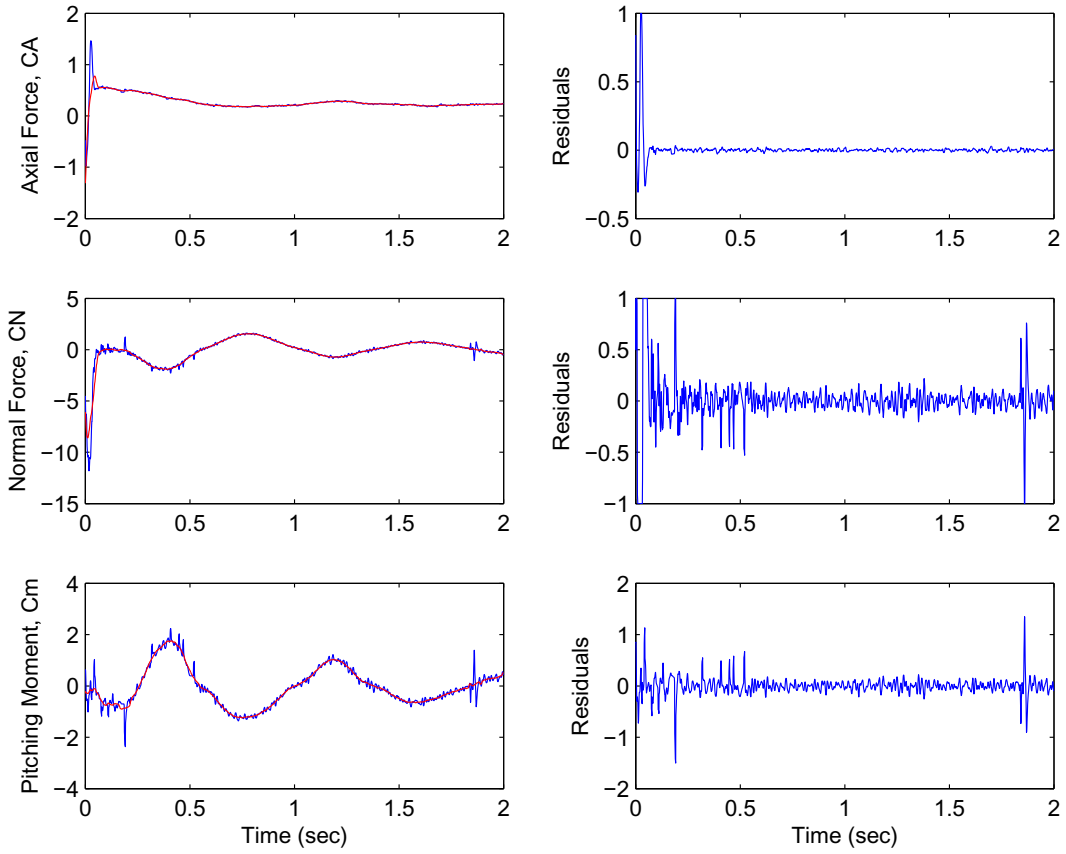

Figure 5-25. Aerodynamic coefficients estimated from flight test data.

Figure 5-26 shows an optimal trajectory and neighboring optimal control in the presence of random disturbances. The effect of the random disturbance is evident in the normal force and pitching moment coefficients. The inertia of the system acts as a low pass filter to mitigate the turbulent effects and the control system performs well amidst the random disturbances.

Figure 5-27 shows a series of neighboring trajectories with increasing values of turbulence. The trajectories were determined with the same turbulence signal amplified

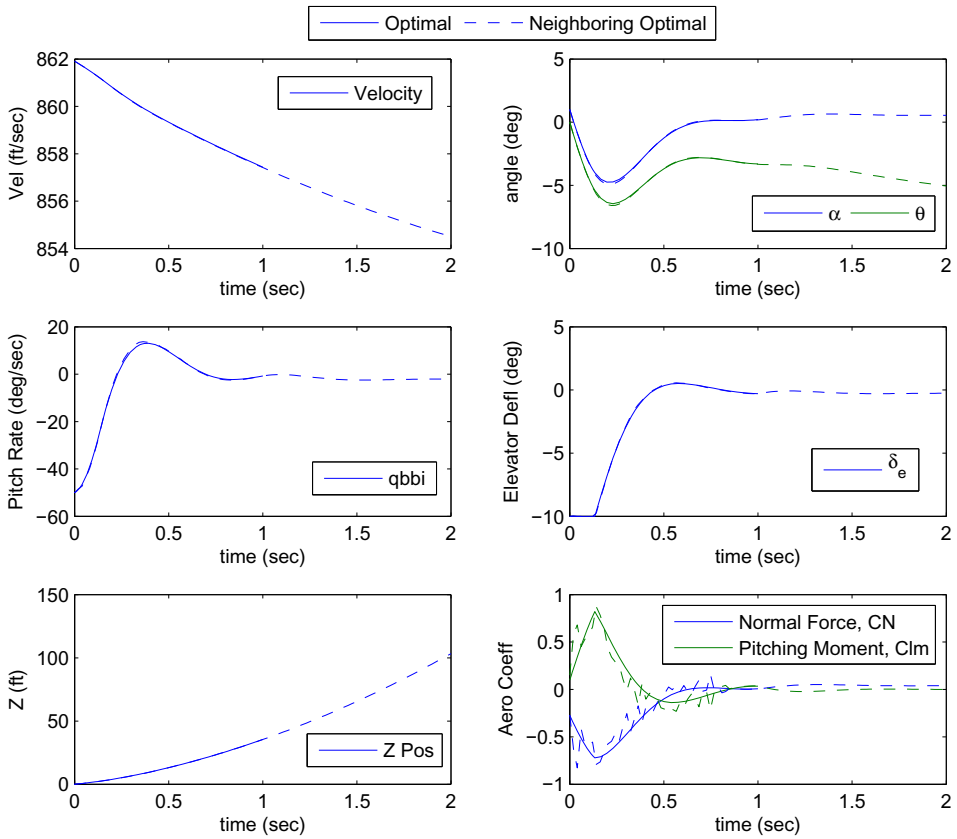

Figure 5-26. Optimal and neighboring optimal trajectories with random disturbances representative of aerodynamic turbulence.

by one, three, and five times the original magnitude. Again, the turbulence is "averaged out" by the inertia of the store and the controller performs well in all three cases.

The random disturbances introduced in Figure 5-25 are not completely stationary signals. It is clear from careful inspection of the plot that the magnitude of the random disturbances is larger near the beginning of the signal, perhaps due to ejection-induced structural vibrations. Even so, the high frequency of the disturbances results in the effect being averaged out by the inertia of the store. To further stress the controller, it is necessary to consider a non-stationary random disturbance with a low frequency component.

Consider the non-stationary signal shown in Figure 5-28. The pitching moment increment is a composition of the original random turbulence signal plus a deterministic

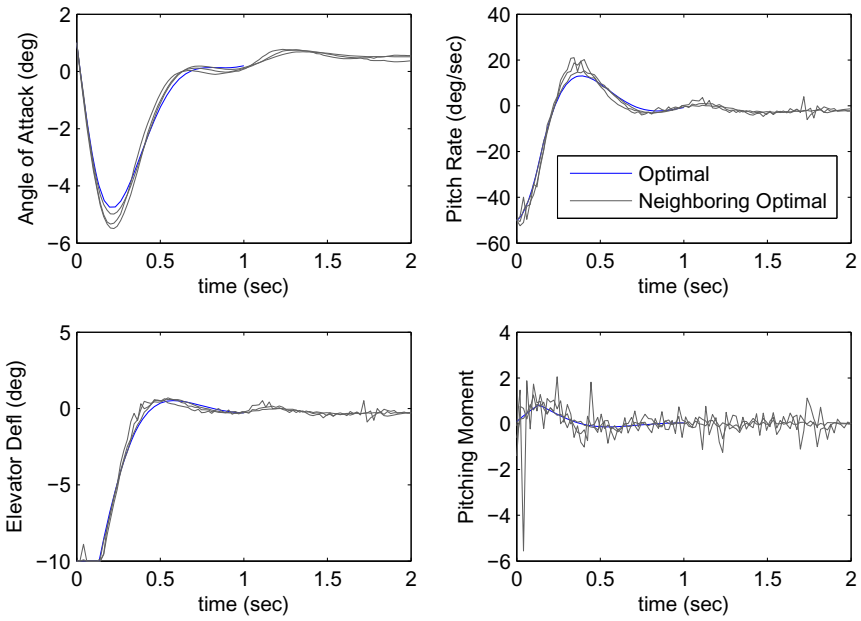

Figure 5-27. Optimal and neighboring optimal trajectories with amplified random disturbances representative of aerodynamic turbulence.

effect due to a hypothetical vertical wind gust given by $f(t) = Ae^{-3t}\sin(2\pi t)$ with $A = 1$.

Figure 5-29 shows the neighboring optimal controller performance in the presence of non-stationary random disturbances, representative of turbulent wind gusts. The trajectories were determined using $f(t) = Ae^{-3t}\sin(2\pi t)$ with $A = -2, -1, 1, 2$, to represent a range of severe vertical gusts. It should be noted that the deterministic disturbance is analogous to an unknown change in system parameters and the neighboring optimal trajectory no longer minimizes the original cost function. Even so, the near-optimal controller performs satisfactorily in the presence of non-stationary random disturbances.

Consideration of the magnitude of the disturbance is warranted to further appreciate the results. The pitching moment sensitivity to angle of attack for this example is given in Table (4-1) as $C_{m_\alpha} = -4.05\, rad^{-1}$. Thus, a unit change in pitching moment $\Delta C_m = \pm 1$ corresponds to a change in angle of attack $\Delta\alpha = \pm 14\, deg$. For the current example, the freestream velocity is $450\ KCAS$. A change in angle of attack by $\Delta\alpha = \pm 14\, deg$ would

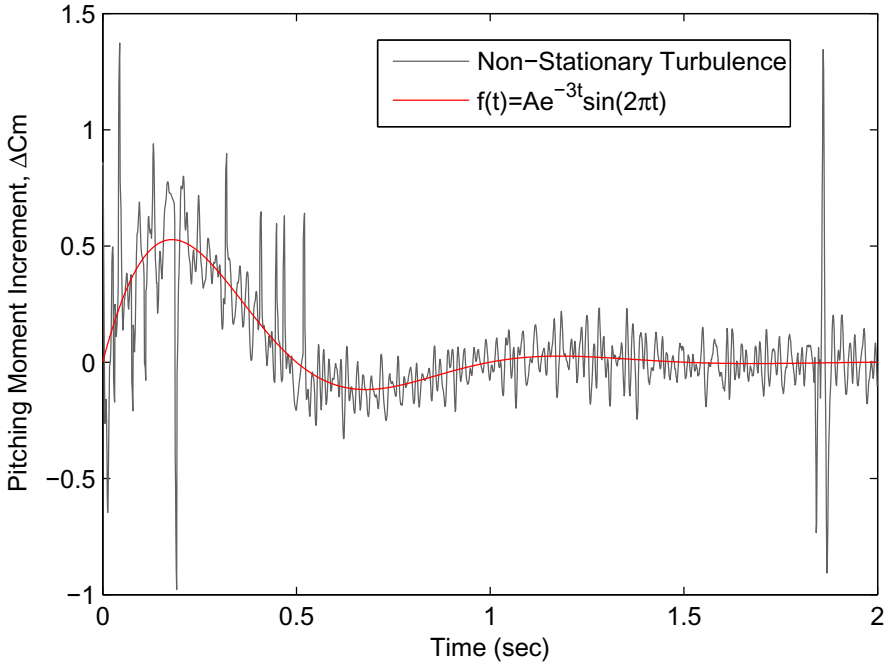

Figure 5-28. Non-stationary signal representative of a turbulent wind gust effect on pitching moment.

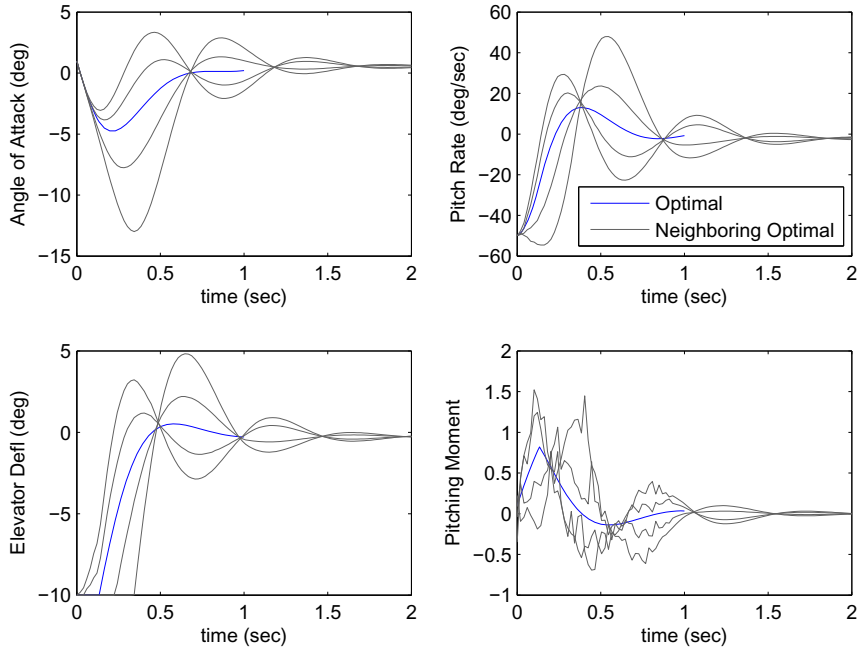

Figure 5-29. Optimal and neighboring optimal trajectories with amplified turbulent wind gusts.

require a vertical wind gust of approximately $\pm 110\ KCAS$. Considering these rough estimates, the magnitude of a vertical gust to produce $\Delta C_m = \pm 1$ is substantial. The maximum elevator deflection of $\delta_e = \pm 10\ deg$ represents a pitching moment change of $\Delta C_m = \pm 1.5$, so the vertical gust considered here is on par with the full control authority of the store. Even so, the controller adequately captures the store motion and safely guides the store away from the aircraft.

The above discussion is not intended to be formal or comprehensive in nature. Rather, it is a "quick look" at the performance that can be expected by NOC in the presence of non-stationary random disturbances, such as aerodynamic turbulence. The reader is cautioned that this is a dramatically simplified investigation and conclusions beyond the scope of this example are not warranted.

5.4.6.2 Response to parameter variations

In Section 5.2.5 it was shown that NOC can be used to provide optimal feedback control in the presence of small constant parameter variations, provided the parameter variation is known or can be estimated. However, when the parameter variation is unknown, the control is necessarily sub-optimal.

The performance of the near-optimal controller for the ongoing example is considered here. The parameter that typically has the most significant effect on the store separation trajectory is the longitudinal center of gravity, x_{CG}. The mass properties of every individual store are unique, subject to variations within manufacturing tolerances. Therefore, it is important to consider variations in mass properties, especially in x_{CG}, to determine if the range of possible store trajectories is safe and acceptable.

The location of the store longitudinal center of gravity relative to the aerodynamic center is known to determine the aerodynamic stability. In fact, if the x_{CG} is too far aft, the store will become inherently unstable. For the example store, this occurs when the x_{CG} is shifted by approximately ten inches, $\Delta x_{CG} = 10\ inches$. Figure 5-30 shows a series of unguided (jettison) trajectories for the center of gravity $-10 \leq \Delta x_{CG} \leq 10$ at 5 inch

increments. The uncontrolled trajectory with $\Delta x_{CG} = -10\ inches$ is clearly unstable and quickly departs from stable flight, as evidenced by the excessive angle of attack $\alpha(t)$ and pitch rate $q(t)$.

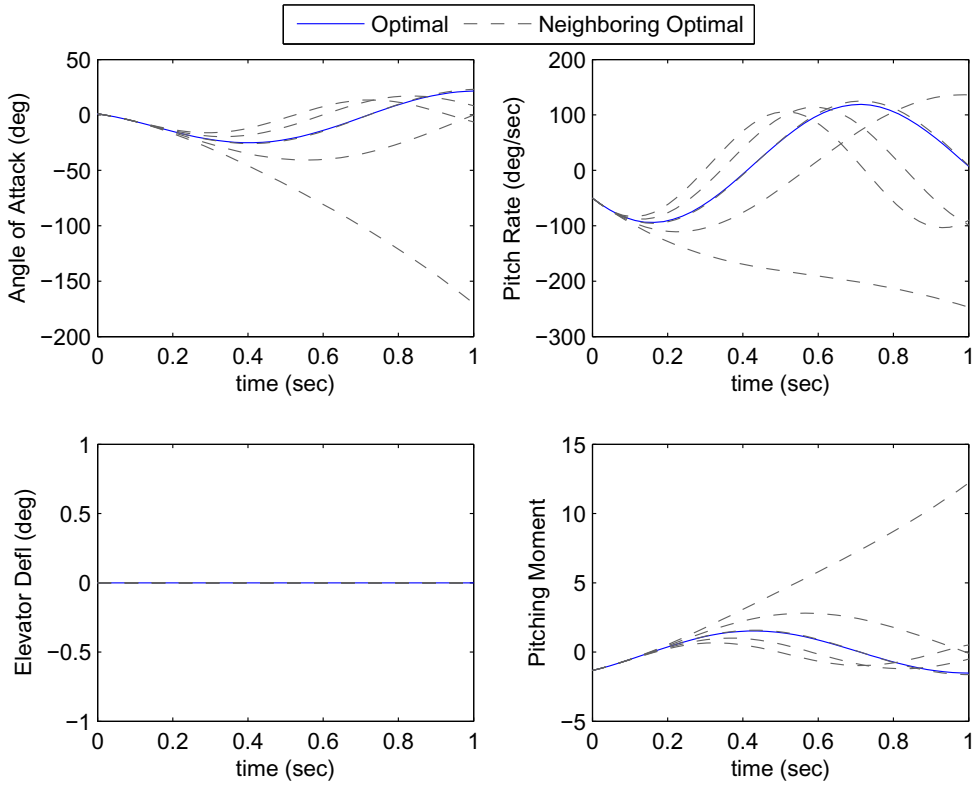

Figure 5-30. Unguided trajectories with parameter variations.

Figure 5-31 shows trajectories using the same range of mass properties with NOC, based on the nominal trajectory with $\Delta x_{CG} = 0$. The results are substantially different. Even for an inherently unstable store with $\Delta x_{CG} = -10\ inches$, the near-optimal controller drives the store to a trimmed flight condition and safely guides the store away from the aircraft. All five of the trajectories converge to a similar trimmed flight condition and exhibit safe and acceptable separation characteristics. These five guided trajectories are a marked improvement over even the best case unguided trajectories.

Further improvement of the separation characteristics (e.g. a reduction in the total cost) could be attained if the constant parameter is measured a priori or if the

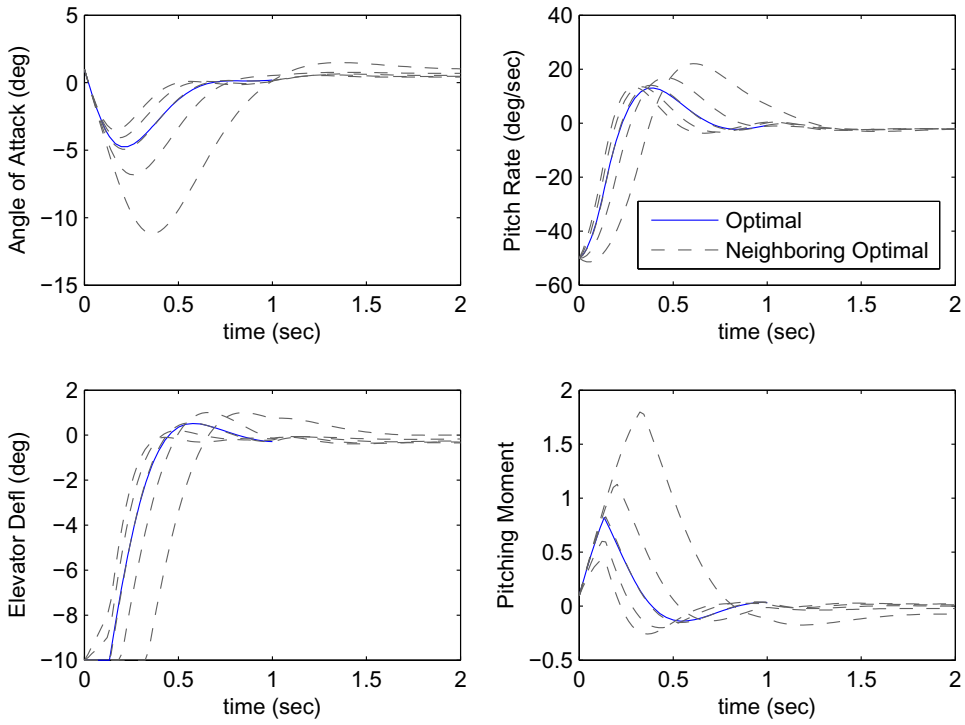

Figure 5-31. Guided trajectories with parameter variations.

parameter is estimated during flight. This is a valid approach for store separation. However, the number of unknown parameters for a realistic system may be exceedingly large and difficult to estimate over the short duration of interest. Furthermore, many of the identified parameters may be time-varying, further complicating the identification procedure. As a result, the neighboring optimal controller is considered “near optimal” in the presence of small unknown parameter variations. However, the above example indicates that even for large parameter variations with off-nominal performance, the neighboring optimal controller may perform adequately, resulting in stable and convergent behavior even for an inherently unstable system. This cursory look at the performance of NOC in the presence of significant parameter variations is promising, but again the reader is cautioned that this is a dramatically simplified investigation and conclusions beyond the scope of this example are not warranted. Further consideration for a realistic case study with parameter variations will be taken up in Chapter 6.

5.5 Chapter Summary

The application of optimal control theory to store separation provides a framework for determining a best case guided trajectory for a store traversing a nonlinear spatially variant flow field. However, the extremal solution is dependent on the specified parameters and initial conditions, and a change in parameters or initial conditions requires the computation of a new extremal solution. The computational burden prohibits the implementation of a real-time optimal controller, rendering an open-loop control strategy. In order to respond to the inevitable variations in initial conditions and system parameters, as well as disturbances along the optimal path, feedback control is necessary. Closed-loop full state feedback control can be accomplished readily using neighboring optimal control.

Neighboring optimal control considers a dynamic model linearized along the optimal path and can be used to minimize the original cost functional to second order. The NOC problem is initially constructed to accommodate perturbations in initial conditions. However, since any time along the extremal trajectory is a valid start time, the neighboring optimal controller naturally accounts for disturbances along the optimal path. NOC can also be extended to provide linear-optimal control for systems with perturbed constant parameters, provided the parameters are known a priori or can be estimated during operation. For systems with unknown parameter variations, NOC affords near-optimal control, provided the parameter variations are small. NOC can also be extended to include problems with path/control constraints and terminal cost or constraints. Finally, NOC is commensurate with the solution to the accessory minimum problem (AMP), and the existence of a neighboring optimal solution provides a sufficient condition for demonstrating the optimality of a candidate extremal solution. Thus, NOC is a comprehensive framework for determining a linear time variant feedback control law when a nominal extremal trajectory is known.

Neighboring optimal control is especially well suited for store separation. The transitional nonlinearities due to the spatially variant flow field surrounding the aircraft become negligible as the distance between the store and aircraft becomes large. Judicious selection of the boundary conditions and cost functional leads to a linear-optimal controller that converges to a time invariant controller in far field conditions, referred to as infinite horizon neighboring optimal control (IHNOC). IHNOC is ideally suited for store separation and provides a linear time variant feedback controller that guides the store away from the aircraft and converges to a time invariant linear quadratic regulator. IHNOC acts as a transitional autopilot and may be used to hold the store in a trimmed flight condition indefinitely, e.g. over an infinite horizon. The result is a compact easily-implemented controller that significantly improves separation characteristics in comparison to an unguided trajectory.

The robustness of the controller was informally demonstrated by application to a variety of challenging scenarios including extreme initial conditions, non-stationary random perturbations representative of aerodynamic turbulence, and large parameter variations. For large deviations from the nominal trajectory, the IHNOC trajectory is substantially different from the true optimal trajectory. However, the neighboring optimal controller performed adequately under even the most extreme cases considered, including stabilization of an otherwise unstable store. This performance analysis was far from comprehensive, but the results are nevertheless promising and further investigation is warranted.

All of the examples considered in this chapter were restricted to a store confined to the vertical plane during separation. As a result, the equations of motion and aerodynamic model were considerably simplified. However, the theory developed herein is equally applicable to a full nonlinear six degree of freedom problem with an arbitrarily complex aerodynamic model, provided the aerodynamic and control gradients can be estimated.

CHAPTER 6
GUIDED STORE SEPARATION

6.1 Overview

The primary objective of this study is to develop a comprehensive approach to improve the separation characteristics of modern ejector-launched guided munitions by utilizing a separation autopilot to guide the store along a preferred trajectory. This investigation is intended to show the significant increase in safety and acceptability that can be achieved through guided store separation with minimal addition in cost and complexity of the guidance and control system.

Development of a guidance and control system for store separation includes (1) identification of a parametric model for the spatially variant aerodynamics, (2) determination of a "best case" trajectory that meets safety and acceptability criteria, and (3) design of an effective feedback controller to account for model uncertainties and operating disturbances. In this research, the parametric model is identified using system identification, the "best case" trajectory is determined using optimal control theory, and the feedback control system is designed using neighboring optimal control; see Figure 6-1. The result is a compact store separation autopilot that explicitly takes into account the spatially variant aerodynamics and leverages the aerodynamic interaction between the aircraft and store to dramatically improve separation characteristics.

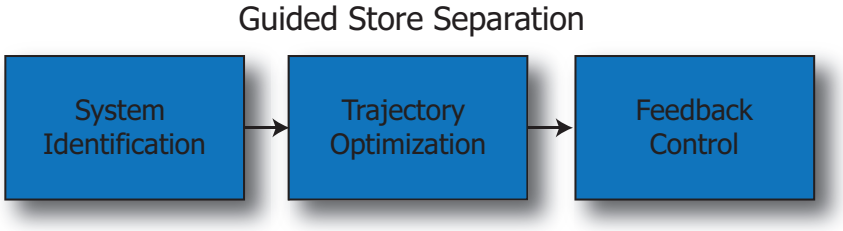

Figure 6-1. Relationship between system identification, trajectory optimization, and feedback control to applied for guided store separation.

System identification, trajectory optimization and feedback control have been examined in detail in Chapters 3, 4, and 5. In each chapter, the theory was developed

in general and applied to store separation in particular, followed by numerical examples to clearly illustrate the application. For instructive clarity, the optimal control examples were limited to consideration of store motion confined to a vertical plane, resulting in a simplified three degree-of-freedom (3DOF) system. In this chapter, the same theory is applied to a full nonlinear six degree-of-freedom (6DOF) store separation analysis. In the same way that earlier chapters were primarily focused on theory, this chapter is primarily focused on application. As a result, mathematical development is sparse and quantitative results are prevalent.

The intent of this chapter is to show the general applicability and readiness of the theory developed in previous chapters. Section 6.2.1 illustrates the application of optimal control theory to determine a preferred separation trajectory that optimizes safety and acceptability criteria using a quadratic cost function. Section 6.2.2 illustrates the application of Neighboring Optimal Control (NOC) to design a linear-optimal feedback controller for store separation. In particular, Infinite Horizon Neighboring Optimal Control (IHNOC) is used to design a control system that accounts for the spatially variant aerodynamics near the aircraft and converges to a time-invariant linear quadratic regulator in far field conditions. Using this approach, the store separation autopilot may be used to safely and effectively transfer the store from release to stable trimmed flight in an optimal manner. These results rely completely on the parametric model developed in Chapter 3; see Section 3.3. In Section 6.3, the IHNOC controller determined using the parametric model is applied to a full nonlinear conventional 6DOF simulation representative of flight test. The store separation autopilot is tested for a wide range of initial conditions and physical parameters with promising results.

6.2 Trajectory Optimization

Trajectory optimization is the process of determining control and state histories for a dynamic system in order to minimize (or maximize) a cost function (or measure of performance) while satisfying prescribed boundary conditions and/or path constraints

[87]. The dynamic system is generally modeled in the time domain using a state space representation. The measure of performance represents a metric or combination of metrics (e.g. time, energy, control effort, deviation from a desired operating condition, etc.) that quantify the desired performance of the system. The boundary conditions include limitations on the initial and/or final state of the dynamic system, as well as limits on the control (e.g. actuator limits, control saturation). Path (or state) constraints are used to exclude trajectories that violate a predetermined range or type of undesirable motion. Each of these components are stated with mathematical precision and combined to create an optimal control problem.

6.2.1 Optimal Control

The objective of an optimal control problem is to determine an admissible control input that minimizes (or maximizes) the desired cost function (or performance index) subject to the specified boundary conditions and dynamic constraints. The solution using an indirect method is based on the calculus of variations. Ordinary calculus is predominantly concerned with the calculus of functions, characterized by the differential operator. Comparatively, the calculus of variations is concerned with the calculus of functionals, characterized by the variational operator. The calculus of variations can be used to derive the classical 1st order optimality conditions, as shown in Section 4.2.1. The optimal control problem statement and optimality conditions are included here for completeness.

6.2.1.1 Problem statement

The objective of an optimal control problem in Bolza form is to minimize a cost functional given by Equation (6–1), subject to dynamic constraints given by Equation (6–2), path and control inequality constraints given by (6–3), and terminal constraints given by Equation (6–4). For brevity, it is assumed that the initial conditions, $\mathbf{x}(t_0)$, and final time, t_f, are specified.

$$J = \phi\big(\mathbf{x}(t_f)\big) + \int_{t_0}^{t_f} L\big(\mathbf{x}(t), \mathbf{u}(t)\big)\, dt \tag{6–1}$$

$$\dot{\mathbf{x}}(t) = \mathbf{f}\big(\mathbf{x}(t), \mathbf{u}(t)\big) \tag{6–2}$$

$$\mathbf{C}\big(\mathbf{x}(t), \mathbf{u}(t)\big) \leq 0 \tag{6–3}$$

$$\psi\big(\mathbf{x}(t_f)\big) = 0 \tag{6–4}$$

Application of optimal control to store separation is straight forward. A quadratic cost functional, given by Equation (6–5) is sufficient for this investigation, where Q is a constant positive semi-definite matrix $Q \geq 0$ and R is a constant positive definite matrix $R > 0$.

$$J = \frac{1}{2}\mathbf{x}(t_f)^T S_f \mathbf{x}(t_f) + \frac{1}{2}\int_{t_0}^{t_f} \left(\mathbf{x}^T Q \mathbf{x} + \mathbf{u}^T R \mathbf{u}\right) dt \tag{6–5}$$

The weighting matrices Q and R are chosen by the user to influence the magnitude of the state and control vector, respectively. The scalar parameters Q_α, Q_β, Q_q, etc. are the elements of Q along the diagonal and may be used to influence the particular state variable of interest. The same is true for the diagonal components of R: R_{δ_a}, R_{δ_e}, R_{δ_r}, which influence the aileron, elevator, and rudder inputs respectively. Non-diagnonal terms for Q and R are not considered in this study. Finally, the matrix $S_f \geq 0$ is specified by the user to achieve satisfactory terminal conditions.

Using the quadratic cost functional, the 1st order optimality conditions without terminal constraints are stated in Equations (6–6) through (6–8), where the subscript notation implies partial differentiation (e.g. $\mathbf{f}_x = \partial\mathbf{f}/\partial\mathbf{x}$).

$$\dot{\mathbf{x}}(t) = \mathbf{f}\left(\mathbf{x}(t), \mathbf{u}(t)\right), \quad \mathbf{x}(t_0) \text{ specified} \tag{6–6}$$

$$\dot{\boldsymbol{\lambda}}(t) = -Q\mathbf{x}(t) - \mathbf{f}_x^T(t)\boldsymbol{\lambda}(t), \quad \boldsymbol{\lambda}(t_f) = S_f\mathbf{x}(t_f) \tag{6–7}$$

$$\mathbf{u}(t) = -R^{-1}\mathbf{f}_u^T(t)\boldsymbol{\lambda}(t) \tag{6–8}$$

These equations represent a boundary value problem that must be solved numerically, provided the system $\dot{\mathbf{x}} = \mathbf{f}(\mathbf{x}, \mathbf{u})$ can be described analytically. For store separation, the equations of motion are documented in Chapter 2 and the aerodynamic model is based on the parametric model developed in Chapter 3. Explicit derivation of the 1st order optimality equations for the full 6DOF store separation problem involves a lot of algebraic manipulation, and is best accomplished using computer software, such as the Matlab Symbolic Math Toolbox®. The resulting equations are lengthy, but easily built into a subroutine for use with a numerical BVP solver. The numerical solutions presented here are based on the Matlab® program $\mathrm{bvp4c}$, which implements a three-stage Lobatto IIIa collocation formula. Further discussion of the numerical methods used in this study are provided in Section 4.2.5.

6.2.1.2 Optimal trajectory

Figure 6-2 shows an optimal trajectory at a subsonic flight condition. The flight conditions are specified to be consistent with store separation flight test 2265 (Mach 0.9 / 550 KCAS / 4800 ft). The initial conditions, $\mathbf{x}(t = 0)$, are taken from the flight test inertial measurements at end-of-stroke and are therefore consistent with an actual flight test event. The user specified weighting matrices were chosen to minimize the magnitude of the angular rates. In particular, $Q_\alpha = Q_\beta = 0$, $Q_p = Q_q = Q_r = 10$ and $R_{\delta_a} = R_{\delta_e} = R_{\delta_r} = 50$. Emphasis is on reducing the angular rates p, q and r without undue control effort. The terminal cost is zero, $S_f = 0$.

The results shown in Figure 6-2 indicate that the optimal control quickly captures the angular rates and drives the store to a stationary attitude. Note that the specific values of the Euler angles ψ, θ, ϕ are not of particular concern; only the rates p, q, r are included in the cost function. Also note that the angle of attack continues to increase steadily. Since the pitch attitude θ is held constant as a result of minimizing $|q|$, the angle of attack is continually increased as the store vertical velocity increases due to the acceleration of gravity.

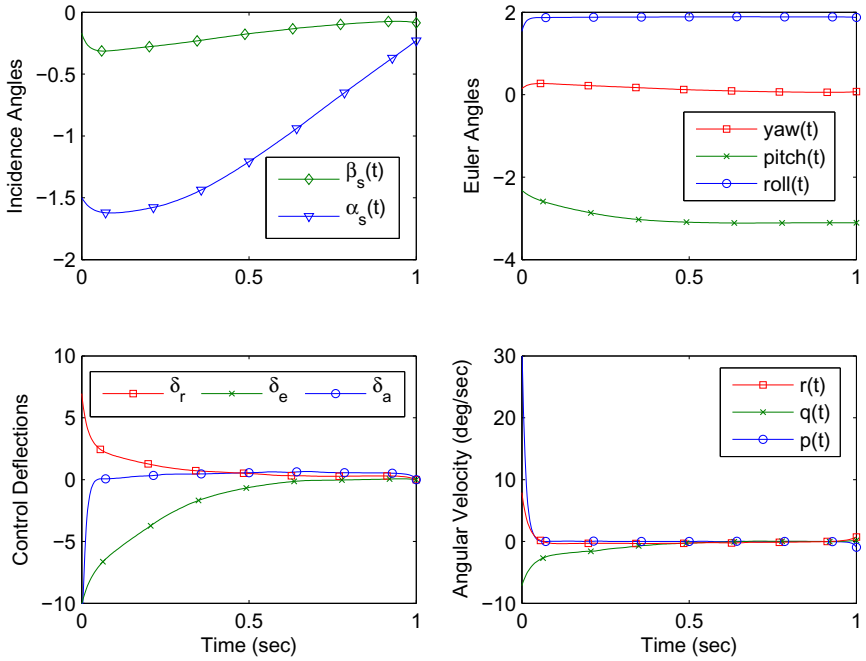

Figure 6-2. Optimal trajectory for rate capture. Initial conditions and flight conditions are based on flight test 2265 (Mach 0.9 / 550 KCAS / 4800 ft).

Figure 6-3 shows an optimal trajectory with an emphasis on angle of attack α and the angle of sideslip β. The flight conditions and initial conditions are identical to those shown in Figure 6-2. In this case, the cost was chosen to minimize α and β without excessive control effort. In particular, $Q_\alpha = Q_\beta = 100$, $Q_q = Q_r = 0$ and $R_{\delta_a} = R_{\delta_e} = R_{\delta_r} = 50$. The terminal cost is specified as $S_{f_\alpha} = S_{f_r} = 10$ to achieve a desirable end point. The pitch and yaw rates are damped due to the kinematic correlation with α and β, but the roll rate coupling is minimal for this axisymmetric store and the roll rate must be damped explicitly. Choosing a cost with $Q_p = 10$ provides effective roll rate damping.

The results in Figure 6-3 show an improvement in the angle of attack and angle of sideslip profile while still providing excellent rate capture performance. The specified cost requires that the incidence angles α and β are kept near the origin, which necessarily implies low angular rates. Thus, the angle of attack capture explicitly

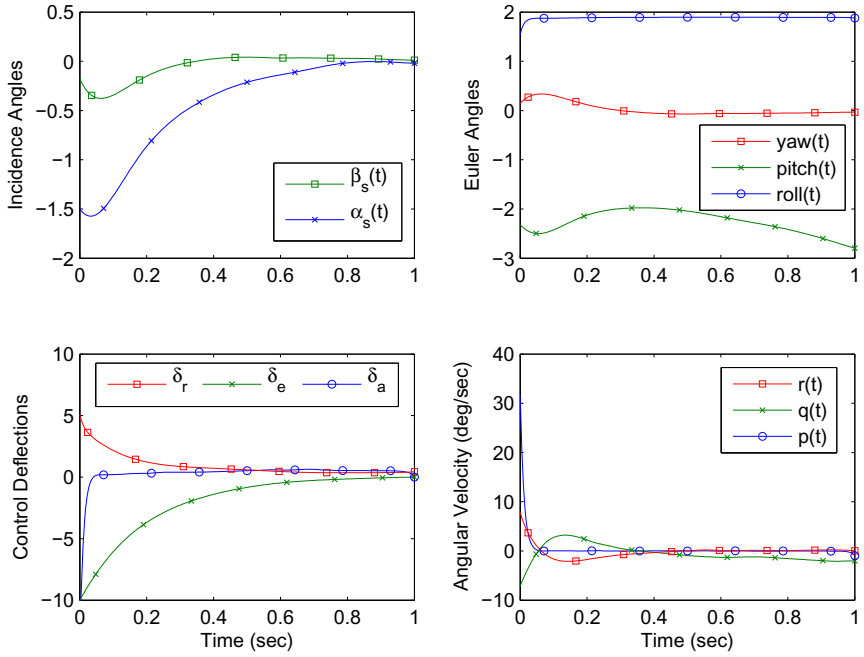

Figure 6-3. Optimal trajectory for angle-of-attack capture. Initial conditions and flight conditions are based on flight test 2265 (Mach 0.9 / 550 KCAS / 4800 ft).

attenuates the incidence angles and implicitly provides rate capture as well. Since angle of attack has a significant role in assessment of safety and acceptability, the angle of attack capture is preferred over pure rate capture. Also note that since the angle of attack is held constant, the pitch angle must continually decrease to compensate for increasing vertical velocity. As such, the steady state pitch rate is slightly negative and the store continues to gently “nose over” into the wind.

Solution to the two point HBVP requires specification of the initial conditions for all twelve state variables. In the figures above, the initial conditions were determined using flight test telemetry data. However, for an actual flight test the initial conditions are not known in advance and may be varied from one mission to the next. Determination of the optimal trajectory requires a new solution for each set of initial conditions, a limitation that is addressed using neighboring optimal control in the next section. Figure 6-4 shows a series of optimal trajectories for a range of initial pitch rates. The pitch rate is

varied between $q(0) = -7 \pm 50\ deg/sec$. The user specified cost function is selected to minimize the total angle of attack using the same weighting values as Figure 6-3.

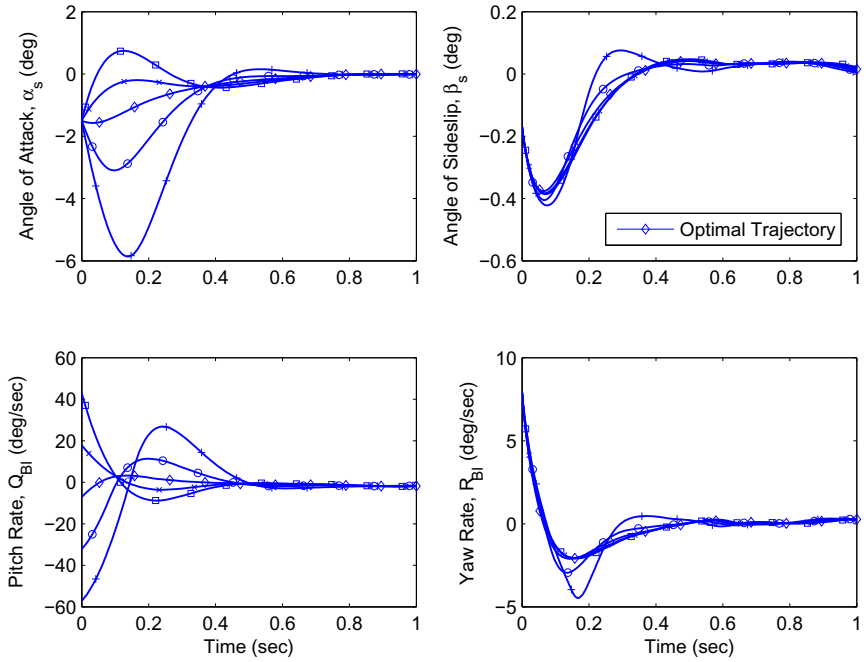

Figure 6-4. Optimal trajectories for varying initial pitch rate. Flight conditions are based on flight test 2265 (Mach 0.9 / 550 KCAS / 4800 ft).

The results in Figure 6-4 indicate that the optimal control adequately accounts for the variation in initial pitch rate and drives the store to a stable trimmed flight condition in less than 1 second. Note that the variability in the angle of sideslip β and the yaw rate r are minimal, indicating only a weak aerodynamic and kinematic coupling between the longitudinal and lateral variables. This is to be expected given the axisymmetric nature of the store.

Figure 6-5 shows a similar series of optimal trajectories for varying initial yaw rates, $r(0) = 8 \pm 50\ deg/sec$. The optimal control produces a family of trajectories that converge rapidly to a benign flight condition using acceptable levels of control. Again, the limited variability of the angle of attack α and pitch rate q is an indicator of weak coupling. It should be noted that this decoupling effect is a convenient result but not a necessary

assumption. The same approach using optimal control will also work for a store with strong aerodynamic and kinematic coupling.

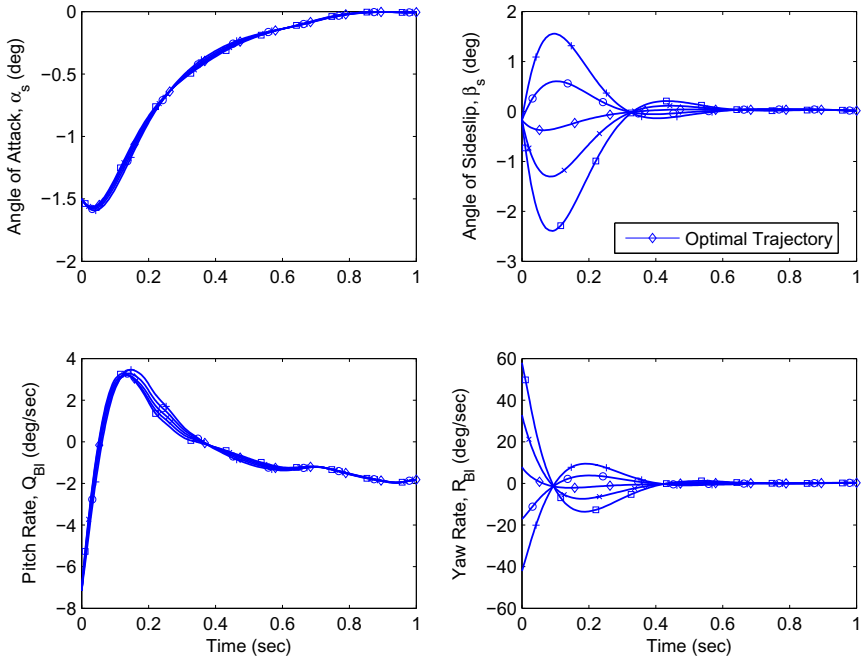

Figure 6-5. Optimal trajectories for varying initial yaw rate. Flight conditions are based on flight test 2265 (Mach 0.9 / 550 KCAS / 4800 ft).

All of the preceding plots in this section are based on subsonic flight conditions consistent with store separation flight test 2265 (Mach 0.9 / 550 KCAS / 4800 ft). Figure 6-6 shows an optimal trajectory for flight test 4535 (Mach 1.2 / 600 KCAS / 18kft). The supersonic flow field results in a much larger nose-down aerodynamic pitching moment near carriage. The optimal control uses maximum control authority $\delta_e = -10$ deg to arrest the pitch rate and angle of attack. The stronger flowfield results in higher deviations in pitch rate throughout the trajectory. Even in these adverse conditions the optimal control successfully brings the store to a stable trimmed flight condition within a 1 second time interval. Figure 6-7 shows a series of optimal trajectories for a range of initial pitch rates $q(0) = -22 \pm 50$ deg/sec and initial yaw rates $r(0) = 21 \pm 50$ deg/sec.

The results provide further evidence for the effectiveness of the optimal control program over a range of initial conditions.

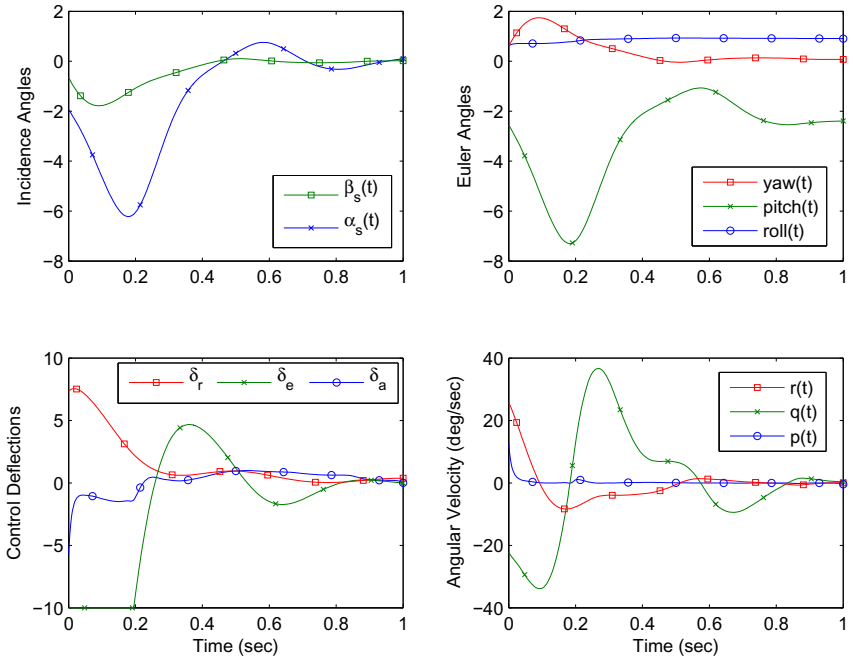

Figure 6-6. Optimal trajectory for angle-of-attack capture. Initial conditions and flight conditions are based on Flight Test Mission 4535 (Mach 1.2 / 600 KCAS / 18kft).

The results shown in Figures 6-2 through 6-7 represent a significant improvement over the actual fight test separation characteristics. For comparison, Figure 6-8A shows the reconstructed flight test trajectory for mission 2265 (Mach 0.9 / 550 KCAS / 4800 ft) with the optimal trajectory determined using the same flight conditions, initial conditions, and mass properties. Figure 6-8B shows a similar comparison for mission 4535 (Mach 1.2 / 600 KCAS / 18kft). In both cases, the controlled separation is a dramatic improvement over the flight test trajectory in terms of acceptability margins. For mission 4535, the maximum angle of attack is reduced from $\alpha_{max} = -20$ deg to $\alpha_{max} = -5$ deg. The maximum pitch rate is reduced from $q_{max} = 130$ deg/sec to $q_{max} = 28$ deg/sec. Comparison of the optimal trajectories between flight conditions is also valuable. Whereas the flight test trajectories are dramatically different between

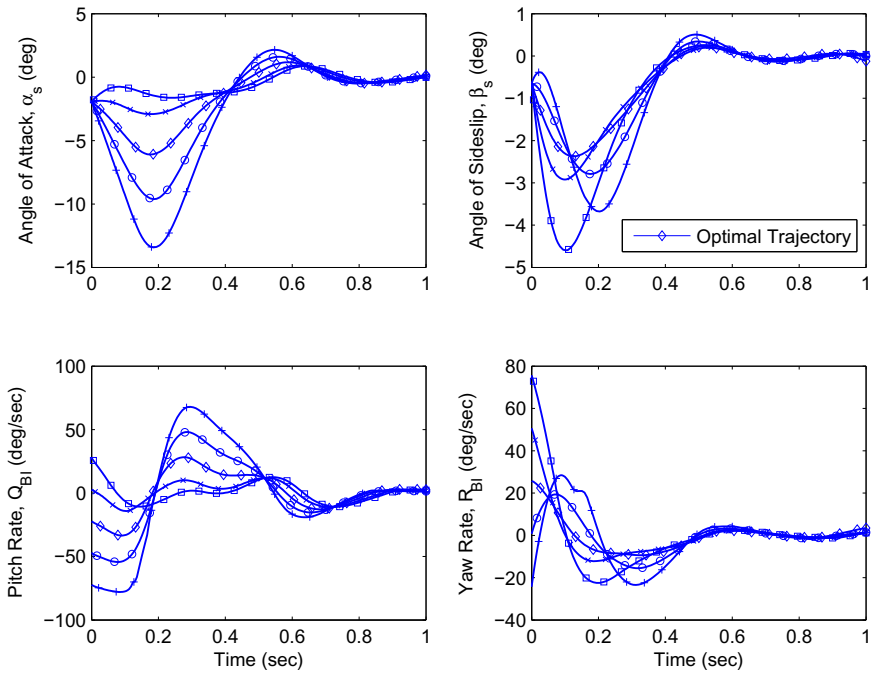

Figure 6-7. Optimal trajectories for varying initial pitch and yaw rate. Flight conditions are based on Flight Test Mission 4535 (Mach 1.2 / 600 KCAS / 18kft).

subsonic and supersonic flight conditions, the optimal trajectories are very similar. The optimal control program not only provides a measurable improvement in safety and acceptability, but it also reduces the variability in trajectory characteristics between flight conditions. The uniformity between flight conditions is an advantage for ensuring safe and acceptable employment across the flight envelope.

6.2.2 Feedback Control

The first order conditions discussed in Section 4.2.1 provide the necessary conditions for an optimal trajectory. The control is determined based on solution of the two point Hamiltonian boundary value problem and implicitly assumes perfect knowledge of the system operating in a disturbance-free environment. However, deterministic disturbances or variations in the initial conditions, terminal conditions, and system parameters alter the optimal state and control history, requiring computation of unique solution for each variation. Stated another way, the optimal control strategy

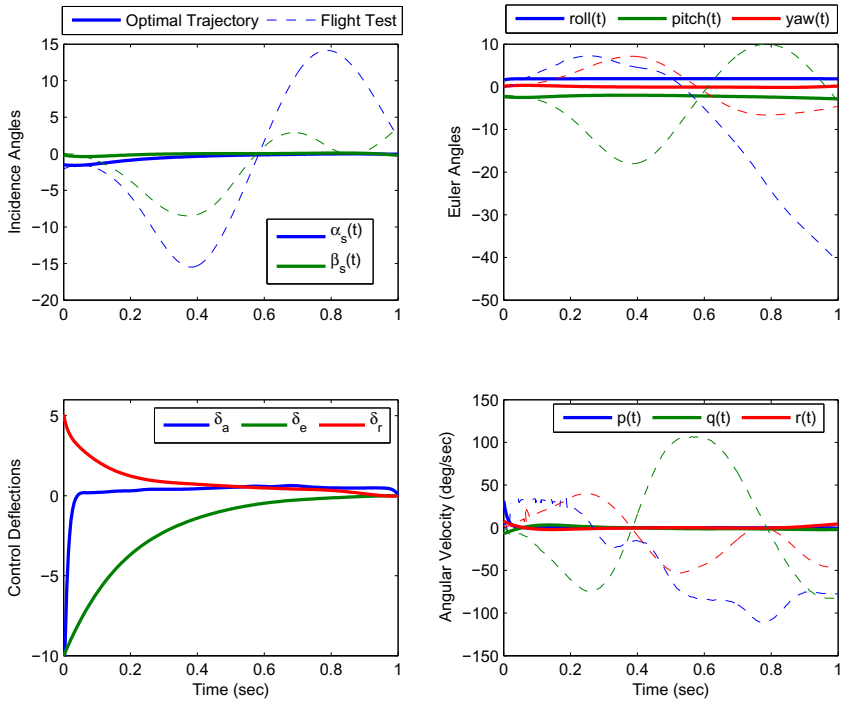

A Mach 0.90 / 550 KCAS / 4800 ft

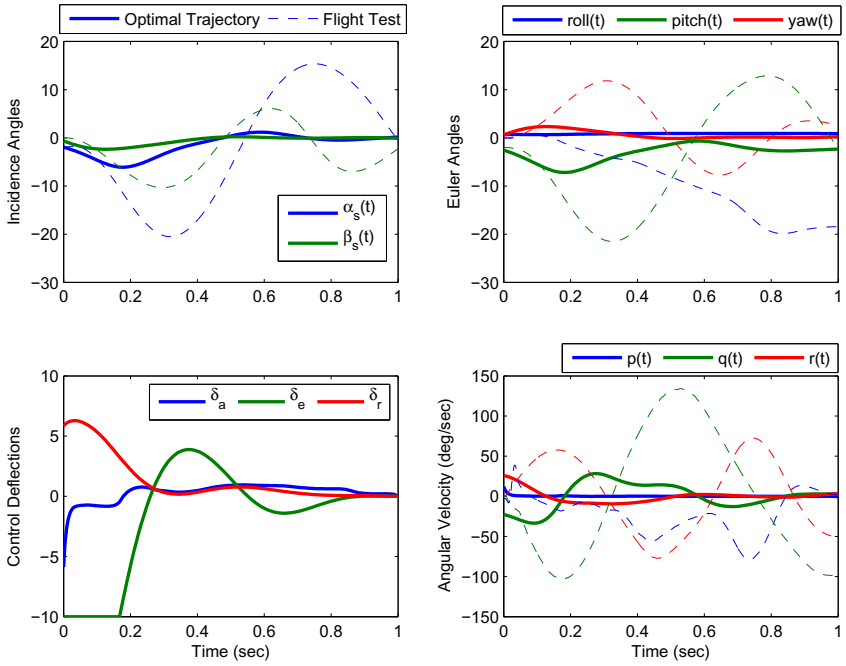

B Mach 1.20 / 600 KCAS / 18000 ft

Figure 6-8. Comparison of optimal (guided) and flight test (unguided) trajectories for subsonic and supersonic flight conditions.

is “open-loop”, meaning the control is specified a priori and fixed regardless of perturbations that may affect the system during operation. In contrast, a “closed-loop” control law is more desirable as it accounts for variations in initial conditions and disturbances along the optimal path. Neighboring optimal control (NOC) provides a powerful approach for implementing feedback control along an optimal path by considering linear perturbations along the optimal solution. NOC relies on a locally linearized dynamic model in combination with a quadratic cost functional derived from the second variation of the original cost functional. The neighboring optimal solution is then approximated as the sum of the original optimal trajectory plus the linear-optimal solution [116].

6.2.2.1 Problem statement

The 1st order necessary conditions for a neighboring extremal without terminal constraints are given by Equations (6–9) through (6–12), where $H = L + \boldsymbol{\lambda}^T \mathbf{f}$ is the Hamiltonian.

$$\delta\dot{\mathbf{x}}(t) = \mathbf{f}_x \delta\mathbf{x} + \mathbf{f}_u \delta\mathbf{u} \tag{6–9}$$

$$\delta\dot{\boldsymbol{\lambda}}(t) = -H_{xx}\delta\mathbf{x} - \mathbf{f}_x^T \delta\boldsymbol{\lambda} - H_{xu}\delta\mathbf{u} \tag{6–10}$$

$$0 = H_{ux}\delta\mathbf{x} + \mathbf{f}_u^T \delta\boldsymbol{\lambda} + H_{uu}\delta\mathbf{u} \tag{6–11}$$

$$\delta\boldsymbol{\lambda}^T(t_f) = [\phi_{xx}\delta\mathbf{x}]_{t=t_f} \tag{6–12}$$

The variations $\delta\mathbf{x}$, $\delta\mathbf{u}$, and $\delta\boldsymbol{\lambda}$ are defined as perturbations along the optimal trajectory, $(\mathbf{x}^*(t), \boldsymbol{\lambda}^*(t), \mathbf{u}^*(t))$. In particular, $\delta\mathbf{x} = \mathbf{x}(t) - \mathbf{x}^*(t)$, $\delta\mathbf{u} = \mathbf{u}(t) - \mathbf{u}^*(t)$, and $\delta\boldsymbol{\lambda} = \boldsymbol{\lambda}(t) - \boldsymbol{\lambda}^*(t)$ are the variations in the state, control, and costate respectively.

Equation (6–11) can be used to solve for the control variation explicitly provided that the matrix inverse H_{uu}^{-1} exists. The costate $\delta\boldsymbol{\lambda}$ can be eliminated from the problem using a differential Riccati equation. The result is a Neighboring Optimal Feedback Law that can be used to correct for varying initial conditions or disturbances along the extremal path. The feedback law with time varying control gains $K(t)$ is given by

Equations (6–13) and (6–14), where $S(t)$ is the numerical solution to the differential Riccati equation. The neighboring optimal control structure is shown graphically in Figure 6-9.

$$\mathbf{u}(t) = \mathbf{u}^*(t) - K(t)\left(\mathbf{x}(t) - \mathbf{x}^*(t)\right) \tag{6–13}$$

$$K(t) = H_{uu}^{-1}\left(H_{ux} + \mathbf{f}_u^T S\right) \tag{6–14}$$

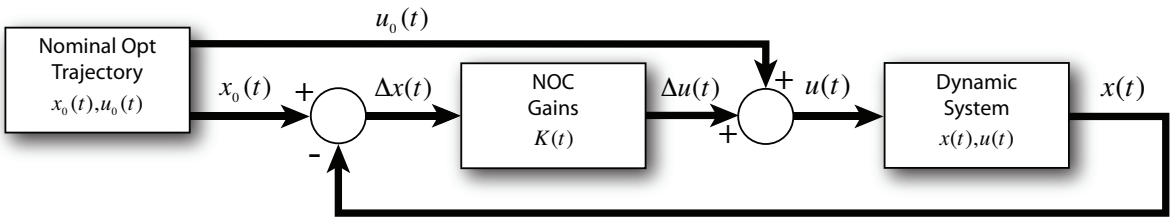

Figure 6-9. Neighboring Optimal Control block diagram.

The neighboring optimal control law can be used to minimize the original cost function to second order in the presence of varying initial conditions and disturbances along the optimal path. The NOC controller provides near-optimal corrections for unknown variations in system parameters, provided the change in parameters is small. Therefore, NOC provides a compact and viable solution for implementing real-time optimal control in a realistic environment.

Neighboring optimal control is especially well suited for store separation. Infinite Horizon NOC (IHNOC) provides a control structure that accounts for the spatially variant aerodynamics near the aircraft and converges smoothly to a time invariant controller in far field conditions. Application of IHNOC to store separation for varying initial conditions, random disturbances, and parameter variations are discussed in Sections 6.2.2.2 through 6.2.2.5.

6.2.2.2 Neighboring optimal trajectory

Figure 6-10 shows optimal and and neighboring optimal trajectories for flight conditions consistent with mission 2265 (Mach 0.9 / 550 KCAS / 4800 ft). The cost was

chosen to minimize the incidence angles without excessive control effort. In particular, $Q_\alpha = Q_\beta = 100$, $Q_q = Q_r = 0$, $Q_p = 10$ and $R_{\delta_a} = R_{\delta_e} = R_{\delta_r} = 50$. Also, the end point cost for the HBVP was specified as $S_{f_\alpha} = S_{f_r} = S_{f_p} = 10$ to keep the end point near a trimmed flight condition. The end point of the HBVP becomes the set point for the neighboring optimal controller. The end point cost for the NOC problem was specified as the solution to the algebraic Riccati equation, as described in Section 5.3.2. As a result, the time varying neighboring optimal controller converges smoothly to a time invariant nonzero set point regulator. The IHNOC policy will continue to hold the store near a trimmed flight condition until transition to a mission autopilot is complete.

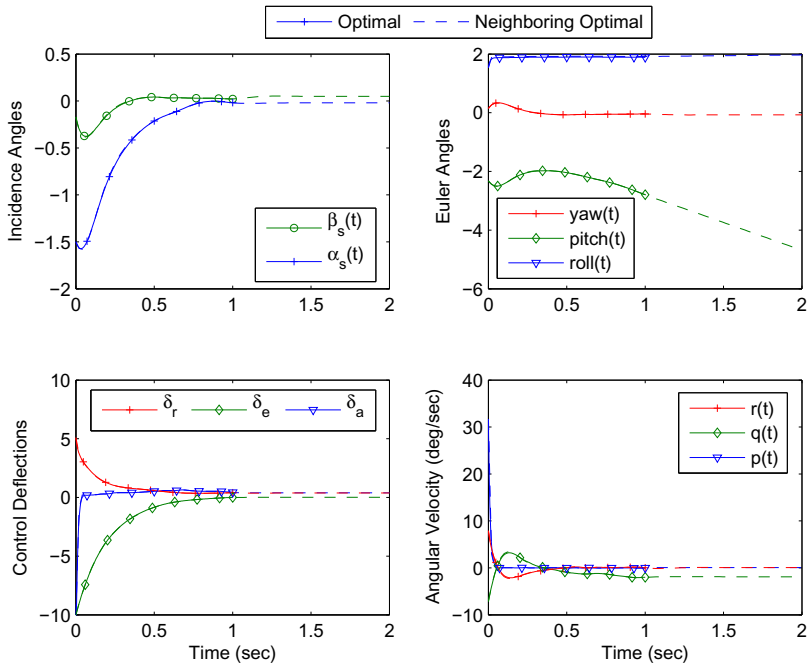

Figure 6-10. Optimal trajectory and extended neighboring optimal trajectory for mission 2265 (Mach 0.9 / 550 KCAS / 4800 ft).

Figure 6-11 shows the Riccati solution $S(t)$ and control gains for the neighboring optimal controller $K(t) = -R^{-1}\mathbf{f}_u^T S(t)$. The time variation of the gains for $t < 0.8$ are a result of the spatially variant aerodynamics of the store traversing the nonuniform flow field. The gains rapidly converge to constant values beyond $t = 0.8$ (about 23 ft below the aircraft), indicating the aircraft flow field effect is no longer significant.

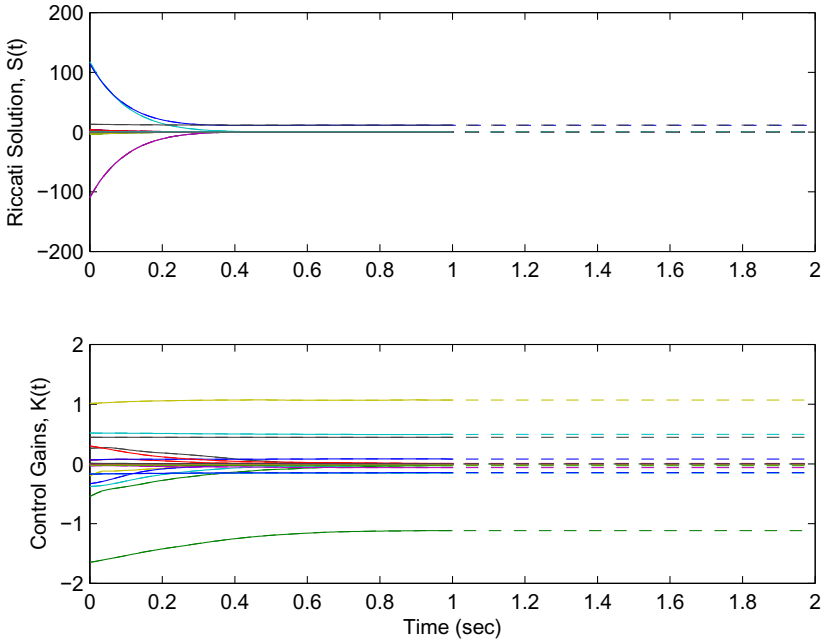

Figure 6-11. Time varying feedback control gains and Riccati solution for Mission 2265 (Mach 0.9 / 550 KCAS / 4800 ft).

Figure 6-12 shows similar trajectories for supersonic flight conditions consistent with flight test 4535 (Mach 1.2 / 600 KCAS / 18kft). Again, the cost was chosen to minimize the total aerodynamic angle of attack, which indirectly provides a rate capture effect as well. In particular, $Q_\alpha = Q_\beta = 200$; all other weighting factors are unchanged from the previous example. The supersonic flow field surrounding the aircraft induces a strong nose-down pitching moment on the store, resulting in a negative angle of attack and pitch angle, despite the maximum elevator deflection for $t < 0.20$ sec. However, the control quickly overcomes the adverse flow field condition and drives the store to a trimmed flight condition within a 1 sec time interval. The neighboring optimal controller emulates the optimal trajectory and may be used to maintain the store near the set point indefinitely.

The Riccati solution $S(t)$ and control gains $K(t)$ for mission 4535 are shown in Figure 6-13. Again, the time variation of the gains near carriage is evident, followed by convergence to stationary values. However, in contrast to Figure 6-11, the gains

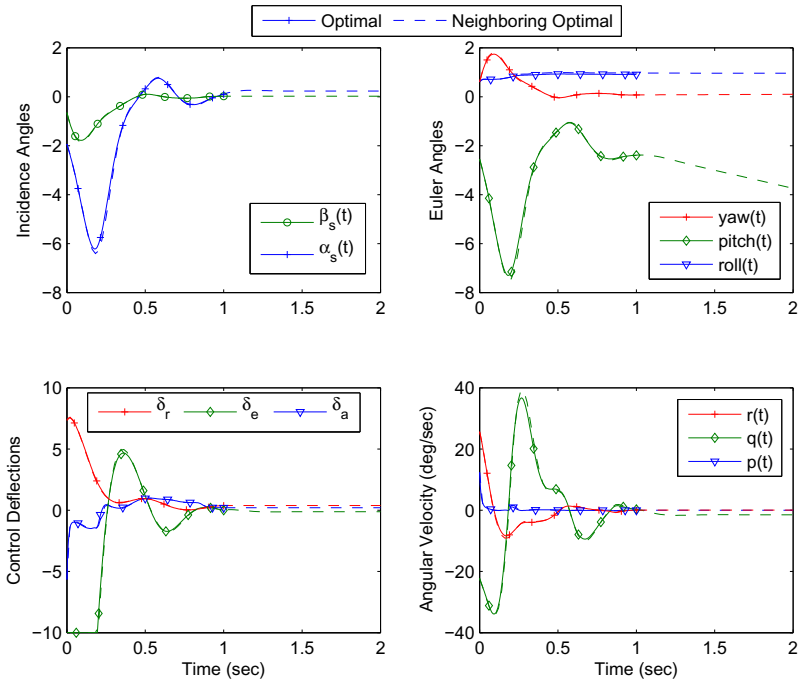

Figure 6-12. Optimal trajectory and extended neighboring optimal trajectory for mission 4535 (Mach 1.2 / 600 KCAS / 18kft).

$K(t)$ are not monotonically decreasing. The supersonic flow field is considerably more complex than the subsonic equivalent, resulting in a more dynamic control schedule. The gains converge to approximately constant values at about $t = 0.9$ sec, which for this example corresponds to about 30 ft below the aircraft. The IHNOC strategy adapts well to the more rigorous flow field and provides a framework that works similarly at both adverse and benign flight conditions.

6.2.2.3 Response to varying initial conditions

In order to solve the nonlinear HBVP discussed in Section 6.2.1.2, the initial conditions must be specified a priori. This a significant limitation for implementing optimal control for store separation, since the initial conditions will in general be different for each release. However, if the HBVP is solved for a nominal set of initial conditions, neighboring optimal control can be used to provide linear-optimal correction for varying initial conditions, provided the perturbed initial conditions are not too far from the

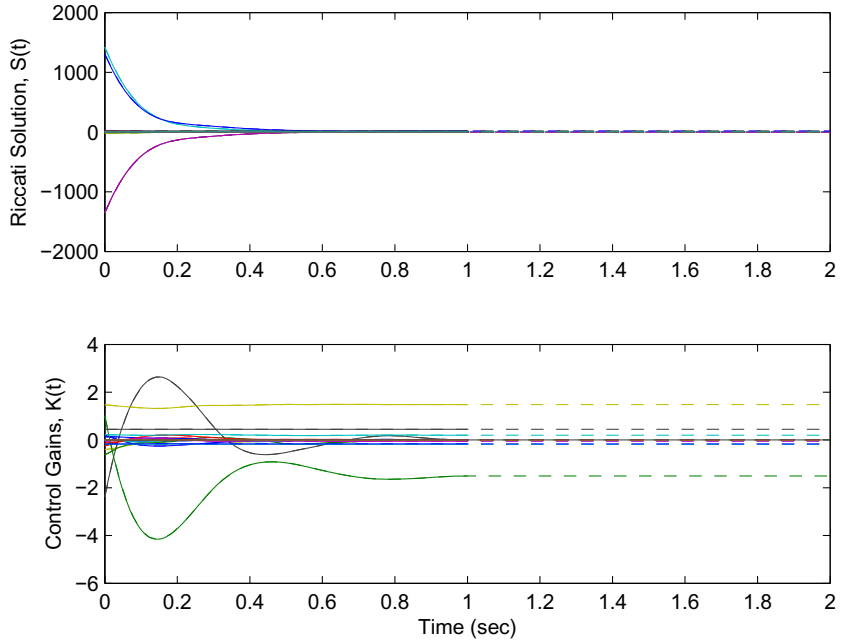

Figure 6-13. Time varying feedback control gains and Riccati solution for mission 4535 (Mach 1.2 / 600 KCAS / 18kft).

nominal values. For the simulations considered in this study, NOC performs quite well even when the perturbations are large; see Section 5.4.2.

Figure 6-14 shows an optimal trajectory and family of neighboring optimal trajectories with varying initial conditions for subsonic flight conditions consistent with mission 2265 (Mach 0.9 / 550 KCAS / 4800 ft). The neighboring optimal solutions were determined using a feedback control simulation with control gains shown in 6-11. The initial conditions include variations in pitch rate $q(0) = -7 \pm 50$ deg/sec and yaw rate $r(0) = 8 \pm 50$ deg/sec. The nominal initial conditions are based on reconstructed flight test data from mission 2265. The cost function is the same as the example shown in Section 6.2.2.2.

The results shown in Figure 6-14 indicate that the neighboring optimal controller adequately captures the angular rates and incidence angles, despite the large variation in initial pitch and yaw rates. All five trajectories converge to the same trimmed flight

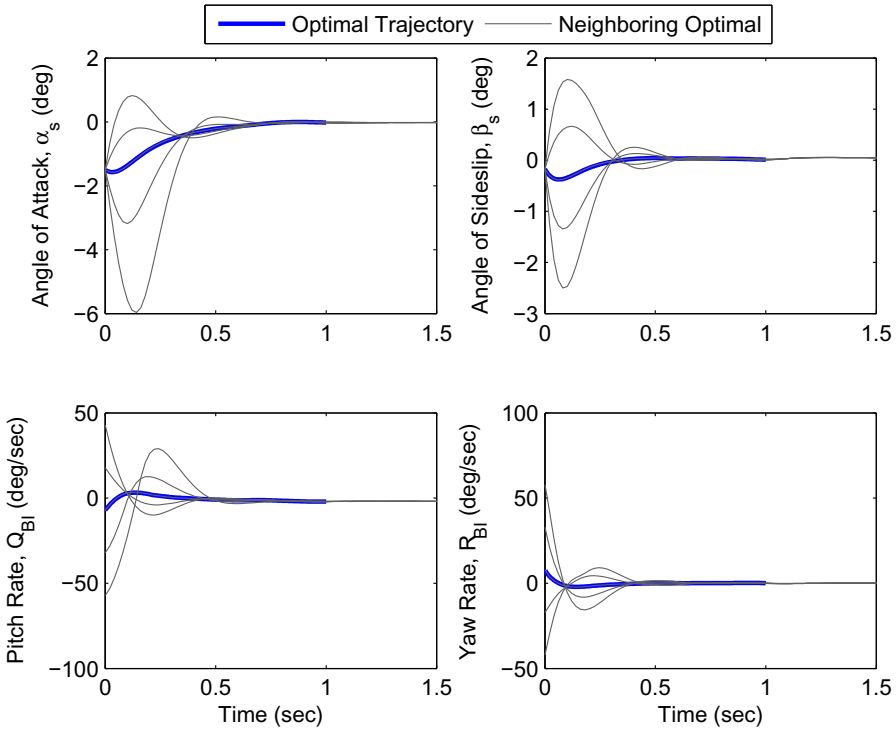

Figure 6-14. Optimal and neighboring optimal trajectories with varying initial rates for mission 2265 (Mach 0.9 / 550 KCAS / 4800 ft).

condition, a feature that is clearly an advantage for ensuring safe and acceptable separation in the presence of initial perturbations.

Figure 6-15 shows a similar series of trajectories for varying initial incidence angles with $\alpha(0) = -1.5 \pm 2$ deg and $\beta(0) = -0.2 \pm 2$ deg. The neighboring optimal controller continues to perform well in the presence of varying initial conditions.

Figure 6-16 shows a family of neighboring optimal trajectories with varying initial conditions for a supersonic flight condition consistent with mission 4535 (Mach 1.2 / 600 KCAS / 18kft). The initial angular rates are varied ± 50 deg/sec and the initial incidence angles are varied ± 2 deg. In all five cases the neighboring optimal controller performs well and drives the store to a trimmed flight condition despite the large initial perturbations.

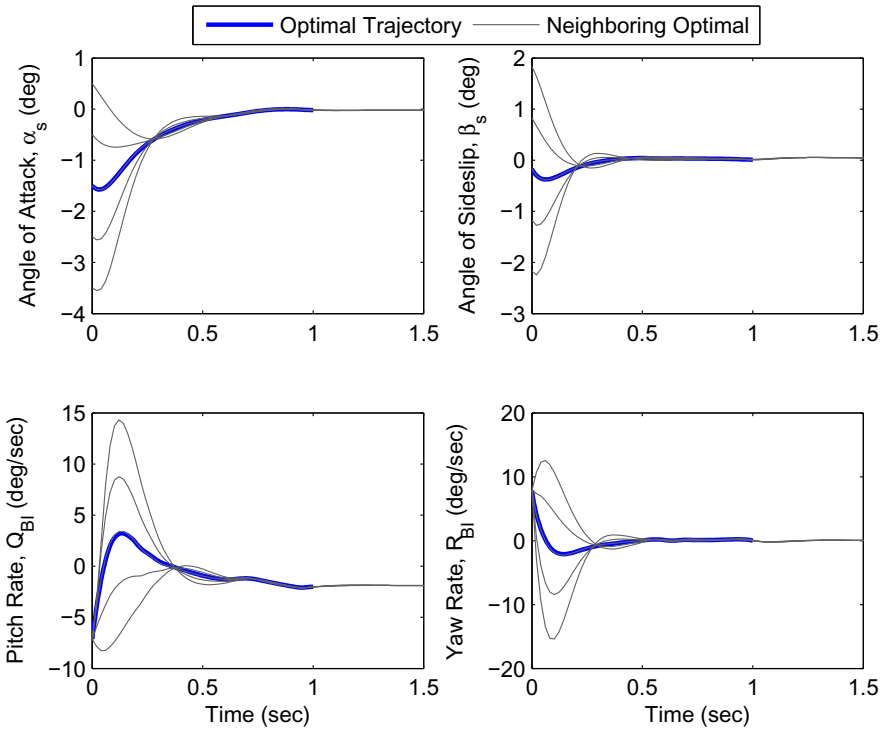

Figure 6-15. Optimal and neighboring optimal trajectories with varying initial incidence angles for mission 2265 (Mach 0.9 / 550 KCAS / 4800 ft).

6.2.2.4 Response to random disturbances

Neighboring optimal control is designed to correct for perturbations in the initial conditions. Since any time is a valid “initial” time, NOC can also be used to correct for disturbances along the optimal path. For store separation, turbulent air near the aircraft is of particular concern.

The study of aerodynamic turbulence is no small matter and a thorough analysis of turbulent effects on store separation is beyond the scope of this investigation. Rather, a more direct approach will be considered to demonstrate the performance of the controller in the presence of random disturbances.

Figure 6-17 shows the aerodynamic coefficients estimated from flight test telemetry data for mission 2265 (Mach 0.9 / 550 KCAS / 4800 ft). The smoothed estimate was determined using a 51-point moving average. The residuals between the estimated and smoothed signals are assumed to include effects from aerodynamic turbulence, sensor

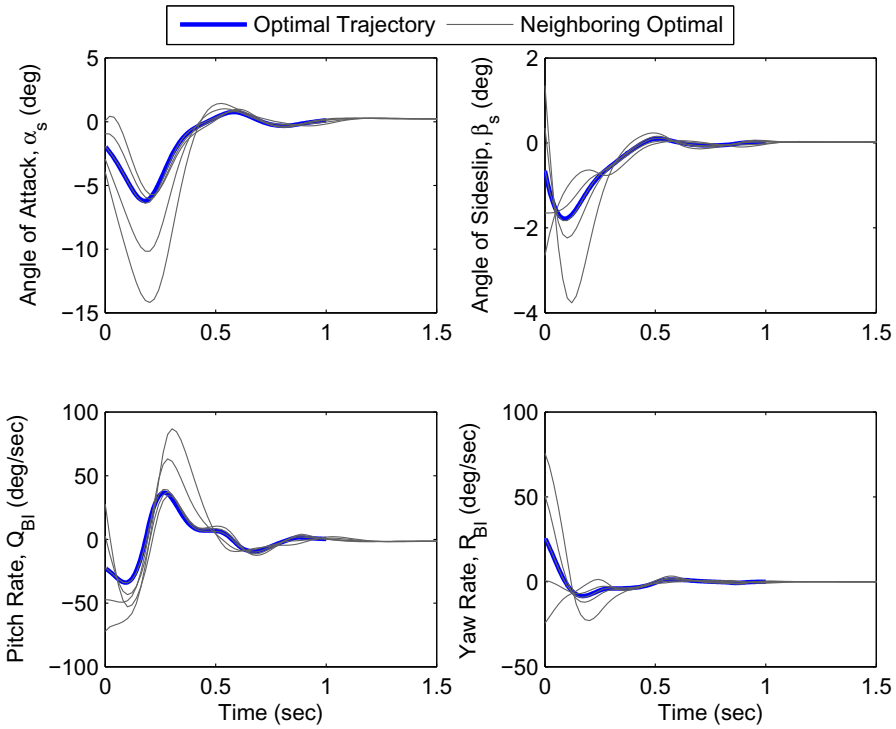

Figure 6-16. Optimal and neighboring optimal trajectories with varying initial conditions for mission 4535 (Mach 1.2 / 600 KCAS / 18kft).

noise, and structural vibration. These residuals will be used to introduce disturbances into the system, representative of the disturbances encountered in flight.

Figure 6-18 shows optimal and neighboring optimal trajectories in the presence of random disturbances representative of aerodynamic turbulence. It is apparent that the turbulence has a minor effect on the trajectory. The inertia of the store acts as a physical filter to reduce the effect of the high frequency disturbances and the controller performs adequately. Figure 6-19 shows the response of the neighboring optimal controller for increasing values of random disturbances. The turbulence signal is amplified one, three, and five times with an increasingly dramatic effect on the trajectory. However, in all five cases the optimal controller performs adequately and continually maintains a near trimmed flight condition in the presence of large random disturbances.

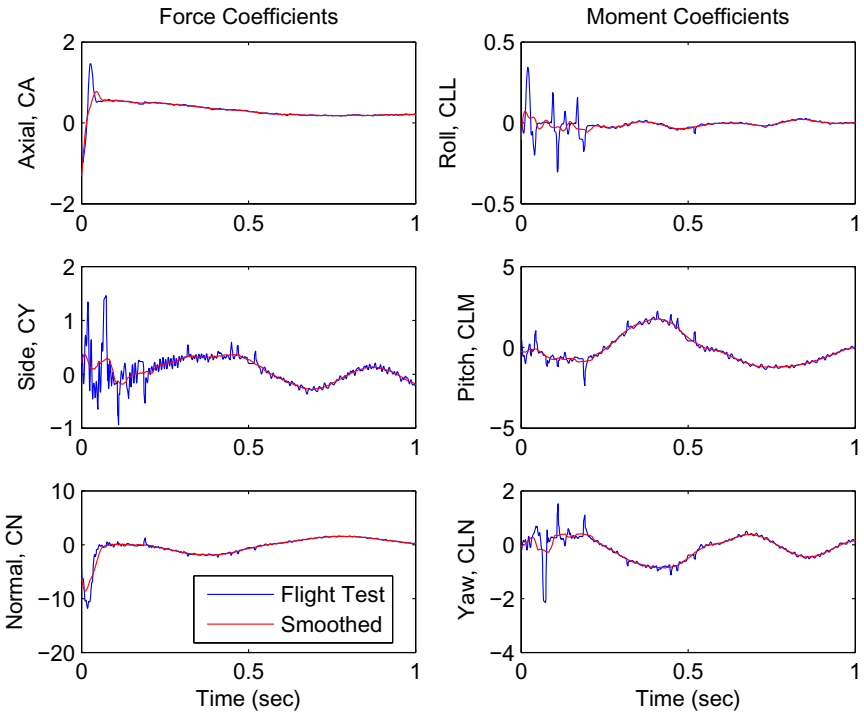

Figure 6-17. Aerodynamic coefficients estimated from flight test telemetry data for mission 2265 (Mach 0.9 / 550 KCAS / 4800 ft).

Further analysis is needed to assess the performance of the neighboring optimal controller for a truly stochastic system. However, this cursory look at the effect of turbulence is promising, indicating further analysis is warranted.

6.2.2.5 Response to parameter variations

NOC can be used to provide optimal feedback control in the presence of small constant parameter variations, provided the parameter variation is known or can be estimated. When the parameter variation is unknown, the control is necessarily sub-optimal but may still perform adequately.

For store separation, the parameter variations in the form of model uncertainties and mass properties are significant. Model uncertainties are largely due to aerodynamic effects, and may be considered a subset of the random disturbances considered in the previous section. Trajectory characteristics are often sensitive to mass properties, such as center of gravity (CG) location. One parameter that typically has a significant effect

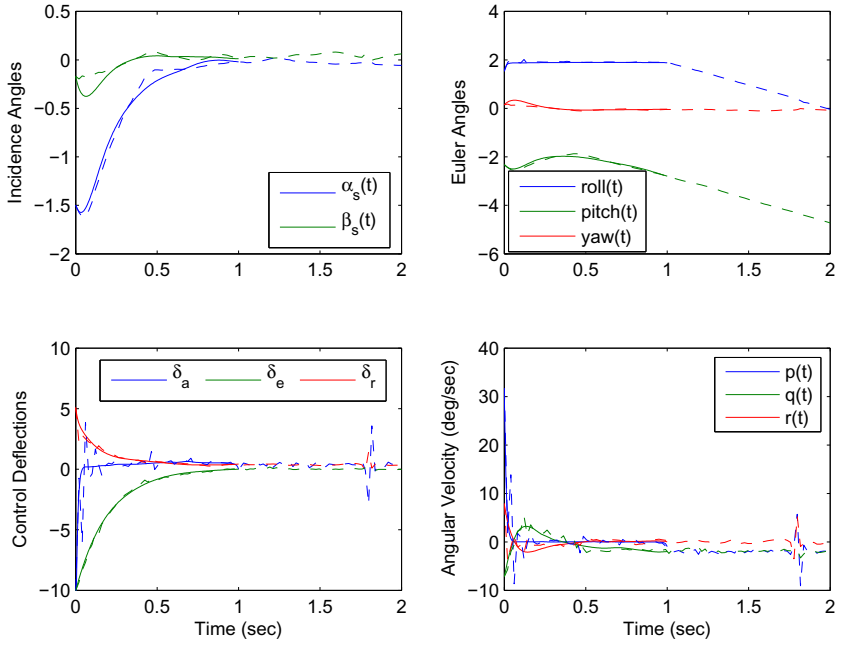

Figure 6-18. Optimal trajectory and neighboring optimal trajectory response to random disturbances for mission 2265 (Mach 0.9 / 550 KCAS / 4800 ft).

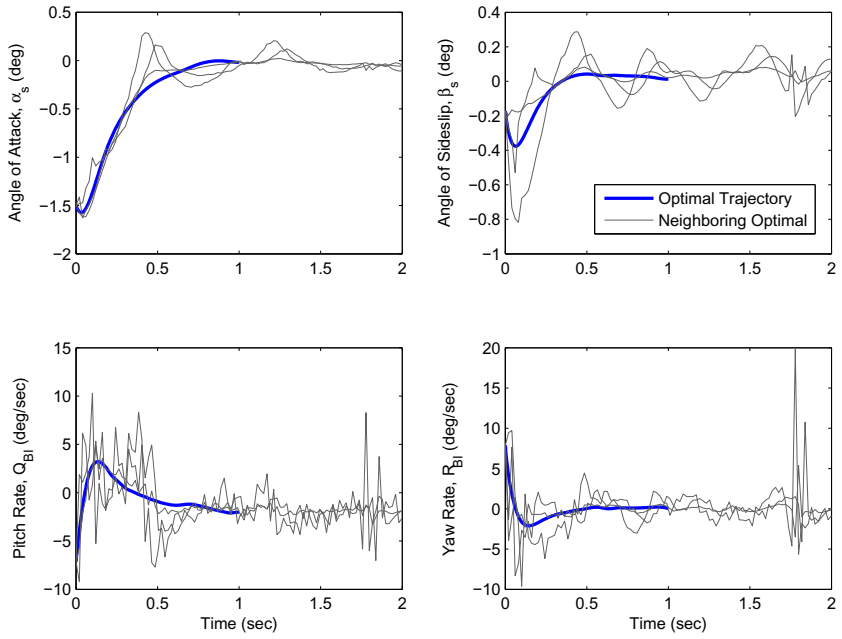

Figure 6-19. Optimal trajectory and neighboring optimal trajectory response to amplified random disturbances for mission 2265 (Mach 0.9 / 550 KCAS / 4800 ft).

on the store separation trajectory is the longitudinal center of gravity, x_{CG}. The location of the store longitudinal center of gravity relative to the aerodynamic center is known to determine the aerodynamic stability. In fact, if the x_{CG} is too far aft, the store will become inherently unstable. For the example store, this occurs when the x_{CG} is shifted by approximately ten inches, $\Delta x_{CG} = 10$ inches. Figure 6-20 shows a series of unguided (jettison) trajectories for the center of gravity $-10 \leq \Delta x_{CG} \leq 10$ at 5 inch increments. The trajectories in Figure 6-20 were determined by setting all cost parameters to zero, e.g. $Q_\alpha = Q_\beta = Q_p = Q_q = Q_r = 0$ and $R_{\delta_a} = R_{\delta_e} = R_{\delta_r} = 0$. The uncontrolled trajectory with $\Delta x_{CG} = -10$ inches is unstable and quickly departs from stable flight.

Figure 6-21 shows a series of trajectories for the same range of parameters. In this case, the neighboring optimal control stabilizes an otherwise unstable store. The control system provides stability augmentation and drives the store to a stable trimmed flight condition for a large range of parameter variations. Thus, the neighboring optimal controller clearly provides an advantage over the uncontrolled jettison.

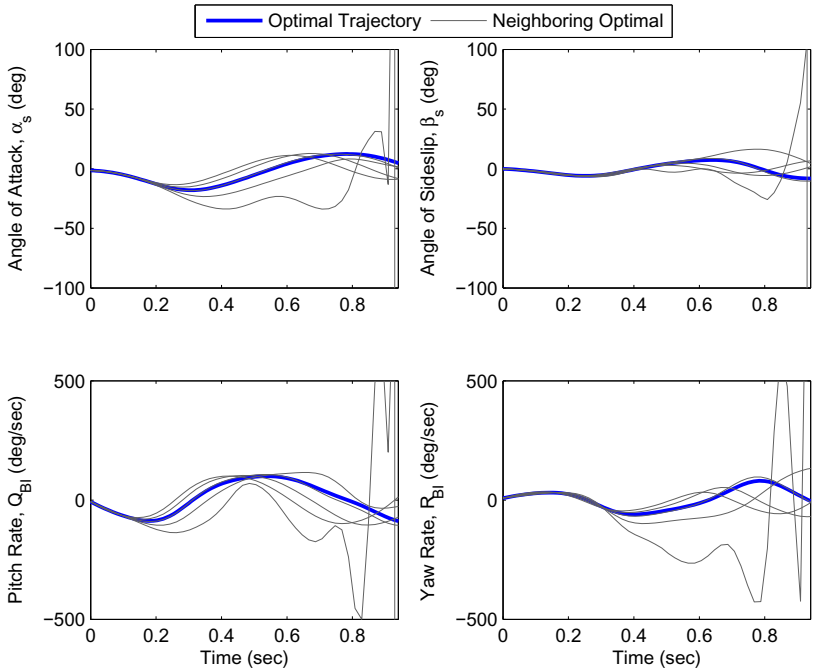

Figure 6-20. Unguided trajectories with parameter variations.

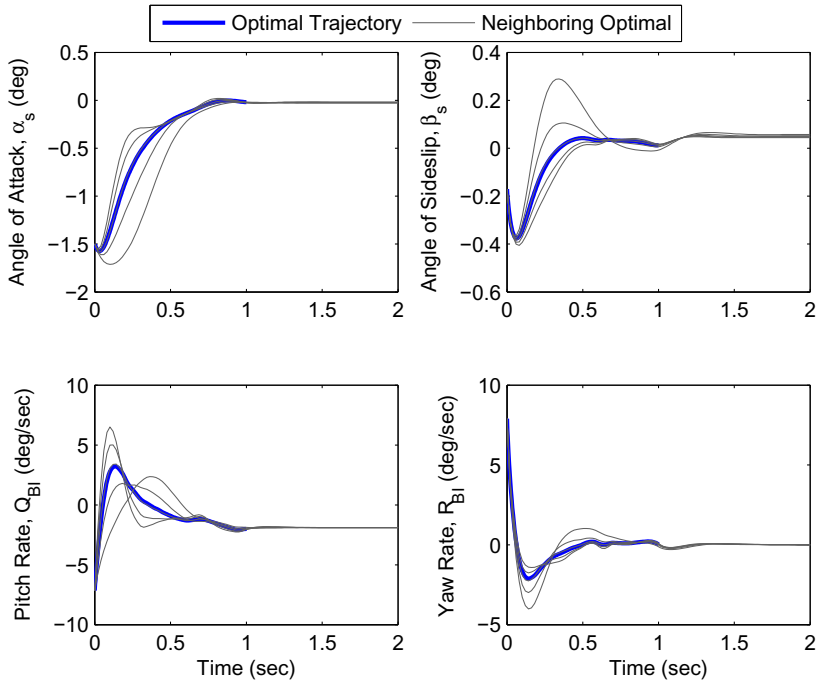

Figure 6-21. Guided trajectories with parameter variations.

6.3 Flight Test Comparison

The examples considered in Sections 6.2.2.2 through 6.2.2.5 are based on the parametric model constructed using system identification methods in Chapter 3. The HBVP is solved using the parametric model, the NOC gains are derived using the parametric model, and the wind axis simulation is executed using the parametric model. This approach ensures consistency between the results; a valuable characteristic for preliminary research. The results can be further examined by considering a blend of parametric modeling and more conventional methods. In particular, the parametric model can be used to solve the HBVP and determine the NOC gains, and then the closed loop control system can be applied to a 6DOF simulation using conventional multi-dimensional interpolation of an aerodynamic database. This approach provides some additional assurance that the control system will operate effectively in the intended environment. Using the NOC full-state feedback with time varying gains, the implementation of a store separation autopilot is straight forward. The results are

considered here in comparison with flight test data for subsonic and supersonic flight conditions.

6.3.1 Subsonic Flight Test

Figure 6-22 shows a comparison of an optimal trajectory determined using parametric modeling and a wind axis simulation using the NOC gains and conventional wind tunnel database interpolation. The NOC gains were determined using the parametric model evaluated along the optimal trajectory. The wind axis simulation is dependent on the parametric model only through the closed loop control gains derived from the HBVP and NOC solution. The nominal optimal trajectory and neighboring optimal control gains are computed and stored external to the wind axis simulation. During simulation, the reference trajectory $\mathbf{x}^*(t)$, reference control $\mathbf{u}^*(t)$, and control gains $K(t)$ are interpolated at each time step to determine the desired control input $\mathbf{u}(t) = \mathbf{u}^*(t) - K(t)\left(\mathbf{x}(t) - \mathbf{x}^*(t)\right)$. The results indicate that the controller performs well when applied to a realistic flight simulation.

Figure 6-23 shows the same nominal optimal trajectory with a series of neighboring optimal trajectories with varying initial conditions. The neighboring optimal trajectories are determined using a wind axis simulation with interpolation of an aerodynamic database in conjunction with closed loop feedback gains determined using parametric modeling. The results substantiate the performance of the controller for a realistic flight simulation with a range of initial conditions.

Store separation trajectory characteristics are affected by many variables, including the initial conditions, flight conditions, store mass properties, and ejection forces. Due to the variability of these effects, no two store separation flight test trajectories are identical. To ensure safe and acceptable separation across the flight envelope, it is important to consider a range of motion for each intended release condition. Repetitive flight testing is prohibitively expensive and the range of motion is typically quantified using modeling and simulation. A range of variables including initial conditions, mass

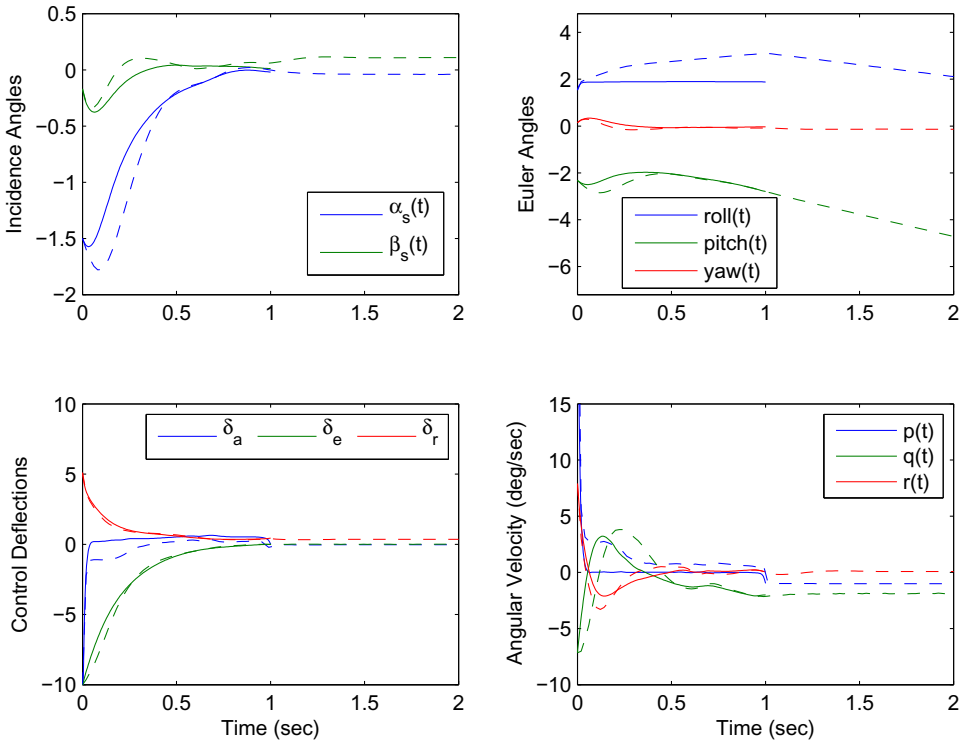

Figure 6-22. Comparison of optimal trajectory and neighboring optimal wind axis simulations for mission 2265 (Mach 0.9 / 4800 ft / 550 KCAS).

properties, ejection forces, etc. can be specified, and a multitude of simulations can be conducted to determine the expected range of motion. The input parameters can be varied randomly or deterministically, or a combination of both, to achieve the desired range of trajectories. Simulations with randomly varying inputs are referred to as Monte Carlo simulations. Those with deterministic inputs are referred to as a parametric analysis or a designed experiment.

To further examine the performance of the store separation autopilot in the presence of deterministic parameter variations, a multitude of flight test simulations were conducted with and without guidance and control. The intent of this comparison is to show the dramatic improvement in safety and acceptability that can be achieved with guided store separation. The parametric analysis included variations in release

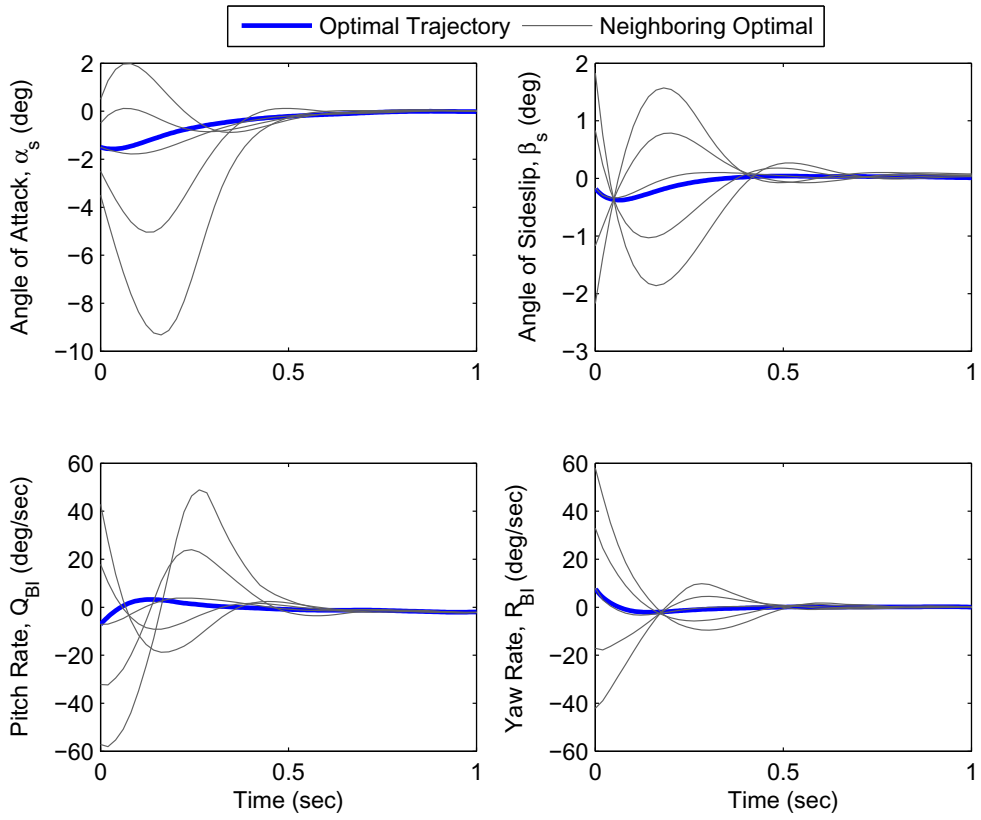

Figure 6-23. Comparison of optimal trajectory and neighboring optimal wind axis simulations with varying initial conditions for mission 2265 (Mach 0.9 / 4800 ft / 550 KCAS).

conditions, store mass properties, ejector properties, and aerodynamic damping derivatives. The nominal and tolerance of each specific parameter is shown in Table 6-1.

Table 6-1. Factors for Parametric Analysis

	Parameter	Nominal	Tolerance
Flight Conditions	Mach	0.9	± 0.05
	Aircraft AoA	1 deg	± 1 deg
Store Properties	Long. x_{CG}	9.6 in	± 2 in
	Lat. y_{CG}	0 in	± 0.5 in
Ejector Properties	Fwd Force	3000 lb Peak Force	± 10%
	Aft Force	8000 lb Peak Force	± 10%
	Total Force	11000 lb Peak Force	± 20%
Damping Derivatives	Roll Damping C_{l_p}	-2.5	± 50%
	Pitch Damping C_{m_q}	-74	± 50%
	Yaw Damping C_{n_r}	-74	± 50%

Nine of the ten factors (excluding Total Force) in Table 6-1 were varied between nominal, high, and low (three levels each) using a $1/2$ fraction central composite designed experiment, for a total of 275 runs.[1] Note that 9 factors at 3 levels each have $3^9 = 19683$ possible combinations, and the central composite design is a very economical way of simulating the range of parameters.

Figure 6-24 shows the angle of attack α_s and angle of sideslip β_s for the parametric analysis. The figure includes 275 jettison (unguided) trajectories, 275 guided trajectories using NOC, the nominal guided trajectory, and the flight test telemetry data for this subsonic flight condition. Note that the guided trajectories begin at $t = 0.05$ sec, which is the end of the ejection stroke. It is clear that the store separation autopilot significantly reduces the variability in the wind axis incidence angles. The entire range of controlled trajectories are within the range of motion demonstrated by a single uncontrolled flight test, whereas the uncontrolled jettison trajectories exhibit large excursions in angle of attack ($-40 < \alpha_s < 40$ deg) and angle of sideslip ($-40 < \beta_s < 30$ deg).

Figure 6-25 shows the vertical position and vertical velocity for the simulated flight test trajectories. The guided trajectories exhibit a tight grouping in comparison to the jettison trajectories. Note that the nominal guided trajectory manifests a constant slope equal to 32.2 ft/sec^2 corresponding the the acceleration of gravity. Since the store is axisymmetric and maintained near zero angle of attack, the aerodynamic lift is essentially zero and the store accelerates evenly under the influence of gravity.

Figures 6-26 and 6-27 show the angular rates and orientation of the store during separation. The store separation autopilot performs well for the entire range of parameter variations and considerably reduces the range of motion in comparison to the jettison (unguided) simulations.

[1] The Total Force parameter was not varied independently. Rather it is a product of the Fwd and Aft force variations, leaving 9 independent parameters.

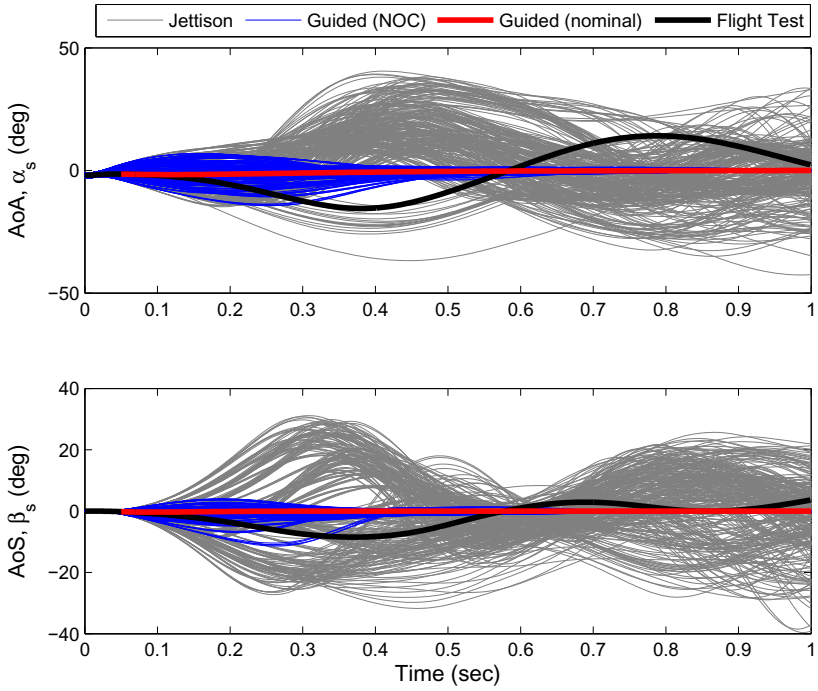

Figure 6-24. Parametric analysis (incidence angles) for jettison and guided store separation corresponding to flight test 2265 (Mach 0.9 / 4800 ft / 550 KCAS).

6.3.2 Supersonic Flight Test

Section 6.3.1 focused on validation results for a subsonic flight condition. A supersonic flight condition corresponding to mission 4535 (Mach 1.2 / 600 KCAS / 18kft) provides a more strenuous test case due to the stronger nonuniform flow field effects. Despite the stronger flow field influence, the separation autopilot continues to perform well.

Figure 6-28 shows optimal and neighboring optimal trajectories for comparison. The optimal trajectory was computed using the parametric model constructed with system identification. The optimal trajectory and control were stored and used to determine the control inputs for the neighboring optimal trajectory. The neighboring optimal trajectory was computed using a wind axis simulation with interpolation into an aerodynamic database. The only dependency of the wind axis simulation on the parametric model is through the time varying feedback control gains. Figure 6-29 shows a series of

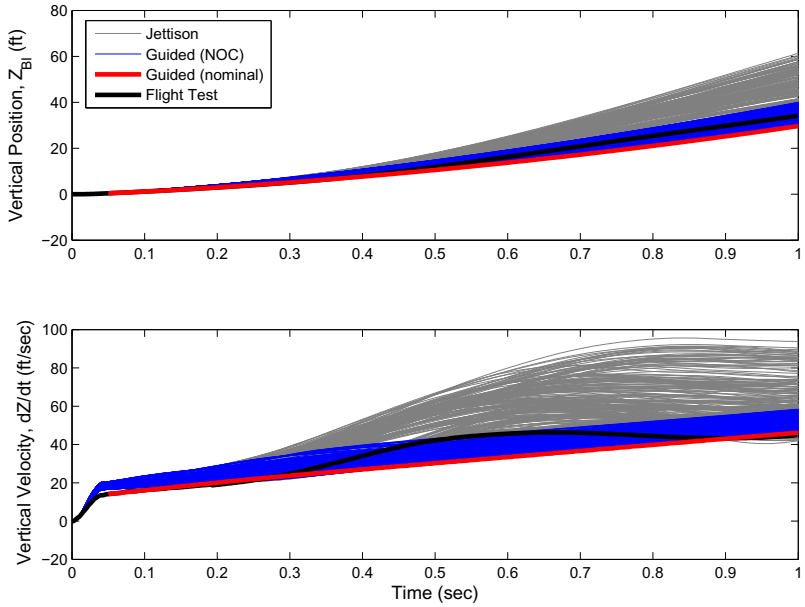

Figure 6-25. Parametric analysis (vertical velocity and translation) for jettison and guided store separation corresponding to flight test 2265 (Mach 0.9 / 4800 ft / 550 KCAS).

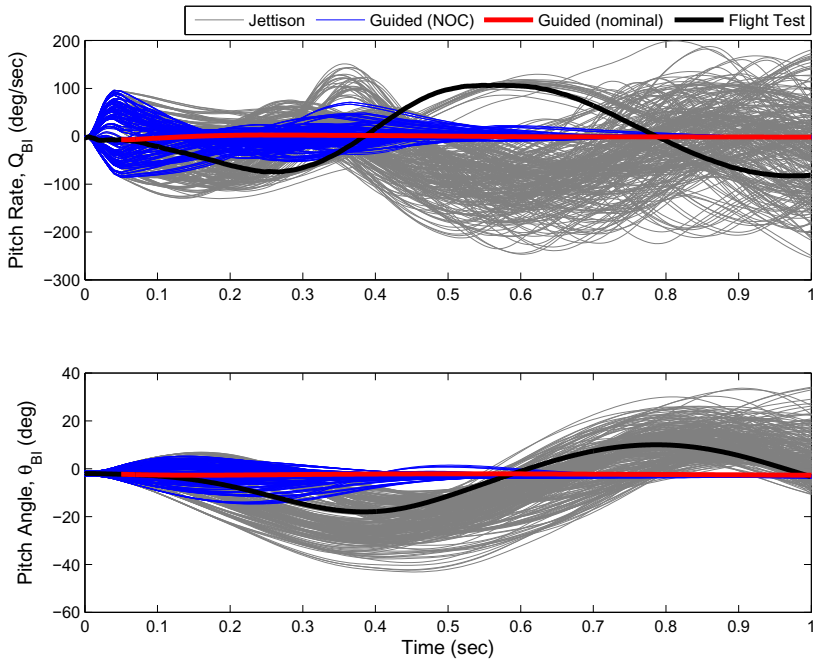

Figure 6-26. Parametric analysis (pitch) for jettison and guided store separation corresponding to flight test 2265 (Mach 0.9 / 4800 ft / 550 KCAS).

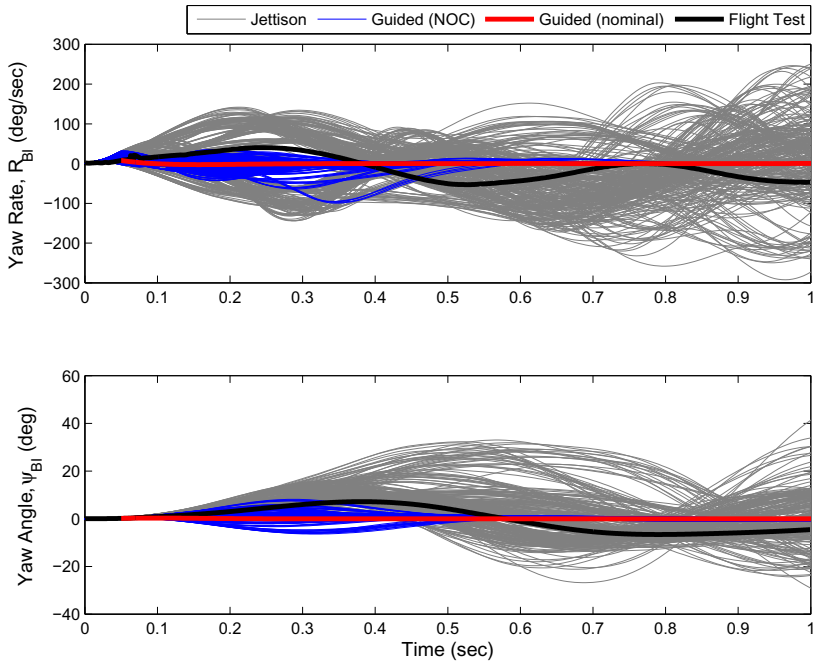

Figure 6-27. Parametric analysis (yaw) for jettison and guided store separation corresponding to flight test 2265 (Mach 0.9 / 4800 ft / 550 KCAS).

neighboring optimal trajectories with varying initial conditions. The results from both figures indicate that the neighboring optimal controller works well when applied to a realistic flight test simulation.

Finally, Figures 6-30 and 6-31 show the results of a parametric analysis using the same set of parameters shown in Table 6-1. The results are similar, providing further validation of the controller in the presence of a strong nonuniform flow field.

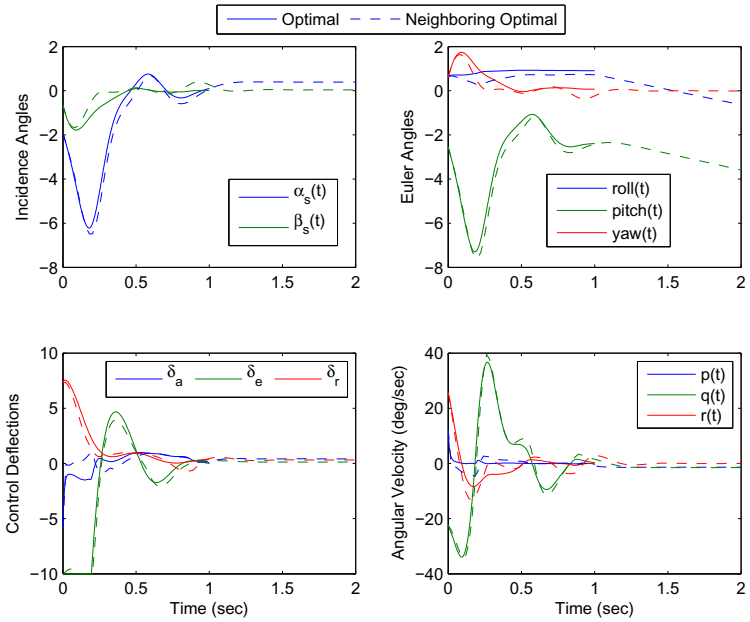

Figure 6-28. Comparison of optimal trajectory and neighboring optimal wind axis simulations for mission 4535 (Mach 1.2 / 600 KCAS / 18kft).

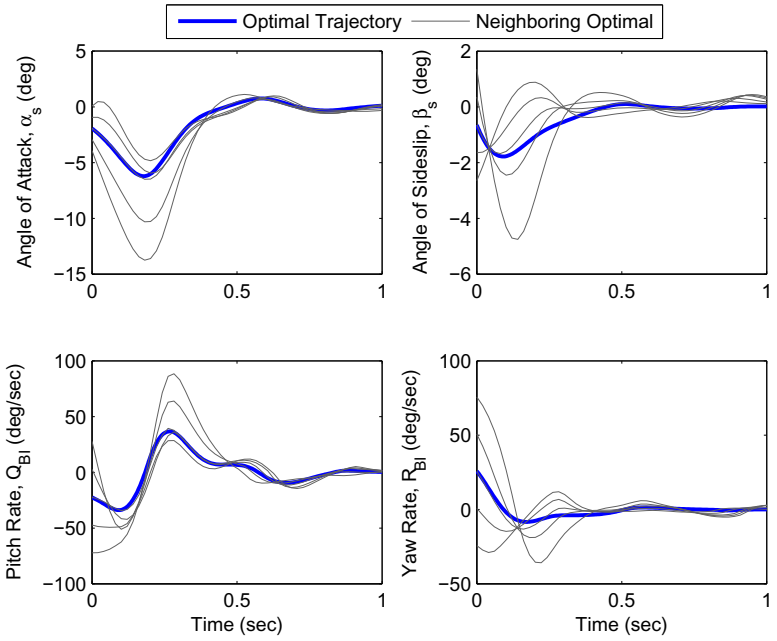

Figure 6-29. Comparison of optimal trajectory and neighboring optimal wind axis simulations with varying initial conditions for mission 4535 (Mach 1.2 / 600 KCAS / 18kft).

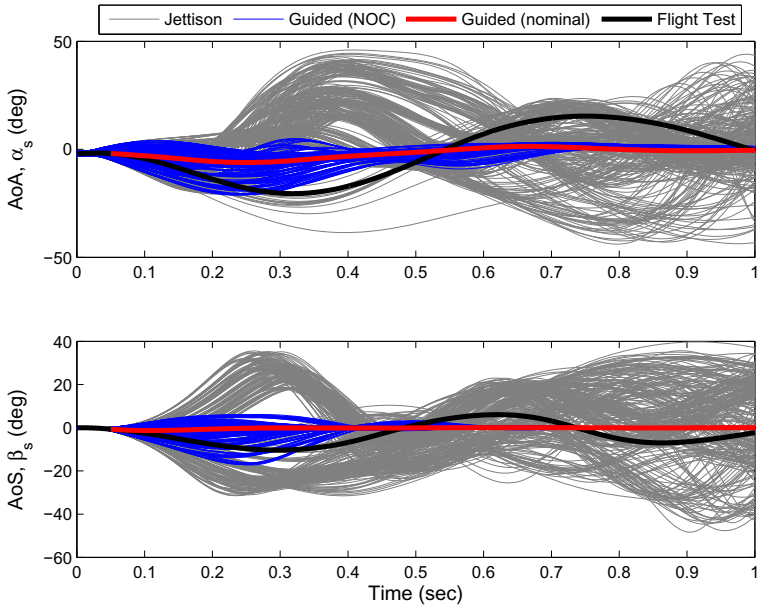

Figure 6-30. Parametric analysis (incidence angles) for jettison and guided store separation corresponding to flight test 4535 (Mach 1.2 / 600 KCAS / 18kft).

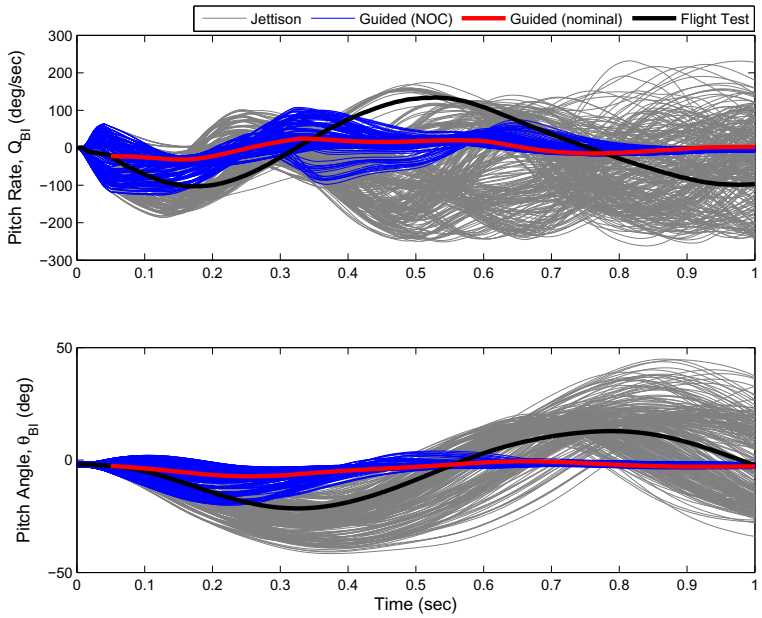

Figure 6-31. Parametric analysis (pitch) for jettison and guided store separation corresponding to flight test 4535 (Mach 1.2 / 600 KCAS / 18kft).

6.4 Chapter Summary

Guided store separation involves parametric modeling of the spatially variant aerodynamics, determination of a preferred trajectory that satisfies safety and acceptability objectives, and design of a feedback controller that accounts for model uncertainties, varying initial conditions, and flow field perturbations. These objectives have been accomplished in detail using system identification, trajectory optimization, and neighboring optimal control. Chapters 3 through 5 presented the necessary theory and examples using a simplified planar store separation problem. This chapter demonstrates the rigorous application of this theory to a full six-dimensional store separation flight test analysis. The optimal trajectories and neighboring optimal feedback gains were computed using a parametric model and a wind axis simulation using conventional database interpolation methods was used to validate the controller in a realistic flight test simulation environment. The results indicate that the store separation autopilot performs well under a variety of conditions, demonstrating the significant improvement in separation characteristics that may be obtained using guided store separation. While this analysis is not exhaustive, the results are promising and indicate that further research and application is warranted.

CHAPTER 7
CONCLUSIONS

7.1 Summary

Combat aircraft utilize expendable stores such as missiles, bombs, flares, and external tanks to execute their missions. Safe and acceptable separation of these stores from the parent aircraft is essential for meeting the mission objectives.

A store released from an aircraft in flight must traverse a nonuniform and unsteady flow field that may include complex shock interactions, large velocity gradients, regions of locally separated or reversed airflow, and severe flow angularity in the form of sidewash and downwash. Stores released from an internal weapons bay may also be subjected to a wake disturbance from the spoiler, dynamic pressure and velocity gradients across the shear layer, high frequency vibrations due to acoustic noise, and large perturbations in flow properties due to cavity oscillations.

Although the region of nonuniform flow near the aircraft is exceedingly small compared to the full length of the store ballistic or fly-out trajectory, the effects are significant. The flow field characteristics may cause the store to exhibit behavior that compromises the safety of the airframe and crew or that compromises the effectiveness of the store itself. Modern guided munitions are designed with an onboard guidance and control system to enable precise engagement of the intended targets. However, the control system is not usually activated until the store is sufficiently far away from the aircraft to avoid any potential interference. Often, the separation-induced transients result in large perturbations from the desired flight attitudes that require a dedicated "rate-capture" phase for recovery before the munition can begin the fly-out trajectory. In the relatively few cases where the autopilot is engaged earlier (to prevent build-up of irrecoverable rates and attitudes), the mutual aerodynamic interference between the store and aircraft is neglected in the autopilot design leading to increased risk through

reduced confidence in simulation capabilities and potentially unsafe behavior of the autopilot reacting to flow field perturbations without consideration of the nearby aircraft.

An alternative approach is to design a guidance and control system that leverages the aerodynamic interaction between the store and aircraft to achieve desirable trajectory characteristics. The development of a store separation guidance and control system, or "store separation autopilot" is the primary focus of this research.

This research and dissertation proceeds in several phases. The store separation equations of motion and aerodynamic modeling approach are developed in Chapter 2. Relevant techniques in system identification are described in Chapter 3 and applied to store separation to develop a parametric model for the spatially variant aerodynamics of a store during separation. Trajectory optimization is explored in Chapter 4 and the 1st order conditions for optimal store separation are developed using classical optimal control theory. Chapter 5 focuses on feedback control using neighboring optimal control to account for variations in initial conditions, system parameters, and flow field perturbations. Finally, Chapter 6 provides an extended application to demonstrate the efficacy of guided store separation for a representative store separating from an F-16 aircraft. A detailed outline for each chapter is summarized below.

Chapter 1. Store separation engineering is described and the motivation for guided store separation is considered. The three-part process of system identification, trajectory optimization, and feedback control is introduced and a brief sketch of the research approach and contributions for each area is presented. Finally, a case study consisting of a representative mid-sized guided munition released from the F-16 tactical aircraft is introduced.

Chapter 2. A comprehensive framework for store separation modeling and simulation is presented. The equations of motion are derived from first principles with consideration of specific coordinate systems and aircraft maneuvers. The equations of motion are derived in both body and wind axes and consolidated in state space form.

Store separation aerodynamic modeling using wind tunnel test data is described and some representative data are presented. The store separation equations of motion are extended for the purpose of flight test data reduction and trajectory reconstruction. Actual flight test data are presented to validate the modeling approach and flight test data are compared to simulated trajectories with favorable results. This brief overview of established store separation methodology provides a solid foundation for the remaining research developments.

Chapter 3. An overview of system identification as applied to flight vehicles is presented and application of SID to store separation is considered. A multisine signal is selected to generate an arbitrary number of inputs that are mutually orthogonal and adhere to a uniform power spectrum, providing an excellent framework for simulation-based system identification. Model structure determination is accomplished using multivariate orthogonal polynomials and parameter estimation is accomplished using the equation error method. Freestream system identification is considered first, resulting in a nonlinear multivariate polynomial model with constant coefficients. The same approach is extended to spatially variant system identification resulting in a nonlinear multivariate polynomial model with spatially variant coefficients. These models are restated in a compact matrix form, providing a single compact parametric model determined directly from wind tunnel test data. The parametric model is compared to wind tunnel and flight test data with favorable results.

Chapter 4. Trajectory optimization is introduced and the store separation problem is restated as an optimal control problem. Store separation is particularly well suited for trajectory optimization using safety and acceptability standards as a performance metric. The equations of motion, parametric model, and desirable trajectory characteristics are combined to establish a well formed optimal control problem and the classical calculus of variation approach is used to derive the first order necessary conditions for optimal store separation. The results form a two point Hamiltonian boundary value problem that

must be solved numerically to determine a feasible open-loop extremal trajectory. The HBVP is readily solved using collocation techniques and provides significant insight into store separation dynamics and control. The final result is a nonlinear, open-loop, extremal trajectory that satisfies the dynamic constraints and minimizes a safety and acceptability performance index. An example using a simplified aerodynamic model and motion confined to the vertical plane is considered in detail.

Chapter 5. The open-loop extremal trajectory considered in Chapter 4 is an exciting development but poses a significant limitation. Each set of initial conditions requires an independent solution of the HBVP. The numerical solution is computationally intensive and not guaranteed to converge. Furthermore, the HBVP implicitly assumes perfect knowledge of the model and operation in a noise free environment. For these reasons, the open-loop control is not suitable for implementation. Rather, neighboring optimal control is used to construct a linear-optimal feedback controller that accounts for variations in initial conditions, model uncertainties, and disturbances along the optimal path. The neighboring optimal controller is based on feedforward of the nominal extremal solution and feedback control that minimizes the original cost function to second order in the presence of disturbances along the optimal path. NOC is extended to consider cases with terminal costs, terminal constraints, path/control inequality constraints, and parameter variations. Infinite Horizon Neighboring Optimal Control is introduced to provide a controller that accounts for the spatially variant aerodynamics through time varying gains near the aircraft and converges to a linear time invariant controller in far field conditions. The IHNOC strategy is ideally suited for store separation and simulation results show favorable performance even in the presence of significant parameter variations and turbulent wind gusts.

Chapter 6. Finally, store separation modeling and simulation, system identification, trajectory optimization, and feedback control are unified in a single extended case study. The case study considers separation of a representative guided munition from the

F-16 aircraft. Trajectory optimization is applied to the nonlinear six-degree-of-freedom equations of motion incorporating the parametric model developed in Chapter 3. Infinite Horizon Neighboring Optimal Control is used to determine time-varying gains that explicitly depend on the spatially variant aerodynamics. The resulting store separation autopilot is validated using a realistic flight test simulation with variations in initial conditions, system parameters, and random disturbances. The analysis is far from exhaustive but the results are promising, indicating that further research is warranted and real world application may be feasible in the near future.

7.2 Contributions

The primary contribution of this research is development of a comprehensive framework for guided store separation that includes parametric modeling, trajectory optimization, and feedback control. The contributions demonstrated in this work along with potential applications are discussed below.

System Identification. This research is the first attempt to construct a parametric model for store separation aerodynamics using system identification. This parametric model is useful in its own right and provides insight into the aerodynamic interaction between the store and aircraft. This approach may also prove to be useful for flight through a nonuniform flow field, such as an aircraft in ground effect or an aircraft flying through a wake vortex, microburst, or wind shear. The key feature of spatially variant system identification is the availability of an accurate aerodynamic database and the techniques demonstrated herein may also be useful for mapping other nonlinear effects, such as high-alpha flight or stall effects. Other applications outside of the aerospace industry may benefit from the demonstration of established techniques in the context of simulation-based system identification.

Trajectory Optimization. This research is the first attempt to apply optimal control theory to determine a “best case” separation trajectory. The more prevalent trend in store separation is to emphasize the “worst case” trajectory to ensure safety and

acceptability in even the most adverse conditions. Trajectory optimization provides a framework for the store separation engineer to actually design a preferred trajectory that inherently satisfies the constraints of the system under consideration. Rather than relying on passive control through aircraft limits and ejector settings, trajectory optimization gives the store separation engineer another degree of freedom for maximizing the capability of a specific aircraft/store combination while providing a direct way to address safety and acceptability. The application of trajectory optimization for guidance of a store through a nonuniform flowfield bears some resemblance to other aerospace challenges, including landing of an aircraft in ground effect or variable winds, aircraft wake-vortex encounter, flight through a microburst or wind shear, flight through severe wind fields in an urban environment, employment of hypersonic research vehicles from high-altitude carrier planes, and flight of multiple aircraft in close proximity such as cooperative configuration or aerial refueling. The first order optimality equations developed in Chapter 4 are general enough to describe many other trajectory optimization problems, provided that the aerodynamics can be modeled appropriately.

Feedback Control. This research is the first attempt to develop a feedback control system that explicitly accounts for the spatially variant aerodynamics of a store during separation. Neighboring optimal control is an elegant and versatile approach for implementing real-time optimal control and it is particularly well suited for store separation. Rather than react to adverse flow conditions during separation, NOC can be used to account for the deterministic flow field features a priori and actually leverage the aerodynamic interaction between the store and aircraft to improve separation characteristics. The heavy computational burden is placed up front and the final result is a simple linear time variant controller than can be readily implemented with existing hardware and firmware common to any modern guided munition. Thus, NOC provides a way to accomplish dramatic improvement in separation characteristics with very little additional complexity of the store guidance and control system. The additional

features incorporated by Infinite Horizon NOC provide a controller that accounts for the spatially variant aerodynamics near the aircraft and rapidly converges to a time invariant regulator in far field conditions. In some cases, the time invariant controller may prove sufficient for the remaining fly out trajectory, allowing construction of a single continuous autopilot for the entire mission profile. The IHNOC strategy may also find application outside of store separation. In particular, IHNOC may be useful for any system that must traverse a nonlinear operating or startup condition, followed by operation near an equilibrium condition for an indeterminate length of time. Regardless, the NOC approach demonstrated here provides a safe and effective method for implementing guided store separation in a realistic environment.

7.3 Future Work

The results presented in this research are inherently dependent on the case study considered. The case study was selected in part due to the benign separation characteristics and adequate control authority. The results demonstrated herein may not be representative of a more challenging system or a store with insufficient control authority. However, every effort has been made to develop a framework that is extensible and applicable to a variety of aircraft/store combinations. Further analysis of stores that are inherently sensitive to flow field conditions or stores that must traverse extremely challenging flow field conditions would be a valuable next step. In particular, application of a store separation autopilot for a store released from an internal weapons bay would offer tremendous insight into the extensibility of this approach.

Store separation from an internal weapons bay would also introduce another challenging element, namely a turbulent and non-stationary flowfield. Although some effort was made in this study to demonstrate the effectiveness of a store separation autopilot in a turbulent flow field, a more appropriate analysis would involve design of an autopilot with explicit consideration of the flow field characteristics. The introduction of a randomly varying disturbance to the system description places the problem in the

domain of stochastic optimal control. Although the application of stochastic optimal control is beyond the scope of this research, the results documented here provide a solid framework for continued research. Extension to stochastic control as well as other extensions are explored in more detail below.

7.3.1 System Identification

The parametric model constructed using system identification in this study is based entirely on wind tunnel test data. This resource was selected primarily due to the ease of implementation and rapid iteration necessary for a preliminary investigation. With improved expectations based on these results, a valuable next step would be to apply system identification to CFD to construct a parametric or reduced order model. The biggest challenge in accomplishing this task is to reduce the amount of "training" data required to construct the model. System identification techniques that have been developed for use with adaptive control, such as recursive least squares [24, 34], may be useful for identifying an aerodynamic model for a store immersed in a nonuniform flow field.

The parameter identification method used in this study is the equation error method. However, this approach may not be valid for CFD-based system identification. Many viscous flow solvers include a turbulence model that is necessary to emulate the flow physics and introduces random perturbations into the predicted aerodynamic coefficients. The equation error method is known to perform poorly in the presence of turbulence [24, 34]. A more suitable choice would be the filter error method, which relies on a Kalman filter variant to propagate the states. Several authors, including Jategaonkar [34], Greenwell [64], Young [69], Klein [24] and Morelli [76], have shown that the filter error method can be used with state augmentation to estimate time-varying parameters. Application of this approach to a CFD-based system identification is promising and merits further investigation.

7.3.2 Trajectory Optimization

The classical indirect approach to optimal control used in this research is very effective and provides a tremendous amount of insight into the dynamics and control of store separation. However, it is also difficult to implement correctly and relies on a fairly complex aerodynamic model. Two methods for improvement are suggested.

First, it is possible to replace the parametric model with a purely empirical model. In the latter case, the aerodynamic coefficients are determined using interpolation of a wind tunnel or CFD database, and the aerodynamic gradients are determined by local finite difference or some other numerical differentiation method. With this approach, an algorithm could be developed once and applied to a range of aircraft / store combinations. A purely numerical approach was considered in this research, with some success, but found to be too computationally expensive for a preliminary investigation.

Second, trajectory optimization using direct methods may be a valuable next step. Optimal control research is dominated by investigations into direct numerical optimization techniques, such as the Gauss Pseudospectral method [95, 108, 118, 119, 125, 157]. These methods do not require an analytical representation of the problem and avoid challenges associated with the costate and 1st order optimality conditions. The convenience comes at the price of less insight into the dynamics and control, but this may be an acceptable tradeoff for long term application of optimal control to store separation.

7.3.3 Feedback Control

The results of the neighboring optimal control approach used in this research is promising. However, further development is required before this approach is suitable for real-world implementation. In particular, two limitations are important to note.

First, careful inspection of the preceding results indicate that the controller is able to respond instantly to changes in the trajectory, which is of course an unrealistic

approximation. In reality, the control surface deflections are limited by the actuator response, which is itself a dynamic system. The control actuators need to be modeled appropriately to assess the impact on the performance of the controller. This feature was not included in the present research because (1) an actuator model is highly specific and requires detailed knowledge of the system that is unavailable to the author and (2) any potential control strategy faces the same actuator limitation, so this limitation is somewhat independent of the particular control strategy employed.

Second, the control strategy in this research is based on full state feedback and it was tacitly assumed that all states are available for feedback. In practice, not all of the states can be measured directly and even those that are can be affected by measurement noise. Thus, full state feedback must incorporate a state estimator to be realized in practice. Due to the nonlinear and spatially varying aerodynamics, development of a suitable state estimation technique is not trivial and may degrade the performance of the controller. This limitation is beyond the scope of the present research, but something that needs to be investigated to improve the readiness of the technology.

7.4 Concluding Remarks

The intent of this research is to demonstrate an improvement in safety and acceptability by applying system identification and trajectory optimization to achieve guided store separation. In many ways, the results exceeded the author's expectations. The application of system identification to store separation required a thorough investigation, but resulted in a compact parametric model with several desirable features. The mathematics behind the classical approach to optimal control are formidable, but provided a comprehensive and robust approach for finding a preferred reference trajectory. The neighboring optimal control strategy required a tremendous amount of problem solving and numerical methods, but resulted in an effective and elegant time varying controller that performed well in every situation examined so far.

Together, system identification, trajectory optimization, and feedback control provide a viable solution to the original research objective with promising potential for future real-world application.

REFERENCES

[1] Thompson, J. T. and Kiber, G. M., "Documentation of a Wind Tunnel 4T Test to Investigate the Separation Characteristics of the [store] Released from the F-16 Aircraft in Support of the Enhanced Smart Triple Ejector Rack (ESTER) Program," Tech. Rep. AEDC-TR-09-F-19, Arnold Engineering Development Center (AEDC), 2009.

[2] Perillo, S. R. and Atkins, D. J., "Challenges and Emerging Trends in Store Separation Engineering – an Air Force SEEK EAGLE Office Perspective," *47th AIAA Aerospace Sciences Meeting*, AIAA-2009-101, American Institute of Aeronautics and Astronautics, Orlando, Florida, 2009.

[3] Keen, K. S., Morgret, C. H., Langham, T. F., and Baker, W. B., "Trajectory Simulations Should Match Flight Tests and Other Lessons Learned in 30 Years of Store-Separation Analysis," *AIAA Aerospace Sciences Meeting*, AIAA 2009-99, American Institute of Aeronautics and Astronautics, Orlando, FL, 2009.

[4] Morelli, E. A., "Global Nonlinear Aerodynamic Modeling Using Multivariate Orthogonal Functions," *Journal of Aircraft*, Vol. 32, No. 2, 1995, pp. 270–278.

[5] Nichols, R. H. and Denny, A. G., "Numerical Simulation of a Store in Controlled Separation," *Applied Aerodynamics Conference*, AIAA-1999-3128, American Institute of Aeronautics and Astronautics, Norfolk, VA, 1999.

[6] Atwood, C. A., "Computation of a Controlled Store Separation from a Cavity," *Journal of Aircraft*, Vol. 32, No. 4, 1995, pp. 846–852.

[7] Rizk, M., Ellison, S., and Prewitt, N. C., "Beggar - A Store Separation Predictive Tool," *32nd AIAA Fluid Dynamics Conference*, AIAA-2002-3190, American Institute of Aeronautics and Astronautics, St. Louis, Missouri, 2002.

[8] Dunworth, K. S., Atkins, D. J., and Lee, J. M., "Incorporation of CFD Generated Aerodynamic Data in Store Separation Predictions," *43rd AIAA Aerospace Sciences Meeting*, AIAA-2005-846, American Institute of Aeronautics and Astronautics, Reno, Nevada, 2005.

[9] Lee, J. M., Dunworth, K. S., Rizk, M., Westmoreland, W. S., and Atkins, D. J., "Studies of Combined Use of CFD and Wind Tunnel Test Approaches to Simulate Store Separation from F-15E Using Efficient CFD Database Generation," *22nd Applied Aerodynamics Conference*, AIAA-2004-4724, American Institute of Aeronautics and Astronautics, Providence, Rhode Island, 2004.

[10] Carter, R. E., "Nominal Performance Characteristics of the Modified MAU-12 Ejector Rack," *2006 International Aircraft-Stores Compatibility Symposium*, International Test and Evaluation Association (ITEA), Fort Walton Beach, Florida, 2006.

[11] Carter, R. E., Diggs, A. S., and Harding, G. H., "Advancements in Ejector Performance Testing: A Technical Overview of the BRU-61 Static Ejection Test," *2010 International Aircraft-Stores Compatibility Symposium*, International Test and Evaluation Association (ITEA), Fort Walton Beach, Florida, 2010.

[12] Baker, W. B., Keen, K. S., and Morgret, C. H., "Validation of Weapon Separation Predictions Using F/A-22 Flight Test Results," *USAF Developmental Test and Evaluation Summit*, AIAA-2004-6803, American Institute of Aeronautics and Astronautics, Woodland Hills, California, 2004.

[13] Morgret, C. H., Dix, R. E., and Lijewski, L. E., "Development of Analytical and Experimental Techniques for Determining Store Airload Distributions," *Journal of Spacecraft and Rockets*, Vol. 19, No. 6, 1982, pp. 489–495.

[14] Rizk, M. and Lee, J. M., "Beggar Code Implementation of the (6+) DOF Capability for Stores with Moving Components," *42nd AIAA Aerospace Sciences Meeting and Exhibit*, AIAA-2004-251, American Institute of Aeronautics and Astronautics, Reno, Nevada, 2004.

[15] Nichols, R. H. and Evans, S. B., "Assesment of Store Control Surface Effectiveness in a Non-Uniform Aircraft Flow Field," *Applied Aerodynamics Conference*, AIAA-1997-2200, American Institute of Aeronautics and Astronautics, Atlanta, Ga, 1997.

[16] Morgret, C. H., "The F-22 Pylon Jettison System: A Case Study in Ejection System Modeling," *2006 International Aircraft-Stores Compatibility Symposium*, International Test and Evaluation Association (ITEA), Fort Walton Beach, Florida, 2006.

[17] Zipfel, P. H., *Modeling and Simulation of Aerospace Vehicle Dynamics*, American Institute of Aeronautics and Astronautics, Reston, Virginia, 2nd ed., 2007.

[18] Roa, A. V., *Dynamics of Particles and Rigid Bodies: A Systematic Approach*, Cambridge University Press, New York, NY, 2006.

[19] Kane, T. R. and Levinson, D. A., *Dynamics, Theory and Applications*, McGraw Hill, 1985.

[20] Mitiguy, P. C. and Kane, T. R., "Motion Variables Leading to Efficient Equations of Motion," *The International Journal of Robotics Research*, Vol. 15, No. 5, 1996, pp. 522–532.

[21] Keen, K. S., "Equations of Store Separation Motion Simulations and Instrumented Model Data Reduction," Tech. Rep. AEDC-TR-95-12, Arnold Engineering Development Center, 1996.

[22] Etkin, B. and Reid, L. D., *Dynamics of Flight: Stability and Control*, John Wiley & Sons, New York, NY, 3rd ed., 1996.

[23] Etkin, B., *Dynamics of Atmospheric Flight*, Dover Publications, Mineola, New York, 1972.

[24] Klein, V. and Morelli, E. A., *Aircraft System Identification: Theory and Practice*, American Institute of Aeronautics and Astronautics, Reston, Virginia, 2006.

[25] Cenko, A., Deslandes, R., Dillenius, M., and Stanek, M., "Unsteady Weapon Bay Aerodynamics – Urban Legend or Flight Clearance Nightmare," *46th AIAA Aerospace Sciences Meeting*, AIAA-2008-189, American Institute of Aeronautics and Astronautics, Reno, Nevada, 2008.

[26] Johnson, R. A., Stanek, M. J., and Grove, J. E., "Store Separation Trajectory Deviations Due to Unsteady Weapons Bay Aerodynamics," *46th AIAA Aerospace Sciences Meeting and Exhibit*, AIAA-2008-188, American Institute of Aeronautics and Astronautics, Reno, Nevada, 2008.

[27] Bamber, M. J., "Store Separation Investigations by Grid Method Using Wind Tunnel Data," Tech. Rep. David Taylor Model Basin Report 2202, 1966.

[28] Morgret, C. H., Moore, D. A., and Smith, M. E., "The FLIP 4 Store-Separation Trajectory Simulation Code," *47th AIAA Aerospace Sciences Meeting*, AIAA-2009-100, American Institute of Aeronautics and Astronautics, Orlando, Florida, 2009.

[29] Veazey, D. T., "Current AEDC Weapons Separation Testing and Analysis to Support Flight Testing," *USAF Developmental Test and Evaluation Summit*, AIAA-2004-6847, American Institute of Aeronautics and Astronautics, Woodland Hills, California, 2004.

[30] Paulick, M. J., "IDAPS - A Store Separation Data Reduction And Analysis System," *2006 International Aircraft-Stores Compatibility Symposium*, International Test and Evaluation Association (ITEA), Fort Walton Beach, Florida, 2006.

[31] Hallberg, E. and Godiksen, W., "MATLAB Based Telemetry Integration Utility for Store Separation Analysis," *U.S. Air Force T&E Days*, AIAA-2007-1643, American Institute of Aeronautics and Astronautics, Destin, Florida, 2007.

[32] Cenko, A. T., Piranian, A. G., and Denihan, S., "Utilizing Flight Test Telemetry Data to Improve Store Trajectory Simulations," *21st Applied Aerodynamics Conference*, AIAA-2003-4225, American Institute of Aeronautics and Astronautics, Orlando, Florida, 2003.

[33] Phillips, W. F., Hailey, C. E., and Gebert, G. A., "A Review of Attitude Kinematics for Aircraft Flight Simulation," *AIAA Modeling and Simulation Conference*, AIAA-2000-4302, American Institute of Aeronautics and Astronautics, Denver, CO, 2000.

[34] Jategaonkar, R. V., *Flight Vehicle System Identification: A Time Domain Methodology*, American Institute of Aeronautics and Astronautics, Reston, VA, 1st ed., 2006.

[35] Astrom, K. J. and Eykhoff, P., "System Identification – A Survey," *Automatica*, Vol. 7, 1971, pp. 123–162.

[36] Eykhoff, P., *System Identification, Parameter and State Estimation*, John Wiley & Sons, New York, NY, 1974.

[37] Goodwin, G. C. and Payne, R. L., *Dynamic System Identification: Experiment Design and Data Analysis*, Academic Press, New York, NY, 1977.

[38] Ljung, L. and Soderstrom, T. S., *Theory and Practice of Recursive Identification*, MIT Press, Cambridge, Mass, 1983.

[39] Schweppe, F. C., *Uncertain Dynamic Systems*, Prentice-Hall, Upper Saddle River, NJ, 1973.

[40] Sage, A. P. and Melsa, J. L., *System Identification*, Academic International Press, New York, NY, 1971.

[41] Hsia, T. C., *System Identification*, Lexington Books, Lexington, Mass, 1977.

[42] Norton, J. P., *An Introduction to Identification*, Academic International Press, London, England, 1986.

[43] Jr., W. F. M., "Progress in Stability and Control Research," *Journal of the Aeronautic Sciences*, Vol. 14, 1947, pp. 494–519.

[44] Greenberg, H., "A Survey of Methods for Determining Stability Parameters of an Airplane from Dynamic Flight Measurements," Tech. Rep. NASA TN 2340, 1951.

[45] Shinbrot, M., "A Least Squares Curve Fitting Method with Applications of the Calculation of Stability Coefficients from Transient-Repsonse Data," Tech. Rep. NACA TN 2341, 1951.

[46] Taylor, L. W., Iliff, K. W., and Powers, B. G., "A Comparison of Newton-Raphson and Other Methods for Determining Stability Derivatives from Flight Data," *American Institute of Aeronautics and Astronautics*, 1969.

[47] Mehra, R. K., "Maximum Likelihood Identification of Aircraft Parameters," *Proceedings of the Joint Automatic Control Conference*, Vol. 18-C, Atlanta, Georgia, 1970.

[48] Stepner, D. E. and Mehra, R. K., "Maximum Likelihood Identification and Optimal Input Design for Identifying Aircraft Stability and Control Derivatives," Tech. Rep. NASA CR-2200, 1973.

[49] Gerlach, O. H., "The Determination of Stability Derivatives and Performance Characteristics from Dynamic Maneuvers," *Society of Automotive Engineers*, , No. Paper 700236, 1970.

[50] Klein, V., "Application of System Identification to High Performance Aircraft," *Proceedings of the 32nd IEEE Conference on Decision and Control*, San Antonio, Texas, 1993.

[51] Klein, V. and Murphy, P. C., "Aerodynamic Parameters of High Performance Aircraft Estimated from Wind Tunnel and Flight Test Data," *System Identification for Integrated Aircraft Development and Flight Testing*, RTO-MP-11, Paper 18, NATO Res. and Techn. Org., 1999.

[52] Mulder, J. A., "Design and Evaluation of Dynamic Flight Test Manoeuvres," Tech. Rep. Report LR-497, Delft Univ. of Tech., Dept. of Aerospace Eng., 1986.

[53] Mehra, R. K., "Optimal Input Signals for Parameter Estimation in Dynamic Systems: Survey and New Results," *IEEE Transactions on Automatic Control*, Vol. AC-19, No. 6, 1974, pp. 753–768.

[54] Mehra, R. K., "Optimal Inputs for Linear System Identification," *IEEE Transactions on Automatic Control*, Vol. AC-19, No. 3, 1974, pp. 192–201.

[55] Morelli, E. A., "Flight Test Validation of Optimal Input Design and Comparison to Conventional Inputs," *AIAA Atmospheric Flight Mechanics Conference*, AIAA-97-3711, American Institute of Aeronautics and Astronautics, New Orleans, Louisiana, 1997.

[56] Morelli, E. A., "Practical Input Optimization for Aircraft Parameter Estimation Experiments," Tech. Rep. NASA Contractor Report 191462, Langley Research Center, 1993.

[57] Iliff, K. W. and Maine, R. E., "Bibliography for Aircraft Parameter Estimation," Tech. Rep. NASA TM 86804, 1986.

[58] Klein, V., "Estimation of Aircraft Aerodynamic Parameters from Flight Data," *Progress in Aerospace Sciences*, Vol. 26, No. 1, 1989, pp. 1–77.

[59] Klein, V., "Identification Evaulation Methods," *Parameter Identification*, AGARD-LS-104, Paper 2, 1972.

[60] Hamel, P. G. and Jategaonkar, R. V., "Evolution of Flight Vehicle System Identification," *Journal of Aircraft*, Vol. 33, No. 1, 1996, pp. 9–29.

[61] Padfield, G. D., "Applications of System Identification in Rotorcraft Flight Dynamics," *Vertica*, Vol. 13, No. 3, 1989, pp. 207–412.

[62] Hamel, P. G. and Kaletka, J., "Advances in Rotorcraft System Identification," *Progress in Aerospace Sciences*, Vol. 33, No. 3/4, 1997, pp. 259–284.

[63] Iliff, K. W., "Flight-Determined Subsonic Longitudinal Stability and Control Derivatives of the F-18 High Angle of Attach Research Vehicle (HARV) With Thrust Vectoring," Tech. Rep. NASA TP-97-206539, 1997.

[64] Greenwell, D. I., "A Review of Unsteady Aerodynamics Modelling for Flight Dynamics of Manoeuvrable Aircraft," *AIAA Atmonspheric Flight Mechanics Conference and Exhibit*, AIAA-2004-5276, American Institute of Aeronautics and Astronautics, Providence, Rhode Island, 2004.

[65] Vicroy, D., Brandon, J., and Greene, G., "Characterizing the Hazard of a Wake Vortex Encounter," *American Institute of Aeronautics and Astronautics*, 1997.

[66] Pete, K. R., Smith, S. T., and Vicroy, D., "Model Validation of Wake-Vortex / Aircraft Encounters," *American Institute of Aeronautics and Astronautics*, 2000.

[67] Fischenberg, D., "Ground Effect Modeling Using a Hybrid Approach of Inverse Simulation and System Identification," *American Institute of Aeronautics and Astronautics*, 1999.

[68] Jategaonkar, R. V., "Identification of Speed Brake, Air-Drop, and Landing Gear Effects from Flight Data," *Journal of Aircraft*, Vol. 34, No. 2, 1997, pp. 174–180.

[69] Young, P., *Recursive Estimation and Time-Series Analysis*, Springer, Berlin, 1984.

[70] Dean, J. P. and Morton, S. A., "Efficient High Resolution Modeling of Fighter Aircraft with Stores for Stability and Control Clearance," *U.S. Air Force Test and Evaluation Days*, AIAA-2007-1652, American Institute of Aeronautics and Astronautics, Destin, Florida, 2007.

[71] Dean, J. P., Morton, S. A., McDaniel, D. R., Clifton, J. D., and Bodkin, D. J., "Aircraft Stability and Control Characteristics Determined by System Identification of CFD Simulations," *AIAA Atmonspheric Flight Mechanics Conference and Exhibit*, American Institute of Aeronautics and Astronautics, Honolulu, Hawaii, 2008.

[72] Green, B. E. and Chung, J. J., "CFD Predictions of the Stability and Control Characteristics of the Pre-Production F/A-18E," *AIAA Atmospheric Flight Mechanics Conference and Exhibit*, AIAA-2005-6122, American Institute of Aeronautics and Astronautics, San Francisco, California, 2005.

[73] Bodkin, D. J., Dean, J. P., and Clifton, J. D., "Computational Stability and Control of Maneuvering Aircraft with Stores Using CFD on DoD HPC Resources," *2010 Aircraft-Stores Compatibility Symposium*, International Test and Evaluation Association, Fort Walton Beach, FL, 2010.

[74] Clifton, J. D., Dean, J. P., and Bodkin, D. J., "Static Stability and Performance Calculations of Fighter Aircraft with Stores Using CFD on DoD HPC Resources," *2010 Aircraft-Stores Compatibility Symposium*, International Test and Evaluation Association, Fort Walton Beach, Florida, 2010.

[75] Schroeder, M. R., "Synthesis of Low-Peak-Factor Signals and Binary Sequences with Low Autocorrelation," *IEEE Transactions on Automatic Control*, Vol. IT-18, No. 1, 1970, pp. 85–89.

[76] Morelli, E. A., "Multiple Input Design for Real-Time Parameter Estimation in the Frequency Domain," *13th IFAC Symposium on System Identification*, Paper REG-360, IFAC, 2003.

[77] Young, P. and Patton, R. J., "Comparison of Test Signals for Aircraft Frequency Domain Identification," *Journal of Guidance, Control, and Dynamics*, Vol. 13, No. 3, 1990, pp. 430–438.

[78] Bosworth, J. T. and Burken, J. J., "Tailored Excitation for Multivariable Stability-Margin Measurement Applied to the X-31A Nonlinear Simulation," *American Institute of Aeronautics and Astronautics*, 1997.

[79] O'Neill, C. R. and Arena, A. S., "Comparison of Time Domain Training Signals for CFD Based Aerodynamic Identification," *42nd AIAA Aerospace Sciences Meeting and Exhibit*, AIAA-2004-209, American Institute of Aeronautics and Astronautics, Reno, Nevada, 2004.

[80] Jirasek, A., Jeans, T. L., and Martenson, M., "Improved Methodologies for Maneuver Design of Aircraft Stability and Control Simulations," *48th AIAA Aerospace Sciences Meeting*, AIAA-2010-515, American Institute of Aeronautics and Astronautics, Orlando, FL, 2010.

[81] Morelli, E. A., "System Identification Programs for Aircraft (SIDPAC)," *AIAA Atmospheric Flight Mechanics Conference and Exhibit*, AIAA-2002-4704, American Institute of Aeronautics and Astronautics, Monterey, California, 2002.

[82] Morelli, E. A., "Global Nonlinear Parametric Modeling with Application to F-16 Aerodynamics," Tech. Rep. ACC-I-98010-2, NASA Langley Research Center, 1998.

[83] Barron, A. R., "Predicted Squared Error: A Criterion for Automatic Model Selection," *Self-Organizing Methods in Modeling*, edited by S.J. Farlow and Marcel Dekker, New York, NY, 1984.

[84] Balakrishnan, A. V., "Stochastic System Identification Techniques," *Stochastic Estimation and Control*, John Wiley & Sons, London, 1968.

[85] Mehra, R. K., "Maximum Likelihood Identification of Aircraft Parameters," *Proceedings of the 11th Joint Automatic Control Conference*, Atlanta, Ga, 1970.

[86] Iliff, K. W., "Identification and Stochastic Control with Applications to Flight Control in Turbulence," 1973.

[87] Bryson, A. E., *Dynamic Optimization*, Taylor and Francis, Menlo Park, CA, 1999.

[88] Athans, M., "The Status of Optimal Control Theory and Applications for Deterministic Systems," *IEEE Transactions on Automatic Control*, 1966, pp. 580–597.

[89] Breakwell, J. V., "The Optimization of Trajectories," *Journal of the Society for Industrial and Applied Mathematics*, Vol. 7, 1959, pp. 215–247.

[90] Duersch, R., "Application of optimization theory to the design of a missile control," *Proceedings of JACC*, 1965, pp. 483–498.

[91] Mendel, J. M., "Self-Organizing Control Systems - Vol 2: Open-loop time-optimal control of a stable maneuverable reentry vehicle," Tech. Rep. SM-47904, Douglas Missile and Space Div, 1965.

[92] Shaffer, P. J. and Ross, M. I., "Optimal Trajectory Reconfiguration and Retargeting for Reusable Launch Vehicles," *Journal of Guidance, Control and Dynamics*, Vol. 30, No. 6, 2007.

[93] Merriam, C. W., *Optimization Theory and the Design of Feedback Control Systems*, McGraw-Hill, New York, NY, 1966.

[94] Bryson, A. E. and Hoffman, W. C., "The Energy-State Approximation in Performance Optimization of Supersonic Aircraft," *AIAA Guidance, Control, and Flight Dynamics Conference*, AIAA-1968-877, American Institute of Aeronautics and Astronautics, Pasedena, California, 1968.

[95] Darby, C. L., *HP–Pseudospectral Method for Solving Continuous-Time Nonlinear Optimal Control Problems*, Ph.D. thesis, University of Florida, 2011.

[96] Fleming, A., Sekhavat, P., and Ross, I. M., "Minimum-Time Reorientation of an Asymmetric Rigid Body," *AIAA Guidance, Navigation and Control Conference*, AIAA-2008-7012, American Institute of Aeronautics and Astronautics, Honolulu, Hawaii, 2008.

[97] Ross, I. M., "Low-Thrust, High-Accuracy Trajectory Optimization," *Journal of Guidance, Control and Dynamics*, Vol. 30, No. 4, 2007.

[98] Infeld, S. I., Josselyn, S. B., and Murray, W., "Design and Control of Libration Point Spacecraft Formations," *Proceedings of AIAA Guidance, Navigation, and Control Conference*, AIAA-2004-4786, American Institute of Aeronautics and Astronautics, Providence, RI, 2004.

[99] Gong, Q. and Ross, I. M., "Triangle Formation Design in Eccentric Orbits Using Pseudospectral Optimal Control," *AIAA/AAS Astrodynamics Specialist Conference*, AIAA-2008-7360, American Institute of Aeronautics and Astronautics, Honolulu, Hawaii, 2008.

[100] Bollino, K. and Lewis, L. R., "Collision-Free Multi-UAV Optimal Path Planning and Cooperative Control for Tactical Applications," *AIAA Guidance, Navigation, and Control Conference*, AIAA-2008-7134, American Institute of Aeronautics and Astronautics, Honolulu, Hawaii, 2008.

[101] Bollino, K. and Lewis, L. R., "Optimal Path Planning and Control of Tactical Unmanned Aerial Vehicles in Urban Environments," *Proceedings of AUVSI's Unmanned Systems North America 2007 Conference*, Washington, D.C., 2007.

[102] Zollars, M., Blue, P., and Burns, B., "Wind Corrected Flight Path Planning for Autonomous Micro Air Vehicles Utilizing Optimization Techniques," *AIAA Atmospheric Flight Mechanics Conference*, AIAA-2007-6497, American Institute of Aeronautics and Astronautics, Hilton Head, SC, 2007.

[103] Jardin, M. R., "Analytical Solutions for Minimum-Time Neighboring Optimal Aircraft Guidance in Winds," *AIAA Guidance, Navigation and Control Conference and Exhibit*, AIAA 2008-6977, American Institute of Aeronautics and Astronautics, Honolulu, Hawaii, 2 - 5 August 2010 2008.

[104] Jardin, M. R. and Bryson, A. E., "Methods for Computing Minimum-Time Paths in Strong Winds," *AIAA Guidance, Navigation, and Control Conference*, AIAA 2010-8398, American Institute of Aeronautics and Astronautics, Toronto, Ontario Canada, 2010.

[105] Mulgund, S. S. and Stengel, R. F., "Optimal Recovery from Microburst Wind Shear," *Journal of Guidance, Control and Dynamics*, Vol. 16, No. 6, 1993, pp. 1010.

[106] Pourtakdoust, S. H., "Optimal trajectory planning for flight through microburst wind shears," *Aerospace Science and Technology*, Vol. 15, No. 7, 2011, pp. 567–576.

[107] Harada, M. and Bollino, K., "Optimal Trajectory of a Glider in Ground Effect and Wind Shear," *Proceedings of AIAA Guidance, Navigation, and Control Conference*, AIAA-2005-6474, American Institute of Aeronautics and Astronautics, San Francisco, California, 2005.

[108] Hurni, M. A., Sekhavat, P., Karpenko, M., and Ross, I. M., "A Pseudospectral Optimal Motion Planner for Autonomous Unmanned Vehicles," *American Control Conference*, ACC, Baltimore, MD, 2010.

[109] D'Alessandro, D., "Contributions of control theory to fundamental quantum mechanics and its applications," *Decision and Control*, Vol. 4, 2002, pp. 4569–4574.

[110] HE, X., "Study of Optimal Control model for environmental economics of regions," *Information and Financial Engineering*, ICIFE, 2010.

[111] Bryson, A. E., *Applied Linear Optimal Control*, Cambridge University Press, Cambridge, 2002.

[112] Bryson, A. E., *Control of Spacecraft and Aircraft*, Princeton University Press, Princeton, New Jersey, 1994.

[113] Bryson, A. E. and Ho, Y. C., *Applied Optimal Control*, Taylor and Francis, New York, 1975.

[114] Kirk, D. E., *Optimal Control Theory*, Dover Publications, Mineola, NY, 2004.

[115] Athans, M. and Falb, P. L., *Optimal Control*, Dover Publications, Mineola, NY, 2007.

[116] Stengel, R. F., *Optimal Control and Estimation*, Collegiate Publishers, New York, 2009.

[117] Ross, I. M., *A Primer on Pontryagin's Principle in Optimal Control*, Collegiate Publishers, San Francisco, 2009.

[118] Ross, I. M., "A Roadmap for Optimal Control: The Right Way to Commute," *Annals of the New York Academy of Sciences*, Vol. 1065, 2006, pp. 132–137.

[119] Ross, I. M., Sekhavat, P., Fleming, A., and Gong, Q., "Optimal Feedback Control: Foundations, Examples, and Experimental Results for a New Approach," *Journal of Guidance, Control, and Dynamics*, Vol. 31, No. 3, 2008.

[120] Press, W. H., Flannery, B. P., and Teukolsky, S., *Numerical Recipes: The Art of Scientific Computing*, Cambridge University Press, Cambridge, 1990.

[121] Keller, H. B., "Numerical Solution of Two Point Boundary Value Problems," *J. Soc. Indus. and Appl. Math*, 1976.

[122] Russell, R. D., "A Collocation Method for Boundary Value Problems," *Numerical Methods*, Vol. 19, No. 1, 1972, pp. 1–28.

[123] Bock, H. G. and Plitt, K. J., "A Multiple Shooting Algorithm for Direct Solution of Optimal Control Problems," *IFAC 9th World Congress*, Budapest, Hungary, 1984.

[124] Hargraves, C. R., "Direct Trajectory Optimization Using Nonlinear Programming Techniques," *Journal of Guidance, Control and Dynamics*, Vol. 10, No. 4, 1987, pp. 338–342.

[125] Rao, A. V., Benson, D. A., and Darby, C. L., "Algorithm 902: GPOPS, A Matlab Software for Solving Multiple-Phase Optimal Control Problems Using the Gauss Pseudospectral Method," *ACM Transactions on Mathematical Software*, Vol. 37, No. 2, 2010, pp. 22:1–22:39.

[126] Shampine, L. F., Kierzenka, J., and Reichelt, M. W., "Solving Boundary Value Problems for Ordinary Differential Equations in Matlab with bvp4c," Tech. rep., Mathworks, 2000.

[127] Kelley, H., "Guidance Theory and Extremal Fields," *IRE Transactions on Automatic Control*, 1962.

[128] Breakwellf, J. V., Speyer, J. L., and Bryson, A. E., "Optimization and Control of Nonlinear Systems Using the Second Variation," *Journal of the Society for Industrial and Applied Mathematics, Series A: Control*, Vol. 1, No. 2, January 1963 1963, pp. 193–223.

[129] Pesch, H., "The Accessory Minimum Problem and Its Importance for the Numerical Computation of Closed-Loop Controls," *Proceedings of the 29th Conference on Decision and Control*, 1990.

[130] Hull, D. G. and Sheen, J. J., "A Shooting approach to suboptimal control," *American Control Conference*, Boston, Ma, 1991.

[131] Jacobson, D. and M.M., L., "A Transformation Technique for Optimal Control Problems with a State Variable Inequality Constraint," *IEEE Transactions on Automatic Control*, Vol. 14, No. 5, October 1969, pp. 457–464.

[132] Lee, A., "Neighboring Extremals of Dynamic Optimization Problems with Path Equality Constraints," *Journal of Optimization Theory and Applications*, Vol. 57, No. 3, June 1988, pp. 519–536.

[133] Kugelmann, B., Pesch, H., and Hull, D., "New General Guidance Method in Constrained Optimal Control, Part 1: Numerical Method," *Journal of Optimization Theory and Applications*, Vol. 67, No. 3, 1990, pp. 421–435.

[134] Kugelmann, B., Pesch, H., and Hull, D., "New General Guidance Method in Constrained Optimal Control, Part 2: Application to Space Shuttle Guidance," *Journal of Optimization Theory and Applications*, Vol. 67, No. 3, 1990, pp. 437–446.

[135] Hymas, C. E., Cavin, R. K., and Colunga, D., "Neighboring Extremals for Optimal Control Problems," *AIAA Journal*, Vol. 11, No. 8, 1973, pp. 1101–1109.

[136] Fisher, M., Grantham, W., and Teo, K., "Neighbouring Extremals for Nonlinear Systems with Control Constraints," *Dynamics and Control*, Vol. 5, 1995, pp. 225–240.

[137] Lee, A. Y. and Bryson, A. E., "Neighbouring Extremals of Dynamic Optimization Problems with Parameter Variations," *Optimal Control Applications and Methods*, Vol. 10, No. 1, 1989, pp. 39–52.

[138] D'Souza, C. and Hull, D., "Second Variation Conditions for Optimal Control Problems with Parameters," *American Control Conference*, 1992, pp. 190–191.

[139] Kim, T. J. and Hull, D. G., "Neighboring Extremal Optimal Control Design Including Model Mismatch Errors," Tech. Rep. SAND94-2902C, Department of Energy, 1994.

[140] Hull, D., "Sufficiency for Optimal Control Problems Inolving Parameters," *Journal of Optimization Theory and Applications*, Vol. 97, 1998, pp. 597–590.

[141] Shaver, D. A. and Hull, D. G., "Advanced Launch System Trajectory Optimization Using Suboptimal Control," *AIAA Guidance, Navigation and Control Conference*, American Institute of Aeronautics and Astronautics, Portland, Oregon, 1990.

[142] Eisler, G. R. and Hull, D., "Guidance law for planar hypersonic descent to a point," *Journal of Guidance, Control, and Dynamics*, Vol. 16, No. 2, 1993, pp. 400–402.

[143] Hull, D. G. and Nowak, M. J., "Neighboring Suboptimal Control for Vehicle Guidance," *Third Annual AAS/AIAA Space Flight Mechanics Conference*, American Institute of Aeronautics and Astronautics, Pasedena, CA, 1993.

[144] Kumar, R. R., Seywald, H., and Cliff, E. M., "Near-Optimal Three-Dimensional Air-to-Air Missile Guidance Against Maneuvering Target," *Journal of Guidance, Control, and Dynamics*, Vol. 18, No. 3, 1995, pp. 457–464.

[145] Korytowski, A., Szymkat, M., and Trunau, A., "Neighboring optimization for constrained control problems in real time," *IEEE International Symposium on Computer Aided Control System Design*, IEEE, Glasgow, Scotland, U.K., 2002.

[146] Yan, H., Fahroo, F., and Ross, M. I., "Real-Time Computation of Neighboring Optimal Control Laws," *AIAA Guidance, Navigation, and Control Conference*, AIAA 2002-4657, American Institute of Aeronautics and Astronautics, Monterey, Ca, 2002.

[147] Jardin, M. R., "Toward Real-Time En Route Air Traffic Control Optimization," 2003.

[148] Jardin, M. R., "Ideal free flight through multiple aircraft neighboring optimal control," *American Control Conference*, Vol. 4, IEEE, 2000, pp. 2879–2885 vol. 4.

[149] Jardin, M. R. and Bryson, A. E., "Nieghboring Optimal Aircraft Guidance in Winds," *AIAA Guidance, Navigation, and Control Conference*, AIAA-2000-4264, American Institute of Aeronautics and Astronautics, Denver, Co, 2000.

[150] Jardin, M. R. and Bryson, A. E., "Neighboring Optimal Aircraft Guidance in Winds," *Journal of Guidance, Control, and Dynamics*, Vol. 24, No. 4, 2001, pp. 710–715.

[151] Ghaemi, R., Sun, J., and Kolmanovsky, I. V., "Neighboring Extremal Solution for Nonlinear Discrete-Time Optimal Control Problems With State Inequality Constraints," *IEEE Transactions on Automatic Control,*, Vol. 54, No. 11, 2009, pp. 2674–2679.

[152] Jiang, Z., "Robust Approach and Landing Trajectory Generation for Reusable Launch Vehicles in Winds," *17th IEEE International Conference on Control Applications*, 2008 IEEE Multi-conference on Systems and Control, San Antonio, Texas, 2008, pp. 930–935.

[153] Gros, S., Srinivasan, B., and Bonvin, D., "Robust Predictive Control based on Neighboring Extremals," *Journal of Process Control*, Vol. 16, 2006, pp. 243–253.

[154] Jiang, Z., "Disturbance Rejection in Approach and Landing Trajectory Generation for RLVs," *Aerospace and Electronics Conference*, 2008.

[155] Jardin, M. R., "Air traffic conflict models," *AIAA 4th Aviation Technology, Integration and Operations (ATIO) Forum*, American Institute of Aeronautics and Astronautics, Chicago, Illinois, 2004.

[156] Elston, J. and Frew, E., "Unmanned aircraft guidance for penetration of pre-tornadic storms," *AIAA Guidance, Navigation and Control Conference*, AIAA-2008-6513, American Institute of Aeronautics and Astronautics, Honolulu, Hawaii, 2008.

[157] Gong, Q., Kang, W., and Ross, I. M., "A Pseudospectral Method for the Optimal Control of Constrained Feedback Linearizable Systems," *IEEE Transactions on Automatic Control*, Vol. 51, No. 7, 2006, pp. 1115.

BIOGRAPHICAL SKETCH

Ryan E. Carter is an aerospace engineer for the United States Air Force. Ryan earned a degree in Aerospace Engineering from Auburn University in 2003 and a Master of Science degree in engineering from the University of Florida in 2005. He has worked as a Store Separation Engineer for the Air Force SEEK EAGLE Office for more than 8 years and has hands-on experience with a variety of aircraft including the F-16, B-1B and F-22. In 2009, Ryan was awarded the highly competitive SMART Scholarship, a collaborative effort of the American Society for Engineering Education (ASEE) and the Naval Postgraduate School (NPS). Under the SMART Scholarship, Ryan is working full-time on a doctorate at the University of Florida, with an expected graduation date of August 2012.

Ryan is also the proud father of five beautiful and lively children, including four boys and one girl between the ages of 4 and 9. Ryan and his family live in Crestview, FL and make the most of every opportunity to enjoy family adventures and outdoor activities. Their favorite activities include traveling, camping, hiking, and mountain biking. After graduation, Ryan plans to resume his career with the USAF as he continues to invest in the discipleship of his family. Perhaps they will even take a trip to Disney World.